UNIVERSIDADE DE SÃO PAULO

INSTITUTO DE FÍSICA

"Um Método para Determinação Experimental da Densidade da Matéria Nuclear"

Marcos Aurélio Gonzalez Alvarez

Tese apresentada ao Instituto de Física da Universidade de São Paulo para obtenção do título de Doutor em Ciências.

Banca Examinadora:

Dr. Diógenes Galetti (IFT)
Dr. Paulo Roberto Silva Gomes (UFF)
Dr. Nelson Carlin Filho (IFUSP)
Dr. Rubens Lichtenthäler Filho (IFUSP)
Dr. Luiz Carlos Chamon (Orientador – IFUSP)

São Paulo
2002

Prof. Armando Corbani Ferraz
Presidente da Comissão de Pós Graduação

def. 12/12/02

FICHA CATALOGRÁFICA
Preparada pelo Serviço de Biblioteca e Informação do Instituto de Física da Universidade de São Paulo

Gonzalez Alvarez, Marcos Aurélio

Um método para determinação experimental da densidade da matéria nuclear. São Paulo, 2002

Tese (Doutoramento) Universidade de São Paulo
Instituto de Física. Departamento de Física Nuclear

Orientador: Prof. Dr. Luiz Carlos Chamon
Área de Concentração: Física Nuclear

Unitermos: 1. Reações nucleares; 2. Íons pesados; 3. Densidade nuclear.

USP/IF/SBI-070/2002

A Aurélio Gonzalez Fernandez e Maria Del Carmen Alvarez Gonzalez.

AGRADECIMENTOS

Agradeço à FUNDAÇÃO de AMPARO à PESQUISA do ESTADO DE SÃO PAULO (FAPESP) na figura do Ilmo. Diretor Científico, Dr. José Fernando Perez, pelo financiamento integral deste projeto.

Agradeço ao Dr. Luiz Carlos Chamon, meu Orientador, a quem também dedico este trabalho, pela sua amizade, liderança, confiança em mim depositada para realização das diversas etapas deste trabalho e pela sua responsabilidade sobre o sucesso dos resultados aqui apresentados.

Aos meus pais Aurélio Gonzalez Fernandez e Maria del Carmen Alvarez Gonzalez, dedico não só este trabalho, mas também toda minha vida.

Agradeço ao meu irmão Dr. Roberto Gonzalez Alvarez.

Agradeço a Daniel Gonzalez Alvarez, Daniela Gomes Alvarez e Ricardo Gomes Alvarez, minha família.

Agradeço ao Sr. Ricardo Alvarez, por todo acompanhamento durante toda minha vida pessoal e acadêmica.

Agradeço ao Dr. Dirceu Pereira, chefe do meu grupo de pesquisa, por sua amizade e apoio.

Agradeço ao Dr. Ernesto Silvio Rossi Jr. e à Dra. Cely Paula Silva pela amizade e colaboração em algumas etapas deste projeto.

Agradeço à colaboração e divido com prazer os "frutos" deste projeto com meu grande amigo e companheiro de várias etapas deste e "outros" trabalhos, o Sr. Leandro Romero Gasques.

Agradeço aos membros da minha segunda família: Dimaura, Alexandre Gadelha, Eneida e de forma especial à Babi por todo seu amor.

Um agradecimento especial ao amigo Fábio Furlan Ferreira.

Dedico este trabalho aos amigos do "TEQUILA F. S."

Agradeço a todos que direta ou indiretamente colaboraram para a existência das páginas que seguem, principalmente aos funcionários do Laboratório Pelletron.

"Obrigado, meu Deus, pelo desenvolvimento e conclusão deste projeto e pela oportunidade de prestar uma homenagem a estas pessoas".

RESUMO

Neste trabalho foi proposto um método de deconvolução para extrair experimentalmente a densidade da matéria nuclear no estado fundamental a partir de dados de espalhamento elástico entre íons pesados em energias baixas (abaixo da barreira de fusão) e intermediárias. A consistência dos resultados foi totalmente verificada. O método se mostrou uma poderosa ferramenta para a determinação experimental da densidade da matéria de núcleos no estado fundamental, particularmente em uma região superficial, onde a diferença entre a densidade de núcleos exóticos e núcleos estáveis vizinhos é muito enfatizada.

Foram realizadas medidas de seções de choque de espalhamento elástico para os sistemas ^{16}O + ^{40}Ca, ^{120}Sn, com o objetivo de ajudar na construção de uma sistemática experimental para a parte real da interação nuclear, e para obter a densidade experimental da matéria nuclear no estado fundamental para o núcleo ^{16}O.

Como complemento, o trabalho apresenta: i-) uma sistemática teórica das densidades nucleares, realizada para toda região de massa da tabela periódica; ii-) o modelo não-local, desenvolvido para descrever a dependência com a energia da parte real da interação nuclear; e iii-) uma nova representação para a absorção de fluxo, devido aos canais de reação. Com isso, foi desenvolvida uma sistematização para o potencial ótico a partir de uma análise consistente de dados de espalhamento elástico de íons pesados em energias baixas e intermediárias. Esta análise resultou em uma previsão extremamente satisfatória para as seções de choque de espalhamento elástico experimentais, para um vasto conjunto de dados, utilizando um modelo bastante fundamental e global para o potencial ótico e, mais importante, sem a utilização de parâmetros livres.

ABSTRACT

An unfolding method is proposed to extract ground-state nuclear matter densities from heavy-ion elastic scattering data analyses at low (sub-barrier) and intermediate energies. The consistency of the results was fully checked. The method is a powerful tool to obtain ground-state nuclear matter densities, particularly at the surface region where the difference between densities of exotic and stable neighbour nuclei is very emphasized.

Precise elastic scattering cross sections were measured for the systems ^{16}O + ^{40}Ca, ^{120}Sn, with the aim of helping the construction of an experimental systematics for the real part of the nuclear interaction, and to obtain the experimental ground-state nuclear matter density for the ^{16}O nucleus.

As a complement, this work presents: i-) A theoretical systematics for nuclear densities which was performed for the whole mass region throughout the periodic table; ii-) the non-local model, developed to describe the energy dependence of the real part of the nuclear interaction; and iii-) a new representation for the absorption of flux due to the reaction channels. This framework has allowed us to obtain a systematization of the optical potential from a consistent heavy-ion elastic scattering data analysis at low and intermediate energies. This analysis resulted a remarkable prediction for a very large elastic scattering cross section data set using a global and fundamental parameter-free model for the optical potential.

ÍNDICE

I INTRODUÇÃO ... 6

I.1 UM BREVE PANORAMA SOBRE A FÍSICA DE REAÇÕES NUCLEARES ... 6
I.2 INTRODUÇÃO HISTÓRICA E ORIGEM DO TRABALHO ... 8
I.3 DENSIDADE NUCLEAR: "UMA QUESTÃO EM ABERTO" ... 12
I.4 DESENVOLVIMENTO DO TRABALHO ... 13

II PARTE TEÓRICA ... 16

II.1 O POTENCIAL SEGUNDO A EQUAÇÃO DE SCHRÖDINGER ... 16
II.2 DESENVOLVIMENTO DO POTENCIAL NUCLEAR ... 18
II.2.1 O Potencial Coulombiano ... 18
II.2.2 O Potencial Ótico ... 18
II.2.3 O Potencial Double-Folding ... 21
II.2.4 O Potencial Não-Local ... 25
II.2.5 A Parte Imaginária do Potencial Ótico ... 28

III O MÉTODO PARA DETERMINAÇÃO EXPERIMENTAL DA DENSIDADE DA MATÉRIA NUCLEAR ... 30

III.1 SISTEMATIZAÇÃO DA DENSIDADE NUCLEAR ... 44

IV SISTEMATIZAÇÃO DO POTENCIAL ÓTICO ... 50

V PARTE EXPERIMENTAL ... 57

V.1 INTRODUÇÃO ... 57
V.2 A FONTE DE ÍONS ... 59
V.3 O ACELERADOR PELLETRON ... 61
V.4 A CÂMARA DE ESPALHAMENTO ... 64
V.5 O SISTEMA DE DETECÇÃO ... 65
V.6 PRINCÍPIO DE OPERAÇÃO DO DETECTOR PROPORCIONAL ... 66
V.7 DESCRIÇÃO DO IDENTIFICADOR DE PARTÍCULAS UTILIZADO ... 68
V.8 CARACTERIZAÇÃO DO DETECTOR PROPORCIONAL A GÁS ... 69
V.9 ELETRÔNICA DE AQUISIÇÃO ... 72
V.10 O ESPECTRO BIPARAMÉTRICO ... 74
V.11 CÁLCULO DA SEÇÃO DE CHOQUE DIFERENCIAL EXPERIMENTAL ... 75
V.12 RESULTADOS EXPERIMENTAIS DOS SISTEMAS ^{16}O+^{40}CA E ^{16}O+^{120}SN ... 78

VI CONCLUSÃO ... 81

VII APÊNDICES ... 83

VIII REFERÊNCIAS E ARTIGOS DO PERÍODO ... 91

I INTRODUÇÃO

I.1 *Um Breve Panorama sobre a Física de Reações Nucleares*

Nas últimas décadas, temos acompanhado os diferentes esforços realizados com o objetivo de obter descrições realistas e aplicações para os fenômenos envolvidos em uma reação nuclear nos diferentes campos da Astrofísica, Cosmologia, Matéria Condensada, Física de Partículas, Estrutura da Matéria etc. Devido à agregação de núcleons que pode ser alcançada em uma colisão entre núcleos pesados, um estado de grande energia pode ser obtido, onde muitas espécies de hádrons podem coexistir. Assim sendo, as colisões centrais mantêm a promessa do estudo de novos estados da matéria.

No interior de estrelas, as reações nucleares são importantes tanto na geração de energia como na dinâmica de evolução destes corpos. O processo de fusão nuclear de elementos leves resulta na liberação de grande quantidade de energia térmica e de radiação, o que aumenta a temperatura da estrela e a probabilidade de ocorrência de novos processos de fusão, um processo de fusão em cadeia é então gerado e será um dos fatores responsáveis em determinar o ritmo de evolução da estrela.

Uma grande contribuição para a núcleo-síntese de elementos do cosmos é gerada a partir de reações nucleares que envolvem os núcleos exóticos, núcleos que possuem uma desproporção entre o número de prótons e nêutrons e que estão longe da linha de estabilidade. Devido à importância dos núcleos exóticos no meio ambiente estelar, avanços técnicos têm tornado possível a criação de muitos destes núcleos, pouco encontrados na natureza e de vida curta, em laboratório, proporcionando assim o estudo de suas propriedades incomuns, em especial suas densidades de matéria nuclear. Este tem sido um assunto de considerável interesse científico e necessário para gerar um sólido entendimento não só da estrutura nuclear, como também de processos nucleares responsáveis pela evolução de estrelas e da origem de elementos no cosmos. Por outro lado, a teoria de núcleo-síntese é conectada a muitas propriedades observadas não só em estrelas, mas também em outros corpos astronômicos, e em particular a numerosos detalhes da composição química do sistema solar e dos raios cósmicos.

Atualmente acredita-se que, em condições ideais de altas temperaturas e densidades, uma colisão de dois núcleos em velocidades relativísticas provocaria uma transição de fase de prótons e nêutrons e, por um breve instante, quarks e glúons seriam liberados dentro dos núcleons, formando um plasma quark-glúon (QGP), exatamente como previsto teoricamente para o início do universo, onde haveria apenas quarks e glúons livres e que, no entanto, com a expansão e o esfriamento do universo, os quarks e glúons agregaram-se e há 13 bilhões de anos permanecem virtualmente inseparáveis. Esta transição de fase de matéria (núcleons) para um plasma quark-glúon é exatamente o oposto do que se acredita ter ocorrido imediatamente após o "Big-Bang", isto é, uma transição de quark-glúon-plasmas para núcleons.

À parte dessas especulações, os fenômenos de uma reação usualmente excitam muitos graus de liberdade de um sistema e um tratamento detalhado torna-se extremamente complicado, fazendo com que muitas questões permaneçam ainda abertas, com suas respostas vinculadas a descrições mais fundamentais. Um dos papéis deste trabalho é mostrar alguns avanços sobre algumas destas descrições e como estas contribuem para um melhor entendimento dos diversos fenômenos envolvidos em reações nucleares, tais como os citados acima.

I.2 *Introdução Histórica e Origem do Trabalho*

O estudo de reações entre íons pesados visa compreender a dinâmica de interação da matéria nuclear. A solução exata de uma colisão entre íons pesados envolve a resolução de um problema de muitos corpos (núcleons) extremamente complexo, onde o potencial nuclear desempenha um papel central. Assim, a descrição dos processos envolvidos em uma colisão nuclear, ao longo dos anos, sempre foi realizada de maneira aproximada, utilizando um potencial médio de interação entre os íons, juntamente com algum modelo para os canais de reação (fusão, transferência de núcleons, espalhamento inelástico). A justificativa para o uso deste método está no ajuste de um imenso número de dados experimentais publicados em artigos nas últimas décadas.

Um dos modelos mais antigos para a análise de dados experimentais de seções de choque de espalhamento elástico é o modelo ótico. No modelo, os graus de liberdade internos dos íons são considerados congelados e o potencial de interação, denominado potencial ótico, é complexo, sendo que a parte real representa o potencial médio íon-íon e a parte imaginária, simula a absorção de fluxo do canal elástico, devido aos diversos canais de reação. Na prática, a solução completa do conjunto de todos os canais de reação acoplados é de dificuldade equivalente à resolução exata para um problema de muitos corpos. Assim, na maioria das aplicações, tais cálculos são realizados com apenas alguns canais acoplados, sendo que ainda mantêm uma parte imaginária do potencial para simular os efeitos de canais que não entram explicitamente nos acoplamentos. Quando um número muito grande de canais acoplados é considerado, o resultado dos cálculos torna-se apenas qualitativo, deixando a desejar no que diz respeito ao ajuste de dados experimentais. A grande complexidade dos muitos canais de reação abertos, principalmente em energias acima da chamada "barreira de fusão" (ou "barreira coulombiana"), faz com que a obtenção do potencial médio de interação entre os íons pesados, a partir de dados experimentais de espalhamento, fique sujeita a muitas ambigüidades [Ta65, Be85, Ho89, Uda89, Sa91, Ch92, Wo93].

Até hoje, ao se analisar dados experimentais de reações entre íons pesados, em geral, o potencial é parametrizado (parte real e parte imaginária), sendo que os valores ajustados dos parâmetros variam fortemente com a energia e são bastante diferentes mesmo entre sistemas semelhantes. Paradoxalmente, alguns trabalhos teóricos [Bl77, Ngô75, Sky59] mostraram que o potencial nuclear entre íons pesados deveria ter uma forma universal, com parâmetros dependentes apenas do caráter geométrico do sistema.

Durante a última década, nosso grupo de pesquisa aumentou consideravelmente o conhecimento acerca do potencial de interação entre dois íons pesados. Este progresso foi estimulado por medidas precisas de seções de choque de espalhamento elástico que cobriram uma vasta região de ângulos (30 a 170 graus) e energias (30 a 1760 MeV) de espalhamento, no referencial de laboratório. O espalhamento elástico é o processo mais simples e direto envolvido em uma reação nuclear e pode ser usado como ponto de partida para um melhor entendimento de processos mais complexos de uma reação. Vale salientar que todas as medidas envolvendo energias dentro da faixa de trabalho do Laboratório Pelletron (até $8.0 \cdot 10^6\,Volts$), conhecida como região de energia da barreira coulombiana, foram realizadas pelo meu grupo de pesquisa no próprio Laboratório Pelletron [Ch95, Ch96, Al99, Si01], enquanto os dados envolvendo medidas nas chamadas energias intermediárias e altas foram extraídos da literatura [Ba75, Oga78, Sa86, Kh94, Br97b, Og00, Ro88, Ho98, Bu81, Bu84]. Paralelo ao acúmulo desses dados, alguns trabalhos teóricos foram desenvolvidos também dentro do nosso grupo de pesquisa [Ri97, Ch97, Ch98, Al02, Ch02]. Estes trabalhos produziram importantes resultados, que ao serem estendidos aos dados experimentais, resultaram em um grande aprendizado sobre as interações íon-íon, não só quando suas superfícies se tocam, mas também quando os dois núcleos se interpenetram e efeitos relativos à não-localidade da interação e estrutura da matéria nuclear passam a ser importantes.

Um método experimental possibilitou obter o potencial íon-íon de forma muito menos ambígua do que vinha sendo feita anteriormente [Ch95, Ch96, Al99, Si01], sendo os trabalhos [Al99, Si01] publicados durante o período de meu doutoramento. O método consistiu em obter dados experimentais de espalhamento elástico e de alguns canais de reação em regiões de energia abaixo da barreira de fusão de cada sistema estudado. Nesta região de energia, um número muito pequeno de canais de reação fica aberto; isto permitiu um cálculo de canais acoplados simples e seguro, sem que houvesse a necessidade da utilização de uma parte imaginária do potencial para simular a absorção de fluxo para os canais de reação. Assim, a ausência de parâmetros ajustáveis da parte imaginária do potencial ótico permitiu obter, com precisão e sem ambigüidade, os parâmetros da parte real do potencial (potencial íon-íon). Enquanto a parte real do potencial era detalhada, os estudos referentes à parte imaginária, necessária para quantificar os processos decorrentes de reações realizadas em energias próximas e acima da barreira de fusão, permaneceram sem qualquer avanço. Após obtermos uma descrição completa da parte real do potencial, passamos a estudar a parte imaginária com o objetivo de quantificar o fluxo perdido para os diversos canais de reação (capítulo IV).

Essa excelente definição na determinação experimental da parte real do potencial, confirmada de maneira ampla em termos de diferentes sistemas e energias, gerou a motivação para compará-la [Ch95, Ch96, Al99 e Si01] com o potencial teórico de caráter mais fundamental, conhecido como potencial Folding [Sa79], e mais tarde com o potencial de proximidade [Bl77], desenvolvido a partir do modelo da gota líquida. O potencial Folding foi desenvolvido em termos das densidades da matéria nuclear dos núcleos interagentes e do potencial de interação efetiva núcleon-núcleon. Este potencial teórico Folding descrevia fielmente efeitos de estrutura encontrados com nosso potencial experimental em baixas energias (abaixo da barreira de fusão); porém, esses potenciais (teóricos e experimentais) se mostravam incompatíveis em termos de intensidades [Ch95, Ch96 e Al99]. Uma análise sobre os diferentes modelos utilizados para descrever as densidades dos núcleos interagentes mostraram discrepâncias significativas para o núcleo ^{16}O, núcleo utilizado como projétil em nossas medidas, principalmente no que se refere à superfície desse núcleo [Al99]. Desta forma, a discrepância observada entre teoria e experimento parecia estar conectada às densidades nucleares envolvidas no potencial Folding.

Neste contexto, este trabalho tem origem na necessidade de três descrições fenomenológicas distintas: i-) a determinação da parte real do potencial nuclear; ii-) a determinação da parte imaginária do potencial nuclear, sem nunca desconectá-las, e mantendo sempre a possibilidade de haver uma relação de dependência entre as mesmas; iii-) uma descrição mais precisa para a densidade da matéria nuclear.

I.3 Densidade Nuclear: "Uma questão em aberto"

Muitas questões sobre estrutura nuclear ainda são colocadas ante a determinação da densidade de nêutrons e prótons. Desde muito tempo, várias pontas de prova (píon, próton, elétron, alpha, etc) têm sido utilizadas no sentido de determinar a densidade de carga ou da matéria nuclear, porém com diferentes tipos de limitação. Por exemplo, muitos trabalhos foram publicados envolvendo espalhamento de elétrons na determinação da densidade de carga, onde diferentes aproximações foram utilizadas na tentativa de descrever os dados experimentais [Si70, Fi70, Fa71, Als72, Fr76]. Devido a limitações na determinação experimental da seção de choque para altos momentos transferidos, a sensibilidade do método é restrita somente a regiões próximas ao raio quadrático médio, e imprecisa na região da superfície (vide apêndice III). Vale salientar que exatamente nessa região superficial de densidade de matéria nuclear, do núcleo ^{16}O, os diferentes modelos para cálculos de densidade por nós estudados apresentavam descrições discrepantes entre si [Al99], sendo esta uma possível causa para que o potencial folding, dependente das densidades de matéria dos núcleos interagentes, discordasse do nosso potencial experimental obtido em [Ch95, Ch96 e Al99].

Os núcleos exóticos, por sua importância em Astrofísica Nuclear, mas principalmente pela desproporção entre as distribuições de prótons e nêutrons, também chamam atenção para este tema. Mesmo com uma meia-vida curta, da ordem de milisegundos, estes núcleos são produzidos em laboratório a partir de reações nucleares e reutilizados em reações futuras, isto é, alguns milisegundos são suficientes para se produzir um feixe de núcleos exóticos e realizar reações com um alvo estável e, desta forma, estudar propriedades desses núcleos. Uma das recentes pesquisas mais excitantes neste campo foi a descoberta da distribuição estendida de nêutrons em núcleos exóticos ricos em nêutrons [Ta85].

Todas essas considerações levaram-me a desenvolver, nesse trabalho, um método para a obtenção experimental da densidade da matéria nuclear [Al02], a partir de dados experimentais de espalhamento elástico de íons pesados em baixas energias. O método deriva da comprovada existência de um raio de sensibilidade, que é um ponto onde a densidade da matéria para um certo núcleo pode ser bem determinada a partir da análise de uma distribuição angular de espalhamento elástico (capítulo III).

I.4 Desenvolvimento do Trabalho

Partindo do conceito no qual o modelo Folding está relacionado com a parte real do potencial (com justificativas teóricas oriundas da teoria de Feshbach de reações nucleares), o objetivo traçado foi então construir um potencial teórico, alterando o já conhecido potencial Double Folding [Sa79], levando em consideração os progressos em nosso entendimento da interação efetiva entre dois núcleons em um meio nuclear, e os progressos quanto à importância dos efeitos da não-localidade de Pauli [Ri97, Ch97, Ch98, Ga98], em energias intermediárias, o que implica em levar em conta a natureza fermiônica da matéria nuclear, e estabelecer a relação de dependência do potencial nuclear com a energia.

Referente à densidade nuclear, neste trabalho estão apresentados os dados de espalhamento elástico, obtidos no laboratório Pelletron, em energias abaixo da barreira de fusão, juntamente com os dados obtidos em energias intermediárias, extraídos da literatura, envolvendo o núcleo ^{16}O como projétil [Al02]. Nossa análise de dados foi realizada com o modelo ótico, onde a parte imaginária do potencial foi assumida em duas direções distintas: a primeira, para baixas energias, parametrizada a partir de uma função do tipo Woods-Saxon; e a segunda, para energias intermediárias, em termos mais fundamentais, utilizando a conhecida aproximação de Glauber para altas energias [Gl69]. O modelo de não-localidade, desenvolvido em São Paulo pelo grupo de pesquisa do qual faço parte [Ri97, Ch97, Ch98], foi assumido com o objetivo de descrever a dependência de energia da parte real da interação nuclear, a qual está conectada com o potencial folding através de uma equação muito simples, conforme discutido na seção II.2.4, obtida em [Ch02].

Os métodos desenvolvidos a partir do núcleo ^{16}O se mostraram poderosas ferramentas para a determinação da densidade de outros núcleos estáveis (^{12}C e ^{18}O) e do núcleo exótico (^{6}He). Estes outros estudos fazem parte de duas teses de doutoramento desenvolvidas por membros do meu grupo de pesquisa, além de já terem sido publicados em periódicos internacionais [Ro02, Ga02a, Ga02b]. Vale destacar, em particular, a eficiência do método em uma região superficial da densidade nuclear, onde as diferenças entre as densidades de núcleos exóticos e núcleos vizinhos estáveis são muito enfatizadas.

Este trabalho é fechado com mais um teste de consistência para a parte real do potencial e uma tentativa de obter um modelo fenomenológico para a parte imaginária do mesmo (capítulo IV). Como continuidade do meu trabalho de doutoramento segui, então, o conceito da aproximação de Glauber de altas energias [Gl69], de usar a mesma forma radial para as partes real e imaginária do potencial ótico e estendi assim nosso modelo desenvolvido para a parte real também para a parte imaginária do potencial nuclear [Al02b]. Além de obtermos um modelo bastante simples para a parte imaginária do potencial, nós obtivemos ainda uma excelente descrição dos dados experimentais de diversos sistemas, e o que é mais importante, sem a utilização de parâmetros livres (vide capítulo IV ou referência [Al02b]).

II PARTE TEÓRICA

II.1 O Potencial segundo a Equação de Schrödinger

Como citado anteriormente, nosso estudo de reações entre íons pesados tem como objetivo uma melhor caracterização da estrutura da matéria nuclear, bem como sua dinâmica de interação. Tanto a solução exata de uma colisão entre íons pesados como a disposição em camadas dos núcleons, componentes de cada núcleo, apresenta sua solução a partir da equação de Schrödinger, com as devidas aproximações pertinentes a cada caso, e um modelo para o potencial médio de interação (U).

$$-\frac{\hbar^2}{2\mu}\nabla^2\Psi(\vec{R})+U(R,E)\Psi(\vec{R})=E\Psi(\vec{R}) \tag{1}$$

Para escrever, por exemplo, a função de onda $\Psi(\vec{R})$ de um núcleo, segundo o modelo de camadas, devemos ter o conhecimento das órbitas ocupadas, o que chamamos de configuração. Desta forma, a partir da função de onda do núcleo, podemos determinar a sua densidade.

Por outro lado, ao tratar o espalhamento elástico entre íons pesados, com as devidas aproximações sobre o potencial nuclear, a função de onda resultante da equação de Schrödinger irá descrever o processo, através de uma distribuição de probabilidades para as partículas espalhadas por um núcleo-alvo. Essa distribuição de probabilidades pode ser convenientemente descrita, através de cálculos da seção de choque diferencial deste processo, em função de seu ângulo de espalhamento (apêndice I).

Nosso objetivo é determinar o melhor potencial $U(R,E)$ que descreva a seção de choque diferencial elástica. Nesse contexto, vários modelos têm sido propostos para o potencial nuclear, principalmente no que se refere à sua parte real. Foi observado que os potenciais fenomenológicos introduzidos para descrever os dados experimentais são significativamente dependentes da energia [Sa79]. Alguns modelos teóricos foram construídos para descrever essa dependência através de potenciais de campo médio real. Até hoje, os mais bem sucedidos pareciam ser os potenciais dependentes da densidade. Temos então a origem da necessidade de uma análise conjunta entre densidade e potencial nuclear no estudo das reações entre íons pesados, uma relação entre dinâmica e estrutura, onde o potencial Folding é sem dúvida o ponto de partida.

Três casos serão discutidos a seguir, com o objetivo de mostrar os avanços na caracterização do potencial. Antes de tratarmos diretamente sobre o potencial Double Folding, base da parte real do potencial nuclear que temos trabalhado nos dias atuais, iremos descrever o modelo que originou a descrição para o potencial nuclear como um potencial médio sem levar em conta cada uma das interações núcleon-núcleon e utilizando uma parte imaginária para descrição de canais de reações responsáveis pela absorção de fluxo: o Modelo Ótico. Vamos desprezar a não-localidade de Pauli e tratar a chamada não-localidade de Feshbach, utilizando um potencial de polarização médio parametrizado. Esse tipo de abordagem corresponde ao modelo ótico em sua forma mais simples. Em seguida continuaremos desprezando a não-localidade de Pauli e detalharemos o potencial Folding em sua origem, para enfim introduzirmos os efeitos da não-localidade de Pauli sobre o potencial.

II.2 Desenvolvimento do Potencial Nuclear

O potencial de interação entre dois núcleos, alvo e projétil, consiste na soma dos termos do potencial ótico $V_{ot}(R,E)$ e o potencial coulombiano $V_C(R)$, ou seja:

$$U(R,E) = V_{ot}(R,E) + V_C(R) \qquad (2)$$

II.2.1 O Potencial Coulombiano

Curiosamente, na maioria das aplicações, o potencial coulombiano entre dois núcleos de raios R_1 e R_2, e números atômicos Z_1 e Z_2 era considerado aproximadamente igual ao potencial entre uma carga Z_1e, puntiforme, e uma esfera carregada de raio R_1+R_2 e carga total Z_2e. No entanto, essa aproximação não é apropriada nos casos de espalhamento em altas energias, para os quais regiões de distâncias de interação bastante internas são testadas. Assim sendo, neste trabalho utilizamos o potencial entre duas esferas uniformemente carregadas, para o qual já foi encontrada uma expressão analítica há mais de duas décadas [De75].

II.2.2 O Potencial Ótico

O modelo ótico possui duas características fundamentais capazes de minimizar o problema do espalhamento elástico de um sistema de muitos corpos:

(i-) O modelo assume que a interação entre o projétil e o alvo pode ser definida através de um potencial médio, resultante de uma média das interações núcleon-núcleon dos respectivos núcleos.

(ii-) Baseado no espalhamento e absorção de luz por um meio ótico, onde a absorção é simulada por um índice de refração complexo, o modelo ótico representa a absorção do canal elástico para os canais de reação (como, por exemplo, espalhamento inelástico, transferência de núcleons e fusão) com uma parte imaginária no potencial nuclear.

Esse potencial nuclear médio, denominado Potencial Ótico, é representado em função da distância entre os núcleos e a respectiva energia de centro de massa, de tal forma que temos:

$$V_{ot}(R,E) = V(R,E) + iW(R,E) \tag{3}$$

$$V(R,E) = V_N(R) + V_{pol}(R,E) \tag{4}$$

sendo $V(R,E)$ a parte real do potencial ótico, a qual é composta da soma do potencial nuclear $V_N(R)$ com a parte real do potencial de polarização $V_{pol}(R,E)$. A maneira pela qual o potencial de polarização surge no potencial ótico é descrita no apêndice II.

Em grande parte das aplicações, a parte real do potencial é representada na forma do tipo Woods-Saxon por:

$$V(R,E) = \frac{-V_0(E)}{1+\exp\left[\frac{R-R_0(E)}{a(E)}\right]}. \tag{5}$$

Na maioria das aplicações, a parte imaginária tem sido considerada na mesma forma:

$$W(R,E) = \frac{-W_0(E)}{1+\exp\left[\frac{R-R_I(E)}{a_I(E)}\right]} \tag{6}$$

Esse procedimento é adotado pela suposição de que o potencial deveria ter aproximadamente a mesma forma da distribuição da matéria nuclear. É importante ressaltar que, apesar de útil, devido à simplicidade e ao ajuste de uma grande quantidade de dados experimentais, tal procedimento está distante de representar efeitos mais fundamentais, e portanto não está bem justificado. Por exemplo, já foi demonstrado [Lo77, Ba79] que o processo de excitações inelásticas coulombianas tem um correspondente potencial de polarização imaginário, de longo alcance, que não pode ser corretamente representado utilizando uma forma do tipo Woods-Saxon.

Ao utilizar o modelo ótico, o procedimento normalmente adotado na análise de dados de espalhamento elástico entre íons pesados é manter alguns parâmetros livres no potencial ótico, de maneira a ajustar a distribuição angular experimental. Foi observado [Sa74] que, para energias próximas da barreira coulombiana, diferentes "famílias" de potenciais óticos, isto é, diferentes valores dos parâmetros livres em (5) e (6), produzem ajustes de dados experimentais muito semelhantes. Os parâmetros estão de tal forma correlacionados, que as diferentes famílias correspondentes à parte real do potencial ótico, $V(R,E)$, cruzam-se (têm a mesma intensidade) somente num ponto conhecido como raio de absorção forte. Ou seja, as previsões de seção de choque teóricas só são sensíveis ao potencial ótico em uma pequena região de distâncias de interação, em torno do raio de absorção forte [Ch95, Ch96, Al99, Sil01]. Essa característica está ligada ao curto alcance da força nuclear e à correspondente absorção forte nos sistemas de íons pesados [Br97]. Isto é, o "contato" entre os núcleos leva quase que inevitavelmente a eventos não-elásticos e a perda de fluxo do canal elástico; conseqüentemente, o espalhamento elástico é dominado pelas condições da "região superficial" de distâncias de interação.

Diante dessa grande dificuldade na determinação do potencial nuclear, através da análise de dados experimentais de espalhamento elástico em energias próximas (acima) da barreira coulombiana, desenvolvemos o método que possibilitou realizar um cálculo de canais acoplados simples e seguro, sem a necessidade da utilização de uma parte imaginária do potencial para simular a absorção de fluxo para os canais de reação, mas sim, apenas um potencial que simule uma pequena absorção interna, devido à penetração de barreira. O método é baseado em dados em energias subcoulombianas, região na qual o potencial nuclear pode ser então considerado uma pequena perturbação do potencial coulombiano e, portanto, os dados experimentais de espalhamento elástico e dos poucos canais de reação foram obtidos com muita precisão, de forma a permitir a obtenção do potencial com boa definição. Uma descrição completa desse método foi realizada em minha dissertação de mestrado e posteriormente publicada em [Al99].

II.2.3 O Potencial Double-Folding

O potencial Folding [Sa79] é construído a partir de uma convolução da interação núcleon-núcleon com as densidades de matéria dos núcleos em colisão.

$$V_{Fold}(R)=\int \rho_1(r_1)v_0(\vec{R}-\vec{r}_1+\vec{r}_2)\rho_2(r_2)d\vec{r}_1 d\vec{r}_2 \qquad (7)$$

Na equação 7, $v_0(\vec{r})$ é a interação efetiva entre dois núcleons. Para tal interação, os modelos conhecidos como M3Y (Reid e Paris) são representativos de interações "realistas" e são, também, os mais utilizados. Em nosso trabalho de desenvolvimento do modelo de não-localidade e da determinação experimental das densidades nucleares [Ri97, Ch97, Ch98, Ga98, Al99, Al02], usamos a interação efetiva M3Y-Reid:

$$v_0(\vec{r}) = 7999\frac{e^{-4r}}{4r} - 2134\frac{e^{-2r}}{2.5r} + J_{00}\delta(\vec{r}) \tag{8}$$

Nesta equação, os dois primeiros termos são responsáveis pela parte direta da interação núcleon-núcleon, enquanto o último termo simula efeitos não-locais de troca entre núcleons do projétil e alvo (não-localidade de Pauli), na aproximação de alcance nulo (o alcance da não-localidade será discutido na próxima seção). A magnitude de J_{00} foi determinada empiricamente, através do ajuste de dados experimentais de espalhamento de prótons em diversos núcleos, e para várias energias (até 80 MeV). Foi obtida a seguinte leve dependência com a energia do próton: $J_{00} \approx 276[1-0.005 \cdot E/A](MeVfm^{-3})$. Outros detalhes acerca da interação M3Y podem ser encontrados em [Be77].

No contexto do Modelo Ótico, o potencial Folding [Sa79] tem sido usado com bastante sucesso, em análises de dados experimentais de espalhamento elástico para energias em torno da barreira coulombiana. Nessas análises, a parte real do potencial ótico tem sido assumida igual ao potencial Folding (equação 7), multiplicado por um fator de normalização (que pode variar com a energia), de forma a simular os efeitos da polarização. O fator de normalização tem sido obtido próximo da unidade [Sa79], que é um indicativo da propriedade desse procedimento. Entretanto, como passaremos a discutir, o potencial Folding nessa versão original, não obteve o mesmo êxito na descrição de dados experimentais em mais altas energias.

Em [Br97a] foi enfatizado que o potencial nuclear pode ser extraído sem ambigüidades, através de medidas de espalhamento elástico em energias intermediárias (várias dezenas de MeV/núcleon). Para ajustar os dados experimentais, o fator de normalização multiplicativo do potencial Folding apresenta grande variação com a energia, em alguns casos tornando-se bastante menor que "1". Isso foi inicialmente observado para sistemas com partículas alpha, onde um fator de normalização de aproximadamente "½" foi encontrado para energias em torno de 35 MeV/nucleon. Posteriormente, resultado semelhante foi encontrado para vários sistemas de íons pesados. Esse fator (bastante menor que 1) não pôde ser associado aos efeitos do potencial de polarização, pois estimativas teóricas [Ma77] para essas energias mostraram que, além de apresentar intensidade muito pequena em comparação ao potencial Folding, a correspondente parte real do potencial de polarização é atrativa (não-repulsiva como seria necessário para explicar os fatores <<1).

Por outro lado, para explicar a saturação da matéria nuclear, já havia sido proposto [Be71] que a interação efetiva entre dois núcleons deveria depender da densidade do meio. Saturação requer que a atração enfraqueça à medida que a densidade aumenta. Assim, surgiram vários modelos para a interação nuclear entre íons pesados (denominados interações dependentes da densidade), baseados no potencial Folding, em que a interação efetiva núcleon-núcleon é considerada dependente da densidade. A primeira versão [Ko82, Ko84] assume a interação M3Y-Reid (equação 8) multiplicada pelo fator:

$$f(\rho, E_N) = C(E_N)[1 + \alpha(E_N) e^{-\beta(E_N)\rho}], \qquad (9)$$

com $\rho = \rho_1(r_1) + \rho_2(r_2)$, e $E_N = E/A$ = energia de bombardeio por núcleon do projétil. Os parâmetros C, α e β, dependentes da energia, foram escolhidos de forma a fazer com que a integral de volume de interação se ajustasse, tão bem quanto possível, aos resultados de cálculos tipo Brueckner, de Jeukenne et al. [Je77], para o espalhamento de um núcleon pela matéria nuclear. Uma dificuldade com a equação (9) é que densidades grosseiramente duas vezes maiores do que a da matéria nuclear "normal", são encontradas quando ocorre grande superposição dos dois íons. Vários modelos mais "realistas" têm sido propostos, por exemplo: [Kh93, Kh94, Kh95a, Kh95b]. Um aspecto interessante dessas interações é que diferentes modelos para a função $f(\rho, E_n)$ fornecem diferentes valores para a incompressibilidade da matéria nuclear [Kh94, Kh95a, Kh95b]. Na matéria nuclear, a energia de ligação por núcleon, ***B***, deve ter um mínimo para a densidade de saturação $\rho_0 \approx 0.17 fm^{-3}$. A curvatura de $B(\rho)$ está conectada com a incompressibilidade por:

$$K = 9\rho_0^2 (\partial^2 B / \partial \rho^2)_{\rho=\rho_0} \qquad (10)$$

Assim, alguns autores acreditam poder extrair informações acerca dessa importante quantidade, através da análise de dados de espalhamento elástico entre íons pesados em energias intermediárias [Kh95a]. Tais análises são realizadas com alguns parâmetros livres na função $f(\rho, E_n)$, utilizados no ajuste dos dados experimentais. Aparentemente, o modelo que fornece melhores ajustes, conhecido como DDM3Y1, implicaria numa incompressibilidade de K=270 MeV [Kh95a], que é compatível com o valor obtido a partir de dados de ressonâncias gigantes isoescalares [Yo99]. Entretanto, para obter resultados satisfatórios na análise dos dados, foi necessário introduzir uma dependência adicional em energia [Kh93]. Dessa forma, consideramos que uma denominação mais apropriada para essas interações seria: "interações dependentes da densidade e da energia". Essa dependência "extra" em energia e o modo "um pouco arbitrário" pelo qual são assumidas as diferentes formas para a dependência de densidade da função $f(\rho, E_n)$ são os pontos mais criticados desses modelos. É necessário comentar que uma descrição alternativa da variação do potencial nuclear com a energia, como aquela apresentada no próximo capítulo, põe em dúvida os resultados para a incompressibilidade da matéria nuclear obtidos com as interações dependentes da densidade (e energia).

II.2.4 O Potencial Não-Local

Como já comentado, foi demonstrado que as ambigüidades relativas à determinação experimental do potencial íon-íon podem ser removidas através da análise de dados de espalhamento elástico em altas energias. Foi observado [Br96] que o potencial nuclear que ajusta tais dados tem uma significativa dependência com a energia.

Nosso grupo de pesquisa publicou vários artigos [Ri97, Ch97, Ch98] os quais mostram que a dependência do potencial nuclear com a energia pode ser explicada com a introdução de uma interação nuclear não-local. A não-localidade do potencial tem origem no caráter fermiônico da matéria nuclear.

Ao tratar o espalhamento elástico entre íons pesados com interações não locais, deve-se resolver a seguinte equação íntegro-diferencial [Ch97]:

$$\begin{gathered} -\frac{\hbar^2}{2\mu}\vec{\nabla}^2\Psi(\vec{R})+[V_C(R)+V_{pol}(R,E)+iW_{pol}(R,E)]\Psi(\vec{R})+ \\ \int U(\vec{R},\vec{R}')\Psi(\vec{R}')d\vec{R}' = E\Psi(\vec{R}), \end{gathered} \tag{11}$$

onde V_C é o potencial coulombiano, assumido como sendo local. V_{pol} e iW_{pol} são as partes real e imaginária do potencial de polarização e contém as contribuições oriundas dos acoplamentos com canais de reação, e $\Psi(\vec{R})$ é a função de onda que descreve o espalhamento elástico do sistema núcleo-núcleo. Por considerações físicas [Ch97], a interação efetiva entre os núcleos deve ser simétrica, $U(\vec{R},\vec{R}')=U(\vec{R}',\vec{R})$. A parte não-local é escrita como:

$$U(\vec{R},\vec{R}')=V_{NL}\left(\frac{R+R'}{2}\right)\left(\frac{1}{\pi^{3/2}b^{3}}\right)exp\left[-\left(\frac{|\vec{R}-\vec{R}'|}{b}\right)^{2}\right] \tag{12}$$

onde $b=b_0m_0/\mu$ é o alcance da não-localidade de Pauli, b_0 = 0.85 fm, m_0 e μ são a massa de um núcleon e a massa reduzida do sistema, respectivamente.

O termo, $U(\vec{R},\vec{R}')$, que denominamos interação íon-íon, representa o valor esperado do operador de interação, o qual contém, basicamente, a força efetiva média núcleon-núcleon. A não-localidade neste termo, como dissemos, é devida à natureza fermiônica dos núcleons que constituem a matéria nuclear. Denominamos este tipo de não-localidade como não-localidade "de Pauli". O termo V_{pol} e iW_{pol} (equação 11), chamado termo de "Feshbach", contém as contribuições oriundas dos canais de reação e de excitações virtuais para estados intermediários (canais inelásticos, de transferência de núcleons etc). A correspondente não-localidade, denominada "de Feshbach", provém de polarizações devido à propagação nos canais intermediários.

Devido à natureza central da interação, podemos realizar a expansão em ondas parciais da equação (11), de tal forma que

$$\begin{aligned}&\frac{\hbar^2}{2\mu}\frac{d^2u_l(R)}{dR^2}+[E-V_C(R)-V_{pol}(R,E)-iW_{pol}(R,E)\\&-\frac{l(l+1)\hbar^2}{2\mu R^2}]u_l(R)=\int_0^\infty V_l(R,R')u_l(R')dR'.\end{aligned} \tag{13}$$

O potencial local equivalente, $U_{LE}(R)$, é então definido como:

$$U_{LE}(R,E)+iW_{LE}(R,E)=\frac{1}{u_l(R)}\int_0^\infty V_l(R,R')u_l(R')dR'. \qquad (14)$$

e podemos então, escrever a equação de Schrödinger na forma:

$$\begin{aligned}\frac{\hbar^2}{2\mu}\frac{d^2u_l(R)}{dR^2}+[E-V_C(R)-V_{pol}(R,E)-iW_{pol}(R,E)]\Psi \\ -[U_{LE}(R,E)+iW_{LE}(R,E)]\Psi=0\end{aligned} \qquad (15)$$

A presença da função de onda na equação 14 indica que o potencial local equivalente é complexo e também dependente de (l) e da energia. Apesar dessa natureza complexa, o potencial local equivalente não é absortivo, $\langle\Psi|W_{LE}|\Psi\rangle=0$ e isso pode ser demonstrado, considerando que a interação não-local é real e simétrica: $U(\vec{R},\vec{R}')=U(\vec{R}',\vec{R})$.

Na equação 12, segundo o modelo [Ri97, Ch97, Ch98], V_{NL} é tomado como o potencial Folding, de tal forma que $V_{NL}(\xi)=V_{fold}(R=\xi)$. Foi mostrado [Ch97] que uma boa aproximação para $U_{LE}(R)$ é obtida por:

$$U_{LE}(R,E)\approx V_{fold}(R)exp\left\{-\frac{\mu b^2}{2\hbar^2}[E-V_C(R)-U_{LE}(R,E)]\right\} \qquad (16)$$

Em energias próximas da barreira coulombiana (E ≈ V$_B$ = V$_C$(R$_B$)) e distâncias perto do raio da barreira (R ≈ R$_B$), o efeito de não-localidade é desprezível (menos que 1%), e $U_{LE}(R\approx R_B;E\approx V_B)\approx V_{fold}(R)$. Para altas energias, porém, o efeito da não-localidade tende a diminuir sensivelmente a intensidade do potencial nuclear [Al99, Si01].

Dentro de um panorama da Física Clássica, o expoente na equação 16 está relacionado à energia cinética (E_K) e à velocidade relativa entre núcleos (v), por

$$v^2 = \frac{2}{\mu} E_K(R) = \frac{2}{\mu}\left[E - V_C(R) - U_{LE}(R,E)\right] \tag{17}$$

e a equação 16 pode ser reescrita na seguinte forma

$$U_{LE}(R,E) \approx V_F(R)\exp-\left[\frac{m_0 b_0 v}{2\hbar}\right]^2 \approx V_F(R)\exp-\left[\frac{4v^2}{c^2}\right]. \tag{18}$$

Portanto, nesse contexto, o efeito da não-localidade de Pauli é equivalente à uma interação nuclear dependente da velocidade relativa (equação 18).

II.2.5 A Parte Imaginária do Potencial Ótico

Com o objetivo de estabelecer uma completa conexão entre o potencial e as densidades, durante nossas análises tentamos dar à parte absortiva do potencial um tratamento fenomenológico mais fundamental, sem a utilização de parâmetros livres para o ajuste dos dados experimentais. Um modelo para essa parte imaginária do potencial de polarização, conhecido como teoria de espalhamento múltiplo de Glauber [Gl70], foi desenvolvido para energias suficientemente altas, em que são satisfeitas as seguintes condições: i) a energia cinética da partícula incidente excede grandemente a magnitude do potencial; e ii) o comprimento de onda da partícula é muito menor que um comprimento característico do potencial (este é da ordem de magnitude da difusividade do potencial, ou seja, aproximadamente 0.5 *fm*). Nestas condições, pode ser considerado que toda a absorção de fluxo do canal elástico provém de processos elementares de espalhamento núcleon-núcleon, os quais ocorrem na superposição das densidades dos núcleos em colisão. Isto corresponde a desconsiderar processos de reação em que são envolvidos mais de dois núcleons, tais como excitações coletivas dos núcleos. Nessa aproximação (conhecida como aproximação LAX), os únicos "ingredientes" necessários nos cálculos são as seções de choque de espalhamento núcleon-núcleon e as densidades de matéria dos núcleos alvo (ρ_T) e projétil (ρ_p). O potencial imaginário é calculado por:

$$W(R,E) = -\frac{\hbar v}{2}\int \overline{\sigma}_{NN}(E_N)\rho_p(|\vec{R}-\vec{r}_T|)\rho_T(r_T)d\vec{r}_T\,, \qquad (19)$$

onde v é a velocidade relativa entre os dois núcleos, e $\overline{\sigma}_{NN}$ é a seção de choque total média para espalhamento núcleon-núcleon com o Bloqueio de Pauli [Hu91], obtida das seções de choque experimentais dos sistemas próton-próton e próton-nêutron, na energia E_N (igual à energia de bombardeio do sistema íon-íon dividida pelo número de nucleons do projétil).

III O Método para Determinação Experimental da Densidade da Matéria Nuclear

O método para determinação da densidade da matéria nuclear a partir de dados de espalhamento elástico de íons pesados, em energias abaixo da barreira coulombiana e energias intermediárias, é resultado da aplicação do potencial não-local (NLM3Y) descrito na seção II.2.4. O potencial NLM3Y foi testado para vários sistemas [Ch97, Ch98] e apresentou excelentes reproduções para as seções de choque de espalhamento elástico e inelástico em uma vasta região de energia, particularmente em energias intermediárias onde efeitos refrativos dos dados de espalhamento elástico são muito sensíveis à parte real da interação [Br97a].

Para energias abaixo da barreira coulombiana, os dados de espalhamento elástico foram obtidos a partir de 43 distribuições angulares de 12 sistemas do tipo ^{16}O + A, onde A é um núcleo alvo mágico ou semimágico, com número de massa variando de 40 (Ca) à 208 (Pb) [Ch95, Ch96, Al99, Si01]. A análise desses dados forneceu informações sobre a densidade do núcleo ^{16}O em regiões superficiais. No caso de energias intermediárias, foram extraídos da literatura dados de espalhamento elástico para o sistema ^{16}O + ^{16}O, na energia de laboratório $(E_{LAB} = 1120 MeV)$, os quais forneceram informações da densidade do ^{16}O em uma região muito mais interna.

Como dito acima, assumimos o modelo para não-localidade na interação entre íons pesados, onde a parte real do potencial nuclear é dado por U_{LE} (equação 18). A densidade de um dos núcleos também foi assumida como conhecida. Assim, um método de deconvolução pôde ser utilizado para extrair a densidade do outro núcleo. Nas análises dos dados, para obter as distribuições nucleares dos núcleos alvos, foram utilizados os modelos de Hartree-Fock, Dirac-Hartree-Bogoliubov (DHB) e Shell-Model. O estudo extensivo e sistemático sobre o potencial íon-íon nos forneceu as evidências de que as densidades para esses núcleos alvos (íons mais pesados), estão bem descritas pelos cálculos teóricos [Al99, Sil01, Ga02a]. Por outro lado, dados de espalhamento de elétrons também indicam que as densidades teóricas para núcleos pesados são bastante realistas, fato que não ocorre para núcleos mais leves (vide Figura 1):

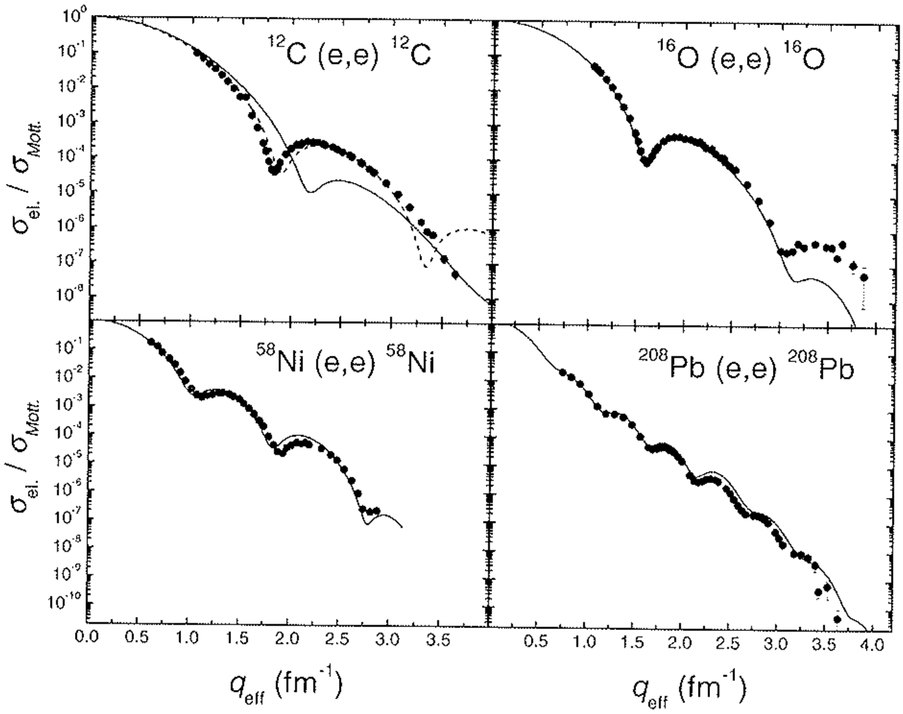

Figura 1: Seções de choque experimentais de espalhamento elástico de elétrons para os núcleos de ^{12}C, ^{16}O, ^{58}Ni, ^{208}Pb como função do momento transferido. As linhas cheias representam previsões teóricas utilizando distribuições teóricas de carga a partir de cálculos do tipo Dirac-Hartree-Bogoliubov (DHB). A linha tracejada corresponde ao cálculo com uma distribuição Fermi-Dirac, conforme [Ga02a].

Diante deste quadro, nosso trabalho foi então, por conveniência, impor a densidade "experimental" do núcleo ^{16}O, na forma de uma Fermi-Dirac com dois parâmetros livres (2PF): a difusividade (a) e o raio (R_0),

$$\rho(r) = \frac{\rho_0}{1 + \exp\left(\frac{r - R_0}{a}\right)}, \qquad (20)$$

onde, mantendo fixo os valores de "R_0" e "a", o valor de ρ_0, fica determinado pela condição de normalização:

$$A = 16 = \int 4\pi\rho(r) r^2 dr. \qquad (21)$$

Para cada distribuição angular de espalhamento elástico, variamos o parâmetro "a" e ajustamos "R_0", de forma a reproduzir os dados das seções de choque experimentais de espalhamento (minimizando o χ^2):

$$\chi^2 = \sum_N \left(\frac{\sigma_{teo} - \sigma_{\exp}}{\Delta\sigma_{\exp}} \right)^2 . \qquad (22)$$

Ao construirmos uma função-densidade, na forma de uma Fermi-Dirac, com os melhores parâmetros para cada valor de difusividade "a", verificamos a existência de um raio de sensibilidade (r_s), onde, para qualquer valor de "a", o valor de $\rho(r_s)$, é o mesmo (Figura 2).

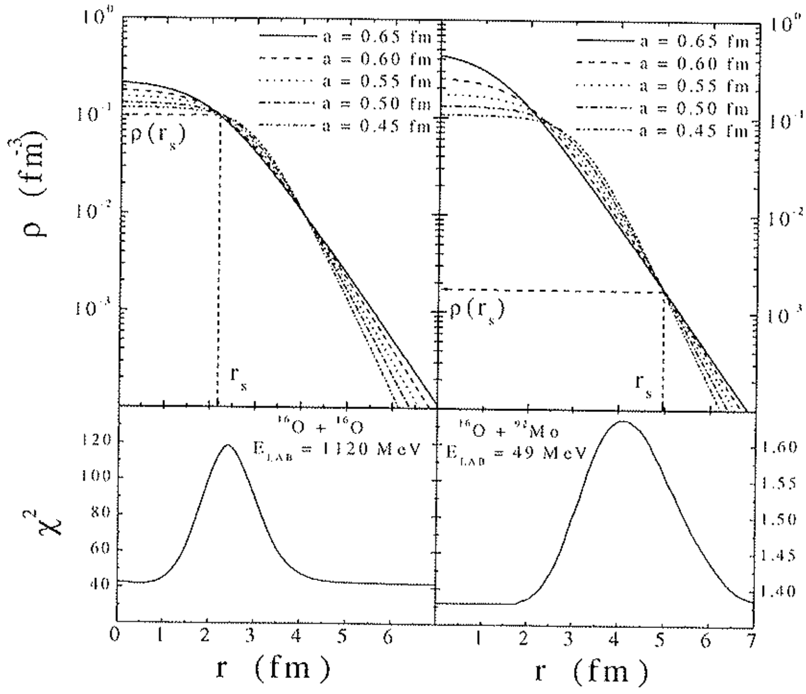

Figura 2: Gráfico de densidade do ^{16}O, com diferentes valores de difusividade, para o sistema $^{16}O+^{16}O$ em 1120 MeV (energia intermediária) e para o sistema $^{16}O+^{92}Mo$ em 49 MeV (energia subcoulombiana). A figura também apresenta um teste de notch para determinação do raio de sensibilidade.

Na Figura 2, está esquematizado um teste de notch no qual, a partir de uma perturbação dada na forma de uma função Gaussiana (equação 23), incluída na função densidade do ^{16}O, a variação da função χ^2 (chi-quadrado) é estudada como uma função da posição desta perturbação (r_p).

$$\rho_{per}(r) = \rho(r)\left\{1+0.2\left[\exp-\left(\frac{r-r_p}{0.3}\right)^2\right]\right\}. \tag{23}$$

O teste de notch garante que (r_s) está na região de sensibilidade, e não surge de cruzamentos espúrios, os quais ocorrem devido à forma particular e à condição de normalização da distribuição de densidade. Por exemplo, no caso do sistema ^{16}O + ^{92}Mo, mostrado na figura 2, o cruzamento próximo a $r = 5\,fm$ está na região de densidade que é importante (pelo teste de notch) para o ajuste dos dados, enquanto este comportamento não é detectado para o cruzamento próximo a $r = 2\,fm$.

A determinação da barra de incerteza para a densidade no raio de sensibilidade é ilustrada na figura 3 para um caso particular de distribuição angular de espalhamento elástico. Em r_S, os valores obtidos para a densidade não dependem da difusividade assumida para a distribuição. Assim, a dependência do chi-quadrado total sobre R_0 é estudada para um valor fixo de a_N, e os parâmetros que correspondem ao valor de $\chi^2(\chi^2_{min})$ e aos valores $\chi^2_{\min} + \left(\frac{\chi^2_{\min}}{n}\right)$ são encontrados (ver a determinação de $R_{0\,min}$, R_{0-} e R_{0+} na figura 3), onde "n" é o número de pontos experimentais da distribuição angular. A figura 3(b) apresenta a distribuição de Fermi para os valores de $R_{0\,min}$, R_{0-} e R_{0+} e a respectiva determinação da barra de erro para a densidade em r_S .

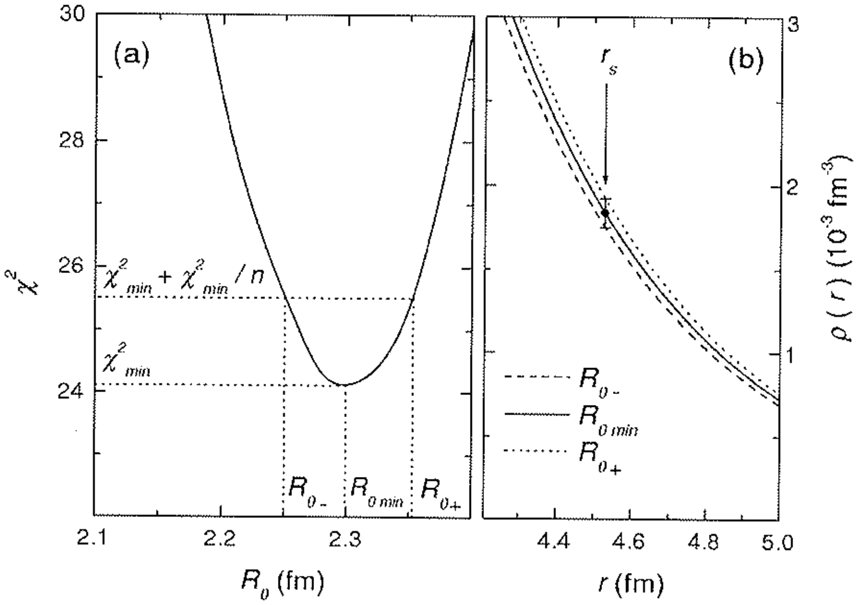

Figura 3: A figura apresenta um exemplo da determinação da barra de incerteza para a densidade do ^{12}C em r_S, para a distribuição angular do sistema ^{12}C + ^{58}Ni em $E_{Lab} = 27 MeV$ (vide [Ga02a]. (a) chi-quadrado total como função do raio da distribuição de Fermi para o parâmetro difusividade fixo em $a = 0.5 fm$, e a determinação dos valores de $R_{0_{min}}, R_{0-}$ e R_{0+}. (b) distribuições de Fermi que correspondem aos valores de $R_{0_{min}}, R_{0-}$ e R_{0+}, e a determinação da barra de incerteza para ρ em r_S.

Com isso, temos a densidade do ^{16}O bem determinada, experimentalmente, em um ponto a partir da análise de uma distribuição angular. Fazendo isso para todos os sistemas e distribuições angulares, verificamos um comportamento similar, com a existência de um raio de sensibilidade variando com a energia. O resultado pode ser observado na figura 4 a seguir.

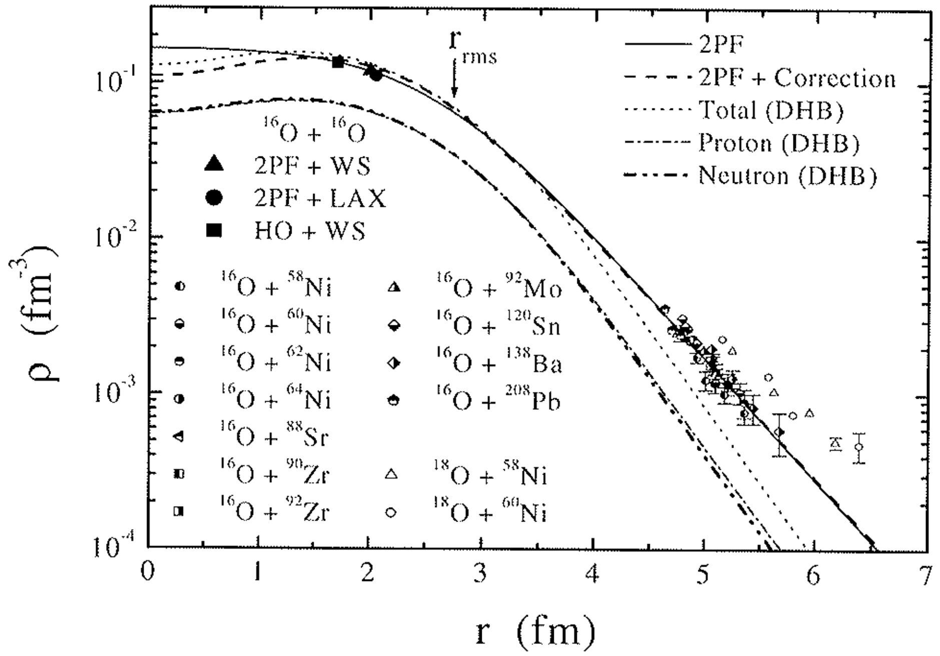

Figura 4: Determinação experimental da densidade do núcleo ^{16}O, obtida da análise de dados de espalhamento elástico de íons pesados para vários sistemas.

Os valores experimentais da densidade do ^{16}O, obtidos em seus respectivos raios de sensibilidade, são mostrados na figura 4, a partir da análise de dados de altas e baixas energias (pontos "escuros" e "semi-escuros", respectivamente). É importante destacar a dependência da posição do raio de sensibilidade com a energia. Abaixo da barreira coulombiana, esta variação está conectada com o ponto de retorno clássico do potencial efetivo e, como pode ser visto, nos permitiu mapear e caracterizar a distribuição da matéria nuclear do núcleo de ^{16}O em uma grande parte da região superficial ($4.5 \le r \le 6.0 fm$ - *figura 4*). Ainda na figura 4, temos um ajuste dos dados da densidade por uma distribuição Fermi-Dirac (2pF – linha cheia), com os correspondentes parâmetros apresentados na tabela 1:

ρ_0	0.169 fm^{-3}
R_0	2.47 fm
a	0.56 fm

Tabela 1: Melhores parâmetros, obtidos em termos de χ^2, para a função densidade de matéria do ^{16}O, representada por uma função Fermi-Dirac (equação 20).

Um estudo mais detalhado foi realizado com dados a uma energia de *1120 MeV* (pontos cheios – figura 4). Primeiramente, consideramos a possibilidade de existir alguma dependência dos resultados obtidos para os raios de sensibilidade devido à forma adotada para a distribuição de densidade, particularmente para energias intermediárias, para as quais regiões mais internas são testadas. Assim, com o objetivo de investigar tal dependência, assumimos como distribuição de densidade do núcleo ^{16}O a forma de um oscilador harmônico com dois parâmetros ajustáveis $(w \, \text{e} \, \alpha)$:

$$\rho(r)=\rho_0\left(1+\frac{\alpha r^2}{w^2}\right)exp-\left(\frac{r^2}{w^2}\right). \qquad (24)$$

Uma vez que o ajuste de dados depende da densidade apenas em uma pequena região do raio nuclear (vide teste de notch – figura 2), a determinação do raio de sensibilidade e do valor de densidade correspondente é praticamente independente da forma assumida para a distribuição nuclear (Fermi-Dirac – 2pF, oscilador harmônico – HO - figura 4).

Além disso, estudamos uma possível dependência do raio de sensibilidade (r_S) e, conseqüentemente, do método, em função do modelo utilizado para o potencial imaginário. Para isso, assumimos um potencial do tipo LAX (equação 19) e outro do tipo Woods-Saxon (equação 6). Na figura 4, apresentamos o teste realizado, também a uma energia de *1120 MeV*, podendo a priori concluir a existência de uma dependência muito pequena, para o valor experimental da densidade.

Assim sendo, os resultados obtidos para a densidade do ^{16}O, são muito pouco sensíveis à forma da distribuição assumida para o ^{16}O e também ao modelo adotado para a parte imaginária do potencial ótico. As correspondentes distribuições angulares de espalhamento elástico também são muito pouco sensíveis a esses fatores (vide figura 5).

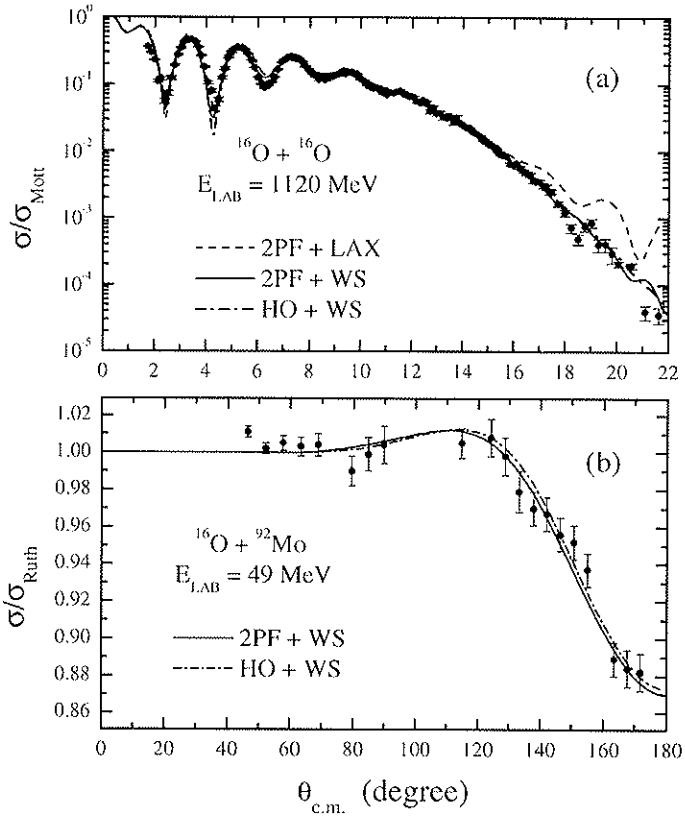

Figura 5: Ajuste de dados de seções de choque de espalhamento elástico em baixa e alta energia. Os ajustes foram obtidos utilizando distribuições de Fermi-Dirac ou Oscilador Harmônico para a densidade do ^{16}O, e uma parte imaginária do potencial ótico do tipo Woods-Saxon ou Lax.

Com a proposta de comparação e demonstração da sensibilidade do método, estendemos nossos cálculos à determinação da densidade experimental do núcleo de ^{18}O (figura 4 - pontos abertos), através da análise de dados de espalhamento elástico em energias abaixo da barreira coulombiana para os sistemas ^{18}O + ^{58,60}Ni, trabalho este que fez parte da tese de doutoramento de um dos membros do meu grupo de pesquisa do Laboratório Pelletron. Como esperado teoricamente [Mi90], e claramente demonstrado pelos nossos resultados, os dois nêutrons extras do núcleo ^{18}O (orbitais $2s_{1/2}$, $1d_{3/2}$ e $1d_{5/2}$) aumentam a densidade do núcleo de ^{18}O, na região superficial, em comparação àquela obtida para o núcleo de ^{16}O.

Um outro ponto que merece ser destacado é a consistência do método independente da grande variação dos núcleos utilizados como núcleos-alvo. Pode ser observado, na figura 4, que sistemas com diferentes núcleos-alvo fornecem valores consistentemente semelhantes para a densidade do ^{16}O.

Uma previsão teórica para a densidade do ^{16}O, derivada do modelo Dirac-Hartree-Bogoliubov (DHB) [Ca00], usando parâmetros do potencial núcleon-núcleon NL3, também é mostrada na figura 4 (linha pontilhada). Na superfície, a densidade experimental do ^{16}O é muito maior do que a prevista teoricamente. Uma análise de cálculos teóricos de níveis de partícula-única mostra como isso pode ser entendido. Embora o conjunto de parâmetros NL3 tenha sido ajustado para reproduzir energias e os raios de carga e de nêutrons tabelados, este não leva em conta propriedades de partícula-única, o que nos sugere a direção para futuras melhoras em tal conjunto de parâmetros.

Na figura 6, apresentamos mais um teste de consistência para o método de determinação experimental da distribuição de densidade do núcleo de ^{16}O. Comparamos os dados experimentais de seções de choque de espalhamento de elétrons, extraídos de [Si70], com a distribuição de carga "experimental" derivada da distribuição de matéria nuclear obtida com o nosso método. Para obter a distribuição de carga do núcleo (ρ_{ch}), utilizamos o método Folding:

$$\rho_{ch}(r) = \int \rho_p(\vec{r}\,')\rho_{chp}(\vec{r} - \vec{r}\,')d\vec{r}\,', \qquad (25)$$

onde (ρ_p) é a distribuição de prótons do núcleo, $\rho_{chp}(\vec{r})$ é a distribuição de carga intrínsica do próton no espaço vazio. Para o núcleo duplo-mágico ^{16}O, a distribuição de prótons (ρ_p) é aproximadamente metade da distribuição total de matéria (próton + nêutron), (vide densidades teóricas de prótons e nêutrons na figura 4).

As seções de choque de espalhamento de elétrons foram calculadas (apêndice III) na aproximação de Born para ondas planas:

$$\frac{\sigma}{\sigma_{Mott}}(q) = \left(\frac{4\pi}{Zeq} \int \rho_{ch}(r) r \sin(qr) dr \right)^2, \qquad (26)$$

onde q é o momento transferido. Para núcleos leves, tais como o ^{16}O, a aproximação de Born deve produzir seções de choque muito próximas do método exato de deslocamento de fase, exceto para momentos transferidos próximos de um mínimo de difração.

Assumindo a densidade do ^{16}O na forma de uma Fermi-Dirac (tabela 1 e Figura 4 – linha cheia), em cálculos para reprodução de dados experimentais de espalhamento elástico de elétrons sobre o núcleo de ^{16}O (Figura 6 - parte de cima), verificamos que o ajuste de dados só deixa a desejar na região de momento transferido $1.5 \leq q \leq 3.0\, fm^{-1}$. Assim sendo, nossa densidade extraída de dados de espalhamento elástico de íons pesados, sem parâmetros livres, ajusta-se perfeitamente aos dados, perdendo um pouco de intensidade em uma região de momentos transferidos mais sensível à densidade para distâncias próximas do raio quadrático médio, para onde esperamos que a função densidade não seja uma Fermi-Dirac perfeita.

Baseado em cálculos teóricos para a densidade do ^{16}O no estado fundamental, tais discrepâncias são entendidas considerando-se o decréscimo na contribuição dos componentes $1p_{\frac{3}{2}}$ e $1p_{\frac{1}{2}}$, para a densidade nuclear numa região de raios mais internos (vide densidade teórica na figura 4). Temos levado em conta esse fato, pois os mesmos dados de espalhamento de elétrons são ajustados, considerando a função Fermi-Dirac somada a uma pequena correção, na forma de uma função oscilatória, na região próxima ao raio quadrático médio (figura 4 – $2pF + correction$). Isto resultou em uma melhor descrição dos dados de seção de choque de elétrons (figura 6 - $2pF + correction$ - linha tracejada). Vale destacar, ainda na figura 6, o ajuste dos dados experimentais a partir de cálculos DHB, os quais apresentam uma séria discrepância com os dados em uma região de momento transferido $q \geq 3 fm^{-1}$. Podemos então concluir a consistência do nosso método, principalmente no que diz respeito à superfície. Além disso, pela primeira vez, foi possível descrever seções de choque de espalhamento de elétrons a partir da densidade da matéria nuclear "experimental", obtida através da análise de dados de espalhamento elástico de íons pesados.

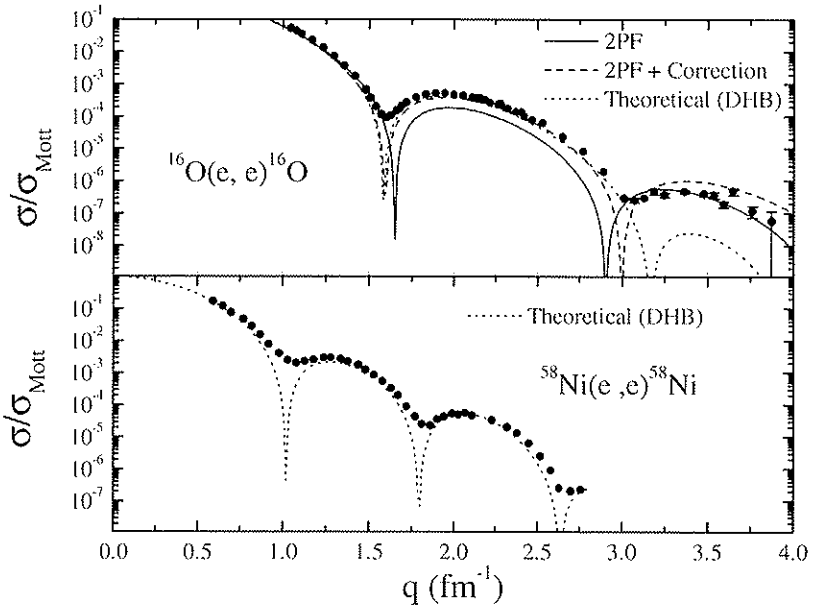

Figura 6: Seções de choque de espalhamento elástico de elétrons para os núcleos de ^{16}O (em cima) e ^{58}Ni (embaixo) como função do momento transferido. As linhas pontilhadas representam previsões teóricas utilizando distribuições de carga a partir de cálculos do tipo Dirac-Hartree-Bogoliubov (DHB) na aproximação de Born para ondas planas. As outras linhas (em cima) representam os resultados para as distribuições de carga derivadas das densidades da matéria nuclear, usando funções Fermi-Dirac 2pF, como mostradas na figura 4, com (linha tracejada) ou sem (linha sólida) uma correção oscilatória amortecida.

III.1 Sistematização da Densidade Nuclear

A necessidade de um modelo preciso para a densidade do núcleo ^{16}O [Al99] foi o ponto de partida para o desenvolvimento do método apresentado neste trabalho. De acordo com o modelo double-Folding, o potencial nuclear para íons-pesados depende essencialmente das densidades dos núcleos em colisão e de um modelo para descrever a dependência com a energia da parte real da interação, sendo que, para este último, já havia sido desenvolvida a sistemática, considerando a não-localidade da interação proposta pelo meu grupo de pesquisa em [Ri97, Ch97, Ch98, Ch02]. Assim, o método concentrou esforços sobre um núcleo específico (^{16}O) e, embora sendo mais tarde aplicado no estudo de outros núcleos pesados-leves, a sistematização da parte real do potencial nuclear requeria uma sistematização preliminar das densidades nucleares de uma maneira mais ampla, (todas as regiões de massa). Dessa forma, um trabalho paralelo ao desenvolvimento do método para determinação experimental da densidade da matéria nuclear para o núcleo ^{16}O foi desenvolvido por nosso grupo, com o objetivo de sistematizar as densidades nucleares de íons pesados, tendo como finalidade sistematizar a parte real do potencial nuclear [Ch02]. Foram calculadas as distribuições teóricas para um grande número de núcleos usando o modelo de Dirac-Hartree-Bogoliubov (DHB) [Ca00], e estudados os resultados de sistemáticas anteriores, para distribuições de cargas [Vr87, Na94] extraídas de experimentos de espalhamento de elétrons. Sistematizamos densidades de carga, prótons, nêutrons, nucleons (prótons + nêutrons) e matéria. De forma análoga à equação 25, assumimos uma definição para a densidade de matéria como sendo uma convolução da distribuição de nucleons do núcleo com a distribuição de matéria intrínsica do núcleon, a qual é assumida para ter a mesma forma da distribuição de carga intrínsica do próton. Por conveniência, as distribuições de carga e matéria são normalizadas pelo número de prótons e de núcleons, respectivamente. Todas as densidades teóricas e a maior parte das densidades "experimentais" não são exatamente distribuições de Fermi. Assim, com o objetivo de obter densidades de equivalente difusividade, foram calculadas as derivadas na região superficial ($r \approx R_0 + 2fm$).

$$a \approx -\frac{\rho(r)}{\frac{d\rho}{dr}}. \qquad (27)$$

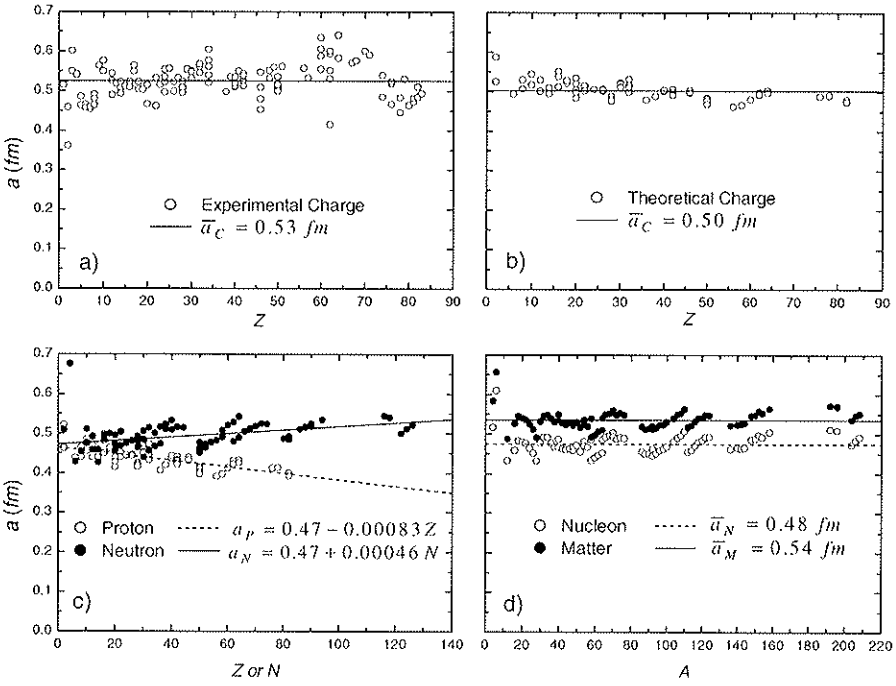

Figura 7: Valores equivalentes de difusividade obtidos para distribuições de carga extraídas a partir de experimentos de espalhamento de elétrons, e densidades teóricas obtidas a partir de cálculos de Dirac-Hartree e Bogoliubov.

A figura (7) [Ch02] mostra os resultados para as distribuições de carga. Os valores de difusividade se distribuem ao redor de uma difusividade média $\overline{a}_c = 0.53 fm$, com um desvio de 0.04 *fm*. A maior parte dessa dispersão é devido a incertezas experimentais. Sem dúvida, nós temos verificado que diferentes análises (diferentes conjuntos de dados de espalhamento de elétrons ou diferentes modelos para a densidade de carga), para um mesmo núcleo, fornecem valores de difusividades que diferem um do outro em cerca de 0.03 *fm*. Portanto, as distribuições de cargas experimentais são compatíveis, dentro da precisão experimental, com um valor de difusividade constante. As distribuições de carga teóricas apresentam um comportamento similar (figura 7b), com um valor médio levemente menor do que o valor experimental. Neste caso, o desvio observado, 0.02 *fm*, está associado a efeitos de estrutura dos núcleos. Apesar da tendência apresentada pela difusividade de nêutrons e de prótons (figura 7c), todas as distribuições de nucleons resultam em um valor de difusividade muito similar $(\overline{a}_N = 0.48 fm)$, com um desvio de 0.025 *fm*. Devido ao procedimento Folding, as distribuições de matéria apresentam valores de difusividade significativamente maiores $(\overline{a}_M = 0.54 fm)$ do que aquela apresentada para as distribuições de nucleons. Levando em consideração que os cálculos teóricos têm levemente subestimado a difusividade de carga experimental, consideramos que valores médios mais realistas, para as difusividades das densidades de nucleons e matéria, sejam 0.50 *fm* e 0.56 *fm*, respectivamente. Uma dispersão (σ_a) de cerca de 0.025 *fm* em torno desta média é prevista devido aos efeitos de estrutura dos núcleos.

O raio quadrático médio (RMS) da distribuição é definido pela equação (28):

$$r_{RMS} = \sqrt{\frac{\int_0^\infty r^4 \rho(r) dr}{\int_0^\infty r^2 \rho(r) dr}} . \qquad (28)$$

Nós determinamos os raios R_0 para as distribuições 2pF assumindo que os correspondentes raios quadráticos médios (RMS) deveriam ser iguais àqueles das densidades experimentais (espalhamento de elétrons) e teóricas (DHB). Os resultados para R_0 a partir das distribuições de carga teóricas (figura 8b) são muito semelhantes aos obtidos com espalhamento de elétrons (figura 8a). As densidades de nucleons e matéria fornecem raios bastante similares (figura 8d), os quais são bem descritos pela seguinte relação linear:

$$R_0 = 1.31 A^{1/3} - 0.84 fm. \qquad (29)$$

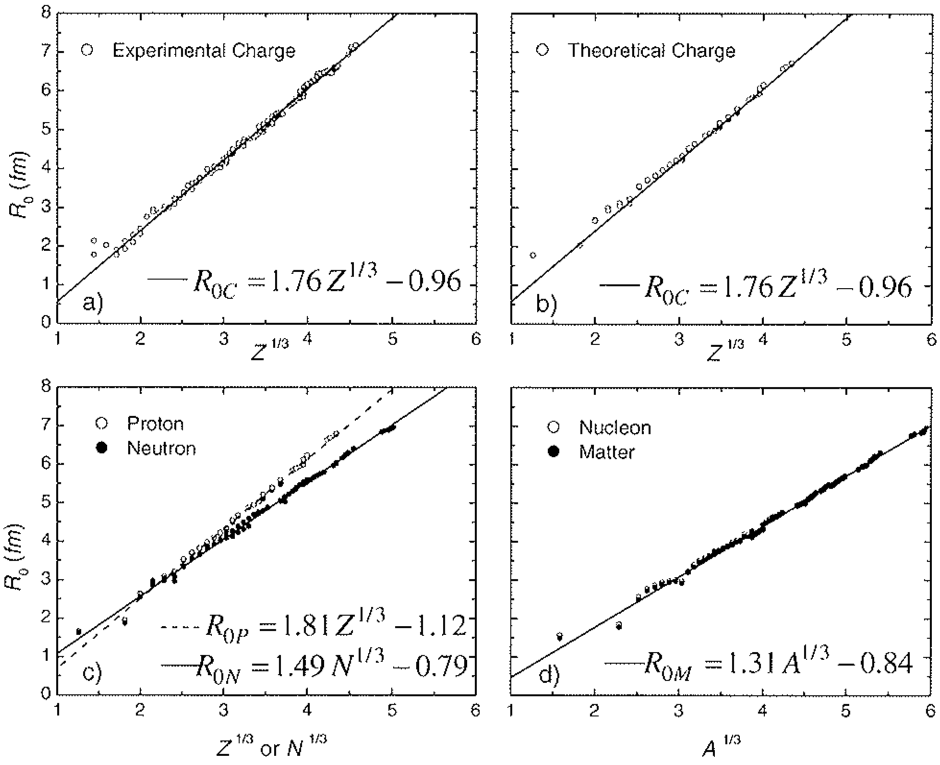

Figura 8: Parâmetros R_0 obtidos para as distribuições de carga extraídas a partir de experimentos de espalhamento de elétrons e para as densidades teóricas obtidas a partir de cálculos de Dirac-Hartree-Bogoliubov.

Devido aos efeitos de estrutura dos núcleos, os valores de R_0 se distribuem em torno desta relação com uma dispersão de 0.07 *fm*, mas, quanto mais pesado é o núcleo, menor é o desvio. Na figura 9 estão apresentadas as densidades de nucleons teóricas (DHB) para uns poucos núcleos, e as correspondentes distribuições 2pF com $a = 0.50\,fm$ e os valores de R_0 obtidos a partir da equação (29).

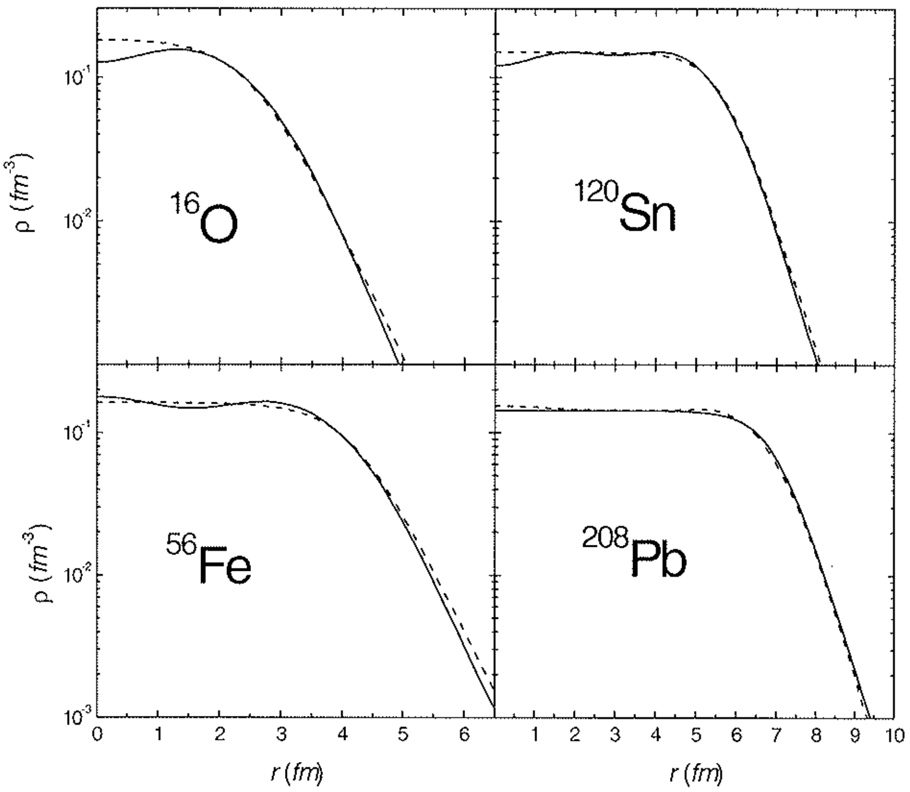

Figura 9: Densidades de núcleons a partir de cálculos Dirac-Hartree-Bogoliubov (linhas sólidas) comparadas às correspondentes distribuições de Fermi-Dirac, 2pF, (linhas tracejadas), com $a=0.50fm$ e R_0 obtidos através da equação 29.

IV Sistematização do Potencial Ótico

Com objetivo de sustentar nossos métodos e todo o estudo sistemático desenvolvido para a parte real do potencial nuclear, voltamos nos para a parte imaginária do potencial ótico, à qual, por não termos ainda um modelo fundamental, podem estar vinculadas algumas discrepâncias apresentadas (por exemplo, figura 5 (a)) entre os dados experimentais e os ajustes gerados a partir dos modelos utilizados. Uma das possibilidades seria tentar estabelecer uma relação entre as partes real e imaginária do potencial. Algumas investigações preliminares [Gl59, Cz69, Br97, Ch97, Br97b], para identificar dependências entre as partes real e imaginária do potencial foram feitas, considerando a interação realista do tipo LAX (equação 19), a qual propiciou ajustes satisfatórios de dados experimentais de espalhamento elástico em energias intermediárias [Br97, Ch97]. A equação 19, a qual deriva da teoria de espalhamento múltiplo, não é válida para baixas energias, onde processos coletivos de reação são importantes. Este fato mantinha os ajustes para baixas energias uma questão aberta na determinação de um potencial fundamental e global. Com a idéia de realizar mais um teste de consistência para a parte real da interação nuclear desenvolvida a partir do modelo de não-localidade e da sistemática das densidades nucleares, nós seguimos o conceito da aproximação de Glauber para altas energias (equação 19) de usar a mesma forma radial para a parte real e imaginária do potencial ótico e estendemos a equação 18, desenvolvida para a parte real do potencial nuclear, para a parte imaginária da interação, de tal forma que:

$$W(R,E) = iNI \cdot V_N(R,E) . \qquad (30)$$

Nós escolhemos os sistemas ^{12}C + ^{12}C, ^{16}O, ^{40}Ca, ^{90}Zr, ^{208}Pb; ^{16}O + ^{208}Pb e ^{40}Ar + ^{208}Pb como testes, devido ao grande número de dados experimentais disponíveis em um grande intervalo de massa e energia, e principalmente devido a efeitos refrativos especiais envolvendo alguns desses sistemas em certas energias. Nas figuras (10 a 16), as linhas sólidas correspondem ao melhor valor obtido procurando o melhor parâmetro "*NI*" nos ajustes de diversas distribuições angulares. Nós optamos por manter nos cálculos o valor de difusividade média para as densidades, mesmo sabendo que poderíamos eventualmente melhorar o ajuste, permitindo que a difusividade fosse um parâmetro livre. Como podemos observar na figura 17, o parâmetro *NI* é aproximadamente independente do sistema e da energia, com um valor médio $NI = 0.78$. Nas figuras (10 a 16), podemos observar as excelentes previsões obtidas para as seções de choque de espalhamento elástico usando este valor médio para todo o conjunto de dados experimentais. Assim sendo, temos conseguido um modelo para o potencial ótico de forma a detalhar diversos fenômenos decorrentes de reações nucleares envolvendo vários sistemas em uma vasta região de energia e, mais importante: sem a utilização de parâmetros livres.

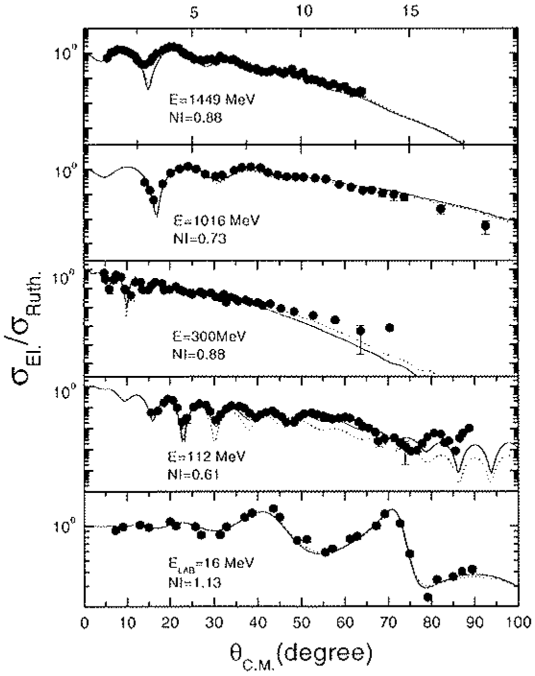

Figura 10: Distribuições angulares de espalhamento elástico para o sistema $^{12}C+^{12}C$ em várias energias de bombardeio. As linhas sólidas correspondem ao melhor ajuste usando a mesma função radial para as partes real e imaginária do potencial nuclear, com o parâmetro NI sendo ajustado para cada distribuição angular. As linhas pontilhadas correspondem às previsões obtidas com o valor médio $NI = 0.78$.

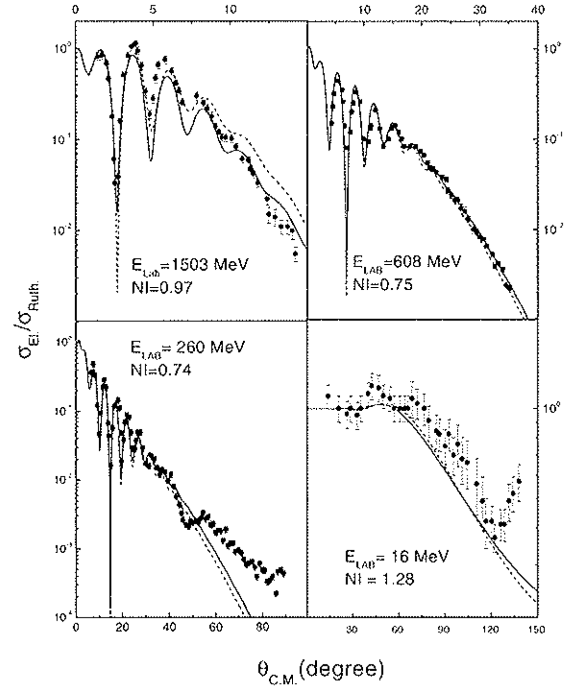

Figura 11: O mesmo da figura 10 para o sistema $^{12}C+^{16}O$.

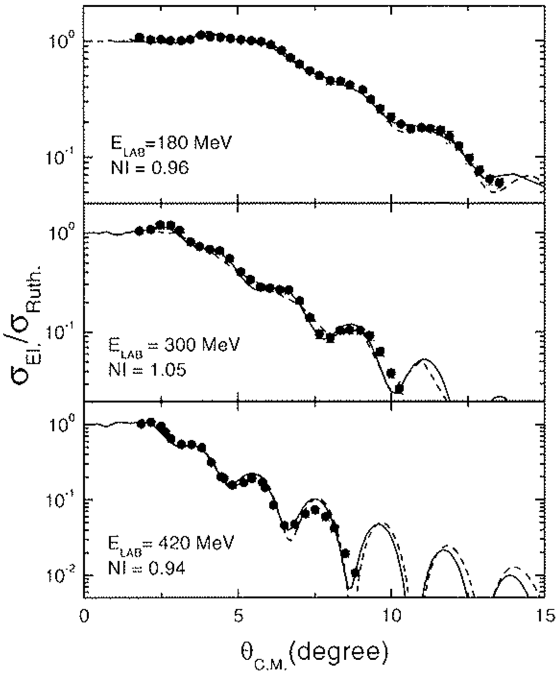

Figura 12: O mesmo da figura 10 para o sistema $^{12}C+^{40}Ca$.

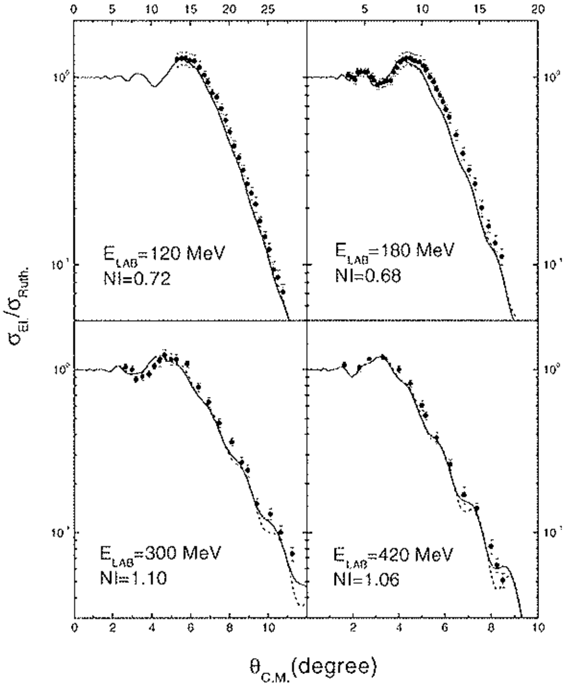

Figura 13: O mesmo da figura 10 para o sistema $^{12}C+^{90}Zr$.

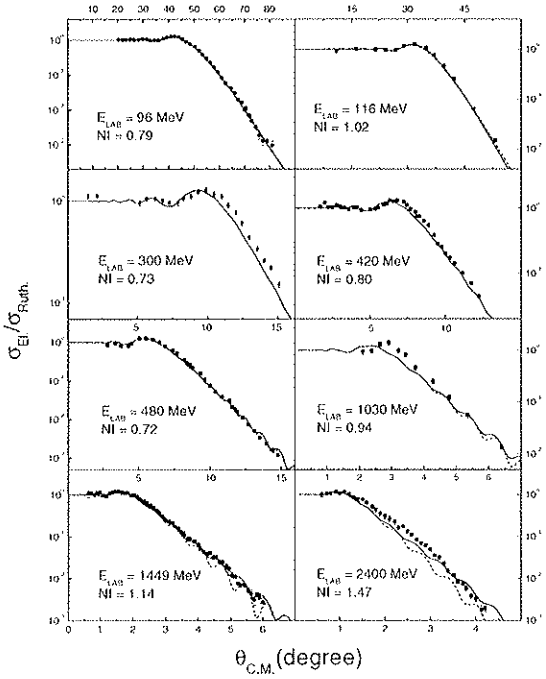

Figura 14: O mesmo da figura 10 para o sistema $^{12}C+^{208}Pb$.

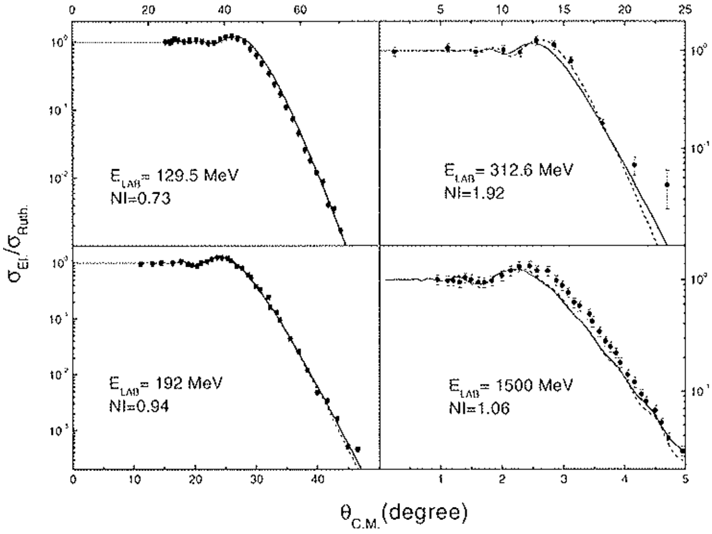

Figura 15: O mesmo da figura 10 para o sistema $^{16}O+^{208}Pb$.

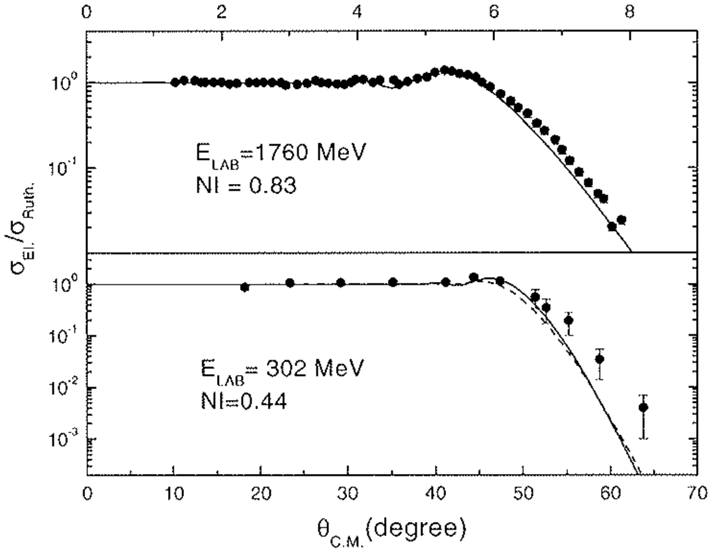

Figura 16: O mesmo da figura 10 para o sistema $^{40}Ar+^{208}Pb$.

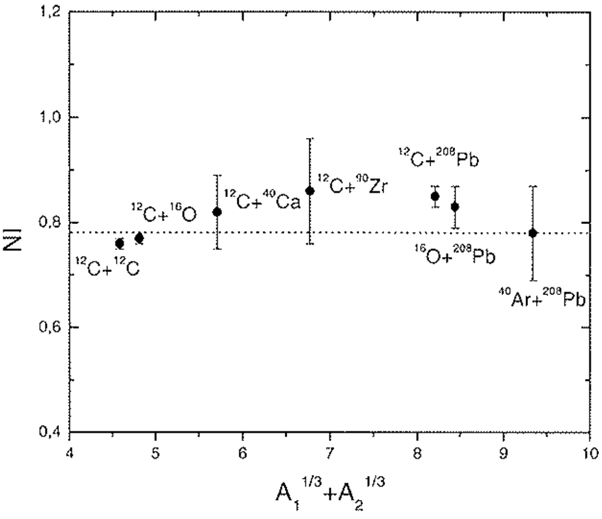

Figura 17: Valores de *NI* obtidos para os diferentes sistemas e energias de bombardeio. A linha tracejada representa o valor médio $NI = 0.78$.

V PARTE EXPERIMENTAL

V.1 Introdução

O projeto inicial deste trabalho previa um amplo e preciso estudo experimental, envolvendo vários canais de reação, para os sistemas ^{16}O + $^{40,48}Ca$, assim como já havia sido realizado para os sistemas ^{16}O+ $^{58,60,62,64}Ni$, ^{88}Sr, $^{90,92}Zr$, ^{92}Mo, ^{208}Pb [Ch95, Ch96, Al99]. Com isso, nosso objetivo seria completar uma sistemática experimental para o potencial nuclear, envolvendo as diferentes regiões de massa da tabela periódica, através dos diferentes núcleos, utilizados como alvo, e o núcleo ^{16}O, fixo como projétil.

Devido a atrasos referentes à importação dos isótopos $^{40,48}Ca$, comecei a parte experimental do projeto de doutoramento trabalhando com a tomada e análise de dados do sistema ^{16}O + ^{120}Sn, um alvo em outra região de massa, mas dentro da mesma sistemática. Os resultados serão descritos mais adiante e podem ser encontrados na referência [Si01]. Este trabalho foi desenvolvido e publicado pelo meu grupo de pesquisa, durante o período de doutoramento.

No entanto, os trabalhos teóricos de desenvolvimento de tal sistemática para o potencial nuclear tiveram um progresso extremamente rápido, através das sistemáticas desenvolvidas para as densidades dos núcleos interagentes [Al99, Al02, Ro02, Ga02a e Ch02] e a dependência em energia abordada pelo tratamento não-local [Ri97, Ch97, Ch98, Ch02], as quais, como discutido no decorrer desta tese, eliminavam discrepâncias entre os dados e os ajustes propiciados pelos modelos teóricos adotados para o potencial. Este fato fez com que os sistemas ^{16}O + $^{40,48}Ca$ se tornassem mais uma forma de testar as sistemáticas do que propriamente uma contribuição indispensável para construção da mesma. Diante de tais mudanças ocorridas sobre as prioridades do trabalho de doutoramento não foi realizada nenhuma experiência envolvendo o sistema ^{16}O + ^{48}Ca, e o nosso trabalho com o sistema ^{16}O + ^{40}Ca se resumiu à determinação das seções de choque de espalhamento elástico, sem que houvesse necessidade de estudarmos outros canais de reação. Desta forma, a parte experimental do trabalho de doutoramento foi composta por medidas de seções de choque de espalhamento elástico envolvendo os sistemas ^{16}O + ^{40}Ca, ^{120}Sn, e a caracterização de um detector proporcional a gás utilizado na realização das experiências envolvendo o sistema ^{16}O + ^{40}Ca.

As experiências para obtenção dos dados foram realizadas no Acelerador Pelletron, do tipo "tandem" 8UD, do Departamento de Física Nuclear do Instituto de Física da Universidade de São Paulo.

V.2 A Fonte de Íons

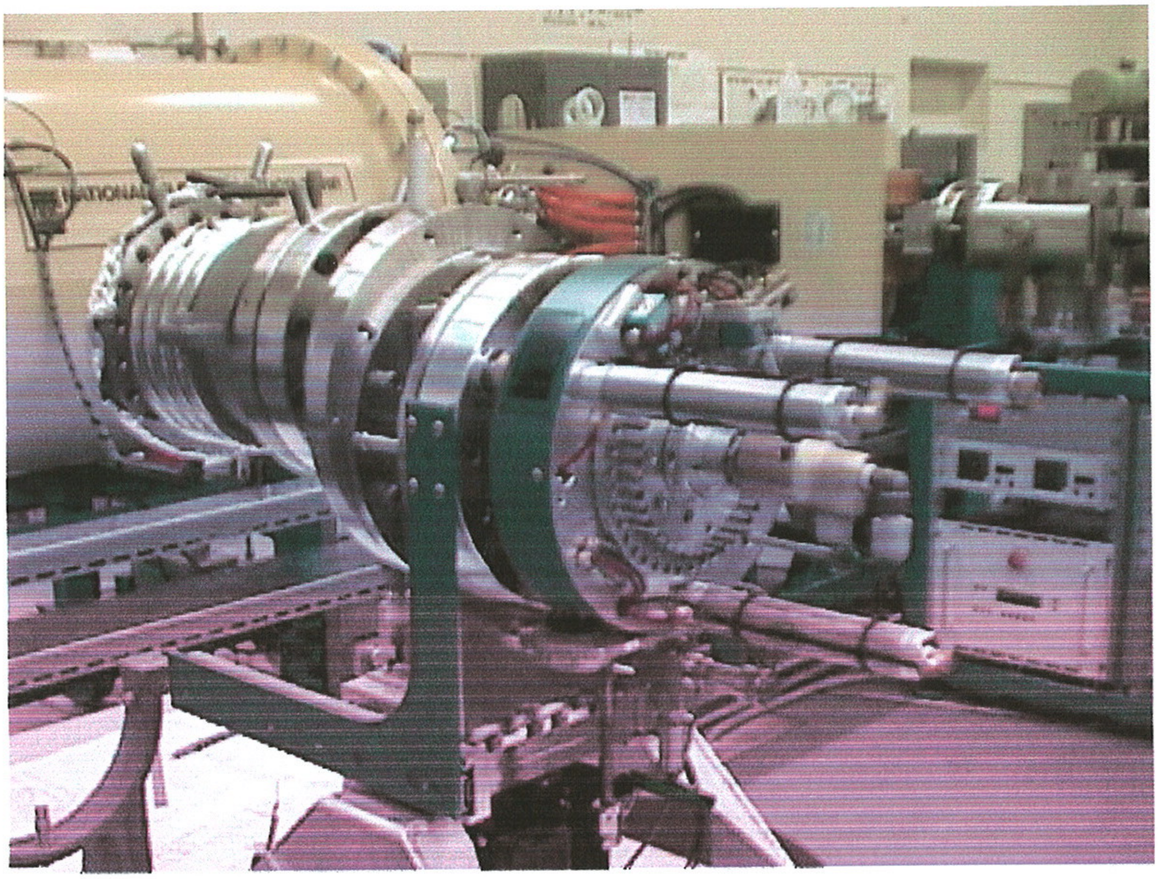

Figura 18: Foto da fonte SNICS desacoplada do acelerador Pelletron.

O feixe de íons negativos de oxigênio a ser injetado no acelerador é gerado por uma fonte de íons do tipo SNICS ("Source of Negative Ions by Cesium Sputtering"). Esta fonte utiliza o processo "sputtering" (com feixe primário de Césio) para produzir o feixe do elemento desejado. Nesse processo, o vapor de césio neutro é introduzido numa região de descarga eletrônica, onde é ionizado por um filamento helicoidal de tungstênio.

Os íons positivos de césio (Cs^+), formados na região em torno do filamento, são focalizados por uma lente eletrostática no catodo. O catodo tem a forma de um pequeno cadinho de cobre, sobre o qual é depositado o elemento (ou composto químico do elemento), que se deseja como feixe, no caso ^{16}O. O choque dos íons de Cs^+ com o catodo é suficiente para arrancar íons negativos desse material ("Césium Sputtering").

Os íons de $^{16}O^-$, assim produzidos, são dirigidos à abertura da fonte por uma diferença de potencial entre o anodo e o catodo, que varia de 1KV a 3KV, e a seguir são extraídos por um potencial extrator de 20 KV.

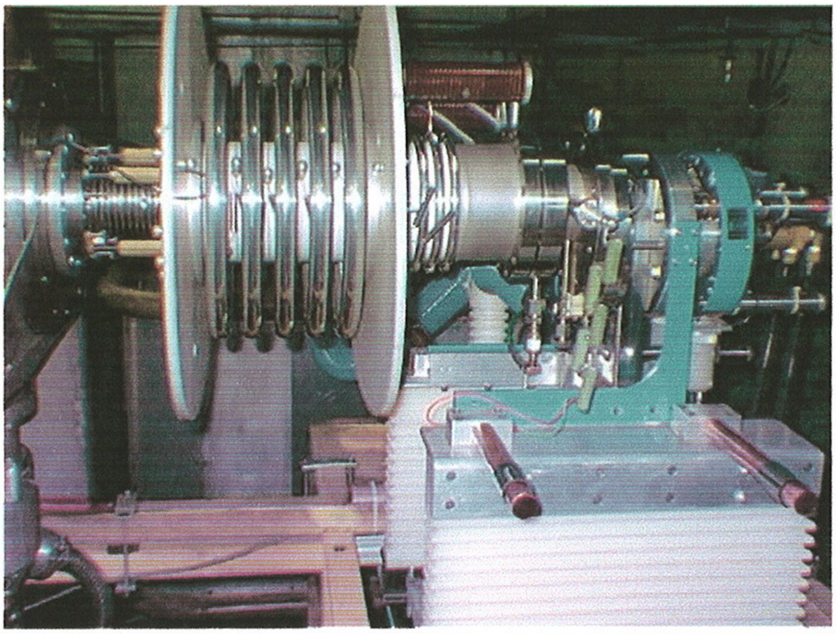

Figura 19: Vista lateral da fonte de íons SNICS, acoplada ao acelerador *Pelletron*.

V.3 O Acelerador Pelletron

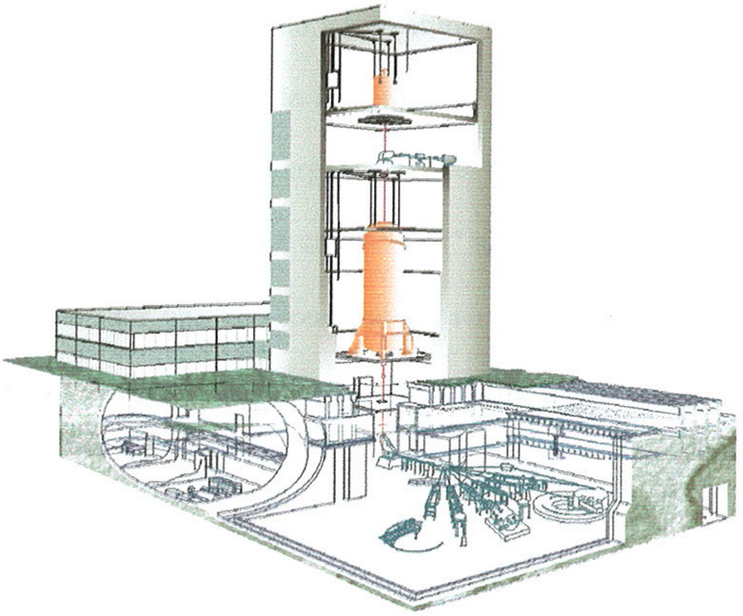

Figura 20: Esquema do Laboratório Pelletron 8UD.

No acelerador, o feixe é acelerado em dois estágios. Após ser extraído da fonte de íons, o feixe é pré-acelerado e focalizado pela ação de um tubo acelerador polarizado com uma tensão $V_i = -80KV$, em relação à terra, e injetado no acelerador.

As condições ópticas para o transporte do feixe até a entrada do acelerador são garantidas por um eletroímã analisador de focalização simples, com valor máximo de poder de deflexão $ME/Z^2 = 20$ (ME-20), e por um dubleto quadrupolar eletrostático.

Este eletroímã seleciona a massa (M) dos íons no feixe pré-acelerado, antes destes entrarem no tubo acelerador.

Após a deflexão de 90° (figura 20), o feixe negativo é acelerado em direção ao terminal de carga do tubo acelerador, até atingir uma fina folha de carbono (Stripper), onde se inicia o segundo estágio de aceleração. Ao atravessá-la, as partículas do feixe perdem vários elétrons, adquirindo carga positiva e, conseqüentemente, formando agora um feixe de íons positivos. Os íons com carga "$+qe$" são novamente acelerados em direção à saída do tubo acelerador por um potencial do terminal (V_t). O feixe emerge do tubo acelerador com uma energia total adquirida segundo a equação

$$E_T = eV_i + (q+1)eV_t, \qquad (31)$$

onde:

V_i é o potencial de extração do feixe no interior da fonte de íons somado ao potencial aplicado no tubo pré-acelerador;

e é a carga eletrônica;

eV_i, a energia de entrada do feixe no acelerador;

q, o estado de carga do íon após atravessar o Stripper;

V_t, a tensão no terminal.

Na saída do acelerador, o feixe passa, ainda, por um segundo eletroímã analisador de dupla focalização, denominado ME-200, que além de defletir o feixe 90°, seleciona sua energia (E).

O controle de energia é feito automaticamente, por um sinal elétrico gerado pela diferença de corrente em um conjunto de fendas situado na saída do ME-200 e conectado por um triodo a uma agulha de corona no terminal de carga do acelerador. Assim, qualquer desvio do feixe, resultante da variação de sua energia, logo é detectado pelas fendas, fazendo com que haja variação de corrente na agulha de corona, que irá atuar diretamente no ajuste do potencial no terminal de carga do acelerador, corrigindo o valor da energia.

Finalmente, o feixe de íons emergentes, selecionado, é defletido por um terceiro eletroímã ("Switching Magnet") que o desvia para uma das canalizações existentes. Este trabalho foi realizado na Câmara de Espalhamento situada na canalização 30B (a 30° em relação ao feixe precedente ao "Switching-Magnet", na sala B-figura 21).

V.4 A Câmara de Espalhamento

A câmara onde são realizadas as medidas de espalhamento da canalização 30B tem uma forma cilíndrica com 1m de diâmetro e 30 cm de altura (figura 21).

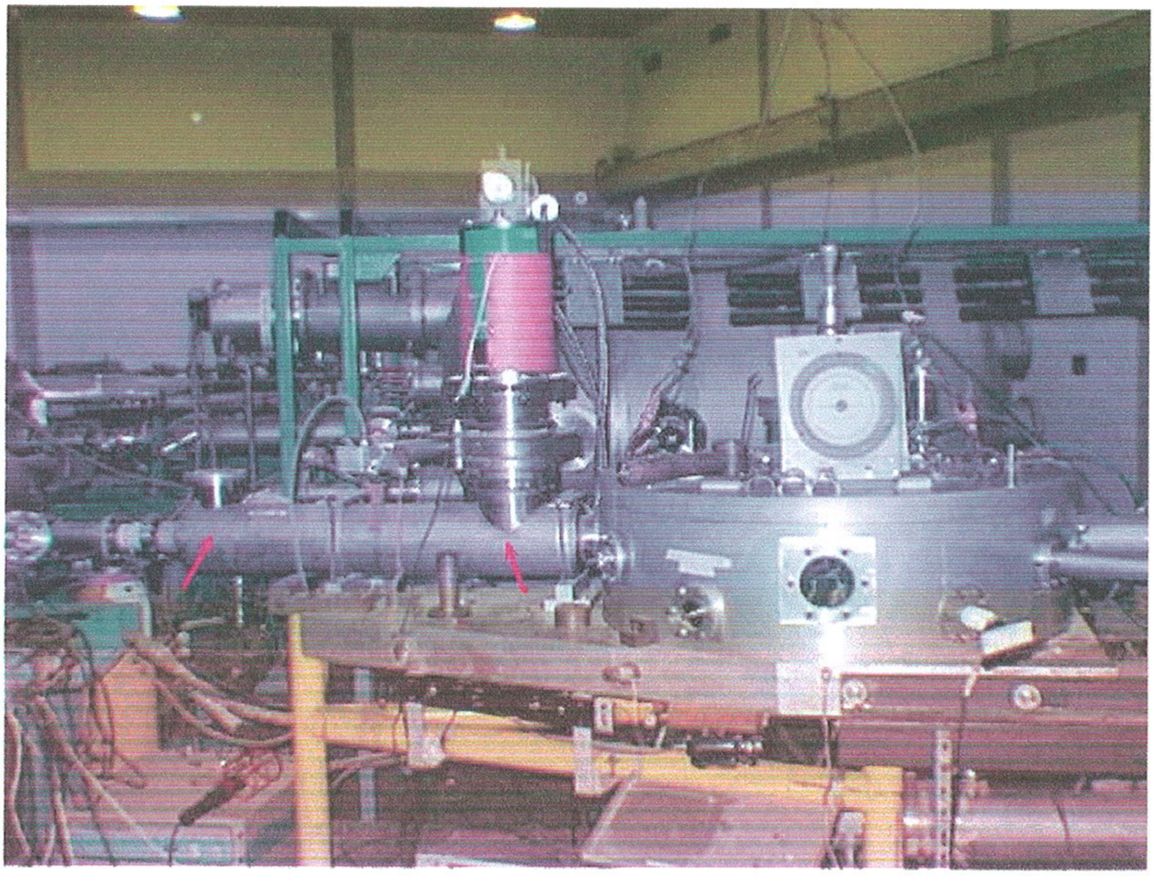

Figura 21: Foto da câmara de espalhamento localizada na canalização 30B (setas vermelhas) do Laboratório Pelletron.

A câmara possui um prato giratório, com uma escala graduada de precisão de leitura de 1', sobre o qual é montado o sistema de detectores. A medida angular é efetuada por uma luneta instalada externamente na parte superior da câmara. Na parte central do interior da câmara, está colocada a torre de alvos, a qual possui a capacidade de comportar quatro alvos, simultaneamente, permitindo que o alvo possa ser trocado sem que haja perda de vácuo no interior da câmara. Durante as medidas, a pressão no interior da câmara é mantida em torno de $1\,\mu\,Torr$ (alto-vácuo), pressão esta obtida utilizando-se uma bomba do tipo turbo molecular e uma tipo criogênica.

Uma escala graduada está acoplada à parte superior da torre de alvos e tem a função de determinar o ângulo em que o alvo fica posicionado com relação à direção do feixe.

A definição da direção do feixe é feita por dois conjuntos de colimadores na entrada da câmara, obtendo-se, no alvo, uma imagem do feixe aproximadamente circular com 2mm de diâmetro.

V.5 O Sistema de Detecção

Iniciando o trabalho experimental com a reação $^{16}O + ^{40}Ca$, realizamos duas experiências com o objetivo de ajustar as condições ideais de trabalho e análise. Nestas primeiras experiências, percebemos a existência de "contaminantes" nos espectros, junto ao processo de espalhamento elástico do sistema, fator que certamente prejudicaria os resultados da análise. Este fato trouxe a necessidade de utilização de um detector proporcional a gás [Pe78].

Devido à grande mobilidade de elétrons e íons, um gás é um meio ideal para usar na "coleta" de ionização devido à radiação. Muitos fenômenos de ionização surgem em gases e há muitos anos estes têm sido estudados e explorados em detectores a gás.

O estudo de muitas reações envolve a identificação de produtos gerados em seus vários canais de saída abertos: espalhamento elástico, espalhamento inelástico, transferência de nucleons, fusão etc. Com o objetivo de estudar essas reações, o detector a gás pode ser utilizado como um sistema capaz de identificar as variações de energia das diferentes partículas geradas em uma reação (sistema E-ΔE). A identificação das partículas, no caso, é feita através da análise de um espectro bi-paramétrico (figura 27), construído com ΔE (perda de energia) em função de E (energia residual das partículas).

Ainda nesse aspecto, em nosso caso específico, a contribuição do detector a gás proporcional é a de eliminar os eventuais "contaminantes", que fatalmente aparecem em algumas medidas experimentais. O gás pode funcionar como filtro para algumas partículas indesejadas que, ao reagirem com o gás perderiam diferentes frações de energia das partículas de interesse. Isto seria detectado por um detector de barreira de superfície, sendo então os processos de interação, envolvendo as partículas de interesse, isolados em um espectro bi-paramétrico (figura 27).

V.6 Princípio de Operação do Detector Proporcional

Os detectores proporcionais são geralmente construídos com geometria cilíndrica. O ânodo consiste em um fio posicionado ao longo do eixo de um tubo cilíndrico que serve como catodo (figura 22a). A diferença de potencial aplicada entre os eletrodos forma um campo eletrostático entre o fio de ânodo e o catodo. A radiação ionizante, ao penetrar no volume sensível, pode interagir com o gás, produzindo um par elétron-íon. Os elétrons são forçados pelo campo eletrostático a dirigirem-se até o fio de ânodo. Nas proximidades do fio, onde o campo elétrico é extremamente intenso, estes elétrons são acelerados até que suas energias sejam altas o suficiente para provocar novas ionizações nas moléculas do gás. Inicia-se então um processo de multiplicação de cargas na forma de uma avalanche (figura 22b).

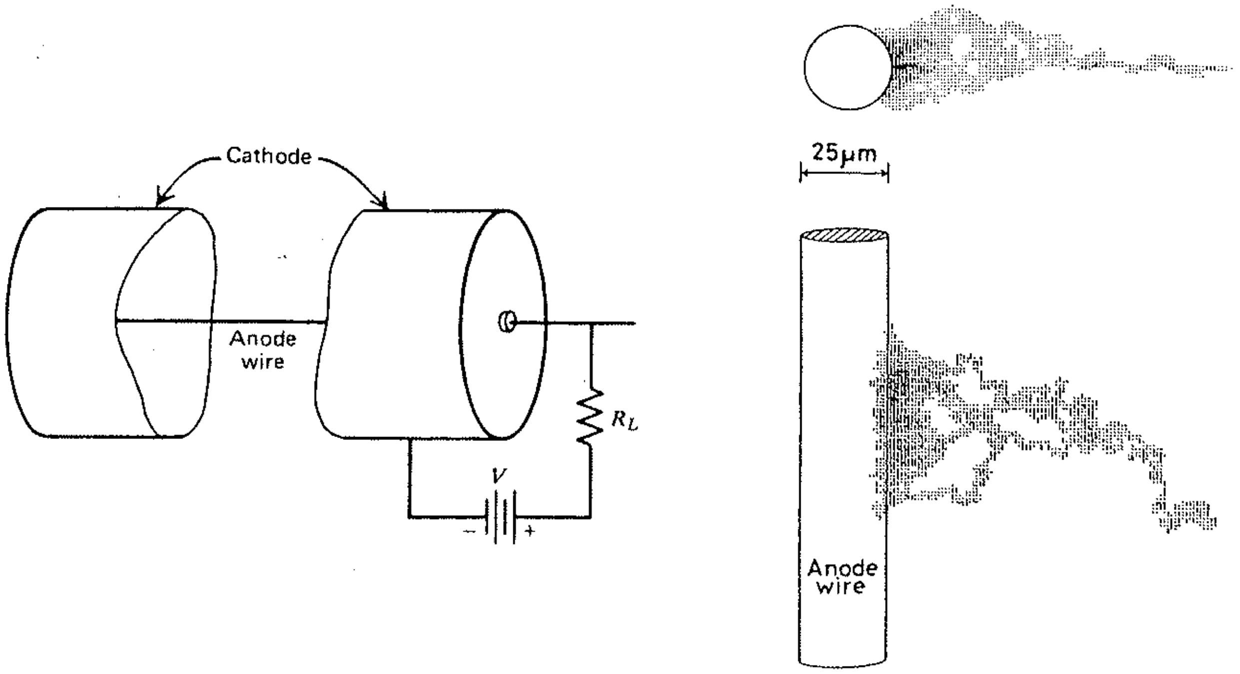

(a-) (b-)

Figura 22: a-) Esquema de um detector proporcional e seu circuito de polarização. b-) Esquema do processo de avalanche de cargas ocorrendo ao redor do fio de anôdo.

Os elétrons produzidos na avalanche são coletados no fio de ânodo após uma fração de nanossegundos. Os íons positivos movem-se na direção do catodo mais lentamente que os elétrons, com velocidades aproximadamente proporcionais à intensidade do campo elétrico local. O movimento de cargas positivas afastando-se do ânodo induz cargas- imagens nos demais eletrodos existentes ao redor, resultando em um sinal negativo sobre o fio de ânodo, onde a avalanche de cargas se originou, e um sinal positivo induzido nos eletrodos vizinhos. A maior fração do sinal do ânodo é formada pelo movimento de afastamento dos íons positivos; a contribuição da coleção de elétrons é geralmente desprezível, sendo da ordem de 1% a 2% da carga total do sinal formado no ânodo.

V.7 Descrição do Identificador de Partículas Utilizado

O esquema do telescópio do contador proporcional é mostrado na figura 23.

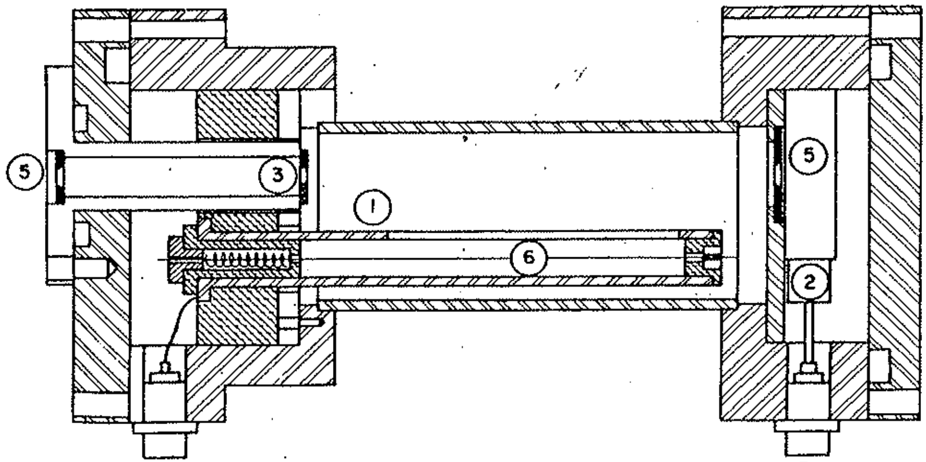

Figura 23: Vista lateral do detector proporcional: 1-) anéis de coleta de carga; 2-) detector de estado sólido; 3-) janela de entrada; 4-) conectores de microponto; 5-) fendas; 6-) fio.

O contador ΔE [Pe78] é um contador proporcional de um único fio de 69 mm de comprimento efetivo, com um diâmetro de 21.5 mm. Um fio de tungstênio recoberto com ouro é cercado por anéis com o objetivo de restringir as cargas coletadas em uma região de campo homogêneo. Um detector de silício localizado dentro do contador proporcional mede a energia final da partícula, após esta passar através do gás. O detector proporcional é operado com uma mistura de gás denominada, P-10 (90% Ar + 10% CH_4). Um manostato mantém um fluxo contínuo de gás através do detector proporcional e a pressão é mantida constante com ± 0.2 *Torr* ou 0.2%, o que for maior. A janela de entrada consiste ou em uma fina camada de um material denominado MAKROFOL de $240\,\mu g / cm^2$ ou em uma fina folha de 30 a $150\,\mu g / cm^2$ produzida através do método VYNS [Fo75].

O telescópio do detector proporcional pode ser facilmente montado, dentro de nossa câmara de espalhamento de 1 metro de diâmetro, localizada no final da canalização 30B do Laboratório Pelletron (figura 21). Para a realização das experiências utilizamos um conjunto de três contadores $E - \Delta E$ espaçados de 10° em laboratório.

V.8 Caracterização do Detector Proporcional a Gás

Com o problema dos contaminantes resolvido através do detector proporcional a gás e com as condições de trabalho do gás utilizado e energias de bombardeio bem estabelecidas, iniciamos uma segunda etapa de experiências e respectivas análises.

Ao fim das análises preliminares sobre os espectros biparamétricos, obtidos a partir da utilização do detector a gás, observamos um possível problema de eficiência nos três componentes do detector proporcional. Este fato gerou a necessidade de quantificarmos esta eficiência com a maior precisão possível, de modo que não houvesse perdas significativas sobre a precisão da seção de choque experimental de espalhamento elástico obtida.

Um estudo detalhado, com diferentes sistemas em diferentes energias, foi então realizado a fim de estabelecer possíveis dependências de tal eficiência. A partir desse estudo, pudemos obter a dependência da eficiência com o sistema, mais especificamente com o alvo, uma vez que usamos sempre o mesmo feixe. Sendo assim, utilizamos o sistema $^{16}O + ^{40}Ca$, em uma energia de bombardeio bem abaixo da barreira de fusão, de modo que a seção de choque experimental esperada fosse a seção de choque de Rutherford, isto é, $\sigma/\sigma_R = 1$ e, a partir disso, determinamos as perdas de eficiência relativas a cada energia e ângulo de espalhamento (cada um dos três detectores, constituintes do detector proporcional). A eficiência como função da energia, obtida para cada detector, pode ser observada nos três gráficos que seguem, onde podemos perceber também a existência de uma relação linear, mas diferente para cada um dos detectores, em uma determinada faixa de energia.

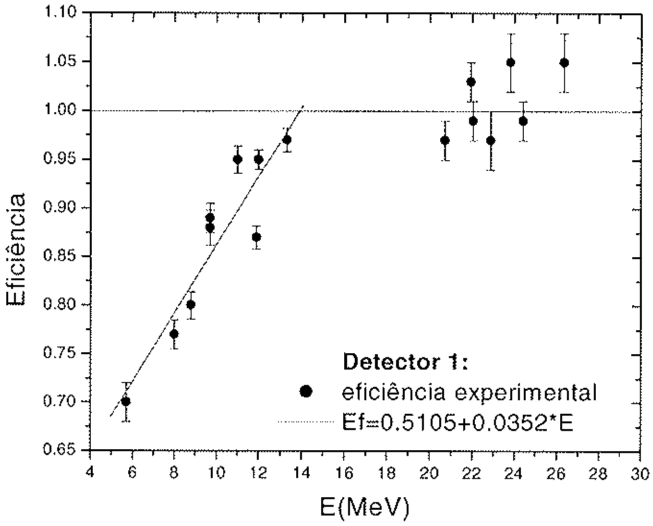

Figura 24: Gráfico da eficiência como função da energia para o detector 1 (detector à esquerda, em uma vista frontal) do detector proporcional, a partir da análise do sistema $^{16}O + {}^{40}Ca$, a uma energia de bombardeio de 28 MeV.

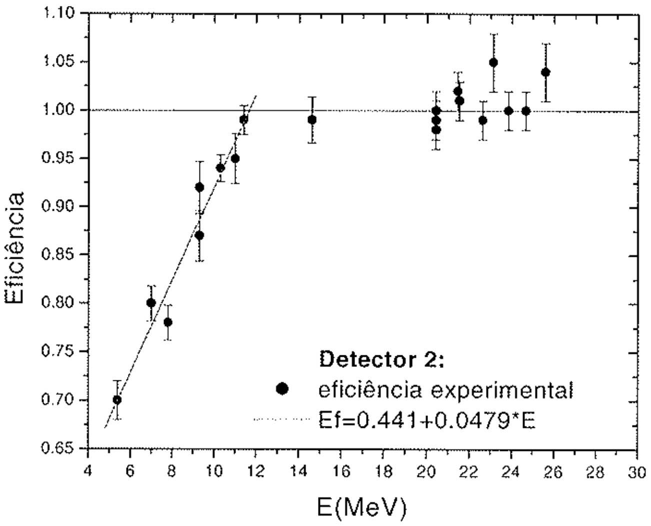

Figura 25: Gráfico da eficiência como função da energia para o detector 2 (central) do detector proporcional, a partir da análise do sistema $^{16}O + {}^{40}Ca$, a uma energia de bombardeio de 28 MeV.

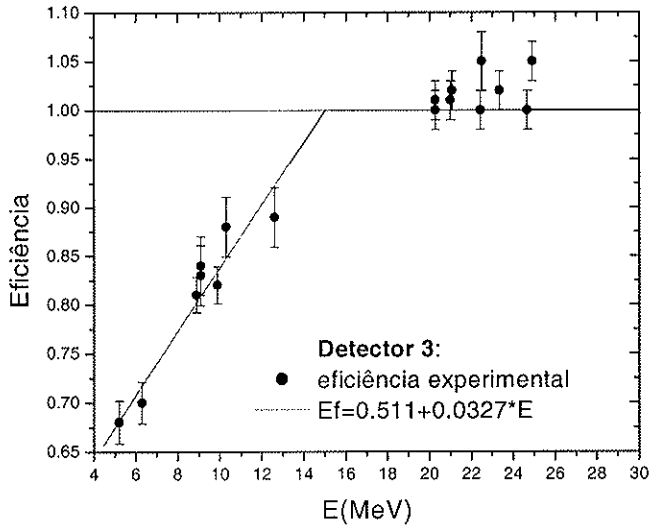

Figura 26: Gráfico da eficiência como função da energia para o detector 3 (detector à direita em uma vista frontal) do detector proporcional, a partir da análise do sistema ^{16}O + ^{40}Ca, a uma energia de bombardeio de 28 MeV.

V.9 Eletrônica de Aquisição

A eletrônica de aquisição de dados fornece um tratamento apropriado às informações transmitidas pelos detectores de barreira de superfície, com a finalidade de torná-las adequadas ao processo de digitalização, que garantirá o armazenamento e conseqüente aproveitamento dessas informações.

Cada detector está ligado a um pré-amplificador, de tal forma que os pulsos produzidos pelos detectores são inicialmente pré-amplificados na saída da câmara de espalhamento. Esses sinais são transmitidos via cabo até a sala de controle do Laboratório Pelletron, onde são amplificados. Cada sinal relativo a um evento é então direcionado a um conversor analógico-digital (ADC), onde é convertido em um endereço e armazenado na memória de um microcomputador.

Neste ponto começa a utilização do sistema CAMAC ("Computer Automated Measurement and Control") instalado na sala de controle do laboratório, onde temos à disposição 16 ADC's.

No sistema CAMAC, é necessário trabalhar com uma eletrônica de coincidência simples. Deve-se produzir, portanto, uma coincidência do pulso de energia com ele próprio. Por essa razão, paralelamente à amplificação de cada pulso, extraímos do mesmo amplificador um sinal atrasado por um analisador tipo monocanal T.S.C.A. ("Timing Single Channel Analyzer"), sendo que os dois devem chegar ao CAMAC simultaneamente, confirmando a ocorrência de um evento.

Cada evento registrado pelo sistema CAMAC, em seu respectivo canal de energia, é somado de tal forma que, após um determinado número de horas de experiência tenhamos registrado um grande número de eventos relativos a cada canal de reação, em forma de picos de energia. Estes picos são exibidos em um terminal gráfico, num processo em linha, gerando assim um espectro de contagens por canal.

Os espectros adquiridos em cada tomada de dados possuem um tamanho de 1024 canais, e esse processo de aquisição de dados é chamado de "modo multicanal". Os espectros podem ser graficados em escala linear ou logarítmica, e armazenados em disquetes, permitindo que a redução dos dados possa ser realizada num processo fora de linha.

O fato dos espectros poderem ser exibidos simultaneamente à ocorrência da experiência nos possibilita observar a existência de eventuais problemas com a eletrônica de aquisição ou com a própria experiência.

V.10 O Espectro Biparamétrico

Com o objetivo de construir um espectro biparamétrico das medidas simultâneas dos dois parâmetros de interesse E e ΔE, os dados são armazenados evento por evento em um computador "on-line", usando uma interface desenvolvida no laboratório Pelletron. Os dados podem então ser automaticamente transferidos para finalmente serem analisados em um processo "off-line", onde o espectro biparamétrico é construído, armazenado e pode ser impresso. Um conjunto de códigos computacionais está disponível para uma análise de um espectro biparamétrico. Com estes códigos é possível selecionar regiões de interesse do espectro, e projetar um ou ambos os parâmetros de interesse.

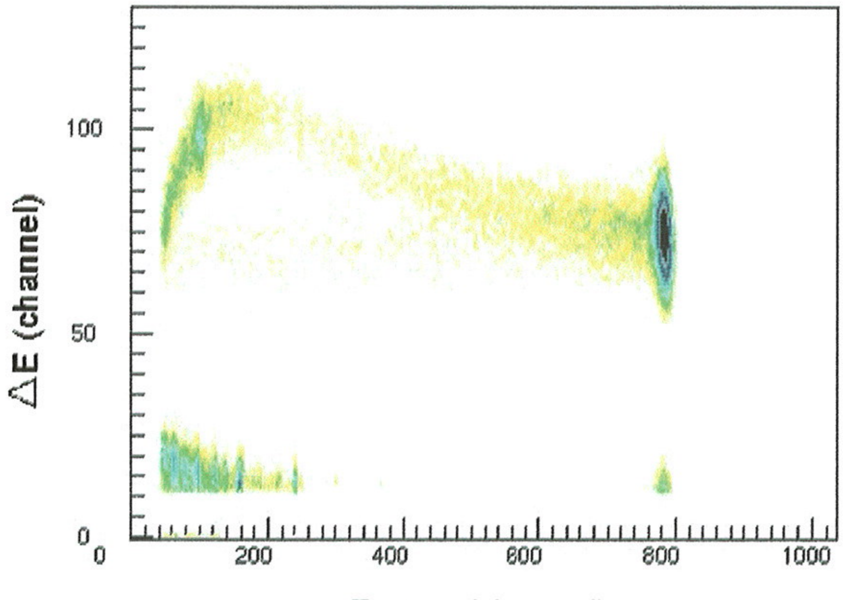

Figura 27: Espectro de energia em função da perda de energia das partículas geradas pela reação $^{16}O + ^{40}Ca$ na energia de laboratório de 32 MeV.

V.11 Cálculo da Seção de Choque Diferencial Experimental

Antes de nos atermos ao cálculo da seção de choque, devemos relatar um detalhe experimental de muita importância no desenvolvimento do mesmo. Todos os nossos alvos foram recobertos por uma camada de ouro, pois além de obtermos maior precisão na calibração em energia dos espectros, o ouro também nos fornece a normalização dos dados sem que haja a necessidade de utilização de um detector do tipo monitor.

A escolha do ouro vem do fato de que nossas energias de trabalho foram muito inferiores à barreira coulombiana do sistema ^{16}O + ^{197}Au, possibilitando assumir, com excelente aproximação, que a seção de choque de espalhamento elástico (σ_{Au}) é igual à seção de choque de Rutherford (σ_{Au}^{R}), sendo este resultado de grande utilidade no cálculo da seção de choque diferencial experimental de espalhamento elástico, como explanaremos a seguir.

A seção de choque diferencial de espalhamento elástico é definida pela equação:

$$Y_X = \sigma_X N_X I \Delta\Omega f_X \, , \tag{32}$$

onde:

$Y \equiv$ contagens do pico elástico;

$X \equiv$ elemento alvo em cada sistema;

$\sigma \equiv$ seção de choque de espalhamento elástico no sistema de centro de massa;

$N \equiv$ número de centros espalhadores por unidade de área;

$I \equiv$ número de partículas incidentes;

$\Delta\Omega \equiv$ ângulo sólido proporcionado pelo sistema de detecção (sistema de laboratório);

$f \equiv$ fator de transformação do ângulo sólido no sistema de laboratório para o sistema de centro de massa.

Na expressão 32, "X" pode representar qualquer um dos elementos alvos com os quais trabalhamos (^{40}Ca, ^{120}Sn). Quando tratarmos do ouro nos cálculos que seguem, utilizaremos o índice Au no lugar de X, de tal forma que:

$$Y_{Au} = \sigma_{Au} N_{Au} I \Delta\Omega f_{Au} \tag{33}$$

Tendo em vista a normalização dos dados, dividimos as equações 32 e 33:

$$\frac{Y_X}{Y_{Au}} = \frac{\sigma_X N_X f_X}{\sigma_{Au} N_{Au} f_{Au}} \tag{34}$$

$$\sigma_X = \frac{Y_X N_{Au} f_{Au}}{Y_{Au} N_X f_X} \sigma_{Au}. \tag{35}$$

Considerando, então, $\sigma_{Au} = \sigma_{Au}^R$ como uma boa aproximação, podemos reescrever 35 na forma:

$$\sigma_X = \frac{Y_X N_{Au} f_{Au}}{Y_{Au} N_X f_X} \sigma_{Au}^R. \tag{36}$$

Dividindo a equação 36 pela seção de choque de Rutherford do alvo em questão temos:

$$\frac{\sigma_X}{\sigma_X^R} = \frac{Y_X N_{Au} f_{Au} \sigma_{Au}^R}{Y_{Au} N_X f_X \sigma_x^R}. \tag{37}$$

A seção de choque de Rutherford é dada por:

$$\sigma_X^R = \left(\frac{Z_X Z_P e^2}{4E_{C.M.X}}\right)^2 \left(\frac{1}{sen^4\left(\theta_{C.M.X}/2\right)}\right), \tag{38}$$

onde: $Z_X \equiv$ número atômico do alvo (^{40}Ca, ^{120}Sn, ^{197}Au);

$Z_P \equiv$ número atômico do projétil (^{16}O);

$e^2 \equiv$ carga eletrônica quadrática ($1.44\,MeV \cdot fm^2$);

$E_{C.M.} \equiv$ energia no referencial de centro de massa;

$\theta_{C.M.} \equiv$ ângulo de espalhamento, também no referencial de centro de massa.

Tomando o ouro (Au) separadamente dos demais alvos, uma vez que este foi utilizado na normalização dos quatro sistemas, temos:

$$\sigma_{Au}^R = \left(\frac{Z_{Au} Z_P e^2}{4E_{C.M.}}\right)^2 \left(\frac{1}{sen^4\left[\frac{\theta_{C.M.(Au)}}{2}\right]}\right) \tag{39}$$

Substituindo as equações 38 e 39 em 37, resulta que a seção de choque diferencial experimental de cada sistema é dada por:

$$\frac{\sigma_X}{\sigma_X^R} = \frac{Y_X}{Y_{Au}} KF(\theta), \tag{40}$$

onde:

$$F(\theta) = \frac{f_{Au}}{f_X} \frac{\text{sen}^4\left(\theta_{C.M.(X)}/2\right)}{\text{sen}^4\left(\theta_{C.M.(Au)}/2\right)} \tag{41}$$

é o fator dependente do ângulo e do sistema analisado. Para o espalhamento elástico, podemos mostrar que f_X e f_{Au} podem ser calculados diretamente pela expressão:

$$f_X = \frac{(A_X + A_p)^2}{A_X A_p \left[\left(\frac{A_X}{A_p} \right)^2 + \operatorname{sen}^2 \theta_{LAB} \right]^{1/2}} \left(1 - \frac{2 A_X A_p}{(A_X A_p)^2} (1 - \cos \theta_{C.M.}) \right). \quad (42)$$

A_X e A_p são as massas atômicas do alvo e do projétil, respectivamente. (θ_{LAB}) é o ângulo de detecção no referencial de laboratório. Assim, para cada sistema fomos capazes de determinar $F(\theta)$ em cada ângulo de detecção.

A constante K é determinada por:

$$K = \frac{N_{Au} Z_{Au} E_{C.M.}}{N_X Z_X E_{C.M.(Au)}} = \frac{N_{Au} Z_{Au} A_{Au}}{N_X Z_X A_X (A_{Au} + A_p)} \quad (43)$$

e depende da relação entre as espessuras do ouro e do elemento X (alvo). Essa constante, a qual independe da energia e também do ângulo, é obtida utilizando medidas em ângulos bem dianteiros $(\theta_{LAB} \approx 40^\circ)$ e energias baixas, onde podemos assumir $\sigma_X = \sigma_X^R$ (seção de choque de Rutherford para o elemento X). Vale salientar que, no caso específico deste trabalho, a equação 40 foi utilizada com uma norma de acordo com a eficiência de cada detector obtida conforme as figuras 24, 25 e 26.

V.12 Resultados Experimentais dos Sistemas $^{16}O+^{40}Ca$ e $^{16}O+^{120}Sn$

Nas figuras 26 e 27 estão apresentados os dados de seção de choque de espalhamento elástico para os sistemas ^{16}O + ^{40}Ca, ^{120}Sn nas energias de laboratório de 30, 31 e 32 MeV e 53, 54 e 55 MeV, respectivamente. As linhas cheias representam ajustes realizados utilizando o potencial não-local, com a densidade do ^{16}O obtida a partir do método desenvolvido neste trabalho, enquanto as densidades do ^{40}Ca e do ^{120}Sn foram obtidas a partir de cálculos DHB.

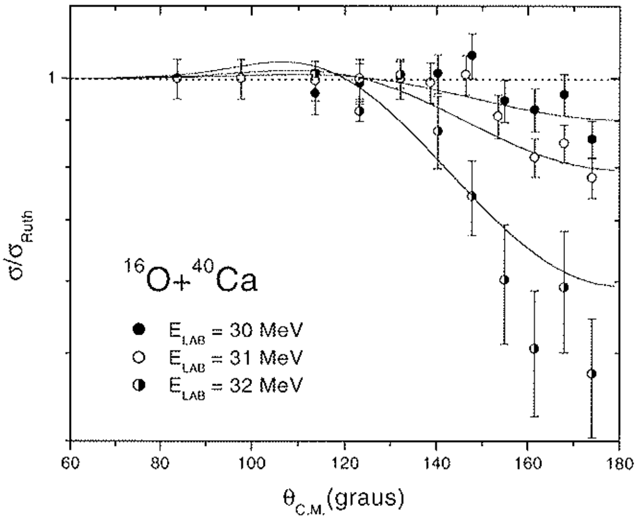

Figura 28: Distribuições angulares referentes ao processo de espalhamento elástico do sistema ^{16}O + ^{40}Ca, nas energias de laboratório de 30, 31 e 32 *MeV*. As linhas cheias representam os ajustes realizados usando a sistemática para o potencial nuclear apresentada nesse trabalho.

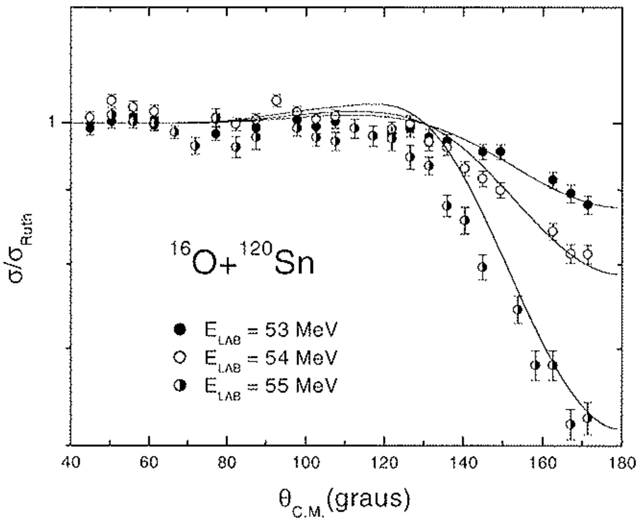

Figura 29: Distribuições angulares referentes ao processo de espalhamento elástico do sistema ^{16}O + ^{120}Sn nas energias de laboratório de 53, 54 e 55 *MeV*. As linhas cheias representam os ajustes realizados usando a sistemática para o potencial nuclear apresentada neste trabalho.

VI CONCLUSÃO

A partir do progresso alcançado nos últimos anos para descrever o espalhamento elástico de íons pesados, desenvolvemos um método para determinação experimental da densidade da matéria de núcleos pesados, com precisão comparável àquela obtida para as distribuições de carga através de experimentos de espalhamento elástico de elétrons. A validade do método foi amplamente verificada através de diversos testes de consistência:

1-) Reproduzimos os resultados experimentais de dados de seções de choque de espalhamento elástico de elétrons sobre o núcleo ^{16}O.

2-) Verificamos a independência do método com a forma assumida para a densidade.

3-) Verificamos a independência do método em relação ao modelo assumido para a parte imaginária da interação nuclear.

4-) Finalmente, verificamos a consistência do método para os vários alvos utilizados nos diferentes sistemas que trabalhamos.

O método se mostrou uma poderosa ferramenta para a determinação da densidade da matéria de núcleos no estado fundamental, particularmente em uma região superficial, onde a diferença entre a densidade de núcleos exóticos e núcleos estáveis vizinhos é muito enfatizada [Ga02b]. O método desenvolvido neste trabalho para o núcleo ^{16}O já foi estendido em outros trabalhos [Ga02a, Ro02, Ga02b], para determinação da densidade de outros núcleos estáveis (^{12}C, ^{18}O) e do núcleo exótico ^{6}He, apresentando resultados bastante significativos.

Como complemento do trabalho, realizamos uma análise consistente de dados de espalhamento elástico de íons pesados em energias baixas e intermediárias. Assumimos a sistemática desenvolvida na seção III.1 para a densidade nuclear; o modelo não-local para descrever a dependência com a energia da parte real da interação nuclear (equação 18); e a absorção de fluxo devido aos canais de reação sendo proporcional à parte real da interação nuclear (equação 30). Esta análise permitiu obter uma previsão extremamente satisfatória para as seções de choque de espalhamento elástico experimentais, para um vasto conjunto de dados, utilizando um modelo bastante fundamental e global para o potencial ótico e, mais importante, sem a utilização de parâmetros livres (capítulo IV).

Diante do sucesso referente à sistematização do potencial nuclear na descrição de colisões entre íons pesados, em uma vasta região de energias de bombardeio, meu grupo de pesquisa pretende agora estender o modelo de forma a obter uma descrição unificada de várias áreas da Física Nuclear. Como continuidade deste trabalho pretendo aplicar o modelo não-local de interação nuclear ao estudo de colisões núcleon-núcleo.

VII APÊNDICES

Apêndice I: Cálculo da Seção de Choque Diferencial Teórica

A distribuição de probabilidades das partículas espalhadas por um núcleo-alvo pode ser convenientemente descrita através de cálculos da seção de choque diferencial deste processo, em função de seu ângulo de espalhamento. Como a seção de choque diferencial elástica depende da amplitude de espalhamento, e esta depende do potencial de interação, vamos detalhar aqui essas grandezas e o formalismo utilizado.

Consideremos a colisão entre dois núcleos que têm números de carga e massa Z_1, A_1 e Z_2, A_2, na energia de centro de massa *E*. A equação estacionária de Schrödinger é dada por:

$$-\frac{\hbar^2}{2\mu}\nabla^2\Psi(\vec{R}) + U(R,E)\Psi(\vec{R}) = E\Psi(\vec{R})\,. \qquad \text{(I.1)}$$

O potencial de interação entre dois núcleos, alvo e projétil, consiste na soma dos termos dos potenciais ótico e coulombiano, $V_{ot}(R,E) + V_C(R)$, ou seja,

$$U(R,E) = V_{ot}(R,E) + V_C(R)\,. \qquad \text{(I.2)}$$

A solução, quando consideramos $V_{ot}(R) = 0$, é uma onda distorcida que, devido à simetria esférica do potencial, pode ser expressa como uma soma de ondas parciais de momento angular $l\hbar$:

$$\Psi_C(\vec{R}) = \frac{1}{2kR}\sum_{l=0}^{\infty}(2l+1)i^{l+1}\left(h_l^-(\eta,kR) - e^{2i\sigma_l}h_l^+(\eta,kR)\right)P_l(\cos\theta) \qquad \text{(I.3)}$$

onde, $k = \sqrt{\dfrac{2\mu E}{\hbar^2}}$,

σ_l = deslocamentos de fase de Coulomb,

$\eta = \dfrac{Z_1 Z_2 e^2 \mu}{\hbar^2 k}$, parâmetro de Sommerfeld;

h^-, h^+ = funções incidente e emergente de Coulomb [Mc75].

Quando incluímos um potencial nuclear central de curto alcance, temos que, na região assintótica $(R \to \infty)$, só a fase da parte emergente da onda é modificada:

$$\Psi(\vec{R}) = \Psi_C(\vec{R}) + \frac{\sqrt{\pi}}{kR}\sum_{l=0}^{\infty}(2l+1)i^{l+1}e^{2i\sigma_l}(1-S_l)h_l^+(\eta, kR)P_l(\cos\theta)\,, \tag{I.4}$$

onde, S_l são os elementos da matriz **S** dos deslocamentos de fase nuclear.

Finalmente, podemos obter a amplitude de espalhamento:

$$f(\theta) = f_C(\theta) + \frac{i}{2k}\sum_{l=0}^{\infty}(2l+1)e^{2l\sigma_l}(1-S_l)P_l\cos(\theta)\,, \tag{I.5}$$

sendo que, na expressão acima, $f_C(\theta)$ é a amplitude de espalhamento coulombiano.

A seção de choque diferencial é dada por:

$$\frac{d\sigma}{d\Omega} = |f(\theta)|^2\,. \tag{I.6}$$

Podemos encontrar a seção de choque de reação através da seguinte expressão:

$$\sigma_R = \frac{\pi}{k^2}\sum_{l=0}^{\infty}(2l+1)(1-|S_l|^2)\,. \tag{I.7}$$

No caso em que $V_{ot}(R) = 0$, obtemos a seção de choque de Rutherford:

$$\left(\frac{d\sigma}{d\Omega}\right)_R = |f_C(\theta)|^2 = \frac{\eta^2}{4k^2\,\mathrm{sen}^4(\frac{\theta}{2})}\,. \tag{I.8}$$

Apêndice II: Cálculos de Canais Acoplados

O formalismo de cálculo de canais acoplados é utilizado quando se deseja considerar com mais exatidão as contribuições de alguns canais de reação específicos para o potencial de polarização. Como exemplo desse tipo de cálculo, nesta seção apresentaremos o caso de acoplamento de um estado excitado 2^+ (espalhamento inelástico) com um estado fundamental 0^+. Uma discussão detalhada e geral (quaisquer spins dos núcleos alvo e projétil), que inclui o acoplamento de canais de transferência, pode ser encontrada na referência Th88.

O conjunto de equações diferenciais acopladas que se obtém ao realizar a expansão da função de onda em ondas parciais é [Bu63]:

$$[T_J - U(R,E) + E]u_J^{0J}(R) = V_{0J:2J}(R)u_J^{2J}(R) + V_{0J:2J-2}(R)u_J^{2J-2}(R) + \\ V_{0J:2J+2}(R)u_J^{2J+2}(R), \tag{II.1}$$

$$[T_J - U(R,E) - V_{2J:2J}(R) + E']u_J^{2J}(R) = V_{2J:0J}(R)u_J^{0J}(R) + \\ V_{2J:2J-2}(R)u_J^{2J-2} + V_{2J:2J+2}(R)u_J^{2J+2}(R), \tag{II.2}$$

$$[T_{J-2} - U(R,E) - V_{2J-2:2J-2}(R) + E']u_J^{J-2}(R) = V_{2J-2:0J}(R)u_J^{0J}(R) + \\ V_{2J:2J-2}(R)u_{2J}^{J}(R), \tag{II.3}$$

$$[T_{J+2} - U(R,E) - V_{2J+2:2J+2}(R) + E']u_{2J+2}^{J} = V_{0J:2J+2}(R)u_{0J}^{J}(R) + \\ V_{2J:2J+2}(R)u_{2J}^{J}(R), \tag{II.4}$$

onde:

$$T_J = \frac{\hbar^2}{2m}\left(\frac{d^2}{dr^2} - \frac{J(J+1)}{R^2}\right); \tag{II.5}$$

u_{0J}^{J} ≡ função de onda referente ao estado fundamental;

$u_{2J}^{J}, u_{2J-2}^{J}, u_{2J+2}^{J}$ ≡ funções de onda referentes ao estado excitado;

E ≡ energia incidente no sistema de centro de massa;

$E' = E - \varepsilon, \varepsilon$ ≡ energia de excitação do estado 2^{+}.

As condições de contorno apropriadas são:

para $r = 0 \rightarrow u_{oJ}^{J} = u_{2J}^{J} = u_{2J-2}^{J} = u_{2J+2}^{J} = 0$,

para $r = R_M \rightarrow u_{c'}^{J} = \frac{i}{2}\left(H_{c'}^{-}\delta_{cc'} - H_{c'}^{+}S_{c'}^{J}\right)$, (II.6)

com:

$H^{+} = G + iF;$

$H^{-} = G - iF;$

G, F ≡ funções de onda irregular e regular de Coulomb;

c ≡ canal incidente;

c' ≡ canal de saída;

$S_{c'}^{J}$ ≡ matriz S;

R_M ≡ distância para a qual o potencial nuclear é desprezível comparado ao Coulombiano.

Os potenciais de acoplamento são obtidos a partir de um modelo que descreva o núcleo. Os modelos mais utilizados são o rotacional e o vibracional. Em ambos podemos fazer:

$$U(R,\theta,\phi) = \frac{-V_0}{1 + \exp\left[\frac{R - R(\theta,\phi)}{a}\right]}. \qquad \text{(II.7)}$$

No modelo rotacional: $R(\theta,\phi) = R_0\left[1 + \beta Y_2^0(\theta)\right]$.

Nesse modelo o potencial de acoplamento é obtido através da seguinte expressão:

$$V_{acop.} = -\sqrt{\pi}\beta R_0 \int_0^{\pi} Y_2^0(\theta)U(R,\theta)\operatorname{sen}\theta d\theta \,. \qquad \text{(II.8)}$$

Para valores pequenos de β obtemos:

$$V_{acop.} \cong -\frac{\beta R_0}{\sqrt{4\pi}}\frac{dV_N(R)}{dR} \,. \qquad \text{(II.9)}$$

No modelo vibracional: $R(\theta,\phi) = R_0\left[1 + \sum_q \beta_q Y_2^q(\theta,\phi)\right]$. (II.10)

Novamente para valores pequenos de β, o potencial de acoplamento pode ser obtido através da expressão (II.9).

A conexão entre $V_{acop.}$ e termos similares a $V_{0J:2J}$ pode ser encontrada no artigo original de Buck, Stamp e Hodgson [Bu63].

O conjunto de equações II.1 a II.4 podem ser integradas numericamente (com passo de integração h) usando-se a relação de diferença de dois pontos.

Para $\frac{d^2u(R)}{dR^2} + K(R)u(R) = H(R)$, temos: (II.11)

$$u(R_{n+1}) = [2 - h^2K(R_n)]u(R_n) - u(R_{n-1}) + h^2H(R_n)\,, \qquad \text{(II.12)}$$

onde $R_n = nh$, n = 0,1,2,...

Para integrarmos as quatro equações (II.1,2,3,4), devemos conhecer as funções de onda em dois pontos do espaço. Sabemos que as funções de onda se anulam em $R = 0$. A técnica padrão, então, resolve as equações quatro vezes (em cada uma delas no ponto n=1, três funções de onda são assumidas nulas e a outra tem um valor arbitrário) e as quatro soluções são objeto de uma combinação linear, de forma a garantir a condição de contorno em $R = R_M$.

Uma discussão bem mais detalhada desse caso, incluindo o cálculo das seções de choque, pode ser obtida em [Bu63].

II.1-) *O Potencial de Polarização*

Tendo em vista as equações (II.1,2,3,4), definimos o potencial de polarização através da expressão:

$$V_{pol}(R) = \frac{V_{0J:2J}u_{2J}^{J} + V_{0J:2J-2}u_{2J-2}^{J} + V_{0J:2J+2}u_{2J+2}^{J}}{u_{0J}^{J}} . \qquad \text{(II.13)}$$

O potencial de polarização "simula" no canal elástico os efeitos do acoplamento devido ao canal inelástico. Na realidade, para obter o potencial de polarização é necessário conhecer as soluções das equações (II.1,2,3,4). A equação para o canal elástico, pode ser reescrita como:

$$\left[T_J - U(R) - V_{pol}(R) + E\right]u_{0J} = 0 \qquad \text{(II.14)}$$

Deve-se observar que $V_{pol}(R)$ é complexo (envolve funções de onda), o que é de se esperar, tendo em vista a absorção de fluxo do canal elástico pelo canal 2^+.

Apêndice III: Estudo da Densidade de Carga de um Núcleo a partir de Dados de Espalhamento Elástico de Elétrons

Para o núcleo de oxigênio de spin-zero, a seção de choque de espalhamento elástico de elétrons é determinada puramente pela distribuição de carga do estado fundamental; isto é verdade desde que as excitações inelásticas sejam desprezíveis. Na aproximação de Born, a distribuição de carga é a transformada de Fourier do fator de forma e vice-versa, sendo o fator de forma derivado de cálculos da difração de Fraunhofer da ótica. Na ótica, o fator de forma é uma função do momento transferido por uma onda incidente, quando difratada, e esses cálculos são aplicáveis ao espalhamento elástico de elétrons por um núcleo atômico, de tal forma a termos a seção de choque, devido a esse processo, proporcional ao fator de forma:

$$F^2 = \frac{d\sigma/d\Omega}{\sigma_{Mott}}, \qquad \text{(III.1)}$$

onde:

$$\sigma_{Mott} = \left(\frac{Ze^2}{2E}\right)\frac{cos^2\frac{1}{2}\theta}{sen^2\frac{1}{2}\theta}\,\frac{1}{1+\frac{2E}{Mc^2}sen^2\frac{1}{2}\theta}; \qquad \text{(III.2)}$$

e da aproximação de Born, aplicada a núcleos leves, a distribuição de cargas então fica

$$\rho(r) = \frac{A}{2\pi^2 r}\int_0^\infty q\,\mathrm{sen}(qr)F(q)dq. \qquad \text{(III.3)}$$

E o Fator de forma é dado por:

$$F(q) = \frac{4\pi}{Aq}\int_0^\infty r\,\mathrm{sen}(qr)\rho(r)dr\,, \qquad \text{(III.4)}$$

onde:

$$q = \frac{2E\,\mathrm{sen}(\frac{\theta}{2})}{\hbar c\sqrt{1+\frac{2E}{Mc^2}\mathrm{sen}^2\left(\frac{\theta}{2}\right)}}. \qquad \text{(III.5)}$$

Portanto, aumentar "q" equivale a medir a ângulos e energias cada vez maiores. O problema, de ordem experimental, em trabalhos passados, era obter seções de choque de espalhamento elástico de elétrons para valores de momento elevados ($q > 4\ fm^{-1}$), sendo a seção de choque uma função de $\frac{1}{E^2}$. Para altas energias (altos momentos transferidos), fica muito difícil se obterem dados experimentais de seção de choque e conseqüentemente de F^2.

Dessa forma, para altos momentos transferidos, o comportamento de F(q) é praticamente desconhecido de um ponto de vista experimental, e a integral em (III.3) fica limitada a $q_{máx} = 4\,fm^{-1}$.

Devido a essa limitação na integral para obter a distribuição de carga, existem ambigüidades na determinação da distribuição de carga em regiões superficiais. Nesse sentido, tentava-se então usar $\rho(r)$ mais simples possível, somando-se apenas a mínima quantidade de componentes de alta freqüência necessários para que esta descrevesse a seção de choque experimental.

VIII Referências e Artigos do Período

As referências destacadas abaixo são artigos que foram publicados durante o período de doutoramento [Al99, Si01, Al02, Ch02, Ga02a, Ro02], ou que estão em fase final de preparação [Al02b, Ga02b]. Todos esses trabalhos serviram de base para esta tese e por esta razão segue anexa uma cópia de cada um destes artigos no final do capítulo.

[Al02] M. A. G. Alvarez, E. S. Rossi Jr., C. P. Silva, L. R. Gasques, L. C. Chamon, D. Pereira, M. N. Rao, B. V. Carlson, C. De Conti, R. M. Anjos, P. R. S. Gomes, J. Lubian, S. Kailas, A. Chatterjee and P. Singh, Phys. Rev. C65, 014602 (2002).

[Al02b] M. A. G. Alvarez, L. C. Chamon, M. S. Hussein, D. Pereira, L. R. Gasques, E. S. Rossi Jr. and C. P. Silva. Artigo em preparação.

[Al99] M. A. G. Alvarez, L. C. Chamon, D. Pereira, E. S. Rossi Jr., C. P. Silva, L. R. Gasques, H. Dias, e M. O. Roos, Nucl. Phys. A656, 187 (1999).

[Als72] J. Alster, B. F. Gibson, J. S. McCarthy, M. S. Weiss and R. M. Wright, Phys. Rev. **C7**, 1089 (1972).

[Ba75] J. B. Ball, C. B. Fulner, E. E. Gross, M. L. Halbert, D. C. Hensley, C. A. Ludemann, M. J. Saltmarsh and G. R. Satchler. Nucl. Phys. **A252**, 208 (1975).

[Ba79] A. J. Balts, N. K. Glendening, S. K. Kauffmann, K. Pruess, Nucl. Phys. **A327**, 221 (1979).

[Be71] H. A. Bethe, Ann. Rev. Nucl. Sci. **21**, 93 (1971).

[Be77] G. Bertsch, J. Borysowics, H. McManus, W. G. Love, Nucl. Phys. **A284,** 399 (1977).

[Be85] M. Beckerman, Phys. Rep. **129**, 145 (1985).

[Bl77] J. Blocki, J. Raudrup, W. J. Swiatecki, C. F. Tsang, Ann. of Phys. **105**, 427 (1977).

[Br 97a] M. E. Brandan and G. R. Satchler, Phys. Rep. **285**, 142 (1997).

[Br97b] M. E. Brandan, H. Chemine and K. W. McVoy, Phys. Rev. **C55**, 1353 (1997).

[Bu63] B. Buck, A. P. Stamp, P. E. Hodgson, Phil. Mag. **8**, 1805 (1963).

[Bu81] M. Buenerd, J. Pinston, J. Cole, C. Guest, D. Lebrun, J. M. Loiseaux, P. Martin, E. Monnand, J. Mougey, H. Nifenecker, R. Ost, P. Perrin, C. Ristori, P. de Saintgnon, F.

Schussler, L. Carlen, H. A. Gustafsson, B. Jakobsson, T. Johansson, G. Jonsson, J. Krumlinde, I. Otterlund, H. Ryde, B. Schroder, G. Tibell, J. B. Bondorf, and O. B. Nielsen, Phys. Lett. **102B**, 242 (1981).

[Bu84] M. Buenerd, A. Lounis, J. Chauvin, D. Lebrun, P. Martin, G. Duhamed, J. C. Gondrand and P. de Saintgnon, Nucl. Phys. **A424**, (1984) 313.

[Ca00] B. V. Carlson and D. Hirata, Phys. Rev. **C62**, 054310 (2000).

[Ch02] L. C. Chamon, B. V. Carlson, L. R. Gasques, D. Pereira, C. De Conti, M. A. G. Alvarez, E. S. Rossi Jr., C. P. Silva and M. A. C. Ribeiro, Phys. Rev. C. 66, 014610 (2002).

[Ch92] L. C. Chamon, D. Pereira, E. S. Rossi Jr, C. P. Silva, G. Ramirez, A. M. Borges, L. C. Gomes, O. Sala, Phys. Lett. **275B**, (1992) 29.

[Ch95] L. C. Chamon, D. Pereira, E. S. Rossi Jr, C. P. Silva, R. Lichtentäler, L. C. Gomes, Nucl. Phys. **A582**, (1995) 305.

[Ch96] L. C. Chamon, D. Pereira, E. S. Rossi Jr, C. P. Silva, H. Dias, L. Losano, C. A. P. Ceneviva, Nucl. Phys. **A597**, (1996) 253.

[Ch97] L. C. Chamon, D. Pereira, M. S. Hussein, M. A. C. Ribeiro e D. Galetti, Phys. Rev. Lett. **79**, 5218 (1997).

[Ch98] L. C. Chamon, D. Pereira e M. S. Hussein, Phys. Rev. **C58**, 576 (1998).

[De75] R. M. De Vries, M. R. Glover, Nucl. Phys. **A243**, (1975) 528.

[Fa71] L. A. Fajardo, J. R. Ficenec, W. P. Trower and I. Sick, Phys. Letters, **37B**, 363 (1971).

[Fi72] J. R. Ficenec, L. A. Fajardo, W. P. Trower, I. Sick, Phys. Letters, **42B**, 213 (1972).

[Fo75] M. M. Fowler and R. C. Jared, Nucl. Instr. & Meth. **124**, 341 (1975).

[Fr76] B. Frois, J. B. Bellicard, J. M. Cavedon, M. Huet, P. Leconte, P. Ludeau, A. Nakada, Phan Zuan Hô and I. Sick, **vol. 38**, n. 4, 152 (1976).

[Ga98] D. Galetti, S. S. Mizrahi, L. C. Chamon, D. Pereira, M. S. Hussein and M. A. C. Ribeiro, Phys Rev. **C58**, 1627 (1998).

[Ga02a] L. R. Gasques, L. C. Chamon, C. P. Silva, D. Pereira, M. A. G. Alvarez, E. S. Rossi Jr., V. P. Likhachev, B. V. Carlson and C. De Conti. Phys. Rev. C65, 044314 (2002).

[Ga02b] L. R. Gasques, L. C. Chamon, D. Pereira, V. Guimarães, A. Lépine-Szily, M. A. G. Alvarez, E. S. Rossi Jr., C. P. Silva, B. V. Carlson, J. J. Kolata, L. Lamm, D. Peterson, P. Santi, S. Vincent, P. A. De Young, G. Peasley. Artigo aceito para publicação.

[Ho89] S. W. Hong, T. Udagawa, T. Tamura, Nucl. Phys. **A491**, 492 (1989).

[Ho98] J. Y. Hostachy, M. Buenerd, J. Chauvin, D. Lebrun, P. Martin, J. C. Lugol, L. Papineau, P. Roussel, N. Alamanos, J. Arviex, and C. Cerruti, Nucl. Phys. **A490**, 441 (1998).

[Hu91] M. S. Hussein, R. A. Rego and C. A. Bertulani, Phys. Rep. **201**, 279 (1991).

[Je77] J. P. Jeukenne, A. Lejeune, C. Mahaux, Phys. Rev. **C16**, 80 (1977).

[Kh93] D. T. Khoa, W. von Oertzen, Phys. Lett. **B304**, 8 (1993).

[Kh94] D. T. Khoa, W. von Oertzen, H. G. Bohlen, Phys. Rev. **C49**, 1652 (1994).

[Kh95a] D. T. Khoa and W. von Oertzen, Phys. Lett. **B342**, 6 (1995).

[Kh95b] D. T. Khoa, W.von Oertzen, H. G. Bohlen, G. Bartnitzky, H. Clement, Y. Sugiyama, B. Gabauer, A. N. Ostrowski, T. Wilpert, M. Wilpert, C. Langner, Phys. Rev. Lett. **74**, 34 (1995).

[Ko82] A. M. Kobos, B. A. Brown, P. E. Hodgson, G. R. Satchler, A. Budzanowski, Nucl. Phys. **A384**, 65 (1982).

[Ko84] A. M. Kobos, B. A. Brown, R. Lindsay and G. R. Satchler, Nucl. Phys. **A425**, (1984).

[La97] G. A. Lalazissis, J. Konig and P. Ring, Phys. Rev. **C55**, 540 (1997).

[Lo77] W. G. Love, T. Terasawa, G. R. Satchler, Nucl. Phys. **A291**, 183 (1977).

[Ma77] N. V. Mau, Phys. Lett. **B71**, 5 (1977).

[Mi90] H. Miyake and A. Mizukami, Phys. Rev. **C41**, 329 (1990).

[Na94] E. G. Nadjakov, K. P. Marinova and Y. P. Gangrsky, Atomic Data and Nucl. Data Tables **56**, 133 (1994).

[Ne70] J. W. Negele, Phys. Rev. **C4**, 1260 (1970).

[Ngô75] C. Ngô, B. Tamain, M.Beiner, R. J. Lombard, D. Mas, H. H. Denbler, Nucl. Phys. **A252**, 237 (1975).

[Oga78] Y. T. Oganessian and Y. E. Penionzhkevich, V. I. Man'ko and V. N. Polyansky, Nucl. Phys. **A303**, 259 (1978).

[Og00] A. A. Ogloblin, Y. A. Glukhov, V. Trzaska, A. S. Demyanova, S. A. Goncharov, R. Julin, S. V. Klebnikov, M. Mutterer, M. V. Rozhkov, V. P. Rudakov, G. P. Tiorin, D. T. Khoa and G. R. Satchler, Phys Rev. **C62**, 44601 (2000).

[Pe78] D. Pereira, J. C. Acquadro Q., O. Sala and N. D. Vieira Junior, Rev. Bras. de Física, Vol. **8**, N. 1, 1978.

[Ri97] M. A. C. Ribeiro, L. C. Chamon, D. Pereira, M. S. Hussein and D. Galetti, Phys. Rev. Lett. **78**, 3270 (1997).

[Ro88] P. Roussel-Chomaz, N. Alamanos, F. Auger, J. Barrette, B. Fernandez and L. Papineau, Nucl. Phys. **A477**, 345 (1998).

[Ro02] E. S. Rossi Jr., D. Pereira, L. C. Chamon, C. P. Silva, M. A. G. Alvarez, L. R. Gasques, J. Lubian, B. V. Carlson, C. De Conti, Nuc. Phys. A707, 325 (2002).

[Sa74] G. R. Satchler, Proc. of the Internacional Conference on Reactions between Complex Nuclei, vol. **2**, Amsterdam 171 (1974).

[Sa79] G. R. Satchler, W. G. Love, Phys. Rep. **55**, 183 (1979).

[Sa86] C. C. Sahm, T. Murakami, J. G. Cramer, A. J. Lazzarini, D. D. Leach, D. R. Tieger, R. A. Loveman, W. G. Lynch, M. B. Tsang and J. Van der Plicht, Phys. Rev. **C34**, 2165 (1986).

[Sa91] G. R. Satchler, Phys. Rep. **199,** 147 (1991).

[Si70] I. Sick and J. S. Mc Carthy, Nucl. Phys. **A150**, 631 (1970).

[Si01] C. P. Silva, M. A. G. Alvarez, L. C. Chamon, D. Pereira, M. N. Rao, E. S. Rossi Jr., L. R. Gasques, M. A. E. Santo, R. M. Anjos, J. Lubian, P. R. S. Gomes, C. Muri, B. V. Carlson, S. Kailas, A. Chatterjee, P. Singh, A. Shrivastava, K. Mahata and S. Santra, Nucl. Phys. A679, 287 (2001).

[Sky59] T. H. R. Skyrme, Nucl. Phys. **9**, 615 (1959).

[Ta65] T. Tamura, Rev. Mod. Phys. **37**, 679 (1965).

[Th88] I. J. Thompson, Computer Physics Reports **7**, 167 (1988).

[Uda89] T. Udagawa, T. Tamura, B. T. Kim, Phys. Rev. **C39**, 1840 (1989).

[Vr87] H. De Vries, C. W. De Jager and C. De Vries, Atomic Data and Nucl. Data Tables **36**, 495 (1987).

[Wo93] C. Y. Wong, Phys. Rev. Lett. **31**, 766 (1993).

[Yo99] D. H. Yongblood, H. L. Clark, Y. W. Lui, Phys. Lett. **82**, 691 (1999).

ELSEVIER

Nuclear Physics A 656 (1999) 187–208

NUCLEAR
PHYSICS A

www.elsevier.nl/locate/npe

Experimental determination of the ion–ion potential in the $N = 50$ target region: A tool to probe ground-state nuclear densities

M.A.G. Alvarez[a], L.C. Chamon[a], D. Pereira[a], E.S. Rossi Jr.[a],
C.P. Silva[a], L.R. Gasques[a], H. Dias[b], M.O. Roos[c]

[a] *Laboratório Pelletron, Instituto de Física da Universidade de São Paulo, Caixa Postal 66318, 05315-970, São Paulo, SP, Brazil*

[b] *Grupo de Física Nuclear Teórica e Fenomenologia de Particulas Elementares, Instituto de Física da Universidade de São Paulo, Caixa Postal 66318, 05315-970, São Paulo, SP, Brazil*

[c] *Departamento de Física, Universidade Federal de Mato Grosso, Av. Fernando Corrêa, 78060-900, Cuiaba, MT, Brazil*

Received 17 March 1999; revised 29 April 1999; accepted 18 May 1999

Abstract

Precise elastic and inelastic differential cross sections have been measured for the ^{16}O + ^{88}Sr, $^{90,92}Zr$, ^{92}Mo systems at sub-barrier energies. From a coupled channel data analysis, the corresponding "experimental" bare potentials have been determined. The comparison of these potentials with those derived from double-folding theoretical calculations and the high energy (96 MeV/nucleon) elastic scattering data analysis indicate that the method is a very sensitive probe of the ground-state nuclear densities in the surface region. © 1999 Elsevier Science B.V. All rights reserved.

Keywords: Nuclear reactions: $^{88}Sr(^{16}O,{}^{16}O)^{88}Sr$, $^{90,92}Zr(^{16}O,{}^{16}O)^{90,92}Zr$, $^{92}Mo(^{16}O,{}^{16}O)^{92}Mo$; Measured elastic and inelastic (2^+) cross sections at $43 \leqslant E_{\rm Lab} \leqslant 49$ MeV; Deduced optical potentials; Shell model and double-folding calculations

---

1. Introduction

In this work, we present elastic and inelastic (2_1^+) differential cross sections for the $^{16}O + {}^{88}Sr$, $^{90,92}Zr$, ^{92}Mo systems at sub-barrier energies, $43 \leqslant E_{\rm Lab} \leqslant 49$ MeV. The main purpose of the experiment was to determine the bare ion–ion potentials for these systems through coupled channel (CC) elastic and inelastic data analyses. Recently, this method has been successfully applied in a study of the $^{16}O + {}^{58,60,62,64}Ni$ systems [1,2].

PII S0375-9474(99)00304-8

As discussed in these previous works, it was possible to study the isotopic dependence of the ion–ion potential for the proton closed shell nuclei ($Z = 28$), because the coupled channel data analyses at sub-barrier energies are very reliable due to the small number of open reaction channels. In the present work, we investigate the isotonic (Z) dependence of the potential for the neutron closed shell targets ($N = 50$) ^{88}Sr, ^{90}Zr and ^{92}Mo, and the influence on the potential due to the two extra neutrons in the ^{92}Zr nucleus.

In the data analysis, the best fits have been achieved with reasonable Coulomb and nuclear phonon amplitudes, and the slopes and strengths of the ion–ion potentials have been determined within 5% accuracy. Through the comparison of the "experimental" (i.e. extracted from data analyses) potentials with those derived from M3Y double-folding calculations, it was possible to probe the ground-state nuclear densities in the surface region ($\rho \simeq 0.01$ fm^{-3}). The consistency of these studies has been tested, for the ^{16}O + ^{90}Zr system, through the comparison of the sub-barrier elastic data analysis with that at much higher energy ($E_{\text{Lab}} = 1503$ MeV), in which an inner region of the nuclear density is probed. In the optical model high energy data analysis, the non-local exchange effects were taken into account.

The paper is organized as follows: Section 2 gives the experimental details and results. The CC data analysis is presented in Section 3. In Section 4, we study the influence on the potentials due to the increasing number of protons in the ^{16}O + ^{88}Sr, ^{90}Zr, ^{92}Mo systems, and also the influence of the two extra neutrons in the ^{16}O + ^{92}Zr system. In Section 5, we discuss the role played by the reaction channels with negligible cross sections in the polarization potential. In Section 6, the sensitivity of our method as a probe of the nuclear densities is discussed. Section 7 contains a brief summary and the main conclusions.

2. Experimental details and results

The measurements were made using the ^{16}O beam from the São Paulo 8UD Pelletron Accelerator. The detecting system has been already described in Ref. [1]; it consisted of a set of nine surface barrier detectors spaced 5° apart. The thickness of the carbon (10 μg/cm^2) backed ^{88}Sr, ^{90}Zr, ^{92}Zr, ^{92}Mo targets were about 40 μg/cm^2, with a layer of gold (50 μg/cm^2) for the purpose of data normalization. We have estimated the Coulomb barrier for the ^{16}O + ^{88}Sr, ^{90,92}Zr, ^{92}Mo systems as $V_B^{\text{Lab}} \simeq 51, 53, 53$ and 55 MeV, respectively. Data were taken in the bombarding energy range $43 \leqslant E_{\text{Lab}} \leqslant 49$ MeV, which corresponds to 5 to 8 MeV below the Coulomb barrier for these systems. Due to the precision (about 1% in the elastic scattering cross sections) required for the experimental data, the following procedures were taken into account in the data acquisition and reduction: (i) the use of two monitor detectors ($\theta_{\text{Lab}} = \pm 35°$) to be sure that no target deterioration occurred during bombardment; (ii) high energy resolution to allow (see Fig. 1) a complete separation among the elastic, inelastic (2_1^+) and also the contaminant associated peaks; (iii) corrections in the counting rate related to the elastic and inelastic processes due to the small background near those peaks.

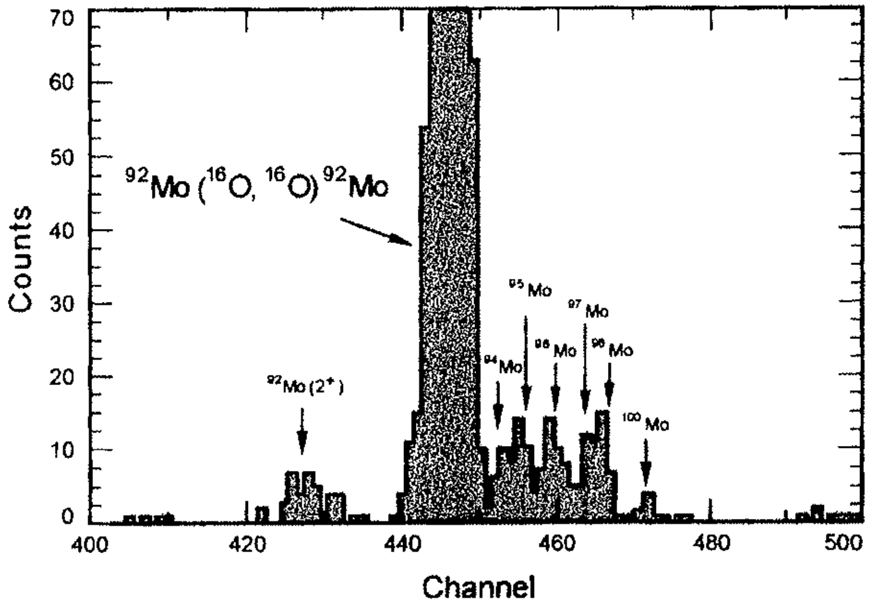

Fig. 1. Energy spectrum for the $^{16}O + ^{92}Mo$ system at $E_{\mathrm{Lab}} = 49$ MeV and $\theta_{\mathrm{Lab}} = 160°$. The molybdenum isotopes ^{94}Mo, ^{95}Mo, ^{96}Mo, ^{97}Mo and ^{100}Mo are the main contaminants in the ^{92}Mo target.

Figs. 2 to 7 exhibit the elastic and inelastic (target – 2_1^+) differential cross sections for the $^{16}O + ^{88}Sr$, ^{90,92}Zr, ^{92}Mo systems. Due to the very small counts in the peaks related to the inelastic process, the corresponding cross sections are somewhat "contaminated" due to the background subtraction, and it was not possible to obtain inelastic cross sections for the $^{16}O + ^{88}Sr$, ^{92}Zr systems. No evidence was found in the energy spectra for population of other excited target or projectile states with cross sections near those for the 2_1^+ state. The integrated inelastic cross sections vary between 5 to 50 mb in the energy range investigated. These values are one or two orders of magnitude larger than those associated to other reaction channels, such as the sub-barrier few nucleon transfer [3] and fusion [4] processes.

3. Data analysis

In the coupled channel calculations, we have adopted a procedure similar to that described in the analysis of the sub-barrier elastic and inelastic data for the $^{16}O + ^{58,60,62,64}Ni$ systems [1,2]. The target nuclei have been assumed spherically symmetric but susceptible to vibrations around their spherical shapes [5]. For these nuclei, we have considered the contribution of the 2_1^+ state. We have used phonon amplitudes according to Refs. [6–8]. The value $r_c = 1.06$ fm, obtained from electron scattering experiments [9], have been assumed for the Coulomb radius. For the real nuclear potential we have assumed a Woods–Saxon shape with a radius parameter equal to the Coulomb radius ($r_0 = r_c = 1.06$ fm). We have used in the CC calculations an inner imaginary potential [1,2], which takes into account the small internal absorption from

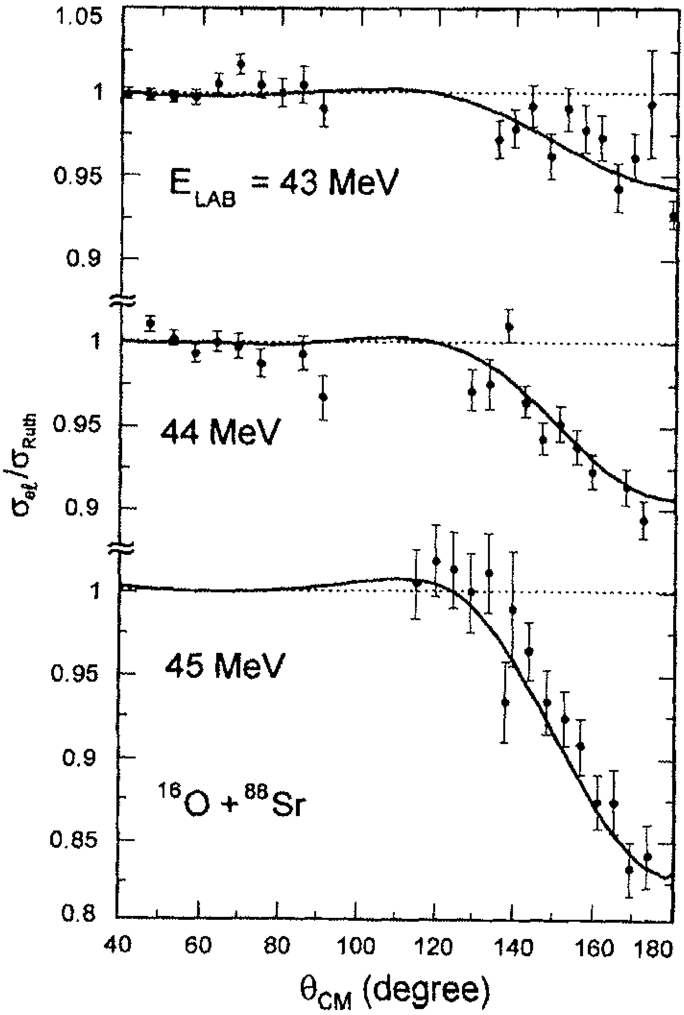

Fig. 2. Elastic scattering angular distributions for the $^{16}O + ^{88}Sr$ system at the bombarding energies E_{Lab} = 43, 44 and 45 MeV. The solid lines correspond to coupled channel calculations (see details in the text).

barrier penetration. In the surface interaction region ($R \geqslant 10$ fm), this potential is very small ($W \leqslant 10^{-4}$ MeV). No sensitivity in the CC cross section predictions has been detected related to strength variations of this absorptive potential. The depth, V_0, and the diffuseness, a, of the real nuclear potential were searched for the best data fits. In a similar way as reported for the $^{16}O + ^{58,60,62,64}Ni$ systems [1,2], for each system and bombarding energy we have found a family of real potentials, with different diffuseness parameters, which give equivalent data fits, as illustrated in Fig. 8 for the $^{16}O + ^{90}Zr$ system at the energies of 46 and 48 MeV. These potentials cross (see Fig. 8) at a particular radius, R_S, which is usually referred as the strong absorption radius in the case of higher energy elastic scattering data analysis. At sub-barrier energies, this radius is related to the classical turning point, and is energy dependent. Due to the small absorption involved in this case, in this work we refer to R_S as the sensitivity radius.

We have used the energy dependence of R_S (see Fig. 9) to characterize the shape of

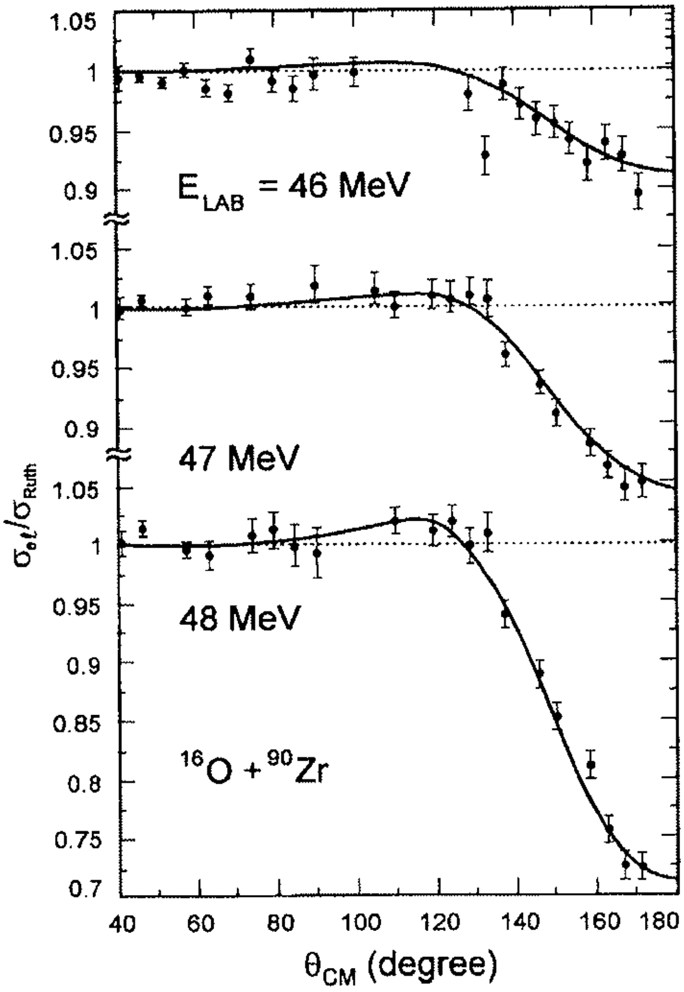

Fig. 3. The same as in Fig. 2, for the $^{16}O + ^{90}Zr$ system at $E_{Lab} = 46, 47$ and 48 MeV.

the real nuclear potential in the surface region. As discussed in Ref. [1], the potential strength error bars were estimated considering the variation by unity of chi-square around the minimum value (see Fig. 5 of Ref. [1]). Due the precision of the elastic scattering data (about 1%), the nuclear potential strengths at the sensitivity radius were obtained within 5% accuracy. The shape of the nuclear potential is quite close to an exponential, represented by solid lines in Fig. 9. Table 1 gives the diffuseness values obtained for the $^{16}O + ^{88}Sr$, $^{90,92}Zr$, ^{92}Mo systems. Within the uncertainties, the diffuseness parameters are compatible with the average value $\overline{a} = 0.64 \pm 0.02$ fm. This diffuseness value is in good agreement with theoretical double-folding calculations, as will be discussed in the next section. Using the value $a = 0.64$ fm for the $^{16}O + ^{88}Sr$, $^{90,92}Zr$, ^{92}Mo systems, we were able to fit all the angular distributions (see Figs. 2 to 7) with an energy-independent bare potential for each system. Table 1 gives the CC potential strengths for all the systems investigated in this work at the interaction radius $R = 11$ fm, which is near the center of the sensitivity region.

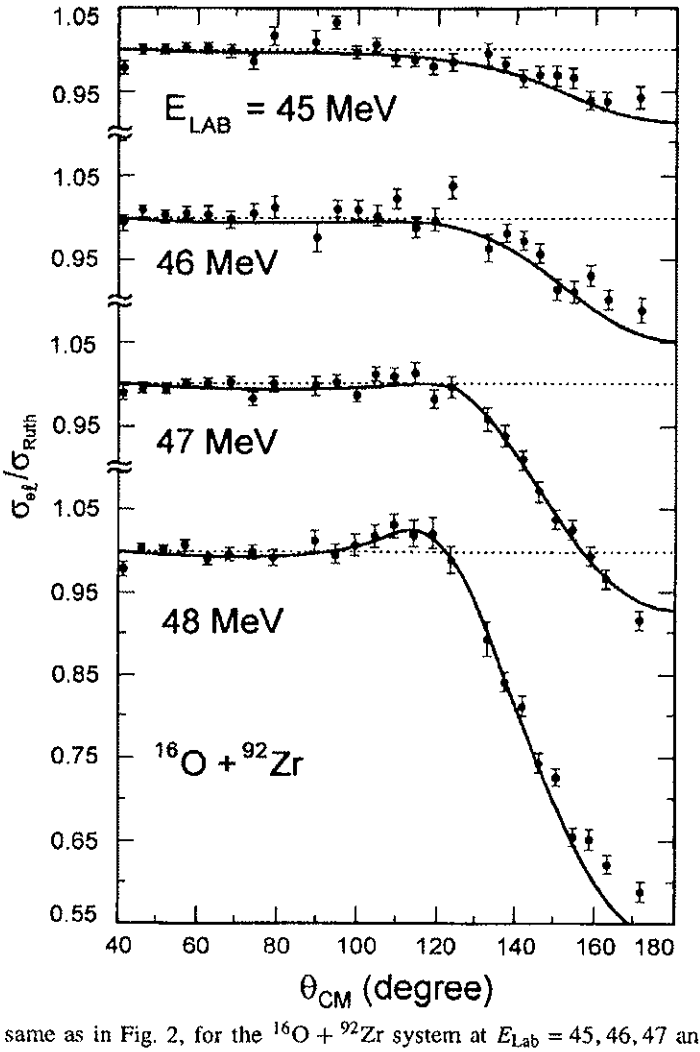

Fig. 4. The same as in Fig. 2, for the $^{16}O + ^{92}Zr$ system at E_{Lab} = 45, 46, 47 and 48 MeV.

Table 1
The diffuseness values from CC (a) and double-folding (α) calculations, and also the strengths of the CC (V_{CC}) and double-folding (V_{fold}) potentials at the interaction distance $R = 11$ fm

Nucleus	a (fm)	α (fm)	V_{CC} (MeV)	V_{fold} (MeV)	V_{CC}/V_{fold}
^{88}Sr	0.71 ± 0.05	0.584	0.90 ± 0.03	0.628	1.43 ± 0.05
^{90}Zr	0.63 ± 0.03	0.586	0.97 ± 0.02	0.675	1.44 ± 0.03
^{92}Zr	0.61 ± 0.05	0.607	1.20 ± 0.04	0.787	1.52 ± 0.05
^{92}Mo	0.63 ± 0.06	0.587	0.98 ± 0.02	0.716	1.37 ± 0.03

4. Double-folding calculations

In this section, we present the theoretical calculations with the aim of evaluating the nuclear ion-ion potential by using the double-folding method [10] with shell model densities. In such analyses, we have used the well known nucleon-nucleon M3Y interaction in its standard form [10]:

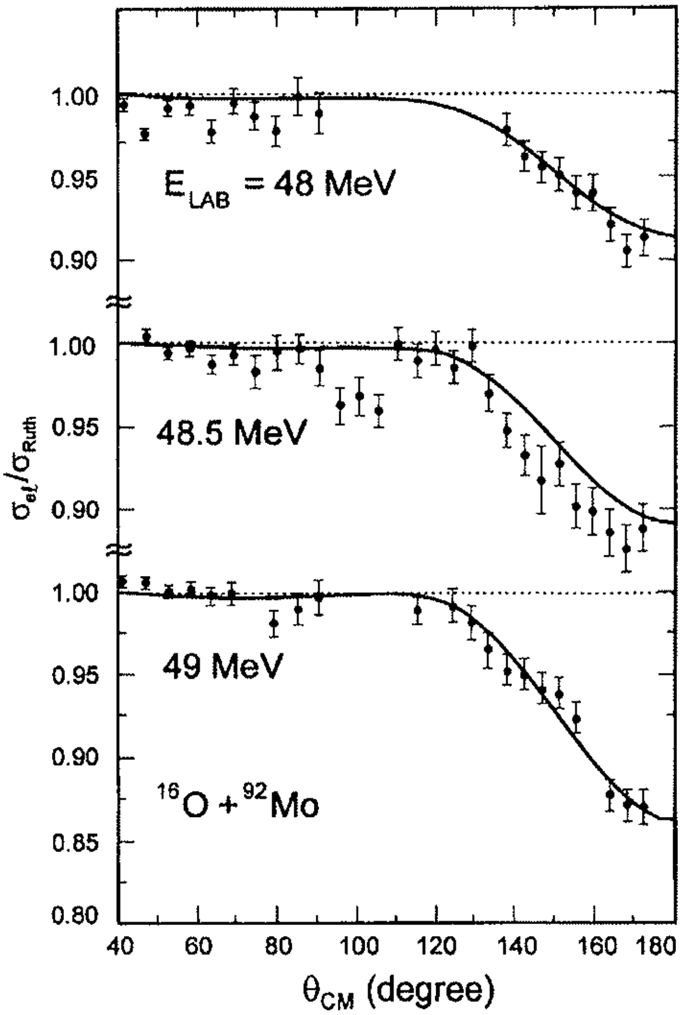

Fig. 5. The same as in Fig. 2, for the $^{16}O + ^{92}Mo$ system at $E_{Lab} = 48, 48.5$ and 49 MeV.

$$v_0(r) = \left[7999\frac{e^{-4r}}{4r} - 2134\frac{e^{-2.5r}}{2.5r}\right] + 262\delta(r)\ \text{MeV}. \tag{1}$$

In our calculations, the ground-state density of the ^{16}O nucleus was derived from electron scattering experimental results [9], with the assumption that the neutron (ρ_n) and proton (ρ_p) densities have the same shape as the charge density (ρ_c). The total nuclear density is expressed by

$$\rho(r) = \rho_n(r) + \rho_p(r) = \rho_0\left[1 + \gamma\left(\frac{r}{c}\right)^2\right]e^{-(r/c)^2}, \tag{2}$$

where $\gamma = 1.544$, $c = 1.833$ fm (charge density parameters of Ref. [9]), and $\rho_0 = 0.1407\ \text{fm}^{-3}$ to satisfy the normalization condition:

$$\int_0^\infty 4\pi\rho(r)\, r^2\, dr = N + Z = A. \tag{3}$$

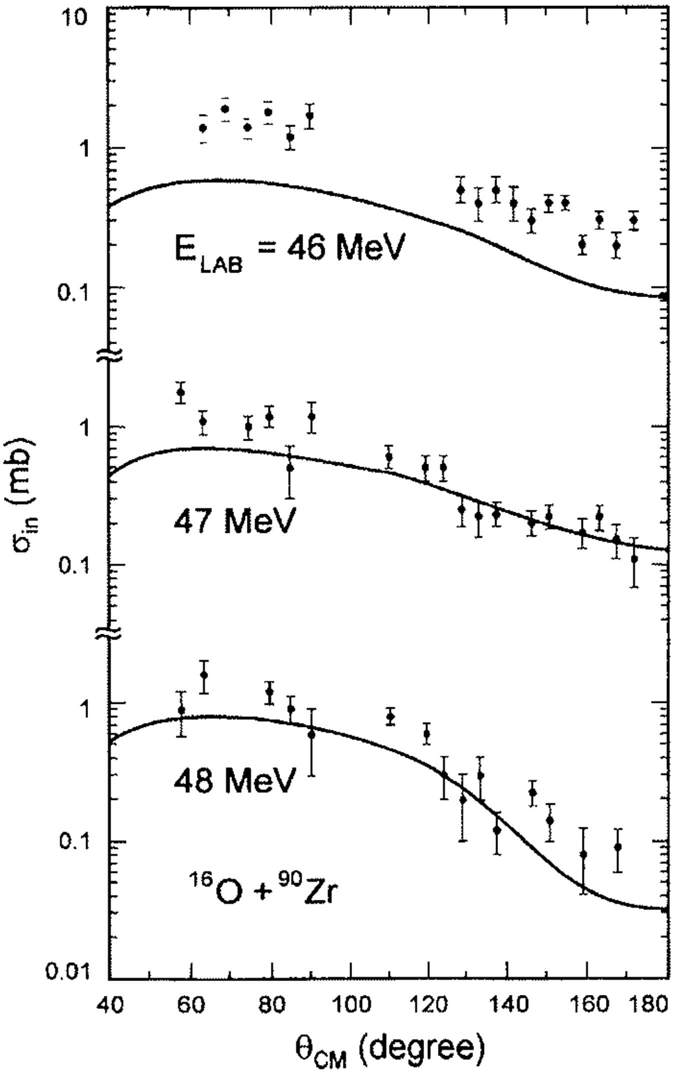

Fig. 6. The inelastic (2_1^+ target state) angular distributions for the $^{16}O + ^{90}Zr$ system at E_{Lab} = 46, 47 and 48 MeV. The solid lines in the figure correspond to coupled channel calculations (see text for details).

For the target nuclei we have used densities from shell model calculations, assuming, for the ^{88}Sr, ^{90}Zr and ^{92}Mo nuclei, the $N = 50$ neutron closed shell and the $(2p_{3/2}, 1f_{7/2}, 2p_{1/2}, 1g_{9/2})^{Z-28}$ proton orbital configuration. For the ^{92}Zr nucleus, we have considered the $(1f_{7/2}, 1f_{5/2}, 2p_{3/2})^{18}(2p_{1/2}, 1g_{9/2})^2$ proton and the $(1g_{9/2})^{10}(1g_{7/2}, 2d_{5/2}, 2d_{3/2}, 3s_{1/2})^2$ neutron orbital configurations. The shell model calculations predict level schemes for these nuclei which are in reasonable agreement with those derived from experiments up to excitation energies of about 3 MeV (see Fig. 10).

Fig. 11 presents the proton (dashed lines) and neutron (solid lines) densities for the ^{88}Sr, $^{90,92}Zr$ and ^{92}Mo nuclei. For these nuclei, the number of protons is significantly smaller than the number of neutrons, thus the proton densities are somewhat more internal as compared to the corresponding neutron ones. We have calculated the folding potential contributions of the proton and neutron target densities according to

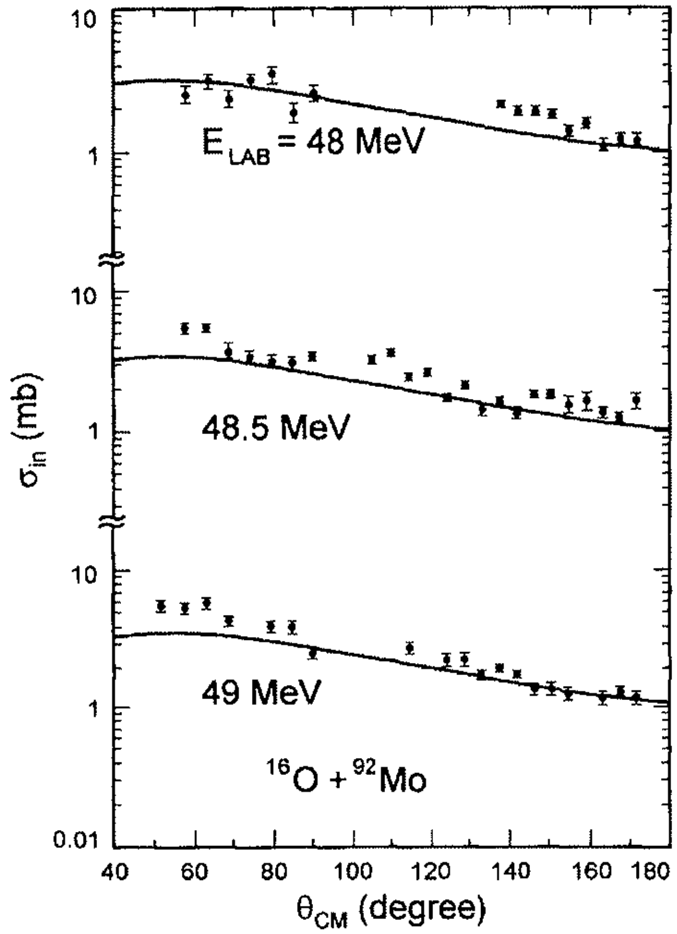

Fig. 7. The same as in Fig. 6, for the $^{16}O + ^{92}Mo$ system at $E_{Lab} = 48, 48.5$ and 49 MeV.

the following expressions:

$$V_p(R) = \int \rho_o(\boldsymbol{r}_1)\, v_o(|\boldsymbol{R} - \boldsymbol{r}_1 + \boldsymbol{r}_2|)\, \rho_p(\boldsymbol{r}_2)\, d\boldsymbol{r}_1\, d\boldsymbol{r}_2\,, \tag{4}$$

$$V_n(R) = \int \rho_o(\boldsymbol{r}_1)\, v_o(|\boldsymbol{R} - \boldsymbol{r}_1 + \boldsymbol{r}_2|)\, \rho_n(\boldsymbol{r}_2)\, d\boldsymbol{r}_1\, d\boldsymbol{r}_2\,, \tag{5}$$

$$V_T(R) = V_p(R) + V_n(R) = \int \rho_o(\boldsymbol{r}_1)\, v_o(|\boldsymbol{R} - \boldsymbol{r}_1 + \boldsymbol{r}_2|)\, \rho_T(\boldsymbol{r}_2)\, d\boldsymbol{r}_1\, d\boldsymbol{r}_2\,, \tag{6}$$

where ρ_o is the total ^{16}O density; ρ_p, ρ_n and ρ_T are the proton, neutron and total target densities, respectively; and V_p, V_n and V_T are the corresponding proton, neutron and total folding potentials. These folding potentials are shown in Fig. 12. As expected, due to the neutron and proton density features (see Fig. 11), the neutron potential contribution in the surface interaction region is significantly more important in comparison to the corresponding proton one.

Since the neutron densities for the ($N = 50$ closed shell) ^{88}Sr, ^{90}Zr and ^{92}Mo nuclei are quite similar in the surface density region (see Fig. 13), the corresponding $^{16}O + ^{88}Sr$, ^{90}Zr, ^{92}Mo systems present, as expected, similar double-folding potentials

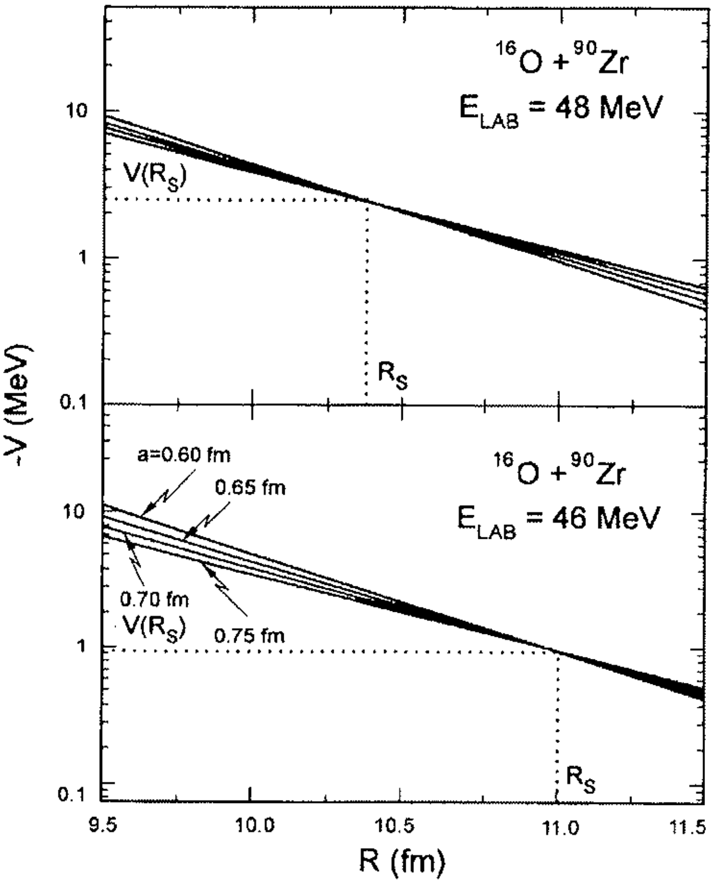

Fig. 8. Determination of the nuclear real bare potential at the sensitivity radius (R_S) for the $^{16}O + ^{90}Zr$, as obtained from CC analysis of the experimental data (E_{Lab} = 46 and 48 MeV) considering different values of diffuseness and potential depth parameters.

for large interaction distances (see Fig. 14 bottom). The neutron density for the two extra neutron ^{92}Zr nucleus, as indicated in Fig. 13, is shifted by about 0.1 fm in the surface region in relation to the other target nuclei. Since this value is of the same order of magnitude of the potential diffuseness ($a \simeq 0.6$ fm), the double-folding theoretical calculations predict for the $^{16}O + ^{92}Zr$ system a bare potential which is about 20% greater in the surface region as compared to those for the $^{16}O + ^{88}Sr$, ^{90}Zr, ^{92}Mo systems (see Fig. 14). We point out that the $^{16}O + ^{92}Zr$, ^{92}Mo systems present different surface folding potentials in spite of the same nucleon number in the target and projectile. The comparison of the potentials extracted from CC data analyses (Fig. 14 top) and those from double-folding calculations (Fig. 14 bottom) indicates clearly that all our expectations about the isotopic and isotonic dependence of these potentials are reasonably met. A similar result was obtained for the isotopic dependence of the nuclear potential for the $^{16}O + ^{58,60,62,64}Ni$ systems, as reported earlier [2]. Nevertheless, the strengths of the "experimental" potentials are about 40% greater than the folding predictions (see Table 1). Again a similar result was found for the $^{16}O + ^{58,60,62,64}Ni$ systems. Possible sources of such discrepancy will be discussed in the next sections.

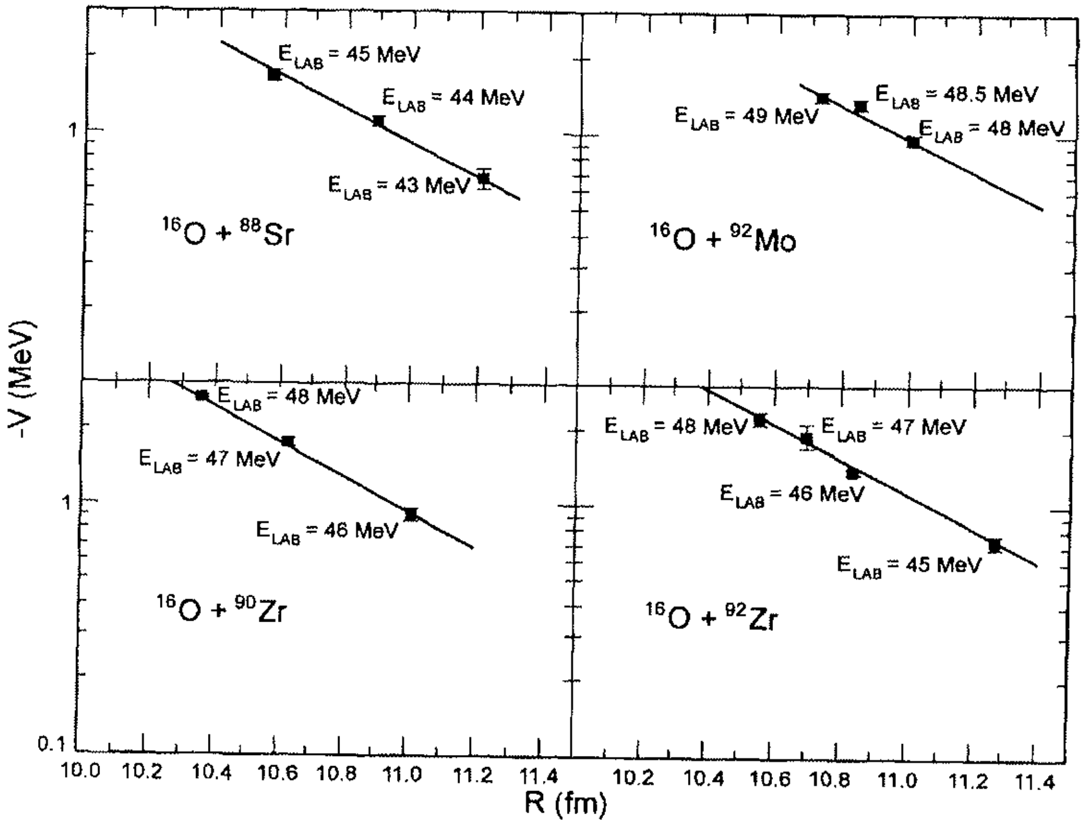

Fig. 9. The nuclear real bare potential as a function of the sensitivity radius for the $^{16}O + ^{88}Sr$, $^{90,92}Zr$ and ^{92}Mo systems. The solid lines in the figure represent the CC potentials with the same diffuseness value ($\bar{a} = 0.64$ fm) for all the systems.

Table 1 gives the "diffuseness parameters" (α) obtained from the slopes of the folding potentials, calculated in the surface region by Eq. (7). The folding diffuseness values are similar for all systems and close to the average "experimental" one (0.64 fm). A similar result has been obtained for the $^{16}O + ^{58,60,62,64}Ni$ systems, and an average value of 0.59 fm has been found [1,2]. These results indicate that the heavy-ion system potentials have a "universal" shape in the surface region rather independent of the "size of the system". As we will discuss in Section 6, the features of the folding potential in the surface interaction region are dependent on the nuclear densities in the nucleus surface region. Since the electron scattering experiments [9] have shown that the heavy nuclei have similar charge diffuseness values, one should expect the potential diffuseness to be similar for different heavy-ion systems,

$$\alpha = \left| \frac{V(R)}{dV/dR} \right| . \qquad (7)$$

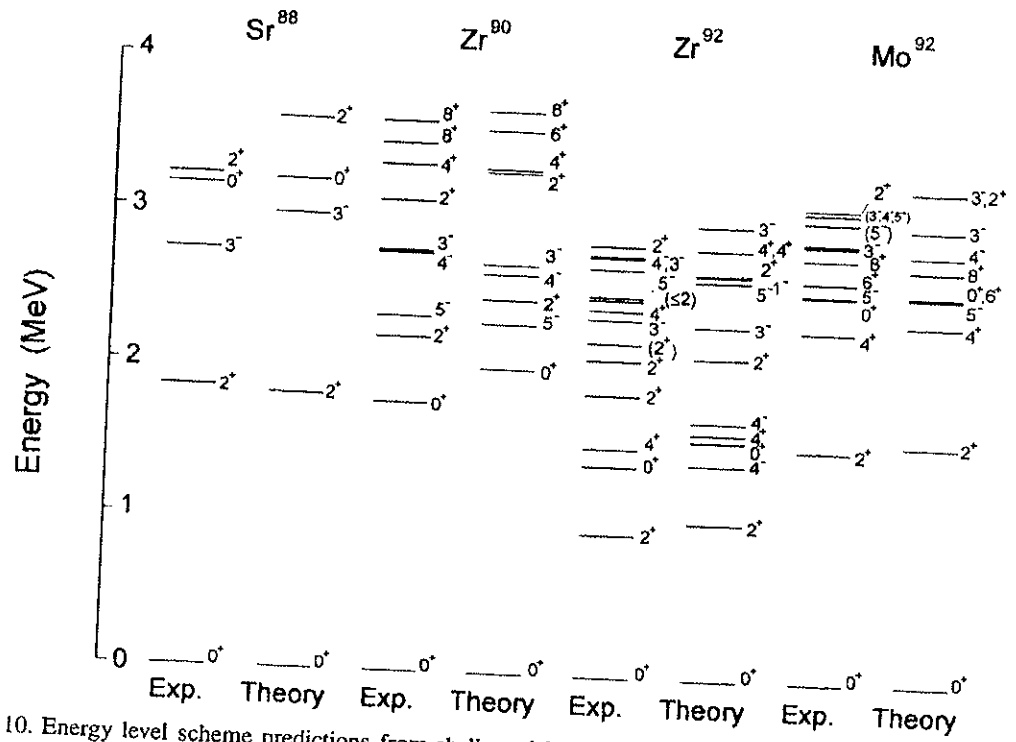

Fig. 10. Energy level scheme predictions from shell model calculations for the ^{88}Sr, ^{90,92}Zr and ^{92}Mo nuclei. For comparison purpose, the corresponding experimental schemes were included in the figure.

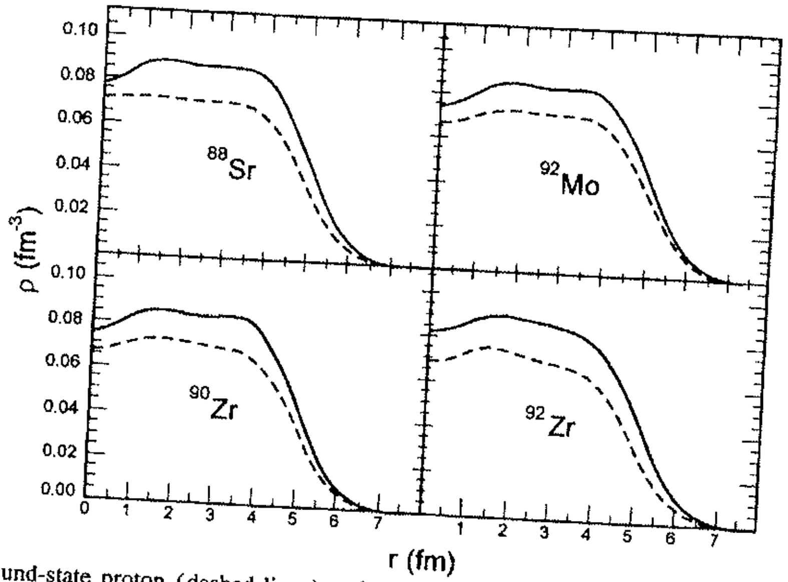

Fig. 11. The ground-state proton (dashed lines) and neutron (solid lines) densities derived from shell model calculations for the ^{88}Sr, ^{90}Zr, ^{92}Zr and ^{92}Mo nuclei.

5. Contributions to the polarization potential

As discussed in the previous section, a difference of about 40% between the folding potential strengths in the surface interaction region and the corresponding "experimental"

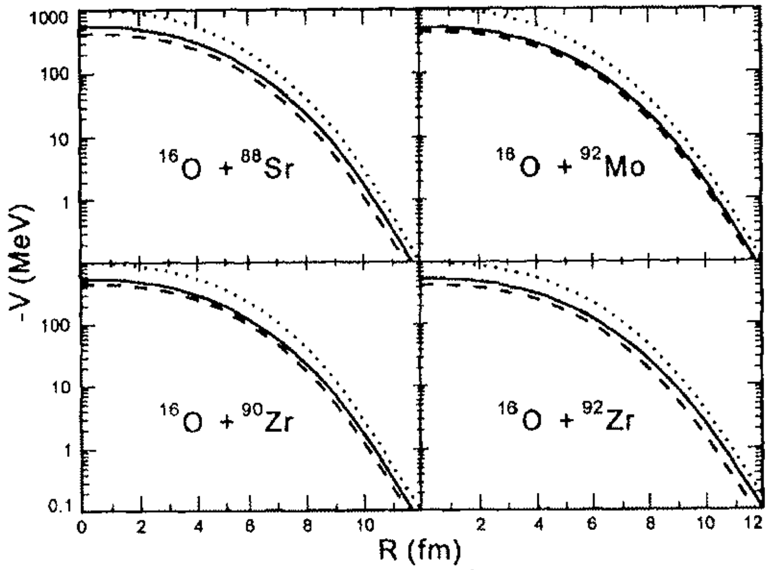

Fig. 12. Proton (dashed line), neutron (solid line), and total (dotted line) double-folding potentials for the $^{16}O + {}^{88}Sr$, $^{90,92}Zr$ and ^{92}Mo systems, using shell model densities for the target nuclei and charge distribution shape density (Eq. (2)) for the projectile (see text for details).

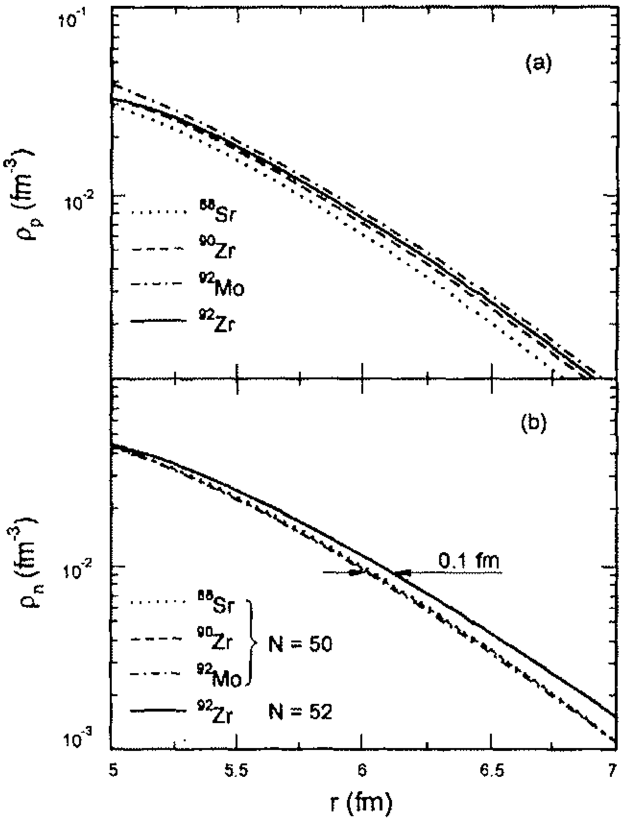

Fig. 13. Comparison between ground-state proton (a) and neutron (b) densities in the surface region, for the ^{88}Sr, ^{90}Zr, ^{92}Zr and ^{92}Mo nuclei.

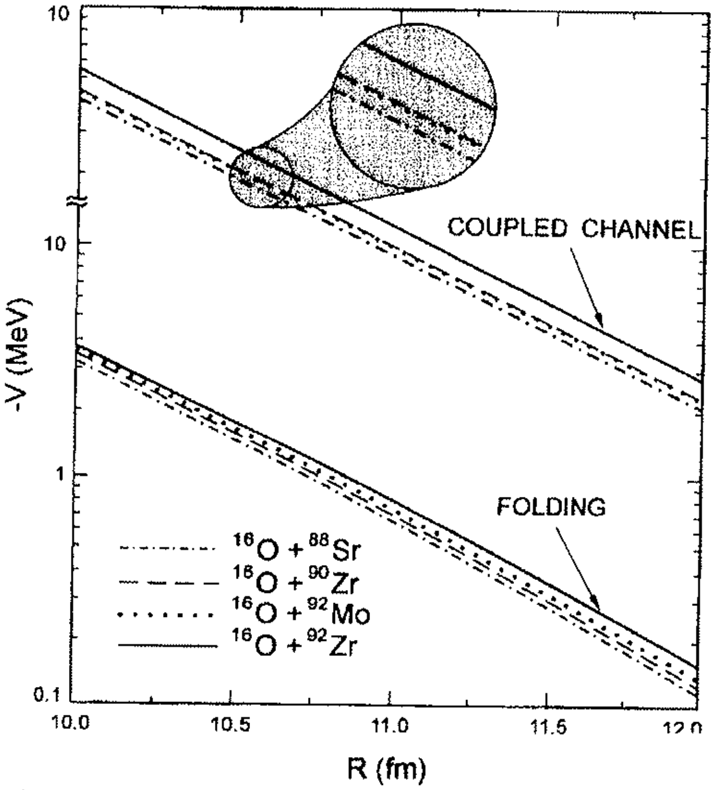

Fig. 14. Comparison between the bare potentials from CC data analyses (top) and double-folding calculations (bottom), for the $^{16}O + ^{88}Sr$, $^{90,92}Zr$ and ^{92}Mo systems (see text for details).

values from CC data analysis was found for the $^{16}O + ^{88}Sr$, $^{90,92}Zr$, ^{92}Mo systems (present work), and also for the $^{16}O + ^{58,60,62,64}Ni$ systems (Refs. [1,2]). We have performed the following studies in order to explain this discrepancy: (i) in this section, we intend to investigate how much of such difference is connected to contributions to the polarization potential arising from couplings of reaction channels with negligible cross sections, which were not included in our CC calculations at low energies; (ii) in the next section, we will discuss the effects on the folding potential associated with different models assumed for the nuclear matter densities.

Referring back to the ^{16}O + Ni studies, an extensive and rather complete coupled channel calculation, that included both inelastic excitation and transfer processes, was performed by Keeley et al. [11] for the $^{16}O + ^{58,62}Ni$ systems, and an "average" polarization potential was extracted through the solution of the coupled equations. Table 2 contains some results extracted from that work for the $^{16}O + ^{58}Ni$ system at E_{CM} = 28 MeV, since this energy is in the energy range in which we have extracted the "experimental" nuclear potential for that system [2]. We point out the following features of the CC calculations: (i) the contribution of the coupling for the ^{16}O 3^- state (which has a large phonon amplitude) is about 50% of the full polarization potential (which corresponds to all coupled channels); (ii) the polarization potential due to this 3^- state is about 8% of the folding potential independent of the interaction distance considered. These results indicate that the polarization potential should not change significantly the

Table 2

Double-folding potential (V_{fold}) and polarization potential contribution corresponding to the coupling for the ^{16}O 3_1^- state only ($V_{\text{pol}}^{3_1^-}$) and also to all reaction channels included in the CC calculations ($V_{\text{pol}}^{\text{full}}$), for the ^{16}O + ^{58}Ni system at $E_{\text{CM}} = 28$ MeV

R (fm)	$V_{\text{pol}}^{3_1^-}$ (MeV)	$V_{\text{pol}}^{\text{full}}$ (MeV)	V_{fold} (MeV)
10.0	0.08	0.16	0.91
10.5	0.03	–	0.37
11.0	0.006	–	0.064

These values were extracted from Refs. [18,2] at three different surface interaction radii.

shape (diffuseness) of the total (folding + polarization) potential in comparison to the folding potential. Another important point is that the strength of the full polarization potential is only about 17% in comparison to the folding potential. This result indicates that the polarization potential should be responsible for less than half of the observed discrepancy (40%) between the "experimental" and the folding potential strengths found in our previous work [2]. In principle, as discussed by Keeley et al. [11], the source of that discrepancy could be other possible couplings such as that for the ^{16}O 3_1^- state. Nevertheless, recent comparison [12] between the predicted fusion cross sections of this full CC analysis and precise fusion data for the ^{16}O + ^{58,62}Ni systems indicate that such CC calculations overpredict the data at energies below the fusion barrier (see Fig. 3 of Ref. [12]). The inclusion of other reaction channels in the CC calculations certainly would worsen the fusion cross section predictions. Thus, we believe that the strengths of the couplings are not so strong as considered in such calculations and the polarization potential strength should be even less significant in comparison to the bare potential.

We have also performed coupled channel calculations for the ^{16}O + ^{90}Zr system including the ^{16}O 3_1^- and ^{90}Zr 3_1^- states, besides that for the ^{90}Zr 2_1^+ state. For the nuclear potential, we have adopted the "experimental" CC potential according to Table 1. Fig. 15 shows the predicted elastic cross sections for $E_{\text{Lab}} = 48$ MeV, considering: no couplings (solid line), only the ^{90}Zr 2_1^+ coupling (also solid line because the difference is negligible), both couplings ^{90}Zr 2_1^+ + ^{90}Zr 3_1^- states (dashed line) and ^{90}Zr 2_1^+ + ^{16}O 3_1^- states (dotted line). The couplings do not have much effect on the elastic scattering cross sections. In order to fit the data considering the coupling for the ^{16}O 3_1^- state, it is necessary to reduce the "experimental" potential strength by about 7% and the diffuseness parameter persists unchanged. These results are very similar to those found for the ^{16}O+Ni systems. Therefore, we consider that also for the systems studied in the present work, ^{16}O + ^{88}Sr, ^{90,92}Zr, ^{92}Mo, the polarization potential is far from being capable of accounting for the detected difference between the folding and the "experimental" potential strengths.

The connection between the real and imaginary parts of the optical potential through the dispersion relation has been verified for several systems [13], including the ^{16}O + Ni [11,14]. We have tested this relation for the ^{16}O+^{88}Sr, ^{90}Zr systems by analyzing the existing elastic scattering data [3,15] for energies at and above the barrier ($48 \leqslant E_{\text{Lab}} \leqslant$

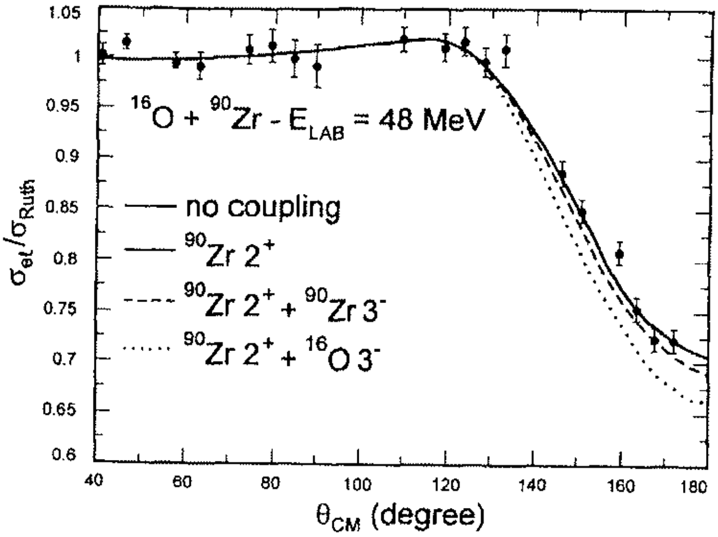

Fig. 15. Comparison between the experimental elastic scattering angular distribution for the ^{16}O + ^{90}Zr system ($E_{\rm Lab}$ = 48 MeV) and different CC calculations which include: (a) no reaction channel (solid line), (b) only the ^{90}Zr 2_1^+ state (also solid line), (c) the 2_1^+ and 3_1^- states of the ^{90}Zr nucleus (dashed line), and (d) the 2_1^+ and 3_1^- states of the ^{90}Zr and ^{16}O nuclei, respectively (dotted line).

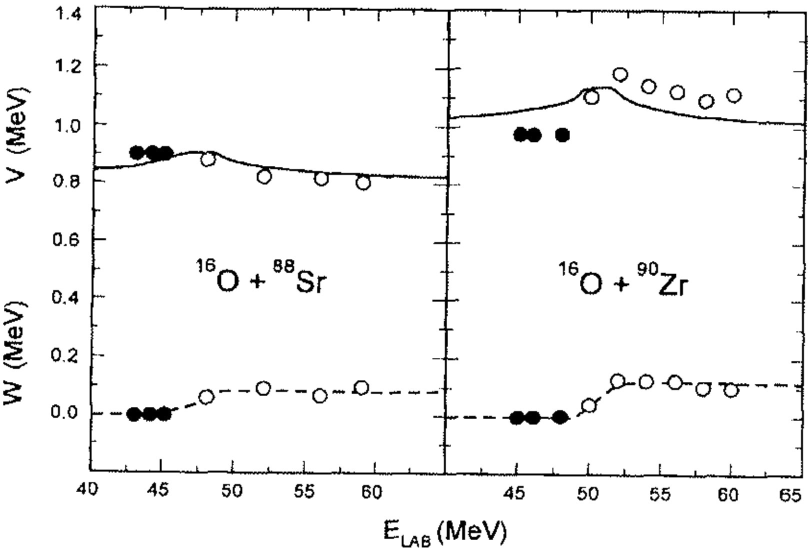

Fig. 16. The real and imaginary potential strengths at R = 11 fm for energies below (closed circles) and above (open circles) the barrier. The solid lines represent predictions for the real part of the optical potential, using the dispersion relation and assuming the energy dependence for the imaginary part as indicated by dashed lines.

60 MeV). In the data analysis, the diffuseness of the real part of the potential was fixed at $\bar{a}$ = 0.64 fm (see Section 3), and the strengths and imaginary part diffuseness of the Woods–Saxon shape optical potential were searched for the best data fits. Fig. 16 shows the potential strengths at the interaction distance R = 11 fm (average sensitivity radius) for the energies below (closed circles – this work, Section 3) and above (open circles) the barrier. The solid lines in the figure represent the dispersion relation predictions for

the real part of the optical potential, assuming the energy dependence for the imaginary part as indicated by dashed lines. The potential strengths resulting from data analysis are in agreement with the dispersion relation within an average precision of 7%.

6. The missing potential strength: Probing the nuclear density

As discussed in the previous sections, the ion–ion potentials extracted from low energy CC data analyses are about 40% greater than the theoretical double-folding predictions for the ^{16}O + ^{58,60,62,64}Ni, ^{88}Sr, ^{90,92}Zr, ^{92}Mo systems, and the polarization potential that arises from couplings to reaction channels with negligible cross sections can only account for part of this difference. We have investigated if the source of such discrepancy is related to the models adopted to describe the ground-state nuclear densities. Since this discrepancy is approximately target independent, we have investigated the projectile density. We have studied which region of the ^{16}O density contributes significantly to the nuclear potential in the surface region. In order to perform such a study, we have taken the ^{90}Zr as the target nucleus and we have included a spline with Gaussian shape, according to Eq. (8), on the nuclear density of the ^{16}O nucleus. We have characterized the sensitivity region of the density by varying the position of the perturbation (R_p), and calculating the percentage difference ($100 \times \Delta V/V_{\mathrm{unperturbed}}$) in the strength of the folding potential at the interaction distance $R = 11$ fm ($\Delta V = V_{\mathrm{perturbed}} - V_{\mathrm{unperturbed}}$). The results of such calculations are shown in Fig. 17. The low energy sensitivity region (LESR) for the ^{16}O density lies at radius around 4 fm, a value about 1.3 fm greater the root-mean-square (RMS) radius of the ^{16}O charge distribution [9]. Double-folding calculations show that an increase of about 30% in the ^{16}O density in this surface region (roughly $3 \leqslant r \leqslant 5$ fm) could explain the theoretical–experimental potential strength discrepancy previously discussed. We point out that nuclear density calculations for the ^{16}O nucleus based on different models give similar density values in the region near the RMS radius, and predict quite different results in the surface region, which differ from each other by about 30% (see Fig. 18). On the other hand, we have not observed such behavior for the targets studied in this work, as illustrated in Fig. 19,

$$\rho_{\mathrm{perturbed}}(r) = \rho_{\mathrm{unperturbed}}(r)\left[1 + 0.1e^{-((r-R_p)/0.5)^2}\right]. \tag{8}$$

The low energy data analysis for the ^{16}O+^{88}Sr, ^{90,92}Zr, ^{92}Mo systems have shown that the elastic scattering cross sections are sensitive to an interaction distance region around 11 fm, which corresponds to a region of sensitivity for the nuclear densities about 1.5 fm larger than the RMS radius. For much higher energies, inner distances are probed by elastic scattering cross section data analysis. Such measurements have been performed for the ^{16}O + ^{90}Zr system at $E_{\mathrm{Lab}} = 1503$ MeV [18]. In this case, the elastic scattering cross sections are sensitive to the nuclear potential in an interaction distance region around 8 fm [18], and our analysis indicate that the corresponding density sensitivity region is near the RMS radius. At such high energies and such internal interaction distance region, as discussed in Refs. [19,20], the polarization potential from reaction

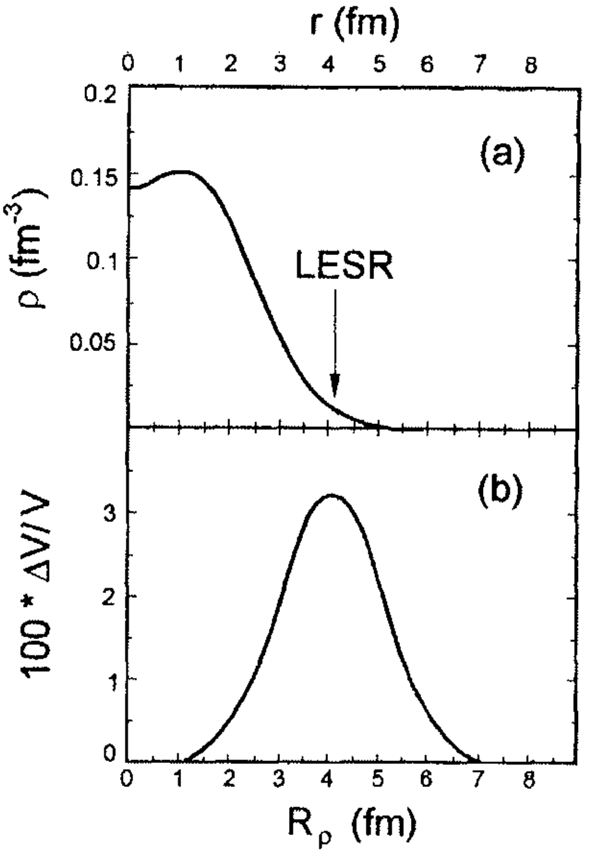

Fig. 17. (a) The charge distribution shape nuclear density for the ^{16}O nucleus (Eq. (2)), indicating the "low energy sensitivity region (LESR)" in the determination of the bare potential through sub-barrier elastic data analysis. (b) The percentage difference ($100 \times \Delta V/V_{\rm unperturbed}$) in the strength of the folding potential at $R = 11$ fm for the ^{16}O + ^{90}Zr system (see text for details).

channel couplings (Feshbach nonlocality) contributes mainly to the imaginary part of the optical potential, while the effects of nucleon exchange (Pauli nonlocality) are important to the real part of the nuclear interaction. Recently, a model [19-21] that takes into account the Pauli non-local nature of the nuclear interaction was developed with the aim to describe the nucleus-nucleus collision at low and high energies. The model is based on the Perey and Buck prescription [22], with the non-local parameter range (b) given by the Jackson and Johnson theoretical prediction [23], $b = b_0(\mu_0/\mu)$ ($b_0 = 0.85$ fm, μ_0 is the nucleon mass and μ is the reduced mass of the system). In the model, the parameter free non-local real nucleus-nucleus interaction is expressed by

$$V(\boldsymbol{R}, \boldsymbol{R}') = V_{\rm folding}\left(\frac{R+R'}{2}\right)\frac{1}{\pi^{3/2}b^3}\, e^{-((R-R')/b)^2}, \tag{9}$$

and the corresponding energy-dependent local equivalent potential is expressed approximately by

$$V_{\rm LE}(R,E) \simeq \frac{1-\sqrt{1-4\gamma V_{\rm folding}(R)\, e^{-\gamma[E-V_C(R)]}}}{2\gamma}, \tag{10}$$

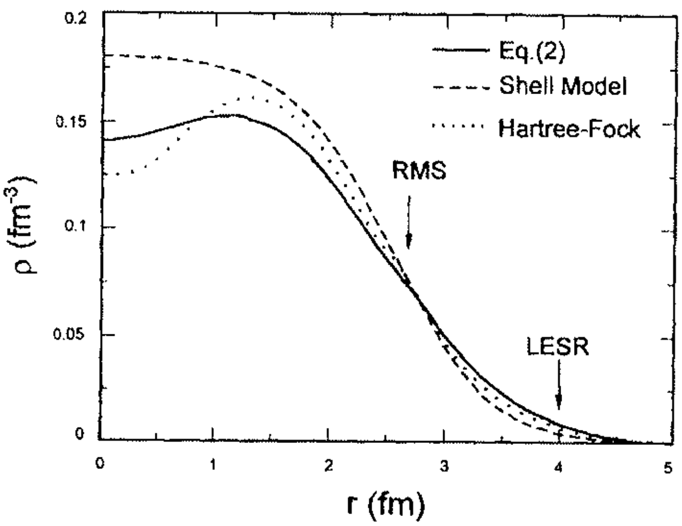

Fig. 18. Different ^{16}O nuclear density predictions considering: (a) the charge distribution shape of Eq. (2) (solid line), (b) shell model calculations from Ref. [17] (dashed line), and (c) Hartree-Fock calculations from Ref. [24] (dotted line). In the figure are indicated the root-mean-square radius (RMS), and the "low energy sensitivity region" in the determination of the CC potential (LESR).

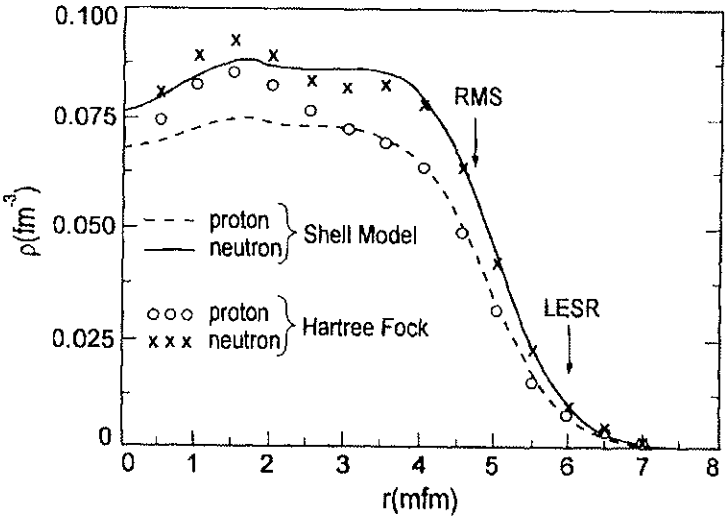

Fig. 19. Comparison between proton and neutron densities for the ^{90}Zr nucleus considering shell model (this work) and Hartree-Fock (Ref. [24]) calculations. In the figure are indicated the root-mean-square radius (RMS) and the "low energy sensitivity region" in the determination of the CC potential (LESR).

where $\gamma = \mu b^2/2\hbar^2$.

For an interaction radius near the barrier radius and energies close to the Coulomb barrier, the local equivalent potential is quite close to the folding one, $V_{\rm LE}(R \simeq R_{\rm B}, E \simeq V_{\rm B}) \simeq V_{\rm folding}(R)$, and the effect of the nonlocality is negligible. Fig. 20 shows the folding potential (dashed line) and the local equivalent potential at $E_{\rm Lab}$ = 1503 MeV (solid line) for the $^{16}{\rm O} + {}^{90}{\rm Zr}$ system. In Fig. 21, the elastic cross section data [18] for the same system and energy are shown. Also the corresponding optical model predictions, either considering the folding potential (dashed line) or the local equivalent

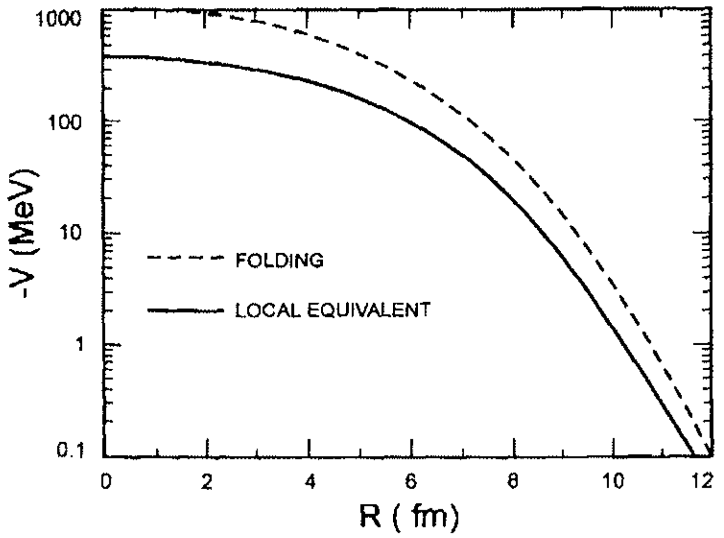

Fig. 20. The local equivalent potential (solid line) for the $^{16}O + ^{90}Zr$ system at the bombarding energy E_{Lab} = 1503 MeV. The dashed line represents the corresponding double-folding potential (Eq. (1)).

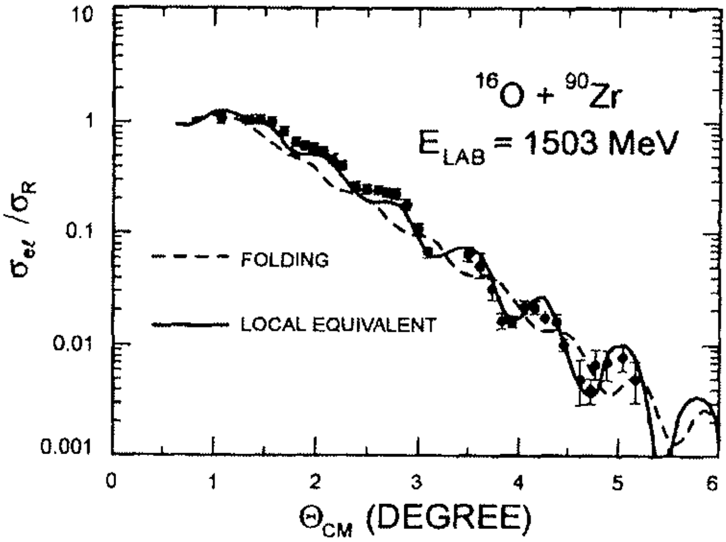

Fig. 21. Optical model elastic scattering data fits for the $^{16}O + ^{90}Zr$ system at the bombarding energy E_{Lab} = 1503 MeV, considering for the nuclear interaction: (a) the double-folding potential (dashed line), and (b) the local equivalent potential (solid line). In the data fits only the Woods-Saxon imaginary potential parameters were allowed to vary.

potential (solid line), are shown in the same figure. In the data fit procedure, as reported in Ref. [20], only the Woods-Saxon imaginary potential parameters were allowed to vary. The elastic scattering cross section predictions are quite similar considering any density model of Fig. 18 for the ^{16}O nucleus. The parameter free local equivalent real potential provides a good data prediction (see Fig. 21) without any normalization of the folding potential included in Eq. (10). This result should be compared to the required normalization of 40% in elastic scattering data fits at sub-barrier energies. We again point out that the density sensitivity regions probed at low and high energies are rather different. We stress that different models usually give similar density results in the region close to the RMS radius, and very different density values in the surface region (LESR). Therefore, the low energy elastic scattering data provide a test for different density models which give similar high energy data fits.

7. Summary and conclusions

In summary, we have performed coupled channel analysis of elastic and inelastic angular distributions for the $^{16}O + ^{88}Sr$, $^{90,92}Zr$, ^{92}Mo systems at the sub-barrier energies $43 \leqslant E_{\rm Lab} \leqslant 49$ MeV. The data are well reproduced with energy-independent nuclear bare potentials, which are real and have an exponential shape in the surface region. These CC potentials have the same diffuseness parameter, $\bar{a} = 0.64$ fm, defined within an accuracy of 5% for all systems. The slope of the resulting CC potentials is well reproduced by the M3Y double-folding calculations using shell model densities for the targets. The isotonic and isotopic dependence of the CC potentials are also reasonably described by the double-folding potential. Very similar results had already been obtained for the $^{16}O + ^{58,60,62,64}Ni$ systems. All these results are closely related to the nuclear density features of the collision partners.

Nevertheless, for both sets of systems the strengths of the sub-barrier CC bare potentials are about 40% greater than the corresponding values from M3Y folding potential calculations. Based on a previous extensive and rather complete coupled channel analysis for the $^{16}O + ^{58,62}Ni$ systems, we have concluded that the contributions to the polarization potential associated to other reaction channel couplings only account for part of such discrepancy. Our studies indicate that the discrepancy is connected mainly to the ^{16}O nuclear density model adopted in the folding calculations. The predictions of the low energy elastic scattering cross section are very sensitive to the nuclear matter densities in the surface region. In the high energy case, in which the effects on the nuclear interaction due to the non-local nucleon exchange are very important, the sensitivity region for the densities is somewhat more internal than the corresponding region for the sub-barrier case. Thus, a consistent low and high energy elastic scattering data analysis has been demonstrated to be a powerful tool to probe ground-state nuclear densities.

Acknowledgements

This work was partially supported by Financiadora de Estudos e Projetos (FINEP), Fundação de Amparo à Pesquisa do Estado de São Paulo (FAPESP), Conselho Nacional de Desenvolvimento Científico e Tecnológico (CNPq), and Programa PICD/CAPES da Universidade Federal de Mato Grosso.

We thank Prof. B.A. Brown from Michigan State University, for providing us the computer shell-model codes.

References

[1] L.C. Chamon, D. Pereira, E.S. Rossi Jr., C.P. Silva, R. Lichtenthaler Filho and L.C. Gomes, Nucl. Phys. A 582 (1995) 305.
[2] L.C. Chamon, D. Pereira, E.S. Rossi Jr., C.P. Silva, H. Dias, L. Losano and C.A.P. Ceneviva, Nucl. Phys. A 597 (1996) 253.
[3] N. Anantaraman, Phys. Rev. C 8 (1973) 2245.
[4] M. Benjelloun, W. Galster and J. Vervier, Nucl. Phys. A 560 (1993) 145.
[5] T. Tamura, Rev. Mod. Phys. 37 (1965) 679.
[6] S. Raman, C.H. Malarkey, W.T. Milner, C.W. Nestor Jr. and P.H. Stelson, At. Data Nucl. Data Tables 36 (1987) 1.
[7] H. Esbensen and F. Videbaek, Phys. Rev. C 40 (1989) 126.
[8] B.J. Lund, N.P.T. Bateman, S. Utku, D.J. Horen and G.R. Satchler, Phys. Rev. C 51 (1995) 635.
[9] C.M. De Jager, H. De Vries and C. De Vries, At. Data Nucl. Data Tables 14 (1974) 479.
[10] G.R. Satchler and W.G. Love, Phys. Rep. 55 (1979) 183.
[11] N. Keeley, J.S. Lilley and J.A. Christley, Nucl. Phys. A 603 (1996) 97.
[12] N. Keeley, J.S. Lilley, J.X. Wei, M. Dasgupta, D.J. Hinde, J.R. Leigh, J.C. Mein, C.R. Morton, H. Timmers and N. Rowley, Nucl. Phys. A 628 (1998) 1.
[13] G.R. Satchler, Phys. Rep. 199 (1991) 147.
[14] B.R. Fulton, D.W. Banes, J.S. Lilley, M.A. Nagarajan and I.J. Thompson, Phys. Lett. B 162 (1985) 55.
[15] A.W. Obst, D.L. MaShan and R.H. Davis, Phys. Rev. C 6 (1972) 1814.
[16] G.R. Satchler, Nucl. Phys. A 329 (1979) 233.
[17] M. El-Azab Farid and G.R. Satchler, Nucl. Phys. A 438 (1985) 525.
[18] P. Roussel-Chomaz, N. Alamanos, F. Auder, J. Barrete, B. Berthier, B. Fernandez and L. Papineau, Nucl. Phys. A 477 (1988) 345.
[19] M.A.C. Ribeiro, L.C. Chamon, D. Pereira, M.S. Hussein and D. Galetti, Phys. Rev. Lett. 78 (1997) 3270.
[20] L.C. Chamon, D. Pereira, M.S. Hussein, M.A.C. Ribeiro and D. Galetti, Phys. Rev. Lett. 79 (1997) 5218.
[21] L.C. Chamon, D. Pereira and M.S. Hussein, Phys. Rev. C 58 (1998) 576.
[22] F. Perey and B. Buck, Nucl. Phys. 32 (1962) 253.
[23] D.F. Jackson and R.C. Johnson, Phys. Lett. B 49 (1974) 249.
[24] J.W. Negele, Phys. Rev. C 4 (1970) 1260.

ELSEVIER
Nuclear Physics A 679 (2001) 287–303
NUCLEAR PHYSICS A
www.elsevier.nl/locate/npe

The heavy-ion nuclear potential: determination of a systematic behavior at the region of surface interaction distances

C.P. Silva [a], M.A.G. Alvarez [a], L.C. Chamon [a,*], D. Pereira [a], M.N. Rao [a], E.S. Rossi Jr. [a], L.R. Gasques [a], M.A.E. Santo [b], R.M. Anjos [b], J. Lubian [b,1], P.R.S. Gomes [b], C. Muri [b], B.V. Carlson [c], S. Kailas [d], A. Chatterjee [d], P. Singh [d], A. Shrivastava [d], K. Mahata [d], S. Santra [d]

[a] *Laboratório Pelletron, Instituto de Física da Universidade de São Paulo, Caixa Postal 66318, 05315-970, São Paulo, SP, Brazil*
[b] *Instituto de Física, Universidade Federal Fluminense, Av. Litoranea, Niterói, RJ, 24210-340, Brazil*
[c] *Depto. de Física, Instituto Tecnológico de Aeronáutica, Centro Técnico Aeroespacial, São José dos Campos, SP, Brazil*
[d] *Nuclear Physics Division, Bhabha Atomic Research Centre, Bombay 400 085, India*

Received 14 April 2000; revised 31 May 2000; accepted 30 June 2000

Abstract

Precise elastic scattering differential cross sections have been measured for the $^{16}O+^{120}Sn$, ^{138}Ba, ^{208}Pb systems at sub-barrier energies. The corresponding "experimental" nuclear potentials have been determined at interaction distances larger than the Coulomb barrier radii. These experimental potentials have been compared with our earlier results for other systems, and with theoretical calculations based on the double-folding and liquid-drop models. We have shown that the nuclear potentials have a systematic behavior at the surface region. The present results for the $^{16}O+^{208}Pb$ system are used to extend earlier studies of the dispersion relation to sub-barrier energies. © 2001 Elsevier Science B.V. All rights reserved.

PACS: 25.60.Bx; 24.10.Ht; 24.10.-i; 21.60.-n
Keywords: NUCLEAR REACTIONS: $^{120}Sn(^{16}O,\ ^{16}O)^{120}Sn$, $^{138}Ba(^{16}O,\ ^{16}O)^{138}Ba$, $^{208}Pb(^{16}O,\ ^{16}O)^{208}Pb$; Measured elastic scattering cross sections; Deduced optical potentials; Double-folding calculations with microscopic densities

---

[*] Corresponding author. E-mail: luiz.chamon@dfn.if.usp.br
[1] Permanent address: CEADEN, PO 6122, Havana, Cuba.

PII: S0375-9474(00)00347-X

1. Introduction

In this work, we present elastic scattering differential cross sections for the $^{16}O+{}^{120}Sn$, ^{138}Ba, ^{208}Pb systems at sub-barrier energies. The main purpose of the experiments was to determine the corresponding nuclear potentials. The method was applied earlier successfully to the $^{16}O+{}^{58,60,62,64}Ni$, ^{88}Sr, $^{90,92}Zr$, ^{92}Mo systems [1–3]. As discussed in these previous works, the imaginary part of the optical potential is negligible at sub-barrier energies due to the small number of reaction channels with relevant cross sections. Thus, the elastic scattering data analysis, at this energy range, determines the real part of the optical potential (nuclear potential). The slopes and strengths of the experimental (i.e., extracted from data analyses) nuclear potentials have been determined within 5% to 10% uncertainty in the surface region, $R \geqslant$ barrier radius $\simeq 1.4 \times (A_1^{1/3} + A_2^{1/3})$ fm.

The optical potential is the result of the addition of the bare and polarization potentials. The bare potential represents the ground-state expectation value of the interaction operator, which contains as basic input the average effective nucleon–nucleon force. The polarization potential contains the contributions arising from nonelastic couplings. Due to the very small reaction cross sections, the absorptive imaginary part of the polarization potential is negligible at sub-barrier energies. We have estimated the contribution of the polarization potential to the real part of the optical potential to be small at the energy region at which our elastic scattering data were taken. Thus, the data extracted experimental potentials are representative of the corresponding bare potentials, and have been compared with those derived from double-folding and liquid-drop (proximity potential) theoretical models.

With the present work, we have completed a set of results (this work and Refs. [1–3]) to demonstrate a systematic behavior of the nuclear potential for systems involving the ^{16}O as projectile. All the target nuclei are magic or semi-magic, with mass number ranging from $A = 58$ to $A = 208$. The systematization indicates a universal exponential shape for the experimental potentials, as predicted by the liquid-drop model, but with a diffuseness value smaller than that from the proximity potential [4]. A similar result was found by Christensen and Winther (hereafter CW) [5] in another systematic study of potential strengths, which were extracted from elastic scattering data analyses at energies above the barrier. In that work, a diffuseness of 0.63 fm was found for the heavy-ion nuclear potential, a value very close to that (0.62 fm) obtained from our sub-barrier data analyses. We have detected a small difference among the potential strengths at the sub-barrier region in comparison with those from the CW work. We have associated this difference to the following sources: (i) variation with the energy of the polarization potential contribution to the optical potential, (ii) variation of the bare potential with the energy, due to nonlocal effects, and (iii) ambiguities in the extraction of potential strengths from the higher-energy data analyses.

The polarization potential is expected to obey a dispersion relation [6] which connects the real and imaginary parts of the optical potential. This relation has been observed for several systems [6], including $^{16}O+{}^{208}Pb$ for which the dispersion relation had already been studied in a large energy range [7]. We have used our present results to extend this study to the sub-barrier region.

The paper is organized as follows: Section 2 gives the experimental details and data analyses. In Section 3, the experimental potentials are compared with those derived from double-folding and liquid-drop models. In Section 4 is presented a comparison between potentials extracted from data analyses at the sub-barrier region with those from higher energies. The dispersion relation for the $^{16}\mathrm{O}+{}^{208}\mathrm{Pb}$ system is analysed in Section 5. Section 6 contains a brief summary and the main conclusions.

2. Experimental results and data analysis

The measurements for the $^{16}\mathrm{O}+{}^{120}\mathrm{Sn}$, $^{138}\mathrm{Ba}$ systems were made using the $^{16}\mathrm{O}$ beam from the São Paulo 8UD Pelletron Accelerator, Brazil, and the data for the $^{16}\mathrm{O}+{}^{208}\mathrm{Pb}$ system were taken at the 14UD BARC-TIFR Pelletron at Bombay, India. The detecting system has already been described in Ref. [1]. The thickness of the $^{120}\mathrm{Sn}$, $^{138}\mathrm{Ba}$ and $^{208}\mathrm{Pb}$ targets were about 70 $\mu\mathrm{g/cm}^2$. Figs. 1–3 exhibit the elastic scattering cross sections for the three systems in the energy ranges: $53 \leqslant E_{\mathrm{LAB}} \leqslant 55$ MeV ($^{120}\mathrm{Sn}$), $54 \leqslant E_{\mathrm{LAB}} \leqslant 57$ MeV ($^{138}\mathrm{Ba}$) and $74 \leqslant E_{\mathrm{LAB}} \leqslant 78$ MeV ($^{208}\mathrm{Pb}$). We have included a small contribution of detected transfer processes in the "elastic" cross sections for the $^{16}\mathrm{O}+{}^{208}\mathrm{Pb}$ system.

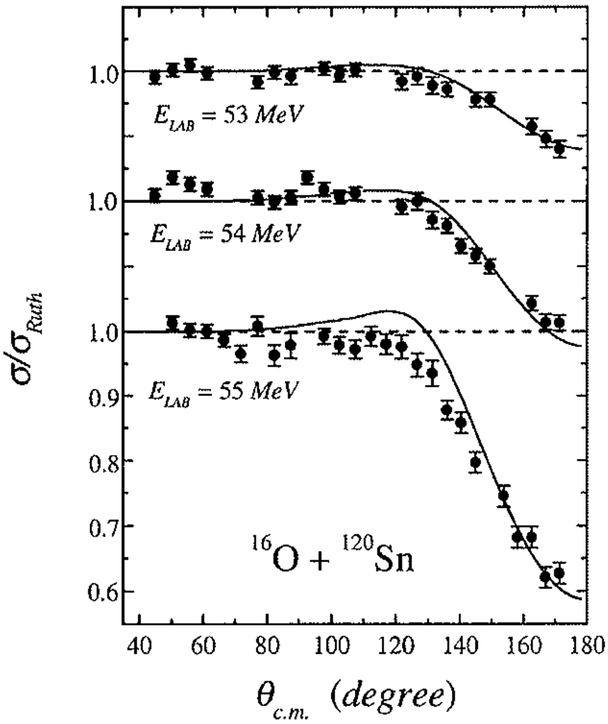

Fig. 1. Elastic scattering angular distributions for the $^{16}\mathrm{O}+{}^{120}\mathrm{Sn}$ system at the bombarding energies $E_{\mathrm{LAB}}=53$, 54 and 55 MeV. The solid lines correspond to optical model calculations with an energy-independent nuclear potential, with diffuseness $a=0.62$ fm (see details in the text).

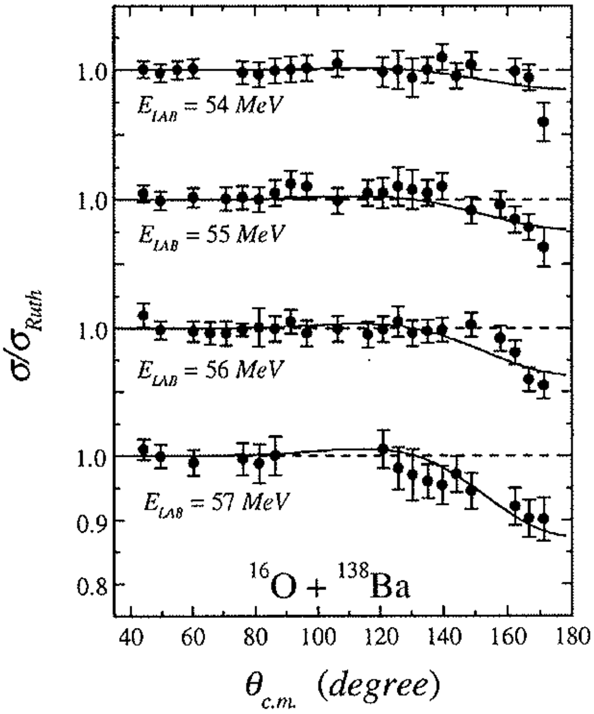

Fig. 2. The same as in Fig. 1, for the $^{16}\mathrm{O}+{}^{138}\mathrm{Ba}$ system at $E_{\mathrm{LAB}} = 54$, 55, 56 and 57 MeV.

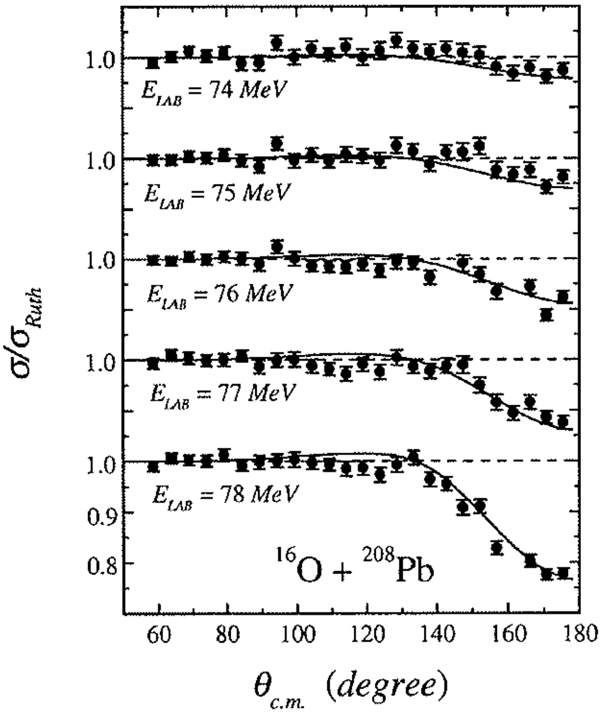

Fig. 3. The same as in Fig. 1, for the $^{16}\mathrm{O}+{}^{208}\mathrm{Pb}$ system at $E_{\mathrm{LAB}} = 74$, 75, 76, 77 and 78 MeV.

In the optical model (hereafter OM) calculations, we have adopted a procedure similar to that described in the analysis of the sub-barrier elastic and inelastic scattering data for the $^{16}O+^{58,60,62,64}Ni$, ^{88}Sr, $^{90,92}Zr$, ^{92}Mo systems [1–3]. We have assumed a Woods–Saxon shape for the real part of the optical potential, with radius parameters equal to the Coulomb radii, which were obtained from electron-scattering experiments [8]. We have also used an inner imaginary potential, which takes into account the rather small internal absorption from barrier penetration. The chosen parameters for this potential result in very small strengths at the surface region. This procedure must be adopted in the data analysis due to the small cross sections of peripherical reaction channels at sub-barrier energies. No sensitivity in the cross section predictions has been detected related to depth variations of this absorptive potential. The depth, V_0, and the diffuseness, a, of the (real) nuclear potential were searched for the best data fits. For each system and bombarding energy we have found a family of potentials, with different depth and diffuseness parameters, which give equivalent data fits, as illustrated in Fig. 4 for the $^{16}O+^{208}Pb$ system at two different energies. These potentials cross at a particular radius, R_S, which is usually referred to as the strong absorption radius in the case of higher-energy elastic scattering

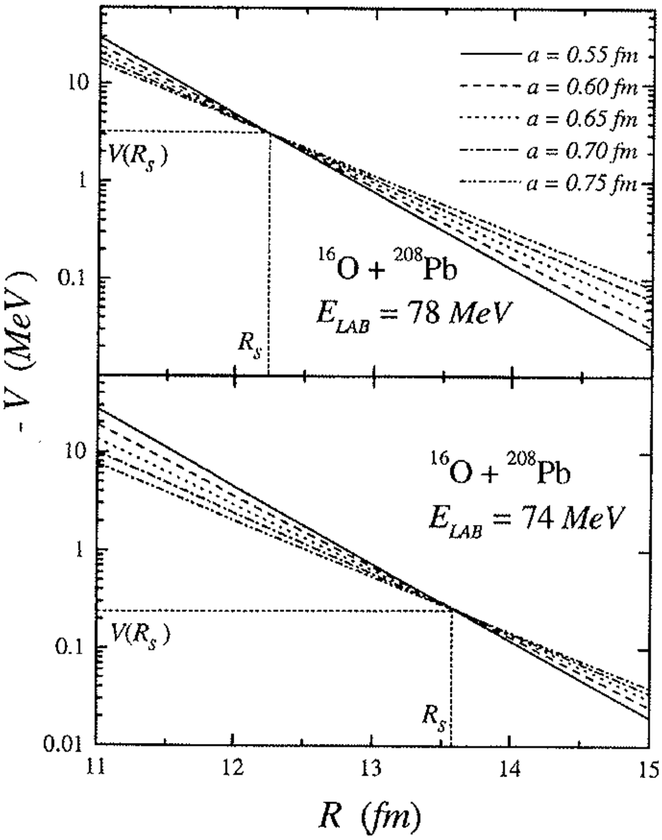

Fig. 4. Determination of the nuclear potential at the sensitivity radius (R_S) for the $^{16}O+^{208}Pb$ system, as obtained from OM analysis of the experimental data ($E_{LAB}=74$ and 78 MeV). The lines represent potentials with different values of diffuseness and depth parameters, which give equivalent data fits.

data analyses. At sub-barrier energies, this radius is related to the classical turning point, and is energy dependent. Due to the small absorption involved in this case, we refer to R_S as the sensitivity radius.

We have used the energy dependence of R_S (see Fig. 5) to characterize the shape of the nuclear potentials at the surface region for the $^{16}O+{}^{120}Sn$, ^{138}Ba, ^{208}Pb systems. For comparison purpose, we have included in Fig. 5 the earlier results [2,3] that we had obtained for two lighter systems. As discussed in Ref. [1], the potential strength error bars were estimated considering the variation by unity of chi-square around the minimum value. The shape of the nuclear potential is quite close to an exponential, represented by solid lines in Fig. 5. Table 1 gives the diffuseness values obtained for the $^{16}O+{}^{120}Sn$, ^{138}Ba, ^{208}Pb systems. We have included, in Table 1, the results for the $^{16}O+{}^{58,60,62,64}Ni$, ^{88}Sr, $^{90,92}Zr$, ^{92}Mo systems that we had obtained previously [1–3]. Within the uncertainties, the diffuseness parameters are compatible with the average value $\bar{a} = 0.62$ fm. This diffuseness value is in good agreement with theoretical double-folding calculations, as will be discussed in the next section. Using the value $a = 0.62$ fm, we are able to fit all the angular distributions (see Figs. 1–3) with an energy-independent nuclear potential for each system (which are represented by solid lines in Fig. 5). Table 1 gives the radii ($R_{1\,\mathrm{MeV}}$) at which the strengths of the energy-independent nuclear potentials equal 1 MeV, and the strengths at these same radii of the corresponding folding (V_f) and proximity (V_{pr})

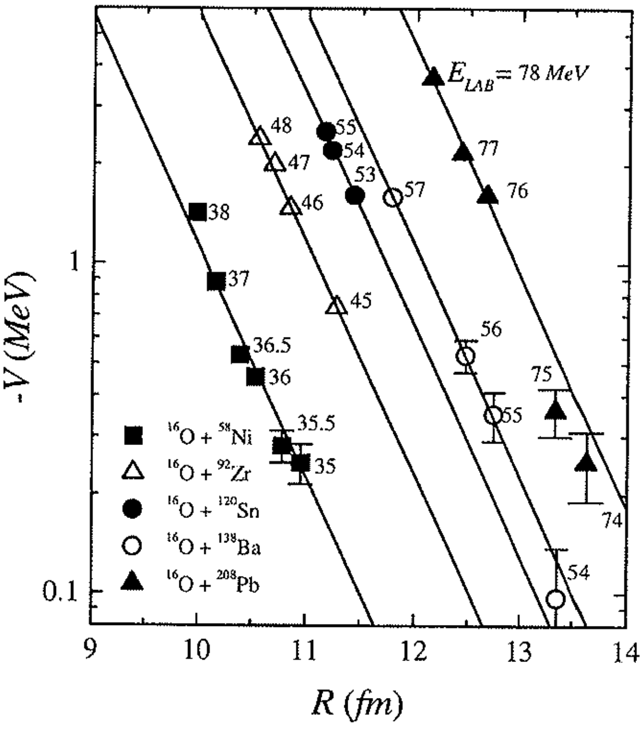

Fig. 5. The nuclear potential strength as a function of the sensitivity radius for the $^{16}O+{}^{58}Ni$, ^{92}Zr, ^{120}Sn, ^{138}Ba and ^{208}Pb systems. The bombarding energies of the elastic scattering angular distributions in which the sensitivity radii have been obtained are indicated in the figure. The solid lines represent potentials with the same diffuseness value, $\bar{a} = 0.62$ fm.

Table 1
The diffuseness values of the nuclear potentials from optical-model data analyses (a) and double-folding calculations (a_f), and the radii ($R_{1\,\mathrm{MeV}}$) at which the strengths of the OM energy-independent nuclear potentials equal 1 MeV. In the calculations of the $R_{1\,\mathrm{MeV}}$ values, $\bar{a} = 0.62$ fm was assumed to be the diffuseness for the OM nuclear potentials. The strengths of the folding (V_f) and proximity (V_{pr}) potentials at the radii $R_{1\,\mathrm{MeV}}$ are also included in the table

Target	a (fm)	a_f (fm)	$R_{1\,\mathrm{MeV}}$ (fm)	V_f (MeV)	V_{pr} (MeV)
^{58}Ni	0.57 ± 0.03	0.57	10.06	0.81	0.62
^{60}Ni	0.58 ± 0.04	0.58	10.21	0.72	0.55
^{62}Ni	0.60 ± 0.05	0.58	10.28	0.72	0.54
^{64}Ni	0.67 ± 0.05	0.59	10.39	0.67	0.50
^{88}Sr	0.71 ± 0.05	0.58	10.93	0.71	0.54
^{90}Zr	0.63 ± 0.03	0.59	10.98	0.70	0.55
^{92}Zr	0.61 ± 0.05	0.61	11.11	0.66	0.48
^{92}Mo	0.63 ± 0.06	0.59	10.99	0.73	0.57
^{120}Sn	0.59 ± 0.07	0.65	11.73	0.76	0.44
^{138}Ba	0.63 ± 0.03	0.61	12.07	0.60	0.42
^{208}Pb	0.56 ± 0.04	0.63	12.94	0.75	0.49

potentials. In the case of the ^{16}O + ^{120}Sn system, the theoretical fit overestimates the data for $E_{\mathrm{LAB}} = 55$ MeV and $\theta_{\mathrm{CM}} \simeq 120°$ (see Fig. 1). Considering the complete set of our measurements, the energy of this angular distribution is the closest to the Coulomb barrier. The small discrepancies between data and OM predictions for this angular distribution are due to effects of reaction channel couplings which are more relevant for energies closer to the barrier.

3. Double-folding and proximity calculations

In this section, we present theoretical calculations with the aim of evaluating the nuclear part of the ion–ion potential, by using the double-folding [9] and liquid-drop [4] models.

The double-folding potentials were calculated in a similar way as described in Refs. [1–3]. The ground-state nuclear density of the ^{16}O nucleus was derived from electron scattering experimental results [8], with the assumption that the neutron and proton densities have the same shape as the charge density. For the ^{208}Pb nucleus, we have used densities of Ref. [10] derived from Hartree–Fock calculations. For the neutron, ^{120}Sn, and proton, ^{138}Ba, superfluid (and semi-magic) nuclei, we have calculated nuclear densities using a self-consistent Dirac–Hartree–Bogoliubov model [11]. Fig. 6 presents the proton (dashed lines), neutron (dotted lines) and total (solid lines) densities for the ^{58}Ni, ^{120}Sn, ^{138}Ba and ^{208}Pb nuclei. For the heavier nuclei, the number of protons is significantly smaller than the number of neutrons, and the proton densities are somewhat more internal as compared to the corresponding neutron ones.

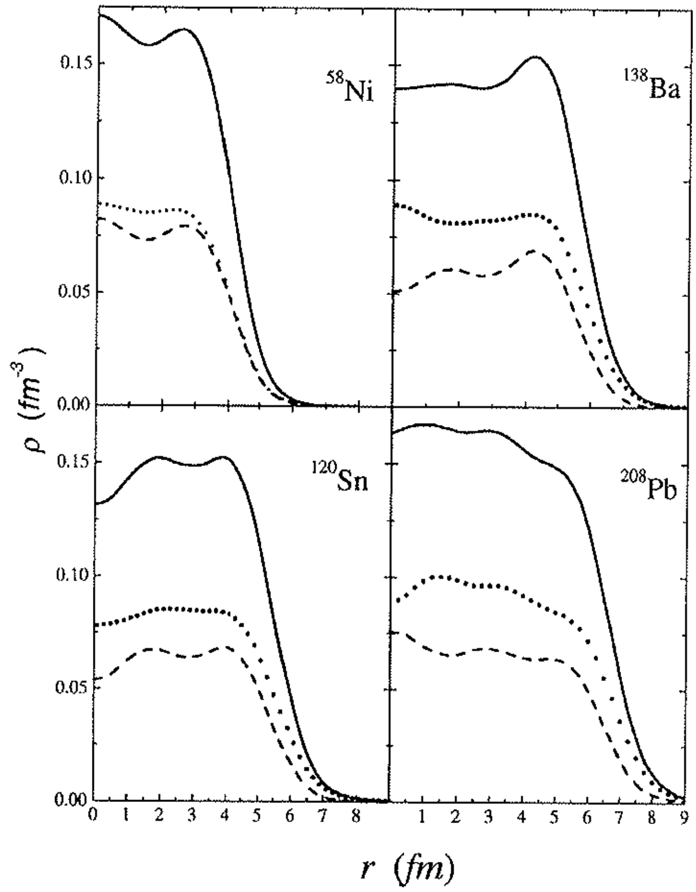

Fig. 6. The ground-state proton (dashed lines), neutron (dotted lines) and total (solid lines) densities derived from theoretical calculations for the ^{58}Ni, ^{120}Sn, ^{138}Ba and ^{208}Pb nuclei. The ^{58}Ni and ^{208}Pb densities were obtained from Refs. [2,10], respectively. The densities for the neutron (^{120}Sn) and proton (^{138}Ba) superfluid nuclei were calculated using a self-consistent Dirac–Hartree–Bogoliubov model [11].

We have calculated the folding potential contributions of the proton and neutron target densities according to the following expressions:

$$V_p(R) = \int \rho_o(\vec{r}_1)\, v_o\ \vec{R}\quad \vec{r}_1 + \vec{r}_2)\, \rho_p(\vec{r}_2)\, d\vec{r}_1\, d\vec{r}_2, \tag{1}$$

$$V_n(R) = \int \rho_o(\vec{r}_1)\, v_o\ \vec{R}\quad \vec{r}_1 + \vec{r}_2)\, \rho_n(\vec{r}_2)\, d\vec{r}_1\, d\vec{r}_2, \tag{2}$$

$$V_f(R) = V_p(R) + V_n(R) = \int \rho_o(\vec{r}_1)\, v_o\ \vec{R}\quad \vec{r}_1 + \vec{r}_2)\rho_t(\vec{r}_2)\, d\vec{r}_1\, d\vec{r}_2, \tag{3}$$

where ρ_o is the total ^{16}O density; ρ_p, ρ_n and ρ_t are the proton, neutron and total target densities, respectively; V_p, V_n and V_f are the corresponding proton, neutron and total folding potentials. These folding potentials at the surface region are shown in Fig. 7. As expected, due to the neutron and proton density features, the heavier the target nucleus

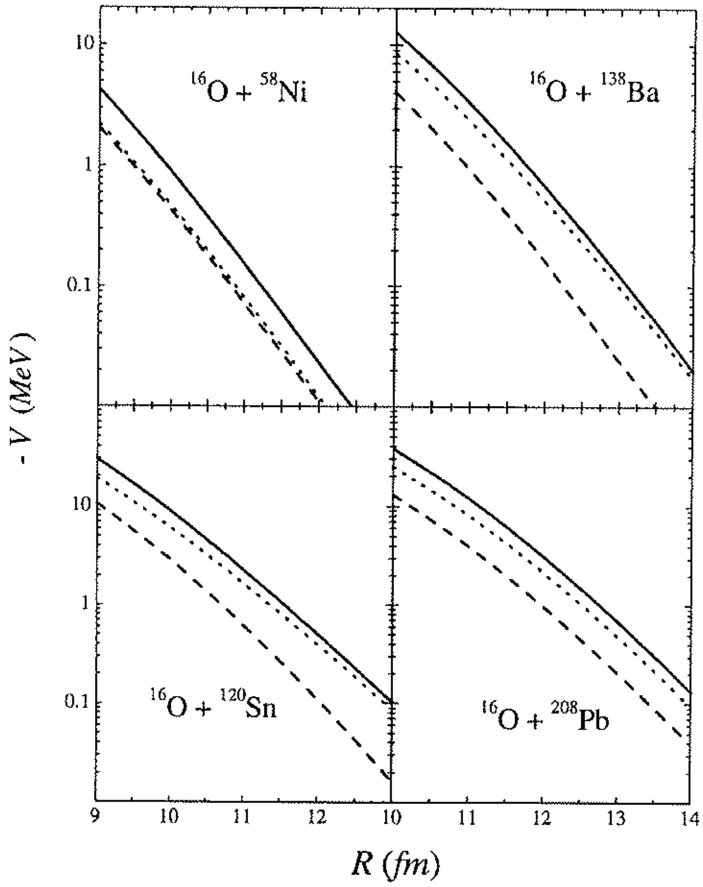

Fig. 7. Proton (dashed lines), neutron (dotted lines) and total (solid lines) double-folding potentials at the surface region for the $^{16}O + ^{58}Ni$, ^{120}Sn, ^{138}Ba and ^{208}Pb systems (see text for details).

the greater is the neutron potential contribution in comparison to the corresponding proton one.

The predictions of the folding calculations for the potential strengths are smaller than the corresponding experimental values (see Table 1). We have previously [1–3] discussed this discrepancy for the $^{16}O + ^{58,60,62,64}Ni$, ^{88}Sr, $^{90,92}Zr$, ^{92}Mo systems. These studies have indicated that the discrepancy is mainly connected to the ^{16}O nuclear density model adopted in the folding calculations [3].

Table 1 gives the "diffuseness parameters" obtained from the slopes of the folding potentials. The folding diffuseness values are similar for all systems and close to the average "experimental" value (0.62 fm). This result indicates that the heavy-ion nuclear potentials have a "universal" shape in the surface region rather independent of the "size of the system". This behavior should be expected, considering that the features of the potential in the surface interaction region are dependent on the nuclear densities in the nucleus surface region, and that heavy ions have very similar nuclear density diffuseness values, as detected for charge distributions from electron scattering experiments [8].

A theoretical interaction, which predicts a universal shape for the heavy-ion nuclear potentials, has been proposed [4] within the framework of the liquid-drop model. This interaction is based on the Proximity Theorem, which relates the force between two nuclei to the interaction between two flat surfaces made of semi-infinite nuclear matter. This theorem leads [4] to an expression for the potential which is a product of a simple geometrical factor and a universal function of the separation ($s = R \quad R_{\mathrm{C1}} \quad R_{\mathrm{C2}}$) between the surfaces of the nuclei

$$V(R) = 4\pi\gamma\overline{R}\alpha\,\Phi(s), \tag{4}$$

with $\gamma = 0.9517(1 \quad 1.7826 I^2)$ MeV/fm^2, $I = \frac{N \ Z}{A}$ and $\alpha \simeq 1$ fm. The mean curvature of the system is obtained from

$$\overline{R} = \frac{R_{\mathrm{C1}} R_{\mathrm{C2}}}{R_{\mathrm{C1}} + R_{\mathrm{C2}}}. \tag{5}$$

R_{C1} and R_{C2} are the central radii of both nuclei, which are related to the effective sharp radii by $R_{\mathrm{C}i} \simeq R_{\mathrm{eff},i}\,(1 \quad \alpha^2/R^2_{\mathrm{eff},i})$. The formula indicated [4] for the effective sharp radius is

$$R_{\mathrm{eff},i} = 1.28 A_i^{1/3} \quad 0.76 + 0.8 A_i^{\ 1/3}. \tag{6}$$

The universal function was calculated [4] using the nuclear Thomas–Fermi model with Seyler–Blanchard phenomenological nucleon–nucleon interaction [12–14]

$$\Phi(s \leqslant 1.2511\,\alpha) \simeq \ \frac{1}{2}\left(\frac{s}{\alpha} \quad 2.54\right)^2 \quad 0.0852\left(\frac{s}{\alpha} \quad 2.54\right)^3, \tag{7}$$

$$\Phi(s \geqslant 1.2511\,\alpha) \simeq \ 3.437\exp\left(\ \frac{s}{0.75\,\alpha}\right). \tag{8}$$

The proximity potential predicts an exponential shape at the surface region (Eq. (8)), but with a diffuseness parameter (0.75 fm) greater than the value (0.62 fm) that we have obtained from data analyses. The radii $R_{1\ \mathrm{MeV}}$ (see Table 1) at which the experimental potential strengths equal 1 MeV, correspond to separation distances about 3 fm. In this region, the strengths of the proximity potentials are about half of the corresponding experimental values (see Table 1). In the same region, similar differences among experimental results and theoretical predictions, concerning both diffuseness and potential strength values, had already been shown in the original paper in which the proximity potential was proposed (see Fig. 9 of Ref. [4]). We believe that such differences are due to the model adopted for the nuclear densities in the derivation of the proximity potential.

4. Systematization of the nuclear potential

The main features of the proximity potential are the universal shape and the dependence of the strengths with the mean curvature ($\overline{R}$) of the system. These features are also included in the empirical potential (Eq. (9)) proposed by Christensen and Winther in the seventies [5]. In that work, the radii involved in the s and $\overline{R}$ calculations were obtained from expression (10). The values $V_0 = 50$ MeV/fm and $a = 0.63$ fm were obtained from the fit of "experimental" potential strengths, extracted from elastic scattering data analyses for several systems at energies above the Coulomb barrier:

$$V(R) = \quad V_0\bar{R}e^{\ \ s/a}, \tag{9}$$

$$R_{Ci} = 1.233A_i^{1/3} \quad 0.978A_i^{\ \ 1/3}. \tag{10}$$

We have selected potential strength "data" from the CW systematization [5] for systems that involve the ^{16}O nucleus. Fig. 8 (bottom) presents the $V/\bar{R}$ values as a function of the nucleus surface separation distance. The solid lines in the figure represent the CW empirical potential. Our sub-barrier strength "data" are also presented in Fig. 8 (top). The sub-barrier strength "data" are systematically greater than the CW empirical potential.

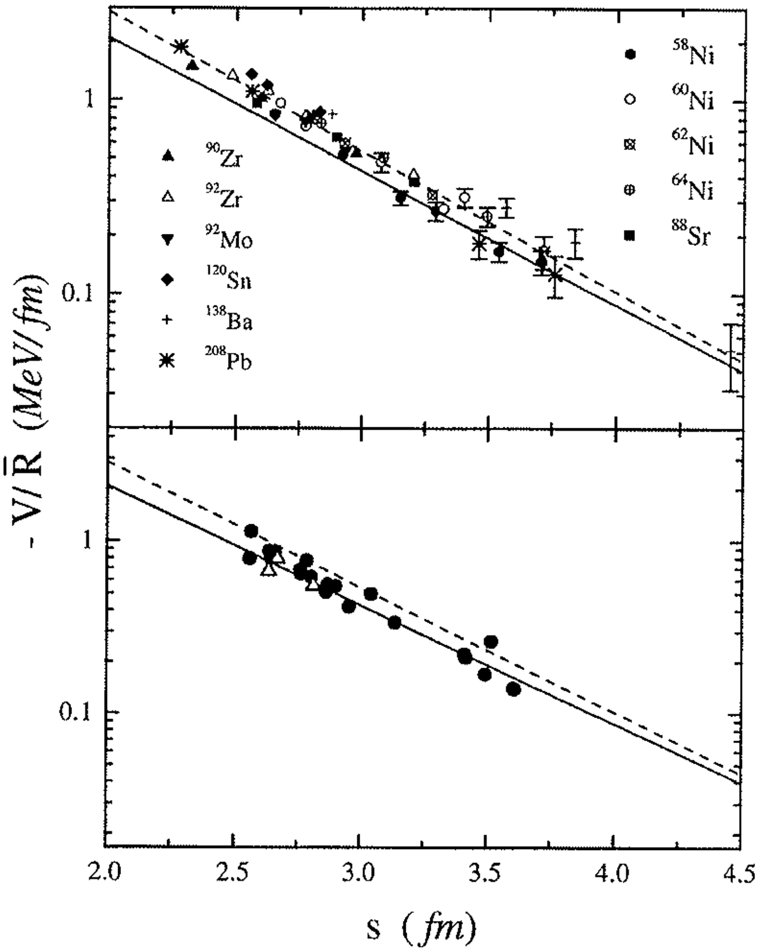

Fig. 8. The "normalized" potential strengths ($V/\bar{R}$) from sub-barrier (top) and above-barrier (bottom) elastic scattering data analyses as a function of the nucleus surface separation distance, s, for systems that involve the ^{16}O nucleus. The open triangles (bottom) represent potential strengths deduced from earlier [15,16] OM analyses of the angular distributions presented in Fig. 9. The Christensen and Winther's (CW) empirical potential [5] is represented by solid lines. The dashed lines represent a fit of the sub-barrier potential strengths by Eq. (9).

The dashed lines in Fig. 8 represent a fit of the sub-barrier strength "data" to expression (9), which resulted the values $a = 0.61$ fm and $V_0 = 75.5$ MeV/fm.

Fig. 8 (top) shows that the difference between sub-barrier strength "data" and the CW empirical potential is slightly dependent on the s value. The average difference between the complete set of sub-barrier strength "data" and the CW empirical potential (solid lines in Fig. 8) is 18%. We point out that also the higher-energy strength "data" for systems with ^{16}O (Fig. 8, bottom) are, in average, slightly greater than the CW empirical potential. We estimate that the average difference among sub and above-barrier strength "data" is about 15%. Thus, the agreement between both analyses is good, and we have associated this small difference to three sources: (i) variation with the energy of the polarization potential contribution to the optical potential, (ii) variation with the energy of the bare potential, due to nonlocal effects (this subject is discussed in the next section), and (iii) ambiguities in the determination of the optical potential from elastic scattering data fits at energies above the barrier.

We have already extensively discussed [1–3] the contribution of the polarization potential to the nuclear potential strengths that we have obtained from sub-barrier data analysis for the $^{16}\mathrm{O}+{}^{58,60,62,64}\mathrm{Ni}$, ^{88}Sr, ^{90,92}Zr, ^{92}Mo systems. Extensive and rather complete coupled channel (hereafter CC) calculations have indicated that the strengths of the polarization potential, at the energy range at which our sub-barrier data have been obtained, are about 17% of the bare potential strengths [3,17], which corresponds to 14% of the optical (polarization + bare) potential. The contribution of the coupling for the ^{16}O 3 state (which has a very large fonon amplitude) is about 50% of the full polarization potential (which corresponds to all coupled channels). Nevertheless, recent comparison [18] between the predicted fusion cross sections of this full CC analysis and precise fusion data indicates that such CC calculations overpredict the data at energies below the barrier (see Fig. 3 of Ref. [18]). Thus, we believe that the couplings are not so strong as considered in such CC calculations, and the polarization potential strength should be even less significant in comparison to the optical potential. Based on these studies, we estimate the contribution of the polarization potential to the experimental potentials extracted from sub-barrier data to be less than 10%. In this sense, we consider the experimental potentials at sub-barrier energies to be representative of the corresponding bare potentials.

In the sub-barrier elastic scattering data analysis, we have assumed the strengths of the imaginary part of the optical potential to be very small in the surface region. As we have already discussed, this procedure is consistent with the very small absorption in this energy region. At higher energies, it is very difficult to set the imaginary part of the optical potential based on physical grounds. Thus, the corresponding OM elastic scattering data analyses usually involve parametrized shapes (mostly the Woods–Saxon one) for the imaginary part of the potential, and this procedure results in ambiguities in the determination of the strengths of the real part of the optical potential. As an example, we have taken elastic scattering data for the $^{16}\mathrm{O}+{}^{208}\mathrm{Pb}$ system [15,16] in three energies, which are included in the CW potential strength systematization (open triangles in Fig. 8, bottom). We have fitted the angular distributions (solid lines in Fig. 9) assuming the sub-barrier energy-independent nuclear potential for the real part of the optical potential.

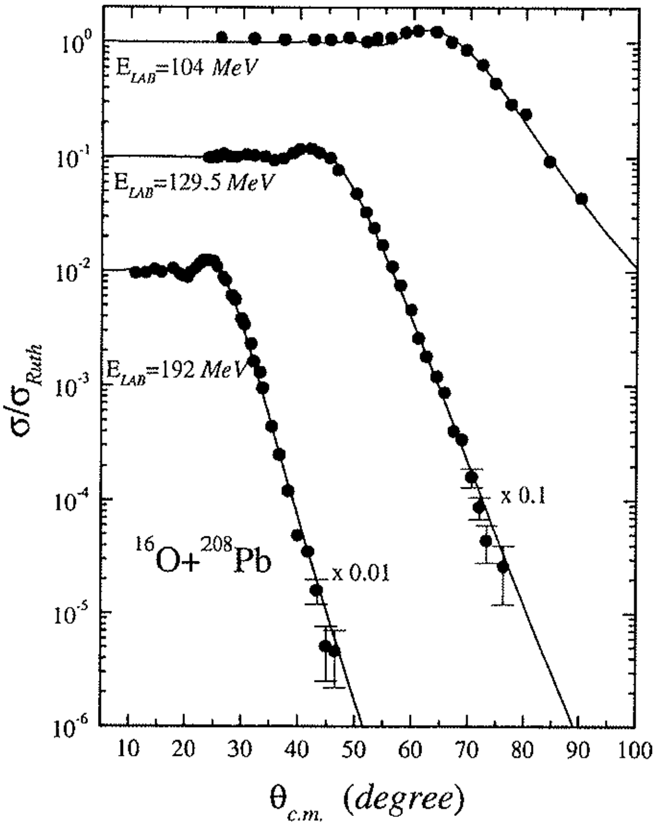

Fig. 9. Elastic scattering angular distributions for the $^{16}O+^{208}Pb$ system at the energies $E_{LAB} = 104$, 129.5 and 192 MeV (the data were extracted from Refs. [15,16]). The solid lines represent data fits, in which the sub-barrier energy-independent nuclear potential was assumed for the real part of the optical potential. In the data fits, only the diffuseness and depth parameters of the Woods–Saxon shape imaginary potential were allowed to vary.

In these fits, only the diffuseness (a_i) and depth (W_0) of a Woods–Saxon shape (with $r_{i0} = 1.2$ fm) imaginary potential were allowed to vary. Table 2 contains the resulting a_i and W_0 values. Table 2 also presents a comparison among the potential strengths at the strong absorption radii of the present sub-barrier energy-independent potential (V_{SB}) with those (V_{CW}) obtained from the earlier OM data fits of Refs. [15,16] (which were used in the CW systematization [5]). There are significant differences between these sets of potential strengths, but the elastic scattering data fits obtained from both sets are equivalent. Therefore, the potential strengths extracted from the data at energies above the barrier are not so well determined as in the sub-barrier case. The degree of ambiguity in the determination of the potential depends on the system and on the energy of the elastic scattering angular distribution. In general, due to the low absorption, lighter systems present less ambiguities in comparison to heavy systems. At energies much higher than the Coulomb barrier the data extracted optical potential is well determined in an interaction region different from that probed at low energies [19]. For instance, data analysis for heavy-ion systems at intermediate energies ($40 \leqslant E_{LAB}/A \leqslant 200$ MeV/nucleon) provides

Table 2
The table presents the diffuseness (a_i) and depth (W_0) parameters of the imaginary part of the OM potential, obtained from the fit of elastic scattering angular distributions for the $^{16}O + ^{208}Pb$ system at $E_{LAB} = 104$, 129.5 and 192 MeV. In these fits, the energy-independent (V_{SB}) nuclear potential, obtained from the sub-barrier data analyses, was assumed for the real part of the optical potential. Also the strong absorption radii (R_{SA}), the corresponding potential strengths from the Christensen and Winther's systematization (V_{CW}), and the sub-barrier potential (V_{SB}) at R_{SA} are included in the table

E_{LAB} (MeV)	a_i (fm)	W_0 (MeV)	R_{SA} (fm)	V_{CW} (MeV)	V_{SB} (MeV)
104.0	0.316	951	12.672	1.088	1.541
129.5	0.523	102	12.520	1.557	1.968
192.0	0.443	176	12.493	1.324	2.056

information of the potential at radii farther inside the barrier radius (see Refs. [20–23]). We stress that the present sub-barrier data analysis determines the real part of the optical potential without ambiguity in the surface region.

5. The dispersion relation

Elastic scattering data analyses for some heavy-ion systems have resulted in a rapid and localized variation of the optical potential with the energy, known as "threshold anomaly" [6]. This variation has been observed in the vicinity of the Coulomb barrier, and has been associated to the contribution of the polarization to the optical potential [6]. The dispersion relation, Eq. (11) [6], describes the connection between the energy dependence of the real and imaginary parts of the polarization potential

$$\Delta V(E) = \frac{P}{\pi} \int_{\infty}^{\infty} \frac{W(E')}{E' \quad E} \, \mathrm{d}E'. \tag{11}$$

The $^{16}O + ^{208}Pb$ system is included among the systems for which the threshold anomaly was first observed [7]. The dispersion relation was verified for this system from the Coulomb barrier to higher energies. We have used the present results to extend these studies to the sub-barrier energy region. In an earlier work [3], we have made a similar study for the lighter systems. Fig. 10 presents the data extracted OM potential strengths from Ref. [7] (closed circles and open triangles) and the present sub-barrier results (open circles). The solid lines in the figure represent the trend suggested in Ref. [7], which is compatible with the dispersion relation.

In Section 4, we have discussed the ambiguity in the determination of potential strengths from elastic scattering data analyses at energies above the Coulomb barrier. This sort of ambiguities is illustrated in Fig. 10. The open triangles in this figure correspond to earlier OM data analyses (from Ref. [7]) for the angular distributions presented in Fig. 9. The closed triangles in Fig. 10 represent the results of our OM analyses for the same

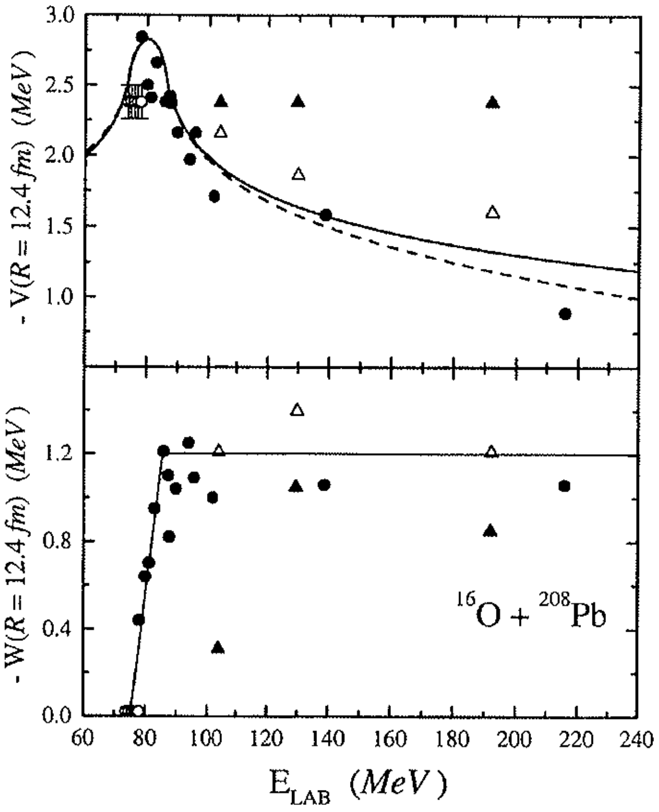

Fig. 10. Potential strength values obtained from earlier [7] OM data analyses of elastic scattering angular distributions at energies above the barrier (closed circles and open triangles). The open circles represent the energy-independent nuclear potential that we have obtained from sub-barrier data analyses. The open triangles correspond to earlier [7] data analyses of the angular distributions presented in Fig. 9. The closed triangles correspond to present OM analyses of the same angular distributions (see text for details). The lines represent behaviors compatible with the dispersion relation, with (dashed line) and without (solid line) the additional effect due to the nonlocal nature of the bare potential.

angular distributions, in which the "sub-barrier" energy-independent nuclear potential was used for the real part of the optical potential. The differences between closed and open triangles provides an estimation about the "error bars" that the potential strengths may have. Thus, the trend adopted for the optical potential suggested based on the "data" behavior is itself also ambiguous. The ambiguity in the determination of potential strengths from OM elastic scattering data analysis at energies above the barrier could be reduced by using a realistic (based on fundamental physical grounds) imaginary part for the optical potential. A model for a realistic polarization potential should be consistent with the dispersion relation.

There is an additional energy dependence of the optical potential that arises from the nonlocal nature of the bare nuclear interaction [6]. This energy dependence has been neglected in most studies of the dispersion relation. The nonlocality of the bare interaction has been studied (for instance, see Refs. [24] to [30]) based on the dependence of the nucleon–nucleon interaction with the nuclear matter density and on intrinsically quantum effects connected to exchange of nucleons between the two nuclei. The difference between solid and dashed lines in Fig. 10 (top) represents the additional variation of the optical potential due to the nonlocality of the bare potential (the calculations have been based on the model proposed in Refs. [28–30]). As demonstrated in Ref. [3], for energies close to the Coulomb barrier the effect of the nonlocality on the bare potential is negligible (see also Fig. 10), and therefore it does not need be taken into account in the determination of potential strengths from sub-barrier data analysis.

6. Summary and conclusions

In summary, we have performed optical model analyses of elastic scattering angular distributions for the ^{16}O + ^{120}Sn, ^{138}Ba, ^{208}Pb systems at sub-barrier energies. The sub-barrier data analyses determine the optical potential without the usual ambiguities found in elastic scattering data analyses at energies above the barrier. The present sub-barrier data are well reproduced with energy-independent nuclear potentials, which are real and have an exponential shape in the surface region. Similar results had been obtained by us earlier for the ^{16}O + ^{58,60,62,64}Ni, ^{88}Sr, ^{90,92}Zr, ^{92}Mo systems. The diffuseness of all these experimental potentials are compatible, within the uncertainties, with the average value $\bar{a} = 0.62$ fm. This result is in agreement with theoretical double-folding calculations, and with the Christensen and Winther's systematization of real potential strengths which were extracted from higher energy OM data analyses. Our sub-barrier results indicate a systematic behavior for the nuclear potential, which contains the main features predicted by the liquid-drop model. By combining exchange nonlocal effects and the liquid-drop model [31], it is possible to describe the heavy-ion nuclear potential in a much larger energy range than that considered in this work.

Acknowledgements

This work was partially supported by Financiadora de Estudos e Projetos (FINEP), Fundação de Amparo à Pesquisa do Estado de São Paulo (FAPESP), Fundação de Amparo à Pesquisa do Estado do Rio de Janeiro (FAPERJ), and Conselho Nacional de Desenvolvimento Científico e Tecnológico (CNPq).

References

[1] L.C. Chamon, D. Pereira, E.S. Rossi Jr., C.P. Silva, R. Lichtenthaler Filho, L.C. Gomes, Nucl. Phys. A 582 (1995) 305.

[2] L.C. Chamon, D. Pereira, E.S. Rossi Jr., C.P. Silva, H. Dias, L. Losano, C.A.P. Ceneviva, Nucl. Phys. A 597 (1996) 253.

[3] M.A.G. Alvarez, L.C. Chamon, D. Pereira, E.S. Rossi Jr., C.P. Silva, L.R. Gasques, H. Dias, M.O. Roos, Nucl. Phys. A 656 (1999) 187.

[4] J. Blocki, J. Randrup, W.J. Swiatecki, C.F. Tsang, Ann. Phys. 105 (1977) 427.
[5] P.R. Christensen, A. Winther, Phys. Lett. B 65 (1976) 19.
[6] G.R. Satchler, Phys. Rep. 199 (1991) 147.
[7] M.A. Nagarajan, C.C. Mahaux, G.R. Satchler, Phys. Rev. Lett. 54 (1985) 1136.
[8] C.M. De Jager, H. De Vries, C. De Vries, At. Data Nucl. Data Tables 14 (1974) 479.
[9] G.R. Satchler, W.G. Love, Phys. Rep. 55 (1979) 183.
[10] J.W. Negele, Phys. Rev. C 4 (1970) 1260.
[11] B.V. Carlson, D. Hirata, submitted to Phys. Rev. C.
[12] W.D. Myers, W.J. Swiatecki, Ann. Phys. 55 (1969) 395.
[13] J. Randrup, Lawrence Berkeley Laboratory Report LBL-4302, 1975; Nucl. Phys. A 259 (1976) 253.
[14] R.G. Seyler, C.H. Blanchard, Phys. Rev. 124 (1961) 227; Phys. Rev. 131 (1963) 355.
[15] F.D. Becchetti, D.G. Kovar, B.G. Harvey, J. Mahoney, B. Mayer, F.G. Puhlhofer, Phys. Rev. C 6 (1972) 2215.
[16] J.B. Ball, C.B. Fulmer, E.E. Gross, M.L. Halbert, D.C. Hensley, C.A. Ludemann, M.J. Saltmarsh, G.R. Satchler, Nucl. Phys. A 252 (1975) 208.
[17] N. Keeley, J.S. Lilley, J.A. Christley, Nucl. Phys. A 603 (1996) 97.
[18] N. Keeley, J.S. Lilley, J.X. Wei, M. Dasgupta, D.J. Hinde, J.R. Leigh, J.C. Mein, C.R. Morton, H. Timmers, N. Rowley, Nucl. Phys. A 628 (1998) 1.
[19] J.G. Cramer, R.M. DeVries, Phys. Rev. C 22 (1980) 91.
[20] H.G. Bohlen, M.R. Clover, G. Ingold, H. Lettau, W. von Oertzen, Z. Phys. A 308 (1982) 121.
[21] E. Stiliaris, H.G. Bohlen, P. Frobrich, B. Gebauer, D. Kolbert, W. von Oertzen, M. Wilpert, Th. Wilpert, Phys. Lett. B 223 (1982) 291.
[22] P. Roussel, N. Alamanos, F. Auger, J. Barrete, B. Berthier, B. Fernandez, L. Papineau, Phys. Rev. Lett. 54 (1985) 1779.
[23] H.G. Bohlen, X.S. Chen, J.G. Cramer, P. Frobrich, B. Gebauer, H. Lettau, A. Miezaika, W. von Oertzen, R. Ulrich, Th. Wilpert, Z. Phys. A 322 (1985) 241.
[24] A.M. Kobos, B.A. Brown, P.E. Hodgson, G.R. Satchler, A. Budzanowski, Nucl. Phys. A 384 (1982) 65.
[25] A.M. Kobos, B.A. Brown, R. Lindsay, G.R. Satchler, Nucl. Phys. A 425 (1984) 205.
[26] D.T. Khoa, Nucl. Phys. A 484 (1988) 376.
[27] D.T. Khoa, W. von Oertzen, A.A. Ogloblin, Nucl. Phys. A 602 (1996) 98.
[28] M.A.C. Ribeiro, L.C. Chamon, D. Pereira, M.S. Hussein, D. Galetti, Phys. Rev. Lett. 78 (1997) 3270.
[29] L.C. Chamon, D. Pereira, M.S. Hussein, M.A.C. Ribeiro, D. Galetti, Phys. Rev. Lett. 79 (1997) 5218.
[30] L.C. Chamon, D. Pereira, M.S. Hussein, Phys. Rev. C 58 (1998) 576.
[31] L.C. Chamon et al., work in progress.

PHYSICAL REVIEW C, VOLUME 65, 014602

Precise nuclear matter densities from heavy-ion collisions

M. A. G. Alvarez,[1] E. S. Rossi, Jr.,[1] C. P. Silva,[1] L. R. Gasques,[1] L. C. Chamon,[1] D. Pereira,[1] M. N. Rao,[1] B. V. Carlson,[2] C. De Conti,[2] R. M. Anjos,[3] P. R. S. Gomes,[3] J. Lubian,[3] S. Kailas,[4] A. Chatterjee,[4] and P. Singh[4]
[1]*Laboratório Pelletron, Instituto de Física da Universidade de São Paulo, 05315-970 São Paulo, SP, Brazil*
[2]*Departamento de Física, Instituto Tecnológico de Aeronáutica, Centro Técnico Aeroespacial, São José dos Campos, SP, Brazil*
[3]*Instituto de Física, Universidade Federal Fluminense, Av. Litoranea, Niterói 24210-340, RJ, Brazil*
[4]*Nuclear Physics Division, Bhabha Atomic Research Centre, Bombay 400 085, India*
(Received 3 April 2001; published 30 November 2001)

An unfolding method is proposed to extract ground-state nuclear matter densities from heavy-ion elastic scattering data analyses at low (sub-barrier) and intermediate energies. The consistency of the results is fully checked. The method should be of value in determining densities for exotic nuclei.

DOI: 10.1103/PhysRevC.65.014602 PACS number(s): 25.70.Bc, 21.10.Gv, 21.10.Ft, 24.10.Ht

A long-standing question of nuclear structure concerns the determination of heavy-ion neutron densities, which are far from being as well known as the proton densities that have been extracted from electron scattering experiments. It is worth mentioning the importance of the determination of nuclear densities to distinguish among different nuclear structure theoretical approaches. Several probes (pion, proton, alpha, etc.) have been used in order to determine nuclear matter densities, with different sorts of limitations [1]. For instance, the use of the strong interacting probes π^+ and π^- is usually accompanied by the need to "calibrate" the method, which means that only average radii and differences in densities are the most reliable results. In a more fundamental philosophy, the possibility of extracting information on nuclear distributions from heavy-ion elastic scattering is a question of using the folding model for the interaction, including all the important effects from first principles and avoiding the use of adjustable parameters as much as possible.

In the present work, a method of determining matter densities from heavy-ion elastic scattering data at sub-barrier and intermediate energies is proposed. It is based on the parameter-free nonlocal energy-independent bare potential (NLM3Y potential), recently developed [2–5] for the real part of the nucleus-nucleus interaction. The NLM3Y potential has been tested for several systems [3,4] and gives excellent reproductions of measured elastic and inelastic cross sections in a large energy range, particularly at intermediate energies where the refractive elastic data are very sensitive to the real part of the interaction [6]. The model (for details see [3]) takes into account the Pauli nonlocality involving the exchange of nucleons between the target and the projectile. The energy-independent real part of the interaction is given by

$$V(\vec{R},\vec{R}')=V_{NL}\left(\frac{R+R'}{2}\right)\frac{1}{\pi^{3/2}b^3}e^{-(|\vec{R}-\vec{R}'|/b)^2}, \qquad (1)$$

where $b=b_0m_0/\mu$ is the range of the Pauli nonlocality, $b_0=0.85$ fm, m_0 and μ are the nucleon mass and the reduced mass of the system, respectively. The nonlocal interaction is connected to the usual folding potential [7] through

$$V_{NL}(R)=\int \rho_1(r_1)v(\vec{R}-\vec{r}_1+\vec{r}_2)\rho_2(r_2)d\vec{r}_1d\vec{r}_2, \qquad (2)$$

where $\rho_1(r_1)$ and $\rho_2(r_2)$ are the ground-state nuclear densities of the colliding partners, and $v(\vec{r})$ is the M3Y effective nucleon-nucleon interaction. The corresponding energy-dependent local equivalent potential is given by [3]

$$V_{LE}(R;E)=\frac{1-\sqrt{1-4\gamma V_{NL}(R)e^{-\gamma[E-V_C(R)]}}}{2\gamma}, \qquad (3)$$

with $\gamma=\mu b^2/2\hbar^2$. We mention in passing that other approaches for the finite range exchange term (for example see [8–10]) are more complicated to calculate and therefore less suitable for extensive studies of nuclear densities.

Within the model above, the central idea of the method proposed is to extract ground-state nuclear distributions from elastic scattering data analyses, with the densities as the result of best fits in an unfolding procedure involving expressions (2) and (3). The data analyses at intermediate energies give information about the total (neutron + proton) distributions in a region close to the root-mean-square radius (r_{rms}), while at sub-barrier energies the surface is the region sensitive to the data fits.

To characterize the absorption from reaction channels, at intermediate energies we have used an imaginary potential based on the Lax-type interaction [11]:

$$W(R;E)=-\frac{E}{k_N}\sigma_T^{NN}(E)\int \rho_1(|\vec{R}-\vec{r}|)\rho_2(r)d\vec{r}, \qquad (4)$$

where $\sigma_T^{NN}(E)$ is the average nucleon-nucleon total cross section with Pauli blocking. For the sub-barrier case, we have selected elastic scattering experimental angular distributions at energies sufficiently below the Coulomb barrier, that couplings to reaction channels are very small. In this case, we have used an inner imaginary potential with Woods-Saxon shape, which takes into account the small internal absorption from barrier penetration. The values adopted for the parameters of this potential result in small strengths at the surface region. This procedure must be used in the sub-barrier data analyses due to the small cross sections of peripherical reaction channels. No sensitivity in the cross sec-

0556-2813/2001/65(1)/014602(4)/$20.00

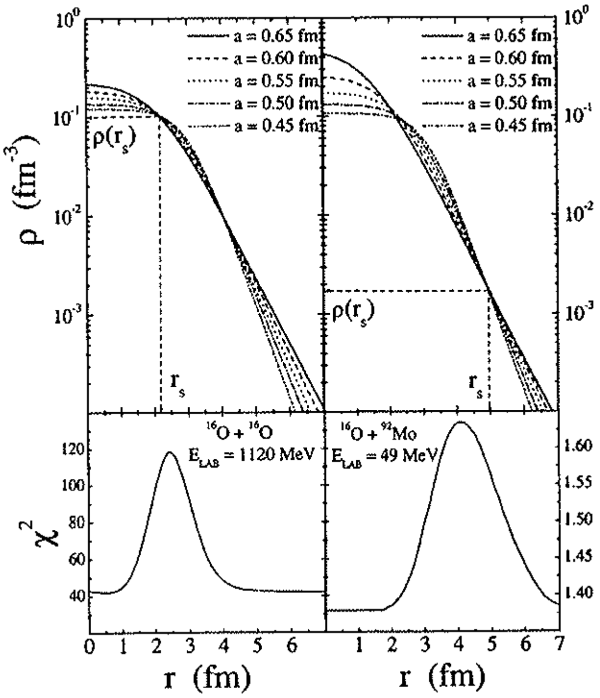

FIG. 1. Top: Examples of the determination of the sensitivity radii, r_s, and the corresponding experimental values for the ^{16}O nuclear matter density, $\rho(r_s)$, using two-parameter Fermi distributions which give equivalent elastic scattering data fits for angular distributions of the ^{16}O+^{16}O (E_{lab}=1120 MeV) and ^{16}O+^{92}Mo (E_{lab}=49 MeV) systems. Bottom: The sensitivity regions for the ^{16}O nuclear matter density characterized by notch tests.

tion predictions has been detected related to depth variations of this absorptive potential. We point out that the polarization potential that arises from reaction channel couplings (Feshbach nonlocality) has been estimated [12–14] through extensive coupled channel calculations for the sub-barrier data set, and represents less than 10% in comparison with the bare (folding) interaction.

We have chosen ^{16}O as a test case, due to the extensive experimental and theoretical information available about this nucleus, and, as discussed in Ref. [12], because different approaches give quite different results for the ^{16}O nuclear density, particularly at the surface region. In the analyses, we have assumed a two-parameter Fermi model (2PF) for the ^{16}O density, with diffuseness (a) and radius (R_0) searched for the best data fits, and with the ρ_0 parameter determined by the normalization condition

$$4\pi\int_0^\infty \frac{\rho_0}{1+\exp\left(\dfrac{r-R_0}{a}\right)}r^2dr=16. \tag{5}$$

In Fig. 1 is presented, as an illustration of our method, the determination of the total (neutron + proton) density for the ^{16}O nucleus at the $r_{\rm rms}$ radius and surface regions, by using elastic scattering data analyses at intermediate and sub-barrier energies, respectively. For each angular distribution, we have found a family of densities which give equivalent data fits. These densities cross (Fig. 1 top) at a particular radius r_s, hereafter referred to as the sensitivity radius. Similar behavior has been observed in the determination of bare potentials from sub-barrier data analyses [12–15], but in that case only one crossing was detected for each angular distribution. In the density case, two crossings are observed (Fig. 1) due to the particular shape and normalization condition imposed on the nuclear density. Thus, the determination of the sensitivity radius is also accompanied by a notch test (Fig. 1 bottom), in which a spline with Gaussian shape is included in the ^{16}O density, and the variation of the chi-square is studied as a function of the position of this perturbation. The notch test guarantees that r_s is in a density region important for the data fit, and does not arise from spurious crossing. Since the data fits depend only on the density in a small range of nuclear radii, the determination of the sensitivity radius and corresponding density value is rather independent of the shape assumed for the nuclear distribution (2PF, harmonic oscillator — see example in Fig. 2). For the ^{16}O+^{16}O system at the energy of 1120 MeV, besides the Lax interaction we have also used a three free parameter imaginary potential, with Woods-Saxon shape, with the aim of evaluating any possible change in the sensitivity radius. The r_s and corresponding density values obtained in this case are quite similar to those from the Lax interaction (see Fig. 2).

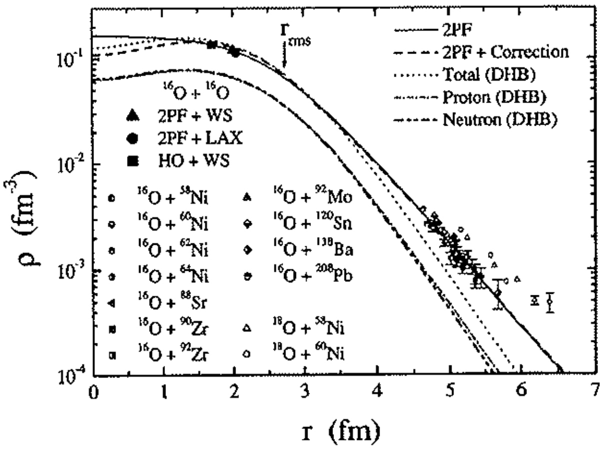

FIG. 2. Experimental nuclear density values for the ^{16}O (semi-closed symbols) and ^{18}O (open symbols) nuclei, as obtained from sub-barrier elastic scattering data analyses for different systems and bombarding energies. The closed symbols represent density values (^{16}O) from intermediate energy data analyses (^{16}O+^{16}O, E_{lab}=1120 MeV), using different models for the shape of the ^{16}O density (2PF or HO) and for the imaginary potential (WS or Lax). The lines correspond to theoretical Dirac-Hartree-Bogoliubov (DHB) calculations for the ^{16}O nucleus, and a two-parameter Fermi distribution (2PF) with or without a damped oscillatory correction.

The ^{16}O experimental density values at the sensitivity radii obtained from heavy-ion data analyses are shown in Fig. 2. For the sub-barrier energies, the elastic scattering data [12–15] are from 40 angular distributions of 11 systems like ^{16}O+A, where A is a magic or semimagic target nucleus with mass number ranging from 58 (Ni) to 208 (Pb). In the data analyses, we have used Hartree-Fock, Dirac-Hartree-

Bogoliubov, and shell-model densities for the target nuclei (see Refs. [12–16]). In this sub-barrier region the position of the sensitivity radius is energy-dependent, with variation connected to the classical turning point of the effective potential. This fact allows us to characterize the ^{16}O nuclear distribution (semiclosed symbols in Fig. 2) in a large and superficial region. The data (from Ref. [17]) analyses at $E_{lab}=1120$ MeV for the ^{16}O+^{16}O system have provided information of the ^{16}O density in a much inner region (closed symbols in Fig. 2). A theoretical prediction for the ^{16}O density derived from the Dirac-Hartree-Bogoliubov (DHB) model [18] using NL3 potential parameters [19] is also shown in Fig. 2. In the surface region, the experimental ^{16}O density is much greater than the theoretical prediction. An analysis of the single-particle levels of the theoretical calculation shows, as one might expect, that the falloff of the density in the surface region is determined by the least bound levels. Although the NL3 parameter set was adjusted to reproduce binding energies and charge and neutron radii across the periodic table, it did not take into account single-particle properties, which suggests a direction for future improvements in such a parameter set.

For the purpose of comparison and demonstration of the sensitivity of the method, we have also shown in Fig. 2 the experimental density values for the ^{18}O nucleus (open symbols) obtained with the same method through optical model analyses of sub-barrier elastic scattering data for the ^{18}O + ^{58,60}Ni systems. As theoretically expected [20] and clearly demonstrated by our results, the two extra neutrons of the ^{18}O ($2s_{1/2}$, $1d_{3/2}$, and $1d_{5/2}$ orbitals) increase the ^{18}O density at the surface region in comparison to that for the ^{16}O nucleus.

In our method, the experimental density values have been extracted based on very fundamental grounds. The parameter-free real part of the interaction contains as basic inputs just the well-known M3Y effective nucleon-nucleon interaction and the model for the Pauli nonlocality, which has been tested extensively [2–5]. Also the imaginary part of the interaction has been based on general assumptions: the lack of superficial absorption at sub-barrier energies and the parameter-free Lax-type interaction (for the ^{16}O+^{16}O system at $E_{lab}=1120$ MeV), which is known to be appropriate for high energies [11]. The adjustable parameters of the method (R_0 and a) are connected only with the quantity to be determined: the projectile nuclear density, and the results obtained are rather insensitive to the (realistic) shape assumed for the distribution. We mention that other experimental data for the ^{16}O density in the region $2 \leq r \leq 4.5$ fm could be found through the analyses of other angular distributions in energies above the barrier, but in this case the imaginary potential must have adjustable parameters and the reliability of the results for the density should be studied very carefully [21]. Thus, we consider the theoretical densities for the target nuclei (in the sub-barrier data analysis) as the only assumption of our method that needs to be checked. The good agreement among the results for the ^{16}O density obtained using different target nuclei indicate that any possible deviation in such theoretical calculations would be systematic.

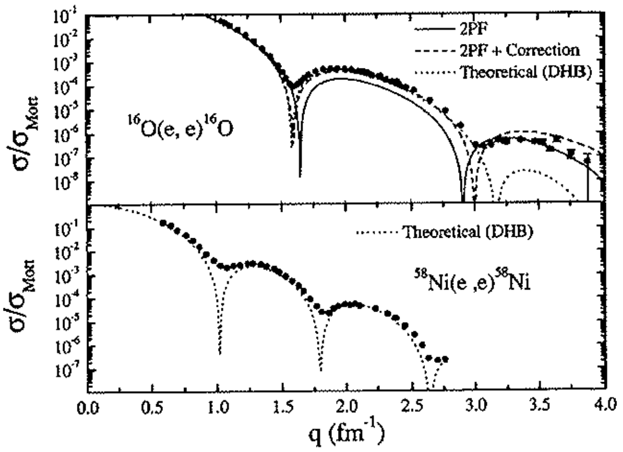

FIG. 3. Experimental electron scattering cross sections for the (top) ^{16}O and (bottom) ^{58}Ni nuclei as a function of the momentum transferred. The dotted lines in the figure are theoretical predictions using charge distributions from Dirac-Hartree-Bogoliubov (DHB) calculations in the plane-wave Born approximation. The other lines (top) are the results for charge distributions derived from experimental nuclear matter densities, using 2PF shapes (as shown in Fig. 2) with (dashed line) or without (solid line) a damped oscillatory correction.

Thus, as a test of the consistency of the assumed hypothesis of the method, we compare in Fig. 3 the data (from Refs. [22,23]) with predictions for electron scattering cross sections. We have used charge distributions obtained by folding the proton density of the nucleus with the intrinsic charge distribution of the proton. For the doubly-magic ^{16}O nucleus, the proton density is quite close to one-half of the total density (see the theoretical neutron and proton distributions in Fig. 2). The electron scattering cross sections have been calculated in the plane-wave Born approximation, which, for light nuclei such as ^{16}O, should produce cross sections close to the exact phase-shift method, except for momentum transferred near a minimum of diffraction.

Considering a best fit 2PF distribution ($R_0=2.49$ fm and $a=0.55$ fm — solid line in Fig. 2) to describe the ^{16}O density, a reasonable description of the electron scattering (solid line in Fig. 3 top) is obtained, with some discrepancies in the momentum transferred region $1.5 \leq q \leq 3.0$ fm^{-1}. Based on the theoretical calculations for the ^{16}O density (see Fig. 2), such discrepancies are understood considering the decreasing contribution of the $1p_{3/2}$ and $1p_{1/2}$ components for the nuclear density in the inner radius region. We have taken this into account by adding a damped oscillatory function to the 2PF distribution (2PF+correction in Fig. 2), resulting in a better overall description of the electron cross section (dashed line in Fig. 3 top). As reported earlier [22], a similar procedure has been adopted to improve ^{16}O electron scattering data fits that have been obtained by using fenomenological charge densities. These fits [22] have precision comparable to those of the present work. We point out that the disagreement between predicted and measured cross sections near the minima of diffraction ($q \approx 1.5$ fm^{-1} and $q \approx 3$ fm^{-1}) is due to the use of the Born approximation in the cross section calculations. Thus, for the first time, it is possible to describe electron scattering cross sections from an experimental ^{16}O nuclear density obtained through heavy-ion elastic scattering data analyses. The theoretical Dirac-Hartree-Bogoliubov (DHB) charge distribution predicts electron scattering cross sections which are in disagreement with the data for large q values (see Fig. 3 top). We point out that, as a further test of the consistency of the assumed hypothesis of the method, the theoretical DHB distributions for the target nuclei used in this work predict electron scattering cross sections in agreement with the data (as illustrated in Fig. 3 bottom for the ^{58}Ni).

In conclusion, using the progress reached in the last 20 years to describe heavy-ion elastic scattering, it is possible to determine ground-state nuclear matter densities. The method presented in this work should be of value in studying densities of exotic nuclei, particularly at the surface region through sub-barrier heavy-ion elastic scattering. We point out that the difference between densities of exotic and neighboring stable nuclei is much emphasized in the surface region. This seems to be borne out by preliminary results [24] for the ^{6}He nucleus in comparison to ^{4}He.

This work was partially supported by Financiadora de Estudos e Projetos (FINEP), Fundação de Amparo à Pesquisa do Estado de São Paulo (FAPESP), Fundação de Amparo à Pesquisa do Estado do Rio de Janeiro (FAPERJ), and Conselho Nacional de Desenvolvimento Científico e Tecnológico (CNPq).

[1] C.J. Batty, E. Friedman, H.J. Gils, and H. Hebel, Adv. Nucl. Phys. **19**, 1 (1989).
[2] M.A.C. Ribeiro, L.C. Chamon, D. Pereira, M.S. Hussein, and D. Galetti, Phys. Rev. Lett. **78**, 3270 (1997).
[3] L.C. Chamon, D. Pereira, M.S. Hussein, M.A.C. Ribeiro, and D. Galetti, Phys. Rev. Lett. **79**, 5218 (1997).
[4] L.C. Chamon, D. Pereira, and M.S. Hussein, Phys. Rev. C **58**, 576 (1998).
[5] D. Galetti, S.S. Mizrahi, L.C. Chamon, D. Pereira, M.S. Hussein, and M.A.C. Ribeiro, Phys. Rev. C **58**, 1627 (1998).
[6] M.E. Brandan and G.R. Satchler, Phys. Rep. **285**, 143 (1997).
[7] G.R. Satchler and W.G. Love, Phys. Rep. **55**, 183 (1979).
[8] D.T. Khoa, Nucl. Phys. **A484**, 376 (1988).
[9] D.T. Khoa, W. von Oertzen, and A.A. Ogloblin, Nucl. Phys. **A602**, 98 (1996).
[10] D.T. Khoa, G.R. Satchler, and W. von Oertzen, Phys. Rev. C **56**, 954 (1997).
[11] See, e.g., M.S. Hussein, R.A. Rego, and C.A. Bertulani, Phys. Rep. **201**, 279 (1991).
[12] M.A.G. Alvarez, L.C. Chamon, D. Pereira, E.S. Rossi, Jr., C.P. Silva, L.R. Gasques, H. Dias, and M.O. Roos, Nucl. Phys. **A656**, 187 (1999).
[13] L.C. Chamon, D. Pereira, E.S. Rossi, Jr., C.P. Silva, R. Lichtenthaler Filho, and L.C. Gomes, Nucl. Phys. **A582**, 305 (1995).
[14] L.C. Chamon, D. Pereira, E.S. Rossi, Jr., C.P. Silva, H. Dias, L. Losano, and C.A.P. Ceneviva, Nucl. Phys. **A597**, 253 (1996).
[15] C.P. Silva, M.A.G. Alvarez, L.C. Chamon, D. Pereira, M.N. Rao, E.S. Rossi, Jr., L.R. Gasques, M.A.E. Santo, R.M. Anjos, J. Lubian, P.R.S. Gomes, C. Muri, B.V. Carlson, S. Kailas, A. Chatterjee, P. Singh, A. Shrivastava, K. Mahata, and S. Santra, Nucl. Phys. **A679**, 287 (2001).
[16] J.W. Negele, Phys. Rev. C **4**, 1260 (1970).
[17] F. Nuoffer, G. Bartnitzky, H. Clement, A. Blazevic, H.G. Bohlen, B. Gebauer, W. von Oertzen, M. Wilpert, T. Wilpert, A. Lepine-Szily, W. Mittig, A.N. Ostrowski, and P. Roussel-Chomaz, Nuovo Cimento A **111**, 971 (1998).
[18] B.V. Carlson and D. Hirata, Phys. Rev. C **62**, 054310 (2000).
[19] G.A. Lalazissis, J. Konig, and P. Ring, Phys. Rev. C **55**, 540 (1997).
[20] H. Miyake and A. Mizukami, Phys. Rev. C **41**, 329 (1990).
[21] M. A. G. Alvarez *et al.* (work in progress).
[22] I. Sick and J.S. McCarthy, Nucl. Phys. **A150**, 631 (1970).
[23] J.R. Ficenec, W.P. Trower, J. Heisenberg, and I. Sick, Phys. Lett. **32B**, 460 (1970).
[24] L. R. Gasques *et al.* (work in progress).

PHYSICAL REVIEW C **66**, 014610 (2002)

Toward a global description of the nucleus-nucleus interaction

L. C. Chamon,[1] B. V. Carlson,[2] L. R. Gasques,[1] D. Pereira,[1] C. De Conti,[2] M. A. G. Alvarez,[1] M. S. Hussein,[1]
M. A. Cândido Ribeiro,[3] E. S. Rossi, Jr.,[1] and C. P. Silva[1]
[1]*Departamento de Física Nuclear, Instituto de Física da Universidade de São Paulo,*
Caixa Postal 66318, 05315-970 São Paulo, SP, Brazil
[2]*Departamento de Física, Instituto Tecnológico de Aeronáutica, Centro Técnico Aeroespacial, São José dos Campos, SP, Brazil*
[3]*Departamento de Física, Instituto de Biociências, Letras e Ciências Exatas, Universidade Estadual Paulista,*
São José do Rio Preto, SP, Brazil

(Received 10 September 2001; published 17 July 2002)

Extensive systematizations of theoretical and experimental nuclear densities and of optical potential strengths extracted from heavy-ion elastic scattering data analyses at low and intermediate energies are presented. The energy dependence of the nuclear potential is accounted for within a model based on the nonlocal nature of the interaction. The systematics indicates that the heavy-ion nuclear potential can be described in a simple global way through a double-folding shape, which basically depends only on the density of nucleons of the partners in the collision. The possibility of extracting information about the nucleon-nucleon interaction from the heavy-ion potential is investigated.

DOI: 10.1103/PhysRevC.66.014610 PACS number(s): 24.10.Ht, 13.75.Cs, 21.10.Ft, 21.10.Gv

I. INTRODUCTION

The optical potential plays a central role in the description of heavy-ion collisions, since it is widely used in studies of the elastic scattering process as well as in more complicated reactions through the distorted-wave Born approximation (DWBA) or coupled-channel formalisms. This complex and energy-dependent potential is composed of the bare and polarization potentials, the latter containing the contribution arising from nonelastic couplings. In principle, the bare (or nuclear) potential between two heavy ions can be associated with the fundamental nucleon-nucleon interaction folded into a product of the nucleon densities of the nuclei [1]. Apart from some structure effects, the shape of the nuclear density along the table of stable nuclides is nearly a Fermi distribution, with diffuseness approximately constant and radius given roughly by $R=r_0A^{1/3}$, where A is the number of nucleons of the nucleus. Therefore, one could expect a simple dependence of the heavy-ion nuclear potential on the number of nucleons of the partners in the collision. In fact, analytical formulas have been deduced [2–4] for the folding potential, and simple expressions have been obtained at the surface region. A universal (system-independent) shape for the heavy-ion nuclear potential has been derived [5] also in the framework of the liquid-drop model, from the proximity theorem which relates the force between two nuclei to the interaction between flat surfaces made of semi-infinite nuclear matter. The theorem leads [5] to an expression for the potential in the form of a product of a geometrical factor by a function of the separation between the surfaces of the nuclei.

The elastic scattering is the simplest process that occurs in a heavy-ion collision because it involves very little rearrangement of matter and energy. Therefore, this process has been studied in a large number of experimental investigations, and a huge body of elastic cross section data is currently available. The angular distribution for elastic scattering provides unambiguous determination of the real part of the optical potential only in a region around a particular distance [6] hereafter referred as the sensitivity radius (R_S). At energies close to the Coulomb barrier the sensitivity radius is situated in the surface region. In this energy region, the systematization [7,8] of experimental results for potential strengths at the sensitivity radii has provided a universal exponential shape for the heavy-ion nuclear potential at the surface, as theoretically expected, but with a diffuseness value smaller than that originally proposed in the proximity potential.

In a recent review article [6] the phenomenon of rainbow scattering was discussed, and it was emphasized that the real part of the optical potential can be unambiguously extracted also at very short distances from heavy-ion elastic scattering data at intermediate energies. Such a kind of data has been first obtained for α-particle scattering from a variety of nuclei over a large range of energies [9–11] and later for several heavy-ion systems. However, differently from the case for the surface region (low energy), a systematization of potential strengths at the inner distances has not been performed up to now, probably because the resulting phenomenological interactions have presented significant dependence on the bombarding energies. Several theoretical models have been developed to account for this energy dependence through realistic mean field potentials. Most of them are improvements of the original double-folding potential with the nucleon-nucleon interaction assumed to be energy and density dependent [6]. Another recent and successful model [12–14] associates the energy dependence of the heavy-ion bare potential with nonlocal quantum effects related to the exchange of nucleons between target and projectile, resulting in a very simple expression for the energy dependence of the nuclear potential. Using the model of Refs. [12–14], in the present work we have realized a systematization of potential strengths extracted from elastic scattering data analyses, considering both low (near-barrier) and intermediate energies. The systematics indicates that the heavy-ion nuclear potential can be described in a simple global way

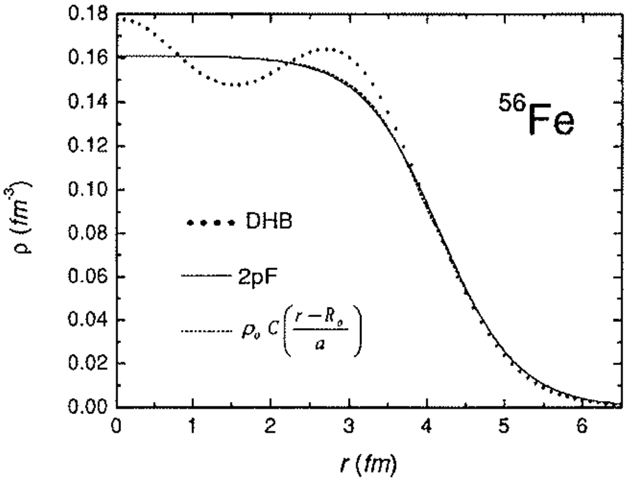

FIG. 1. Nucleon density for the ^{56}Fe nucleus represented through Dirac-Hartree-Bogoliubov calculations (DHB) and a two-parameter Fermi distribution (2pF), with $a=0.5$ fm and $R_0=4.17$ fm. The small difference between the 2pF distribution and the function $\rho_0 C((r-R_0)/a)$ [Eqs. (12), (13), and (14)] is hardly seen in the figure.

through a double-folding shape, which basically depends only on the number of nucleons of the nuclei.

The paper is organized as follows. In Sec. II, as a preparatory step for the systematization of the potential, an extensive and systematic study of nuclear densities is presented. This study is based on charge distributions extracted from electron scattering experiments [15,16] as well as on theoretical densities derived from the Dirac-Hartree-Bogoliubov model [17]. In Sec. III, analytical expressions for the double-folding potential are derived for the whole (surface and inner) interaction region, and a survey of the main characteristics of this potential is presented. Section IV contains the nonlocal model for the heavy-ion bare interaction, including several details that have not been published before. Section V is devoted to the nuclear potential systematics. In Sec. VI, we discuss the role played by the nucleon-nucleon interaction, and we present, in a somewhat speculative way, an alternative form for the effective nucleon-nucleon interaction, which is consistent with our results for the heavy-ion nuclear potential. Finally, Sec. VII contains a brief summary and the main conclusions.

II. SYSTEMATIZATION OF THE NUCLEAR DENSITIES

According to the double-folding model, the heavy-ion nuclear potential depends on the nuclear densities of the nuclei in collision. Thus, a systematization of the potential requires a previous systematization of the nuclear densities. In this work, with the aim of describing the proton, neutron, nucleon (proton+neutron), charge, and matter densities, we adopt the two-parameter Fermi (2pF) distribution, which has also been commonly used for charge densities extracted from electron scattering experiments [15]. The shape, Eq. (1) and Fig. 1, of this distribution is particularly appealing for the density description, due to the flatness of the inner region, which is associated with the saturation of the nuclear medium, and to the rapid falloff (related to the diffuseness parameter a) that brings out the notion of the radius R_0 of the nucleus:

$$\rho(r)=\frac{\rho_0}{1+\exp\left(\frac{r-R_0}{a}\right)}. \tag{1}$$

The ρ_0, a, and R_0 parameters are connected by the normalization condition

$$4\pi\int_0^\infty \rho(r)r^2dr=X, \tag{2}$$

where X could be the number of protons Z, neutrons N, or nucleons $A=N+Z$. In our theoretical calculations, the charge distribution (ρ_{ch}) has been obtained by folding the proton distribution of the nucleus (ρ_p) with the intrinsic charge distribution of the proton in free space (ρ_{chp}):

$$\rho_{ch}(r)=\int \rho_p(\vec{r}\,')\rho_{chp}(\vec{r}-\vec{r}\,')d\vec{r}\,', \tag{3}$$

where ρ_{chp} is an exponential with diffuseness $a_{chp}=0.235$ fm. In an analogous way, we have defined the matter density by folding the nucleon distribution of the nucleus with the intrinsic matter distribution of the nucleon, which is assumed to have the same shape of the intrinsic charge distribution of the proton. For convenience, the charge and matter distributions are normalized to the number of protons and nucleons, respectively.

In order to systematize the heavy-ion nuclear densities, we have calculated theoretical distributions for a large number of nuclei using the Dirac-Hartree-Bogoliubov (DHB) model [17]. The DHB calculations were performed using the NL3 parameter set [18]. This set was obtained by adjusting the masses and the charge and neutron radii of ten nuclei in the region of the valley of stability, ranging from ^{16}O to ^{214}Pb, using the Dirac-Hartree-BCS (DH-BCS) model. For the cases in which they have been performed, calculations using this parameter set and either the DHB [17] or the DH-BCS [18–20] model have shown very good agreement with experimental masses and radii. The quality of the description of nuclear masses and charge radii, calculated in various microscopic approaches, has been presented in a recent paper [21]. In this work, the difference between experimental rms charge radii of stable nuclei with the corresponding theoretical predictions has been found to be around 0.05 fm for all models, including the DH-BCS model with the NL3 parameter set. This precision is quite satisfactory taking into account our purpose of systematizing the optical potential strengths. In the present paper, we have also used the results of previous systematics for charge distributions [15,16], extracted from electron scattering experiments, as a further check of our DHB results. All the theoretical and most of the "experimental" densities are not exact Fermi distributions. Thus, with the aim of studying the equivalent diffuseness of

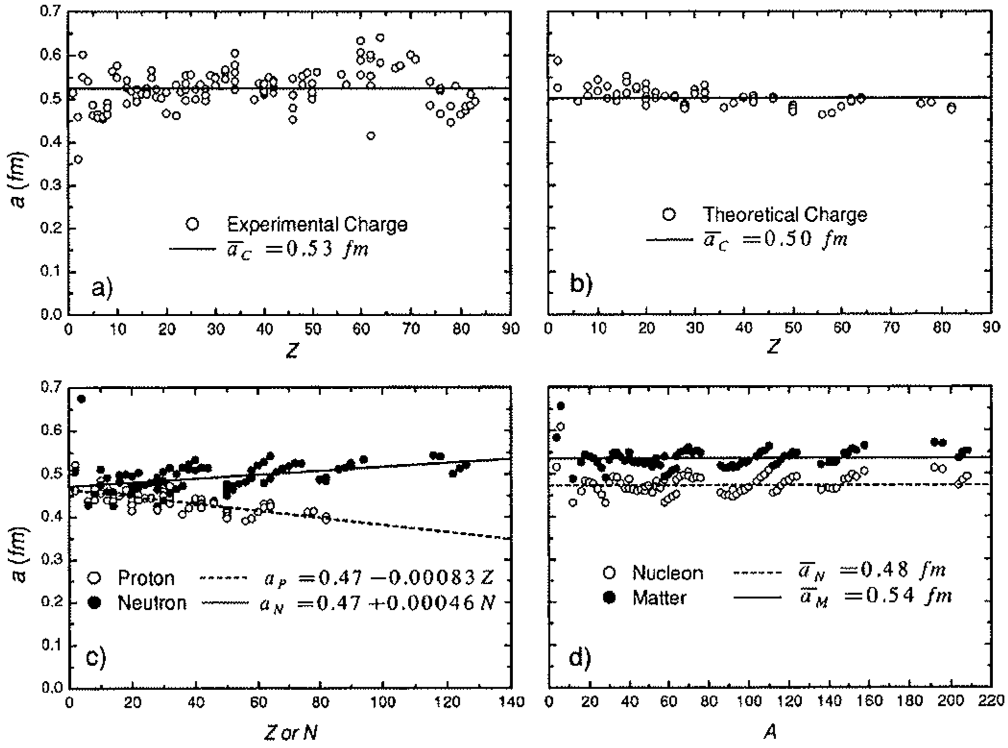

FIG. 2. Equivalent diffuseness values obtained for charge distributions extracted from electron scattering experiments and for theoretical densities obtained from Dirac-Hartree-Bogoliubov calculations.

the densities, we have calculated the corresponding logarithmic derivatives [Eq. (4)] at the surface region (at $r \approx R_0 + 2$ fm):

$$a \approx -\frac{\rho(r)}{\dfrac{d\rho}{dr}}. \tag{4}$$

Figure 2(a) shows the results for the experimental charge distributions: the diffuseness values spread around an average diffuseness $\bar{a}_c = 0.53$ fm, with standard deviation 0.04 fm. Most of this dispersion arises from experimental errors. Indeed, we have verified that different analyses (different electron scattering data set or different models for the charge density) for a given nucleus provide diffuseness values that differ from each other by about 0.03 fm. Therefore, the experimental charge distributions are compatible, within the experimental precision, with a constant diffuseness value. The theoretical charge distributions present similar behavior [Fig. 2(b)], with an average value slightly smaller than the experimental one. In this case, the observed standard deviation, 0.02 fm, is associated with the effects of the structure of the nuclei. Despite the trend presented by the neutron and proton diffuseness [Fig. 2(c)], all the nucleon distributions result in very similar diffuseness values ($\bar{a}_N = 0.48$ fm), with standard deviation 0.025 fm. As a result of the folding procedure, the matter distributions present diffuseness values significantly greater ($\bar{a}_M = 0.54$ fm) than those for the nucleon distributions. Taking into account that the theoretical calculations have slightly underestimated the experimental charge diffuseness, we consider that more realistic average values for the nucleon and matter density diffuseness are 0.50 and 0.56 fm, respectively. A dispersion (σ_a) of about 0.025 fm around these average values is expected due to effects of the structure of the nuclei.

The rms radius of a distribution is defined by Eq. (5):

$$r_{rms} = \sqrt{\frac{\int r^2 \rho(r) d\vec{r}}{\int \rho(r) d\vec{r}}}. \tag{5}$$

We have determined the radii R_0 for the 2pF distributions assuming that the corresponding rms radii should be equal to those of the experimental (electron scattering) and theoretical (DHB) densities. The results for R_0 from theoretical charge distributions [Fig. 3(b)] are very similar to those from electron experiments [Fig. 3(a)]. This fact indicates that the radii obtained through the theoretical DHB calculations are quite realistic. The nucleon and matter densities give very similar radii [Fig. 3(d)], which are well described by the following linear fit:

$$R_0 = 1.31 A^{1/3} - 0.84 \text{ fm}. \tag{6}$$

As a result of effects of the structure of the nuclei, the R_0 values spread around this linear fit with dispersion $\sigma_{R_0} = 0.07$ fm, but the heavier the nucleus is, the smaller is the deviation. In Fig. 4 are shown the theoretical (DHB) nucleon

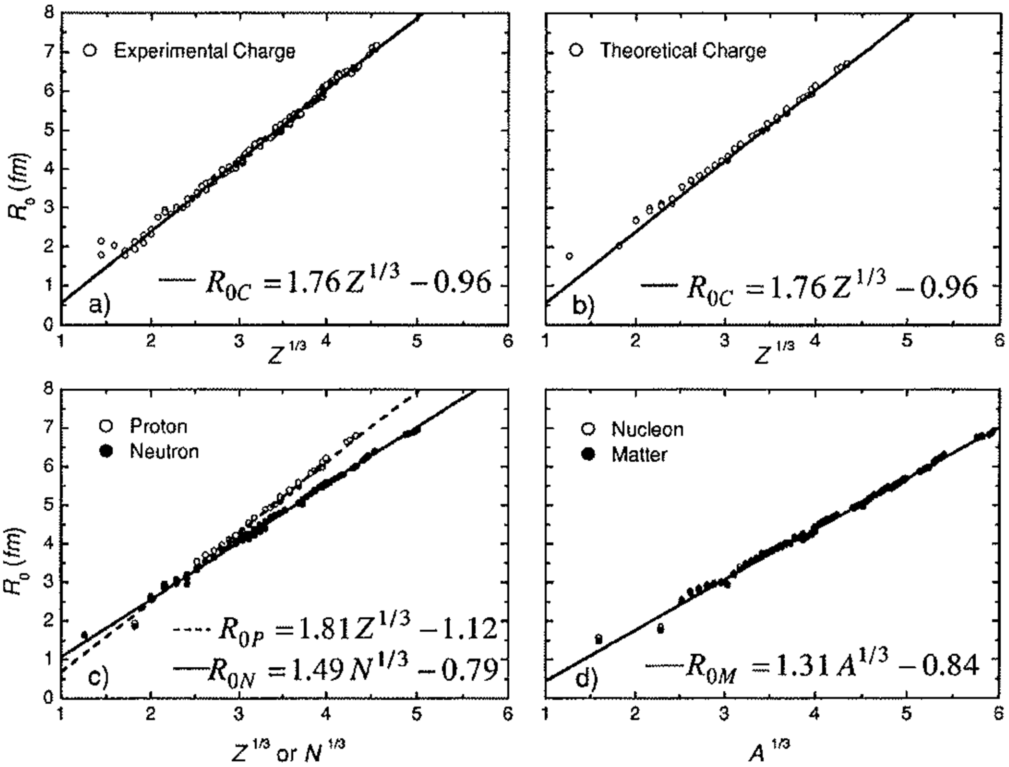

FIG. 3. The R_0 parameter obtained for charge distributions extracted from electron scattering experiments and for theoretical densities obtained from Dirac-Hartree-Bogoliubov calculations.

densities for a few nuclei and the corresponding 2pF distributions with $a = 0.50$ fm and R_0 values obtained from Eq. (6).

III. ESSENTIAL FEATURES OF THE FOLDING POTENTIAL

The double-folding potential has the form

$$V_F(R) = \int \rho_1(r_1)\rho_2(r_2)v_{NN}(\vec{R} - \vec{r}_1 + \vec{r}_2)d\vec{r}_1 d\vec{r}_2, \quad (7)$$

where R is the distance between the centers of the nuclei, ρ_i are the respective nucleon distributions, and $v_{NN}(\vec{r})$ is the effective nucleon-nucleon interaction. The success of the folding model can only be judged meaningfully if the effective nucleon-nucleon interaction employed is truly realistic. The most widely used realistic interaction is known as M3Y [1,6], which can usually assume two versions: Reid and Paris.

For the purpose of illustrating the effects of density variations on the folding potential, we show in Fig. 5 the results

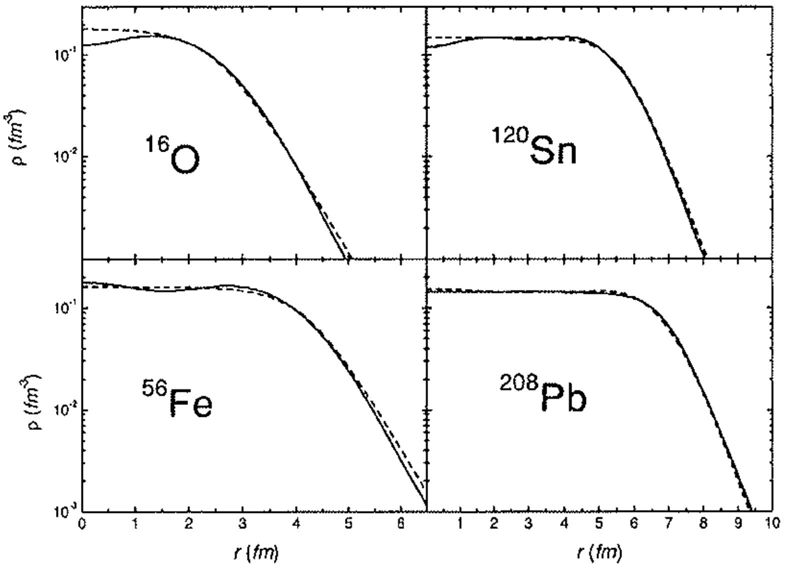

FIG. 4. Nucleon densities from Dirac-Hartree-Bogoliubov calculations (solid lines) compared with the corresponding two-parameter Fermi distributions (dashed lines), with $a = 0.50$ fm and R_0 obtained through Eq. (6).

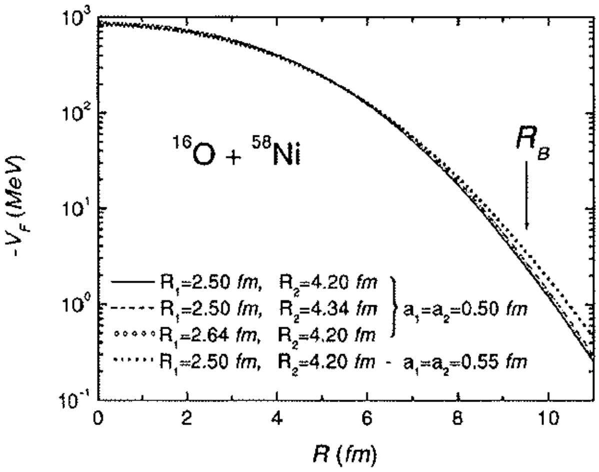

FIG. 5. Folding potential for different sets of 2pF densities that may represent the $^{16}\mathrm{O}+^{58}\mathrm{Ni}$ system. The approximate position of the s-wave barrier radius (R_B) is indicated in the figure.

obtained for different sets of 2pF distributions. In Sec. II, we have estimated the dispersions of the R_0 and a parameters, $\sigma_{R_0}\approx 0.07$ fm and $\sigma_a \approx 0.025$ fm, that arise from effects of the structure of the nuclei. Observe that these standard deviations are one-half of the corresponding variations considered in the example of Fig. 5, $\Delta R_0 = 0.14$ fm and $\Delta a = 0.05$ fm. The surface region of the potential ($R \geqslant R_1 + R_2$) is much more sensitive to small changes of the density parameters than the inner region. Our calculations indicate that, as a result of such structure effects, the strength of the nuclear potential in the region near the barrier radius may vary by about 20%, and the major part of this variation is connected to the standard deviation of the parameter a. Therefore, concerning the nuclear potential, the effects of the structure of the nuclei are mostly present at the surface and mainly related to the diffuseness parameter.

The six-dimensional integral [Eq. (7)] can easily be solved by reducing it to a product of three one-dimensional Fourier transforms [1], but the results may only be obtained through numerical calculations. In order to provide analytical expressions for the folding potential, we consider, as an approximation, that the range of the effective nucleon-nucleon interaction is negligible in comparison with the diffuseness of the nuclear densities. In this zero-range approach, the double-folding potential can be obtained from

$$v_{NN}(\vec{r}) \approx V_0 \delta(\vec{r}) \Rightarrow V_F(R) = \frac{2\pi V_0}{R} \int_0^\infty r_1 \rho_1(r_1) \left[\int_{|R-r_1|}^{R+r_1} r_2 \rho_2(r_2) dr_2 \right] dr_1 . \tag{8}$$

As discussed in Sec. II, the heavy-ion densities involved in Eq. (8) are approximately 2pF distributions, with $R_0 \gg a$. In the limit $a \to 0$, the double integral results in

$$V_F(R \leqslant R_2 - R_1) = V_0 \rho_{01} \rho_{02} \frac{4}{3} \pi R_1^3 , \tag{9}$$

$$V_F(R_2 - R_1 \leqslant R \leqslant R_1 + R_2) = V_0 \rho_{01} \rho_{02} \frac{4}{3} \pi \mathcal{R}^3 \left(\frac{\tau^2}{1+\zeta\tau} \right) \left[\frac{3}{8} + \frac{\tau}{4} + \zeta \frac{\tau^2}{16} \right], \tag{10}$$

$$V_F(R \geqslant R_1 + R_2) = 0, \tag{11}$$

where $s = R - (R_1 + R_2)$, $\mathcal{R} = 2R_1R_2/(R_1+R_2)$, $\zeta = \mathcal{R}/(R_1 + R_2)$, $\tau = s/\mathcal{R}$, and R_1 and R_2 are the radii of the nuclei (hereafter we consider $R_2 \geqslant R_1$). We need a further approximation to obtain analytical expressions for the folding potential in the case of finite diffuseness value.

The Fermi distribution may be represented, with precision better than 3% for any r value (see Fig. 1), by

$$\frac{\rho_0}{1 + \exp\left(\frac{r - R_0}{a} \right)} \approx \rho_0 C\left(\frac{r - R_0}{a} \right), \tag{12}$$

$$C(x \leqslant 0) = 1 - \frac{7}{8} e^{x} + \frac{3}{8} e^{2x}, \tag{13}$$

$$C(x \geqslant 0) = e^{-x} \left(1 - \frac{7}{8} e^{-x} + \frac{3}{8} e^{-2x} \right). \tag{14}$$

This approximation is particularly useful in obtaining analytical expressions for integrals that involve the 2pF distribution. If both nuclei have the same diffuseness a, the double integral [Eq. (8)] can be solved analytically using the approximation represented by Eq. (12), and the result expressed as a sum of a large number of terms, most of them negligible for $a \ll R_0$. Rather simple expressions can be found after an elaborate algebraic manipulation:

$$V_F(R \leqslant R_2 - R_1 + a) \approx V_0 \rho_{01} \rho_{02} \frac{4}{3} \pi R_1^3 \left\{ 1 + 9.7 \left(\frac{a}{R_1} \right)^2 - \left[0.875 \left(\frac{R_2^3}{R_1^3} - 1 \right) + \frac{a}{R_1} \left(2.4 + \frac{R_2^2}{R_1^2} \right) \right] e^{-(R_2 - R_1)/a} \right\}, \tag{15}$$

$$V_F(R_2 - R_1 + a \leqslant R \leqslant R_1 + R_2) \approx V_0 \rho_{01} \rho_{02} \frac{4}{3} \pi \mathcal{R}^3 \left(\frac{1}{1+\zeta\tau} \right) \left\{ \tau^2 \left[\frac{3}{8} + \frac{\tau}{4} + \zeta \frac{\tau^2}{16} \right] + 2.4 \eta^2 \left[1 - \frac{5}{8}\eta - \zeta\tau^2 + \left(\frac{5}{4}\eta - \frac{1}{2} \right) e^{\varepsilon} + \left(1 + \frac{5}{8}\eta \right) e^{-(\varepsilon + 2R_1/a)} \right] \right\}, \tag{16}$$

$$V_F(R \geqslant R_1 + R_2) \approx V_0 \rho_{01} \rho_{02} \pi a^2 \mathcal{R} g(\tau) f(s/a), \tag{17}$$

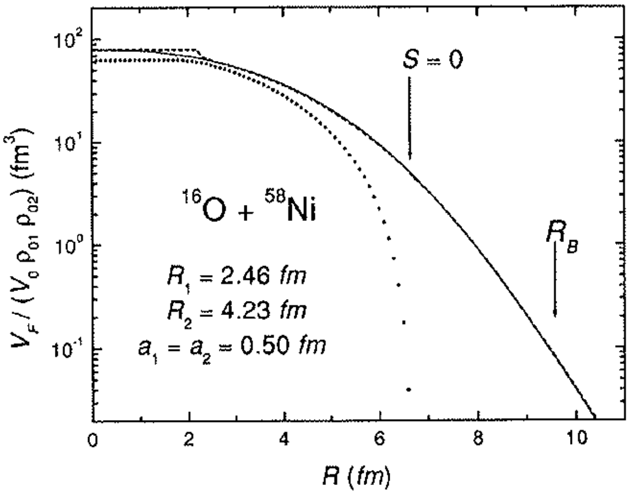

FIG. 6. Folding potential in the zero-range approach calculated from numerical integration of Eq. (8) (solid line), for 2pF densities that may represent the $^{16}O+^{58}Ni$ system. The dashed line represents the approximate analytical expressions, Eqs. (15), (16), and (17), while the dotted line concerns the exact result for $a=0$, Eqs. (9), (10), and (11). The approximate positions of the s-wave barrier radius (R_B) and of the distance $R=R_1+R_2$ ($s=0$) are indicated in the figure.

with $\eta=a/\mathcal{R}$, $\varepsilon=s/a$. The functions g and f are given by

$$g(\tau)=\frac{1+\tau+\tau^2\zeta/3+\eta+(\eta+1/2)e^{-\varepsilon}}{1+\zeta\tau}, \tag{18}$$

$$f(s/a)=(1+s/a)e^{-s/a}. \tag{19}$$

If the nuclei have slightly (about 10%) different diffuseness, the formulas are still valid with $a\approx(a_1+a_2)/2$. As an example of the precision of the analytical expressions above, we exhibit in Fig. 6 the results of numerical calculations [Eq. (8)] and compare them with those from Eqs. (15), (16), and (17) and also with the exact expressions for $a=0$, Eqs. (9), (10), and (11).

Equation (17) presents some similarity with the proximity potential [5]:

$$V_P=2\pi\Gamma\mathcal{R}d\Phi(s/d), \tag{20}$$

where d is the "surface width" and Φ is an universal (system-independent) function. For a 2pF distribution, the surface width is related to the diffuseness parameter through $d\approx(\pi/\sqrt{3})a$ [22]. The theoretical value adopted for d is 1 fm [5], which corresponds to a diffuseness $a\approx0.55$ fm. Taking into account that the Γ value is rather system independent [5], systematizations of heavy-ion potential strengths extracted from elastic scattering data analyses have been performed by using the following expression, which should be valid for surface distances:

$$\frac{V_P(s\geqslant0)}{\mathcal{R}}=V_0e^{-s/a}. \tag{21}$$

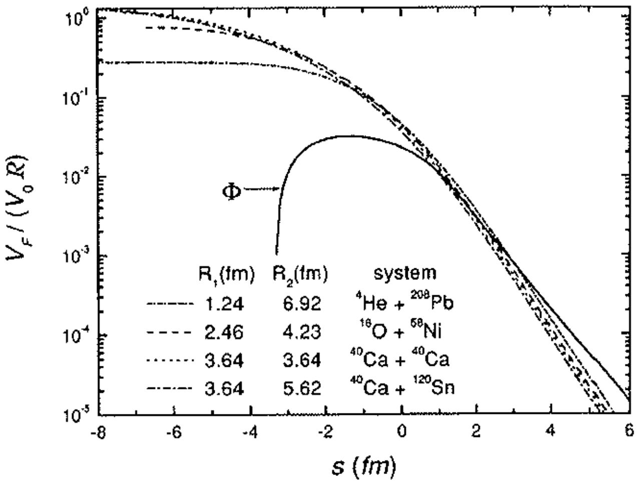

FIG. 7. Normalized folding potential $V_F/(V_0\mathcal{R})$ in the zero-range approach [Eq. (8)] as a function of the distance $s=R-(R_1+R_2)$, for several sets of 2pF distributions (with $a=0.50$ fm) that may represent the systems indicated in the figure. The proximity universal function Φ is also presented in arbitrary units.

The resulting experimental α values are quite similar, $\alpha\approx0.62$ fm [7,8], but smaller than the theoretical prediction of the proximity potential, $\alpha\approx0.75$ fm [5]. Such systematics have included only experimental potential strengths in the surface region, in contrast to the case of the proximity potential where $V/\mathcal{R}$ should be a universal function of s also for inner distances. The proximity potential does not fully agree with our results for the double-folding potential in the zero-range approach (see Fig. 7). In fact, Eq. (17) indicates that a better choice for a universal quantity at the surface region would be

$$V_{red}(s\geqslant0)=\frac{V_F}{\rho_{01}\rho_{02}\pi a^2\mathcal{R}g(\tau)}, \tag{22}$$

which results [from Eqs. (17), (19), and (22)] in the system-independent expression

$$V_{red}(s\geqslant0)\approx V_0(1+s/a)e^{-s/a}. \tag{23}$$

However, it is not clear that one can find a simple form for such a universal quantity at inner distances from Eqs. (15) and (16). In Sec. V, the reduced potential V_{red} is useful for addressing the potential strength systematization. Thus we define V_{red} for $s\leqslant0$ through the following trivial form:

$$V_{red}(s\leqslant0)=V_0. \tag{24}$$

The end of this section is devoted to the study of the effect on the folding potential of a finite range for the effective nucleon-nucleon interaction. The tridimensional delta function $V_0\delta(\vec{r})$ can be represented through the limit $\sigma\rightarrow0$ applied to the finite-range Yukawa function

$$Y_\sigma(r)=V_0\frac{e^{-r/\sigma}}{4\pi r\sigma^2}. \tag{25}$$

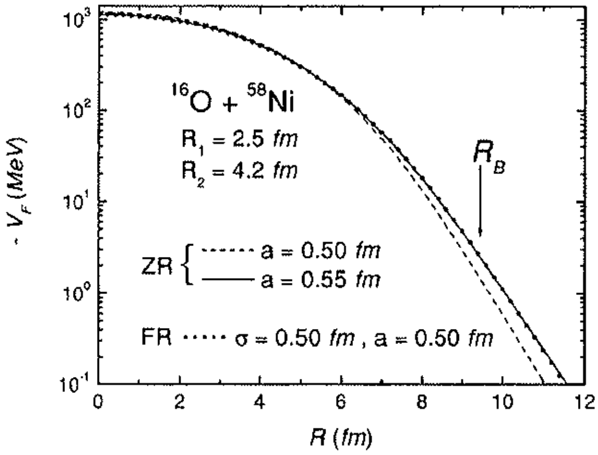

FIG. 8. Double-folding potentials for 2pF distributions with different diffuseness values (a) that may represent the ^{16}O+^{58}Ni system. The potentials have been calculated in the zero-range approach (ZR) or with a finite-range (FR) Yukawa function for the effective nucleon-nucleon interaction.

Figure 8 shows a comparison of folding potentials in the zero-range approach [Eq. (8)] with the result obtained [from Eq. (7)] using an Yukawa function for the effective nucleon-nucleon interaction. The finite range is not truly significant at small distances and can be accurately simulated at the surface, within the zero-range approach, just by slightly increasing the diffuseness of the nuclear densities.

IV. NONLOCAL DESCRIPTION OF THE NUCLEUS-NUCLEUS INTERACTION

Before proceeding with the systematization of the potential, we first set the stage for the model of the heavy-ion nuclear interaction [12–14]. When dealing with nonlocal interactions, one is required to solve the following integro-differential equation:

$$-\frac{\hbar^2}{2\mu}\nabla^2\Psi(\vec{R})+[V_C(R)+V_{pol}(R,E)+\imath W_{pol}(R,E)]\Psi(\vec{R}) + \int U(\vec{R},\vec{R}')\Psi(\vec{R}')d\vec{R}'=E\Psi(\vec{R}). \tag{26}$$

V_C is the Coulomb interaction assumed to be local. V_{pol} and W_{pol} are the real and imaginary parts of the polarization potential, and contain the contribution arising from nonelastic channel couplings. The corresponding nonlocality, called the Feshbach nonlocality, is implicit through the energy dependence of these terms, consistent with the dispersion relation [23]. $U(\vec{R},\vec{R}')$ is the bare interaction, and the nonlocality here, the Pauli nonlocality, is solely due to the Pauli exclusion principle and involves the exchange of nucleons between target and projectile.

Guided by the microscopic treatment of the nucleon-nucleus scattering [24–28], the following ansatz is assumed for the heavy-ion bare interaction [13]:

$$U(\vec{R},\vec{R}')=V_{NL}\left(\frac{R+R'}{2}\right)\frac{1}{\pi^{3/2}b^3}e^{-(|\vec{R}+\vec{R}'|/b)^2}, \tag{27}$$

where b is the range of the Pauli nonlocality. Introduced in this way, the nonlocality is a correction to the local model, and in the $b\rightarrow 0$ limit, Eq. (26), reduces to the usual Schrödinger differential equation. The range of the nonlocality can be found through $b\approx b_0 m_0/\mu$ [29], where $b_0=0.85$ fm is the nucleon-nucleus nonlocality parameter [24], m_0 is the nucleon mass, and μ is the reduced mass of the nucleus-nucleus system. This type of very mild nonlocality in the nucleon-nucleus and nucleus-nucleus interaction is to be contrasted with the very strong nonlocality found in the pion-nucleus interaction in the Δ region [30]. In such cases, even the concept of an optical potential becomes dubious. In our case, however, we are on very safe ground.

The relation between the nonlocal interaction and the folding potential is obtained from [13]

$$V_{NL}(R)=V_F(R). \tag{28}$$

As a result of the central nature of the interaction, it is convenient to write down the usual expansion in partial waves,

$$\Psi(\vec{R})=\sum \imath^l(2l+1)\frac{u_l(R)}{kR}P_l[\cos(\theta)], \tag{29}$$

$$U(\vec{R},\vec{R}')=\sum \frac{2l+1}{4\pi RR'}V_l(R,R')P_l[\cos(\phi)], \tag{30}$$

$$V_l(R,R')=V_{NL}\left(\frac{R+R'}{2}\right)\frac{1}{b\pi^{1/2}} \times\left\{Q_l\left(\frac{2RR'}{b^2}\right)\exp\left[-\left(\frac{R-R'}{b}\right)^2\right](-)^{l+1}Q_l \times\left(\frac{-2RR'}{b^2}\right)\exp\left[-\left(\frac{R+R'}{b}\right)^2\right]\right\}, \tag{31}$$

where Q_l are polynomials and ϕ is the angle between $\vec{R}$ and $\vec{R}'$ [24]. Thus, the integro-differential equation can be recast into the following form:

$$\frac{\hbar^2}{2\mu}\frac{d^2u_l(R)}{dR^2}+\left[E-V_C(R)-V_{pol}(R,E)-\imath W_{pol}(R,E) -\frac{l(l+1)\hbar^2}{2\mu R^2}\right]u_l(R)=\int_0^\infty V_l(R,R')u_l(R')dR'. \tag{32}$$

When confronting theory and experiment, one usually relies on the optical model with a local potential. This brings into light the issue of extracting from Eq. (32) a local-equivalent (LE) potential

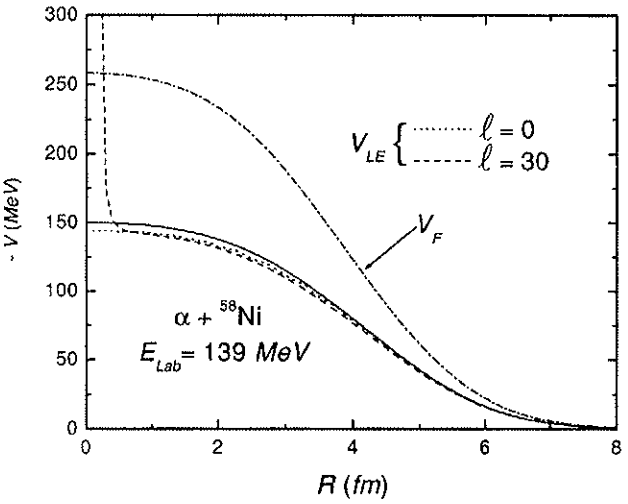

FIG. 9. Double-folding (V_F) and l-dependent local-equivalent (V_{LE}) potentials for the $\alpha+{}^{58}$Ni system at $E_{Lab}=139$ MeV. The solid line represents the approximate expression, Eq. (34), for the local-equivalent potential.

$$V_{LE}(R,E)+iW_{LE}(R,E) = \frac{1}{u_l(R)}\int_0^\infty V_l(R,R')u_l(R')dR'. \qquad (33)$$

The presence of the wave function in Eq. (33) indicates that the LE potential is complex and also l and energy dependent. Despite its complex nature, the LE potential is not absorptive, $\langle\Psi|W_{LE}|\Psi\rangle=0$; this statement can be demonstrated by considering that the nonlocal interaction is real and symmetrical, $V_l(R,R')=V_l(R',R)$. For neutron-nucleus systems, the LE potential is only weakly l dependent, and an approximate relation to describe its energy dependence has been obtained [24]. A generalization of this relation for the ion-ion case is given by [12,13]

$$V_{LE}(R,E)\approx V_F(R)e^{-\gamma[E-V_C(R)-V_{LE}(R,E)]}, \qquad (34)$$

with $\gamma=\mu b^2/2\hbar^2$. In order to provide an example of the precision of expression (34), in Fig. 9 the corresponding result is compared to the exact LE potential [Eq. (33)] obtained from the numerical resolution [13] of the respective integro-differential equations [Eq. (32)]. The local-equivalent potential is quite well described by Eq. (34) for any l value, except at very small distances ($R\approx 0$), which are not probed by heavy-ion experiments.

Expression (34) has accounted for the energy dependence of experimentally extracted potential strengths for several systems in a very large energy range [12–14]. At near-barrier energies $E\approx V_C(R_B)+V_{LE}(R_B)$, the effect of the Pauli nonlocality is negligible and $V_{LE}(R,E)\approx V_F(R)$, but the higher the energy is, the greater is the effect. At energies about 200 MeV/nucleon the local-equivalent potential is about one order of magnitude less intense than the corresponding folding potential (see examples in Refs. [12,13]). In a classical physics framework, the exponent in Eq. (34) is related to the kinetic energy (E_k) and to the local relative speed between the nuclei (v) by

$$v^2=\frac{2}{\mu}E_k(R)=\frac{2}{\mu}[E-V_C(R)-V_{LE}(R,E)], \qquad (35)$$

and Eq. (34) may be rewritten in the following form:

$$V_{LE}(R,E)\approx V_F(R)e^{-[m_0b_0v/(2\hbar)]^2}\approx V_F(R)e^{-4v^2/c^2}, \qquad (36)$$

where c is the speed of light. Therefore, in this context the effect of the Pauli nonlocality is equivalent to a velocity-dependent nuclear interaction [Eq. (36)]. Another possible interpretation is that the local-equivalent potential may be associated directly with the folding potential [Eq. (37)], with an effective nucleon-nucleon interaction [Eq. (38)] dependent on the relative speed (v) between the nucleons:

$$V_{LE}(R,E)=V_F=\int \rho_1(r_1)\rho_2(r_2) \times v_{NN}(v,\vec{R}-\vec{r}_1+\vec{r}_2)d\vec{r}_1d\vec{r}_2, \qquad (37)$$

$$v_{NN}(v,\vec{r})=v_f(\vec{r})e^{-4v^2/c^2}. \qquad (38)$$

V. SYSTEMATIZATION OF THE NUCLEAR POTENTIAL

As already mentioned, the angular distribution for elastic scattering provides an unambiguous determination of the real part of the optical potential in a region around the sensitivity radius (R_S). For bombarding energies above (and near) the barrier, the sensitivity radius is rather energy independent and close to the barrier radius (R_B), while at intermediate energies many inner distances are probed. At subbarrier energies, the R_S is strongly energy dependent, with its variation connected to the classical turning point; this fact has allowed the determination of the potential in a wide range of near-barrier distances, $R_B\leq R_S\leq R_B+2$ fm. With the aim of avoiding ambiguities in the potential systematization, we have selected "experimental" (extracted from elastic scattering data analyses) potential strengths at the corresponding sensitivity radii, from works in which the R_S has been determined or at least estimated. In several articles, the authors claim that their data analyses at intermediate energies have unambiguously determined the nuclear potential in a quite extensive region of interaction distances. In such cases, we have considered potential strength "data" in steps of 1 fm over the whole probed region. Tables I and II provide the systems included in the nuclear potential systematics for the subbarrier and intermediate energies, respectively. For the energy region above (and near) the barrier, the present systematics contains potential strengths for a large number of different heavy-ion systems from the previous Christensen-Winther systematization [7]. Our systematics is not even near to being complete, but it is rather extensive and diversified enough to account well for the very large number of data that have been obtained in the last decades.

The experimental potential strengths represent the real

TABLE I. Systems, sub-barrier bombarding energies, and corresponding references that have been included in the nuclear potential systematics.

System	E_{Lab} (MeV)	Reference
$^{16}O+^{58}Ni$	35, 35.5, 36, 36.5, 37, 38	[8,32]
$^{16}O+^{60}Ni$	35, 35.5, 36, 37, 38	[31,32]
$^{16}O+^{62,64}Ni$	34, 35, 36	[32]
$^{16}O+^{88}Sr$	43, 44, 45	[33]
$^{16}O+^{90}Zr$	46, 47, 48	[33]
$^{16}O+^{92}Zr$	45, 46, 47, 48	[8,33]
$^{16}O+^{92}Mo$	48, 48.5, 49	[33]
$^{16}O+^{120}Sn$	53, 54, 55	[8]
$^{16}O+^{138}Ba$	54, 55, 56, 57	[8]
$^{16}O+^{208}Pb$	74, 75, 76, 77, 78	[8]
$^{18}O+^{58}Ni$	35.1, 35.5, 37.1, 38	[34]
$^{18}O+^{60}Ni$	34.5, 35.5, 37.1, 38	[34]

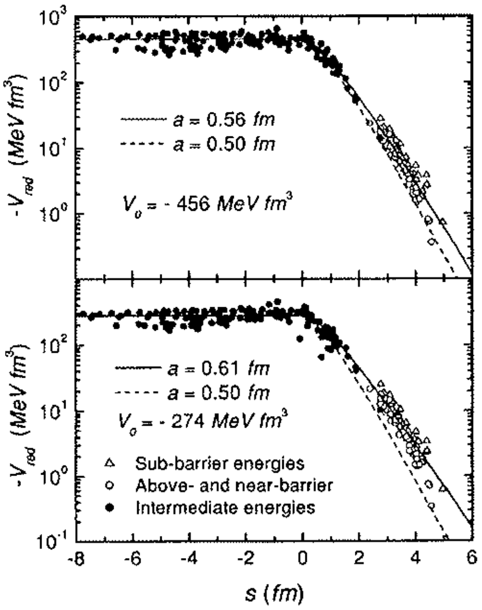

FIG. 10. Experimental and theoretical reduced potentials in the context of the zero-range approach, with (top) or without (bottom) considering in the calculations the energy dependence of the local-equivalent potential [Eq. (34)] that arises from the Pauli nonlocality.

part of the optical potential, which corresponds to the addition of the bare and polarization potentials. The contribution of the polarization to the optical potential depends on the particular features of the reaction channels involved in the collision and is therefore quite system dependent. If this contribution were very significant, it would be too difficult for one to set a global description of the heavy-ion nuclear interaction. In the present work, we neglect the real part of the polarization potential and associate the experimental potential strengths (V_{expt}) with the bare interaction (V_{LE}). The success of our findings seems to support such a hypothesis.

In analyzing experimental potential results for such a wide energy range and large number of different systems, we consider quite appropriate the use of system- and energy independent quantities. We have removed the energy-dependence from the experimental potential strengths through the calculation of the corresponding folding potential strengths, $V_{F\text{-expt}}$, based on Eq. (34). The system dependence of the potential data set has then been removed with the use of the experimental reduced potential, $V_{red\text{-expt}}$. For $s \geqslant 0$ this quantity was calculated from Eq. (22), and for inner s values we have adopted the following simple definition:

$$V_{red\text{-expt}} = V_0 \frac{V_{F\text{-expt}}}{V_{F\text{-theo}}}, \tag{39}$$

with $V_{F\text{-theo}}$ calculated through Eq. (8). The other useful quantity is the distance between surfaces: $s = R_S - (R_1 + R_2)$, where R_S is associated with the sensitivity radius and the radii of the nuclei have been obtained from Eq. (6).

In Fig. 10 (top), the experimental reduced potential strengths are confronted with the theoretical prediction [Eqs. (23) and (24)] for different diffuseness values. The fit to the

TABLE II. The same as Table I, but for intermediate energies.

System	E_{Lab} (MeV)	Reference
$p+^{40}Ca$, ^{208}Pb	30.3	[35]
$d+^{40}Ca$, ^{208}Pb	52	[35]
$^{4}He+^{40}Ca$, ^{208}Pb	104	[35]
$^{6}Li+^{12}C$, ^{28}Si	210, 318	[36,37]
$^{6}Li+^{40}Ca$, ^{58}Ni, ^{90}Zr, ^{208}Pb	210	[38]
$^{7}Li+^{12}C$, ^{28}Si	350	[39]
$^{12}C+^{12}C$	300, 360, 1016, 1440, 2400	[40–42]
$^{12}C+^{208}Pb$	1440	[42]
$^{13}C+^{208}Pb$	390	[41]
$^{16}O+^{16}O$	250, 350, 480, 704, 1120	[44,45]
$^{16}O+^{12}C$, ^{28}Si, ^{40}Ca, ^{90}Zr, ^{208}Pb	1504	[43]
$^{40}Ar+^{60}Ni$, ^{120}Sn, ^{208}Pb	1760	[46]

data in the inner region ($s \leqslant 0$) results unambiguously in the value $V_0 = -456$ MeV fm^3 and is quite insensitive to the diffuseness parameter, in agreement with the discussion about the folding features of Sec. III. The fit for $s \geqslant 0$ is sensitive to both: V_0 and a, and the corresponding best fit values are $a = 0.56$ fm and the same V_0 found for the inner region. The standard deviation of the data set around the best fit (solid line in Fig. 10, top) is 25%, a value somewhat greater than the dispersion (20%) expected to arise from effects of the structure of the nuclei (as discussed in Sec. III). We believe that the remaining difference comes from two sources: uncertainties of the experimentally extracted potential strengths and the contribution of the polarization potential that we have neglected in our analysis. We point out that the best fit diffuseness value $a = 0.56$ fm is equal to the average diffuseness found (Sec. II) for the matter distributions and greater than the average value ($a = 0.50$ fm) of the nucleon distributions. This is a consistent result because we have calculated the reduced potential strengths based on the zero-range approach (through Eqs. (8), (22), (23), and (24)]. As discussed in Sec. III, the effect of a finite range for the effective nucleon-nucleon interaction can be simulated, within the zero-range approach, by increasing the diffuseness of the (nucleon) densities of the nuclei. This subject is dealt with more deeply in the next section.

In order to characterize the importance of the Pauli nonlocality, in Fig. 10 (bottom) are shown the results for the reduced potential through calculations performed without the correction [Eq. (34)] due to the energy dependence of the LE potential, i.e., associating the experimental potential strengths directly with the folding potential. The quality of the corresponding fit (Fig. 10, bottom) is similar to that obtained with the nonlocality (Fig. 10, top), but the V_0 and a parameters are significantly different. In the next section, we show that the values found without considering the nonlocality, $a = 0.61$ fm and $V_0 = -274$ MeV fm^3, seem to result in an unrealistic nucleon-nucleon interaction.

VI. EFFECTIVE NUCLEON-NUCLEON INTERACTION

After removing the energy dependence of the experimental potential strengths, the corresponding results are compatible with the double-folding potential in the zero-range approach [Eq. (8)], provided that the matter densities of the nuclei be adopted in the folding procedure instead of the nucleon densities. In this section, we study the consistency of our results for the nuclear potential in the case that the double-folding model is treated in the more common interpretation: the nucleon distributions and a finite-range nucleon-nucleon interaction are assumed in Eq. (7). With the purpose of keeping the comparison between experimental and theoretical results through the use of system-independent quantities, it is necessary to change the definition of the experimental reduced potential:

$$V_{red\text{-expt}} = V_{red\text{-theo}} \frac{V_{F\text{-expt}}}{V_{F\text{-theo}}}, \qquad (40)$$

TABLE III. The width, volume integral, and root-mean-square radius for several effective nucleon-nucleon interactions considered in this work.

Interaction	σ or a_m (fm)	V_0 (MeV fm^3)	r_{rms} (fm)
M3Y-Reid	-	-408	1.62
M3Y-Paris	-	-447	1.60
Yukawa	0.58	-439	1.42
Gaussian	0.90	-448	1.56
Exponential	0.43	-443	1.49
Folding-type	0.30	-456	1.47

where $V_{F\text{-theo}}$ is now calculated through Eq. (7). $V_{red\text{-theo}}$ is still obtained from Eqs. (23) and (24), with the V_0 parameter being associated with the volume integral of the effective nucleon-nucleon interaction (actually, this same procedure has also been adopted in the zero-range case):

$$V_0 = 4\pi \int v_{NN}(r) r^2 dr. \qquad (41)$$

The effective nucleon-nucleon interaction should be based upon a realistic nucleon-nucleon force, since our goal is to obtain a unified description of the nucleon-nucleon, nucleon-nucleus, and nucleus-nucleus scattering (a discussion about the "realism" of the interaction is found in Refs. [1,6]). For instance, a realistic interaction should match the empirical values for the volume integral and root-mean-square radius of the nucleon-nucleon interaction, $V_0 \approx -430$ MeV fm^3 and $r_{rms} \approx 1.5$ fm, which were extrapolated from the main features of the optical potential for the nucleon-nucleus scattering at $E_{nucleon} = 10$ MeV [1,47–49]. The M3Y interaction has been derived [1] with its basis on the G matrix for two nucleons bound near the Fermi surface and certainly is representative of realistic interactions. In Table III are presented the volume integral and root-mean-square radius for several nucleon-nucleon interactions used in this work, including the M3Y at 10 MeV/nucleon.

The M3Y interaction is not truly appropriate for use in the context of the nonlocal model, because it already contains a simulation of the exchange effects included in its knock-on term. Furthermore, according to the nonlocal model the energy dependence of the local-equivalent potential should be related only to the finite range of the Pauli nonlocality, but the knock-on exchange term in the M3Y interaction is also energy dependent. Therefore, the use of the M3Y in the nonlocal model would imply a double counting of the energy dependence that arises from exchange effects. In Sec. IV, we have demonstrated that the LE potential is identical with the double-folding potential for energies near the barrier, which are in a region around 10 MeV/nucleon. In this same energy range, the folding potential with the M3Y interaction has provided a very good description of elastic scattering data for several heavy-ion systems [1]. Thus, we believe that an appropriate nucleon-nucleon interaction for the nonlocal model could be the M3Y "frozen" at 10 MeV/nucleon [13], i.e., considering the parameters of the Reid and Paris versions as energy-independent values. Figure 11 (top) shows a compari-

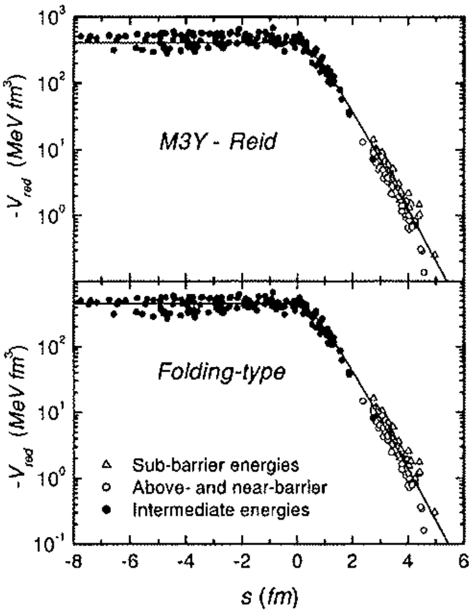

FIG. 11. Comparison between experimental and theoretical reduced potentials in the context of the finite-range approach, with a M3Y-Reid (top) or folding-type (bottom) effective nucleon-nucleon interaction.

son between experimental and theoretical heavy-ion reduced potentials, in which the "frozen" M3Y-Reid was considered for the nucleon-nucleon interaction. We emphasize that no adjustable parameter has been used in these calculations, but even so good agreement between the data and theoretical predictions has been obtained. The "frozen" M3Y-Paris provides similar results.

With the aim of investigating how much information about the effective nucleon-nucleon interaction can be extracted from our heavy-ion potential systematics, we have considered other possible functional forms for this effective interaction. Besides the Yukawa function [Eq. (25)], we have also used the Gaussian [Eq. (42)] and the exponential [Eq. (43)], which reduce to the tridimensional delta function in the limit $\sigma \rightarrow 0$,

$$G_\sigma(r) = V_0 \frac{e^{-r^2/2\sigma^2}}{(2\pi)^{3/2}\sigma^3}, \tag{42}$$

$$E_\sigma(r) = V_0 \frac{e^{-r/\sigma}}{8\pi\sigma^3}. \tag{43}$$

The fits obtained with all these functions are of similar quality and comparable with that for the M3Y interaction (Fig. 11, top). The resulting best fit widths (σ), volume integrals, and corresponding root-mean-square radii are found in Table III. All the V_0 and r_{rms} values, including those of the M3Y, are quite similar. Also the "experimentally" extracted intensity of the nucleon-nucleon interaction in the region $1 \leq r \leq 3$ fm seems to be rather independent of the model assumed for this interaction (see Fig. 12).

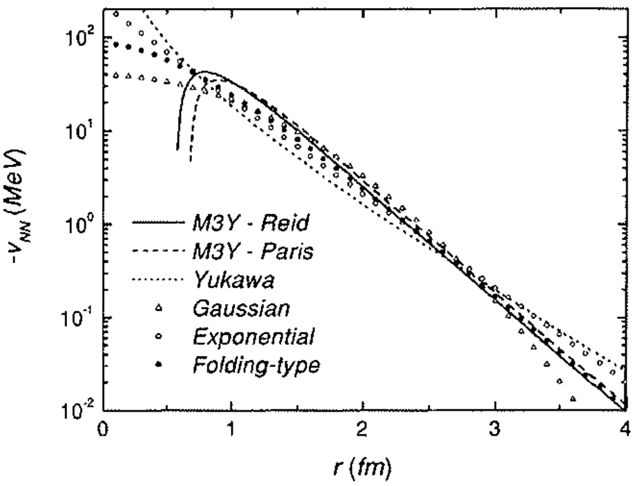

FIG. 12. The complete set of effective nucleon-nucleon interactions considered in this work.

In Sec. V, we have demonstrated that the major part of the "finite range" of the heavy-ion nuclear potential is related only to the spatial extent of the nuclei. In fact, even considering a zero range for the interaction v_{NN} in Eq. (8), the shape of the heavy-ion potential could be well described just by folding the matter densities of the two nuclei. One would ask whether the finite-range shape of the effective nucleon-nucleon interaction can be derived in a similar way. Thus, we have considered a folding-type effective nucleon-nucleon interaction built from

$$v_{NN}(\vec{r}) \approx v_f(r)$$
$$= \int \rho_m(r_1)\rho_m(r_2) V_0 \delta(\vec{R} - \vec{r}_1 + \vec{r}_2) d\vec{r}_1 d\vec{r}_2$$
$$= \frac{2\pi V_0}{r} \int_0^\infty r_1 \rho_m(r_1) \left[\int_{|r-r_1|}^{r+r_1} r_2 \rho_m(r_2) dr_2 \right] dr_1, \tag{44}$$

where $V_0 = -456$ MeV fm^3 as determined by the heavy-ion potential analysis and ρ_m is the matter density of the nucleon. Based on the intrinsic charge distribution of the proton in free space, which has been determined by electron scattering experiments, we have assumed an exponential shape for the matter density of the nucleon:

$$\rho_m(r) = \rho_0 e^{-r/a_m}. \tag{45}$$

Of course, ρ_0 and a_m are connected by the normalization condition, Eq. (2). The integration of Eq. (44) results in

$$v_f(r) = \frac{V_0}{64\pi a_m^3} e^{-r/a_m} \left(1 + \frac{r}{a_m} + \frac{r^2}{3a_m^2} \right). \tag{46}$$

With this finite-range folding-type effective nucleon-nucleon interaction, a good fit of the reduced heavy-ion potential strengths is obtained (see Fig. 11, bottom), with realistic volume integral and root-mean-square radius (see Table III).

The folding-type interaction is quite similar to both versions of the M3Y interaction in the surface region (see Fig. 12).

The folding-type interaction in the context of the nonlocal model provides a very interesting unification between the descriptions of the nucleus-nucleus, nucleon-nucleus, and effective nucleon-nucleon interactions. This can be appreciated through the comparison between Eqs. (36) and (38), with the subtle detail that V_F [in Eq. (36)] and v_f [in Eq. (38)] can both be calculated by folding the matter densities in the zero-range approach and with the same V_0 value. Therefore, the interaction between two nuclei (or nucleons) can be obtained from

$$V_{LE}(R)=\int \rho_1(r_1)\rho_2(r_2)V_0\delta(\vec{R}-\vec{r}_1+\vec{r}_2)e^{-4v^2/c^2}d\vec{r}_1d\vec{r}_2, \tag{47}$$

where $V_0=-456\ \mathrm{MeV\,fm}^3$, ρ_i are the matter densities, and v is the relative speed between the nuclei (or nucleons). An alternative way to calculate the heavy-ion interaction is with Eq. (37) [and Eq. (38)], but in this case the nucleon distributions must be used [in Eq. (37)] instead of the matter densities. All these findings seems to be quite consistent. However, the best fit value obtained for the diffuseness ($a_m=0.30$ fm) of the matter density of the nucleon inside the nucleus is considerable greater than that ($a_{chp}=0.235$ fm) found for the charge distribution of the proton in free space. This finding is consistent with the swelling of the nucleon observed in the EMC effect [50], but should be contrasted with the opposite picture of a smaller nucleon inside the nucleus as advanced within the concept of color transparency [51].

Finally, we mention that, if the energy dependence of the Pauli nonlocality is not taken into account and the experimental potential strengths are associated directly with the folding potential, our calculations indicate that the corresponding effective nucleon-nucleon interaction should have the following unrealistic values: $V_0\approx-270\ \mathrm{MeV\,fm}^3$ and $r_{rms}\approx 1.9$ fm.

VII. CONCLUSION

The experimental potential strengths considered in the present systematics have been obtained at the corresponding sensitivity radii, a region where the nuclear potential is determined from the data analyses with the smallest degree of ambiguity. The Fermi distribution was assumed to represent the nuclear densities, with parameters consistent with an extensive amount of theoretical (DHB calculations) and experimental (electron scattering experiments) results. The potential data set is well described in the context of the nonlocal model by the double-folding potential in the zero-range as well as in the finite-range approaches. The dispersion of the potential data around the theoretical prediction is 25%, which is compatible with the expected effects arising from the variation of the densities due to the structure of the nuclei. If the nonlocal interaction is assumed, the heavy-ion potential data set seems to determine a few characteristics of the effective nucleon-nucleon interaction, such as volume integral and root-mean-square radius, in a model-independent way.

The description of the bare potential presented in this work is based only on two fundamental ideas: the folding model and the Pauli nonlocality. We have avoided as much as possible the use of adjustable parameters, and in the case of the "frozen" M3Y interaction no adjustable parameters were necessary to fit the experimental potential strengths. Nowadays, the other important part of the heavy-ion interaction, the polarization potential, is commonly treated within a phenomenological approach, with several adjustable parameters which usually are energy dependent and vary significantly from system to system. The association of the nonlocal bare potential presented in this work with a more fundamental treatment of the polarization should be the next step toward a global description of the nucleus-nucleus interaction.

ACKNOWLEDGMENTS

This work was partially supported by Financiadora de Estudos e Projetos (FINEP), Fundação de Amparo à Pesquisa do Estado de São Paulo (FAPESP), and Conselho Nacional de Desenvolvimento Científico e Tecnológico (CNPq).

[1] G. R. Satchler and W. G. Love, Phys. Rep. **55**, 183 (1979).

[2] L. J. B. Goldfarb and Y. K. Gambhir, Nucl. Phys. **A401**, 557 (1983).

[3] D. M. Brink and N. Rowley, Nucl. Phys. **A219**, 79 (1974).

[4] R. A. Broglia and A. Winther, Phys. Rep., Phys. Lett. **4C**, 153 (1972).

[5] J. Blocki, J. Randrup, W. J. Swiatecki, and C. F. Tsang, Ann. Phys. (N.Y.) **105**, 427 (1977).

[6] M. E. Brandan and G. R. Satchler, Phys. Rep. **285**, 143 (1997), and references therein.

[7] P. R. Christensen and A. Winther, Phys. Lett. **65B**, 19 (1976).

[8] C. P. Silva, M. A. G. Alvarez, L. C. Chamon, D. Pereira, M. N. Rao, E. S. Rossi, Jr., L. R. Gasques, M. A. E. Santo, R. M. Anjos, J. Lubian, P. R. S. Gomes, C. Muri, B. V. Carlson, S. Kailas, A. Chatterjee, P. Singh, A. Shivastava, K. Mahata, and S. Santra, Nucl. Phys. **A679**, 287 (2001).

[9] D. A. Goldberg and S. M. Smith, Phys. Rev. Lett. **29**, 500 (1972).

[10] D. A. Goldberg and S. M. Smith, Phys. Rev. Lett. **33**, 715 (1974).

[11] D. A. Goldberg, S. M. Smith, and G. F. Burdzic, Phys. Rev. C **10**, 1362 (1974).

[12] M. A. C. Ribeiro, L. C. Chamon, D. Pereira, M. S. Hussein, and D. Galetti, Phys. Rev. Lett. **78**, 3270 (1997).

[13] L. C. Chamon, D. Pereira, M. S. Hussein, M. A. C. Ribeiro, and D. Galetti, Phys. Rev. Lett. **79**, 5218 (1997).

[14] L. C. Chamon, D. Pereira, and M. S. Hussein, Phys. Rev. C **58**, 576 (1998).

[15] H. De Vries, C. W. De Jager, and C. De Vries, At. Data Nucl. Data Tables **36**, 495 (1987).

[16] E. G. Nadjakov, K. P. Marinova, and Y. P. Gangrsky, At. Data Nucl. Data Tables **56**, 133 (1994).

[17] B. V. Carlson and D. Hirata, Phys. Rev. C **62**, 054310 (2000).

[18] G. A. Lalazissis, J. König, and P. Ring, Phys. Rev. C **55**, 540 (1997).

[19] G. A. Lalazissis, D. Vretenar, and P. Ring, Phys. Rev. C **57**, 2294 (1998).

[20] G. A. Lalazissis, D. Vretenar, P. Ring, M. Stoitsov, and L. Robledo, Phys. Rev. C **60**, 014310 (1999).

[21] Z. Patyk, A. Baran, J. F. Berger, J. Decharge, J. Dobaczewski, P. Ring, and A. Sobczewski, Phys. Rev. C **59**, 704 (1999).

[22] W. D. Myers, Nucl. Phys. **A204**, 465 (1973).

[23] G. R. Satchler, Phys. Rep. **199**, 147 (1991).

[24] F. Perey and B. Buck, Nucl. Phys. **32**, 253 (1962).

[25] T. H. R. Skyrme, Philos. Mag. **1**, 1043 (1956).

[26] G. Ripka, Nucl. Phys. **42**, 75 (1963).

[27] W. Bauhoff, H. V. von Geramb, and G. Palla, Phys. Rev. C **27**, 2466 (1983).

[28] W. E. Frahn and R. H. Lemmer, Nuovo Cimento **5**, 1564 (1957).

[29] D. F. Jackson and R. C. Johnson, Phys. Lett. **49B**, 249 (1974).

[30] F. Lenz and E. J. Moniz, Phys. Rev. C **12**, 909 (1975).

[31] L. C. Chamon, D. Pereira, E. S. Rossi, Jr., C. P. Silva, R. Lichtenthaler Filho, and L. C. Gomes, Nucl. Phys. **A582**, 305 (1995).

[32] L. C. Chamon, D. Pereira, E. S. Rossi, Jr., C. P. Silva, H. Dias, L. Losano, and C. A. P. Ceneviva, Nucl. Phys. **A597**, 253 (1996).

[33] M. A. G. Alvarez, L. C. Chamon, D. Pereira, E. S. Rossi, Jr., C. P. Silva, L. R. Gasques, H. Dias, and M. O. Roos, Nucl. Phys. **A656**, 187 (1999).

[34] E. S. Rossi, Jr., L. C. Chamon, D. Pereira, C. P. Silva, and G. Ramirez, J. Phys. G **23**, 1473 (1997).

[35] M. Ermer, H. Clement, G. Frank, P. Grabmayr, H. Heberle, and G. J. Wagner, Phys. Lett. B **224**, 40 (1989).

[36] A. Nadasen, T. Stevens, J. Farhat, J. Brusoe, P. Schwandt, J. S. Winfield, G. Yoo, N. Anantaraman, F. D. Becchetti, J. Brown, B. Hotz, J. W. Janecke, D. Roberts, and R. E. Warner, Phys. Rev. C **47**, 674 (1993).

[37] A. Nadasen, M. McMaster, G. Gunderson, A. Judd, S. Villanueva, P. Schwandt, J. S. Winfield, J. van der Plicht, R. E. Warner, F. D. Becchetti, and J. W. Janecke, Phys. Rev. C **37**, 132 (1988).

[38] A. Nadasen, M. McMaster, M. Fingal, J. Tavormina, P. Schwandt, J. S. Winfield, M. F. Mohar, F. D. Becchetti, J. W. Janecke, and R. E. Warner, Phys. Rev. C **39**, 536 (1989).

[39] A. Nadasen, J. Brusoe, J. Farhat, T. Stevens, J. Williams, L. Nieman, J. S. Winfield, R. E. Warner, F. D. Becchetti, J. W. Janecke, T. Annakkage, J. Bajema, D. Roberts, and H. S. Govinden, Phys. Rev. C **52**, 1894 (1995).

[40] H. G. Bohlen, M. R. Clover, G. Ingold, H. Lettau, and W. von Oertzen, Z. Phys. A **308**, 121 (1982).

[41] M. Buenerd, A. Lounis, J. Chauvin, D. Lebrun, P. Martin, G. Duhamel, J. C. Gondrand, and P. de Saintignon, Nucl. Phys. **A424**, 313 (1984).

[42] J. Y. Hostachy, M. Buenerd, J. Chauvin, D. Lebrun, Ph. Martin, J. C. Lugol, L. Papineau, P. Roussel, N. Alamanos, J. Arvieux, and C. Cerruti, Nucl. Phys. **A490**, 441 (1988).

[43] P. Roussel-Chomaz, N. Alamanos, F. Auger, J. Barrete, B. Berthier, B. Fernandez, L. Papineau, H. Doubre, and W. Mittig, Nucl. Phys. **A477**, 345 (1988).

[44] G. Bartnitzky, A. Blazevic, H. G. Bohlen, J. M. Casandjian, M. Chartier, H. Clement, B. Gebauer, A. Gilibert, Th. Kirchner, Dao T. Khoa, A. Lepine-Szily, W. Mittig, W. von Oertzen, A. N. Ostrowski, P. Roussel-Chomaz, J. Siegler, M. Wilpert, and Th. Wilpert, Phys. Lett. B **365**, 23 (1996).

[45] F. Nuoffer, G. Bartnitzky, H. Clement, A. Blazevic, H. G. Bohlen, B. Gebauer, W. von Oertzen, M. Wilpert, T. Wilpert, A. Lepine-Szily, W. Mittig, A. N. Ostrowski, and P. Roussel-Chomaz, Nuovo Cimento A **11**, 971 (1998).

[46] N. Alamanos, F. Auger, J. Barrete, B. Berthier, B. Fernandez, J. Gastebois, L. Papineau, H. Doubre, and W. Mittig, Phys. Lett. **137B**, 37 (1984).

[47] F. D. Bechetti and G. W. Greenlees, Phys. Rev. **182**, 1190 (1969).

[48] G. W. Greenlees, G. J. Pyle, and Y. C. Yang, Phys. Rev. **171**, 1115 (1968).

[49] G. W. Greenlees, W. Makofske, and G. J. Pyle, Phys. Rev. C **1**, 1145 (1970).

[50] J. J. Aubert *et al.*, Phys. Lett. **123B**, 275 (1983).

[51] See, e.g., L. L. Frankfurt and M. I. Strikman, Phys. Rep. **76**, 214 (1981); **160**, 235 (1988).

ELSEVIER

Nuclear Physics A 707 (2002) 325–342

NUCLEAR PHYSICS A

www.elsevier.com/locate/npe

Effect of the ^{18}O nuclear density on the nuclear potentials of the $^{18}\text{O} + {}^{58,60}\text{Ni}$ systems

E.S. Rossi Jr. [a], D. Pereira [a], L.C. Chamon [a,*], C.P. Silva [a], M.A.G. Alvarez [a], L.R. Gasques [a], J. Lubian [b,1], B.V. Carlson [c], C. De Conti [c]

[a] *Departamento de Física Nuclear, Instituto de Física da Universidade de São Paulo, Caixa Postal 66318, 05315-970 São Paulo, SP, Brazil*

[b] *Instituto de Física, Universidade Federal Fluminense, Av. Litoranea, Niterói, RJ, 24210-340, Brazil*

[c] *Departamento de Física, Instituto Tecnológico de Aeronáutica, Centro Técnico Aeroespacial, São José dos Campos, SP, Brazil*

Received 3 January 2002; received in revised form 18 April 2002; accepted 6 May 2002

Abstract

Quasi-elastic, inelastic, one- and two-neutron transfer differential cross sections have been measured for the $^{18}\text{O} + {}^{58,60}\text{Ni}$ systems at sub-barrier energies. The corresponding bare potentials have been determined at interaction distances larger than the respective barrier radii, and the results have been compared with those previously obtained for systems involving the ^{16}O as projectile. The detected difference between the ^{18}O and ^{16}O nuclear potentials has allowed the determination of the nuclear density that corresponds to the two extra neutrons of the ^{18}O nucleus. © 2002 Elsevier Science B.V. All rights reserved.

PACS: 24.10.Ht; 21.10.Ft; 21.10.Gv

Keywords: NUCLEAR REACTIONS $^{58,60}\text{Ni}(^{18}\text{O},{}^{18}\text{O}')$, $(^{18}\text{O},{}^{17}\text{O})$, $(^{18}\text{O},{}^{16}\text{O})$, $E = 34$–38 MeV; measured quasielastic, inelastic, transfer σ, $\sigma(\theta)$; deduced nuclear potential features. ^{18}O deduced neutron density distribution. Comparisons with previous results, model predictions.

---

[*] Corresponding author.
E-mail address: luiz.chamon@dfn.if.usp.br (L.C. Chamon).

[1] Permanent address: CEADEN, PO 6122, Havana, Cuba.

PII: S0375-9474(02)01009-6

1. Introduction

In this work we present quasi-elastic, inelastic, one- and two-neutron transfer differential cross sections for the $^{18}O + ^{58,60}Ni$ systems at sub-barrier energies. The purpose of the experiments was the determination of the corresponding nuclear potentials in an interaction region near the respective barrier radii. The method was earlier applied to several systems involving the ^{16}O nucleus as projectile [1–4]. The quasi-elastic cross section is defined as the sum of the elastic scattering with all peripheral reaction channels. No extra peripheral absorption should be expected in analysing the quasi-elastic data set, and therefore the imaginary part of the optical potential must be negligible at the surface region. Thus, the optical model quasi-elastic data analysis unambiguously determines the real part of the interaction. The optical potential is composed of the bare and polarization potentials, the latter containing the contribution arising from nonelastic couplings. The real part of the polarization has been estimated earlier [1–3] through extensive coupled-channel calculations for the ^{16}O sub-barrier data set, and represents about 10% in comparison with the bare (nuclear) interaction. Therefore, in the ^{16}O case the experimentally extracted optical potential strengths at sub-barrier energies can be associated with the bare potential within 10% precision. In the present work, we demonstrate that the real part of the optical potential extracted from quasi-elastic data analysis for the $^{18}O + ^{58,60}Ni$ systems can also be associated with the bare potential within a similar precision.

In a recent work [5], an extensive systematics of optical potential strengths extracted from heavy-ion elastic scattering data analyses at low and intermediate energies was presented. The energy-dependence of the nuclear potential has been accounted for within a model based on the nonlocal nature of the interaction [5–8]. The systematics indicates that the heavy-ion potential can be described in a global way, through a double-folding shape which basically presents a simple dependence only on the densities of the partners in the collision. In the present work, by assuming this nonlocal model for the interaction and considering the detected difference between the nuclear potentials for systems involving ^{18}O and ^{16}O as projectiles, we have obtained information about the nuclear density that corresponds to the two extra neutrons of the ^{18}O nucleus.

The paper is organized as follows. In Section 2, we present the experimental results. The determination of the bare potential strengths from optical model data analyses for the $^{18}O + ^{58,60}Ni$ systems is described in Section 3. A brief summary of the nonlocal model, and the comparison between the present results with those for systems with ^{16}O are contained in Section 4. Section 5 is devoted to the study of the nuclear densities for the $^{16,18}O$ nuclei. Section 6 contains a brief summary and the main conclusions.

2. Experimental results

The measurements were made at the São Paulo 8UD Pelletron Accelerator, Brazil. The thickness of the targets was about 60 $\mu g/cm^2$. The detecting system is composed (see Fig. 1(a)) of nine surface barrier detectors (SBD) and three position sensitive detectors (PSD). The data acquisition has been performed through two modes: with and without coincidence of lighter particles in the SBD with heavier recoil particles in the PSD (see

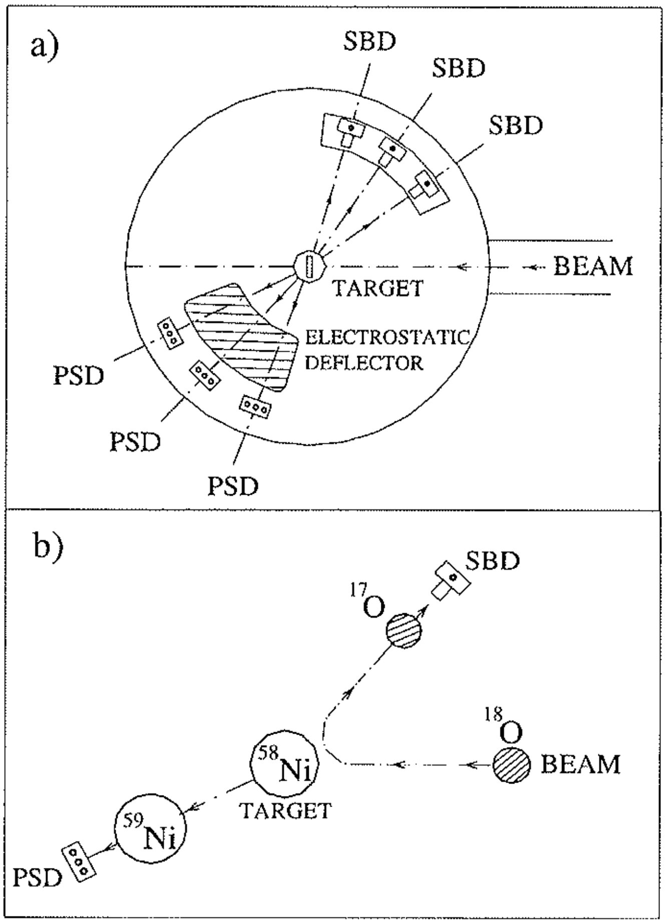

Fig. 1. (a) The detecting system used in the experiments, with the surface barrier detectors (SBD), position sensitive detectors (PSD) and electrostatic deflector. (b) Schematic view of the collision for one-neutron transfer, showing the detection of the lighter particle in the SBD and the heavier particle in the PSD.

Fig. 1(b)). As the PSD have been positioned at forward angles, an electrostatic deflector has been used to decrease the number of ^{18}O nuclei elastically scattered by the nickel target that reach the detectors. The electrostatic potential between the plates of the deflector was chosen to allow the detection of the heavier recoil particles. The kinematics of the reaction provides the following expression for the mass of the lighter particle detected in the SBD:

$$A = \frac{E_{\mathrm{Lab}} A_{\mathrm{P}} \sin^2(\theta_{\mathrm{R}})}{E_{\mathrm{L}} \sin^2(\theta_{\mathrm{R}} + \theta_{\mathrm{SBD}})}, \tag{1}$$

where E_{Lab} = bombarding energy, A_{P} = mass of the projectile, E_{L} = lighter particle energy, θ_{SBD} = angle of the SB detector, θ_{R} = angle of the heavier recoil particle detected in coincidence at the PSD. Fig. 2 presents a typical mass *versus* energy spectrum for the lighter particle, and also a projection of all events on the energy axis. The coincidence mode has been used only to identify the different processes (elastic, inelastic and transfer) that occur in the collision (see Fig. 2). The corresponding cross sections have been obtained by considering events in the no-coincidence mode energy spectra. This procedure is

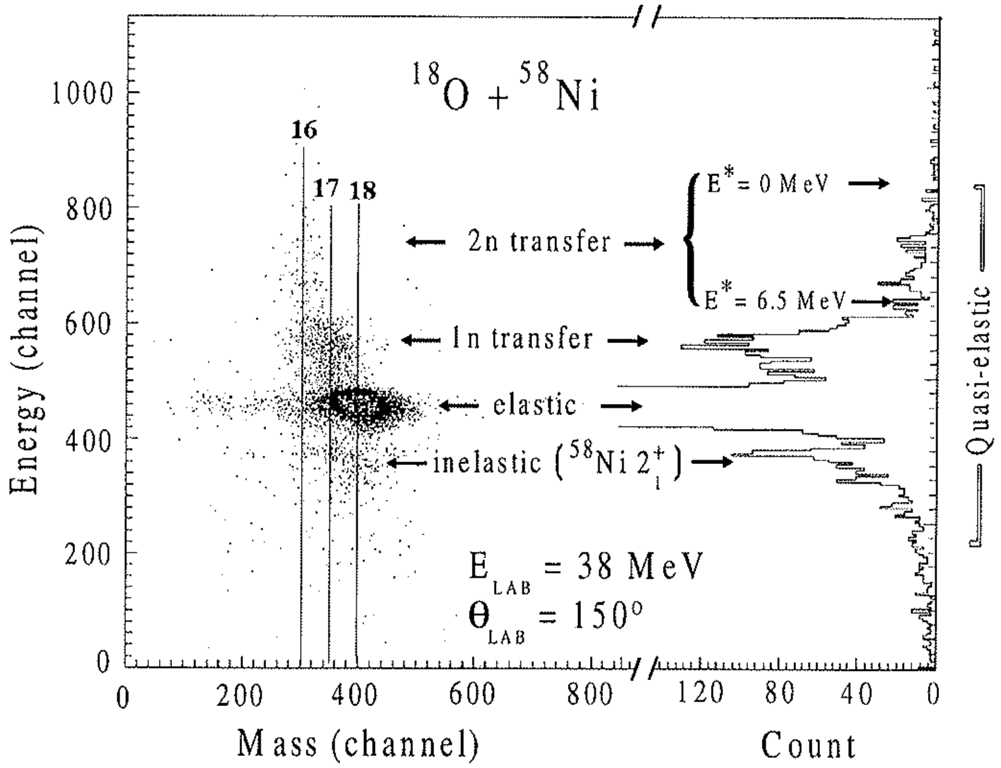

Fig. 2. Typical mass versus energy spectrum for the lighter particle and the projection of all events on the energy axis. The mass regions $A = 16$, 17 and 18, and the energy region of relevant channels, including the elastic and quasi-elastic processes, are indicated in the figure.

appropriate to obtain experimental cross sections without the inclusion of an efficiency of detection in the calculations, which should be included if the cross sections are calculated considering events obtained in the coincidence mode.

We define the quasi-elastic cross section as the sum over all channels with energy between the inelastic excitation of the ^{18}O 2_1^+ state and the ground-state ($E^* = 0$ MeV) two-neutron transfer, including the elastic scattering (see Fig. 2). Our experiments indicate that all reaction channels with significant cross section are included in the quasi-elastic process as defined above. Figs. 3 to 6 present the data sets obtained for several sub-barrier energies.

3. Data analysis

The determination of the bare potential has been performed by first analysing only the quasi-elastic data. In the optical model calculations, we have adopted a procedure similar to that described in the analysis of the sub-barrier data for the $^{16}\mathrm{O} + {}^{58,60,62,64}\mathrm{Ni}$, ^{88}Sr, ^{90,92}Zr, ^{92}Mo, ^{120}Sn, ^{138}Ba, ^{208}Pb systems [1–4]. We have adopted a Woods–Saxon shape for the optical potential, with an inner imaginary part which takes into account the rather small internal absorption from barrier penetration. The values assumed for the parameters of the imaginary part of the potential result in very small strengths at the surface region.

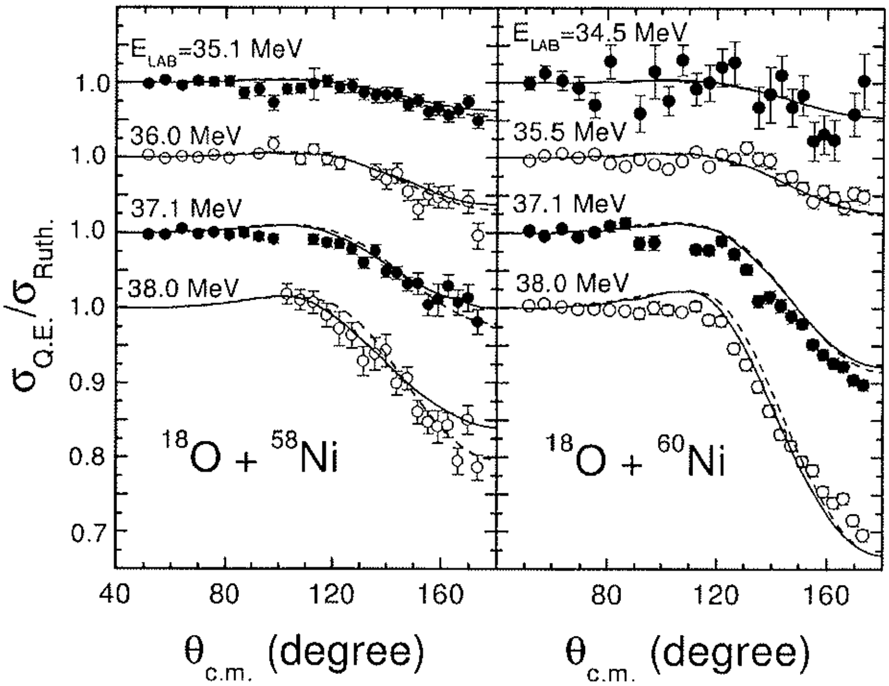

Fig. 3. Quasi-elastic cross sections for the $^{18}O + ^{58,60}Ni$ systems at several sub-barrier energies. The lines represent the results of optical model (dashed lines) and coupled-channel (solid lines) calculations using energy-independent bare potentials.

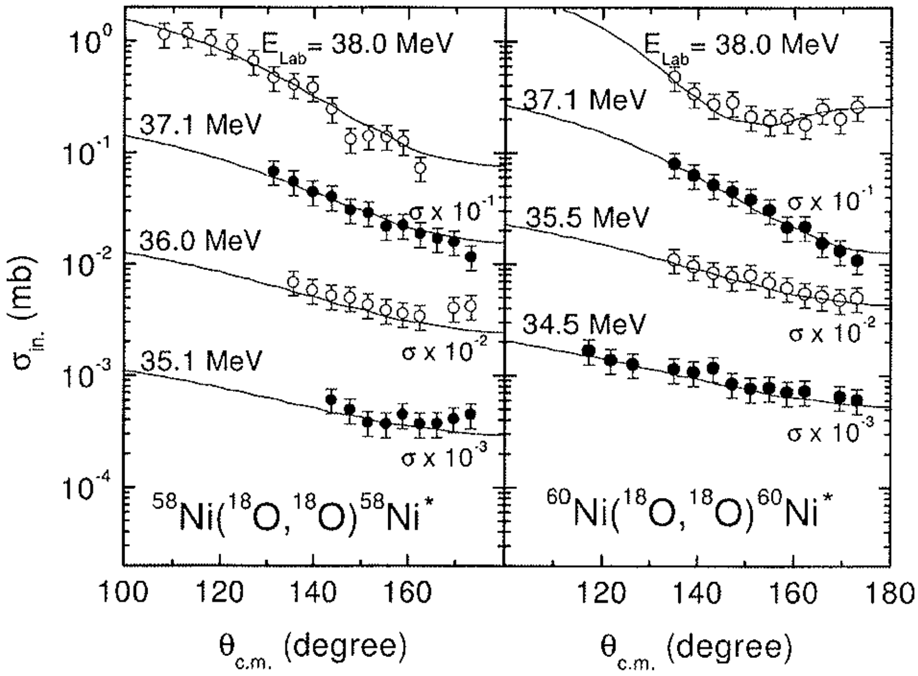

Fig. 4. Inelastic scattering cross sections, with excitation of the 2_1^+ target state, for the $^{18}O + ^{58,60}Ni$ systems at several sub-barrier energies. The lines represent the results of channel-coupled calculations using energy-independent bare potentials.

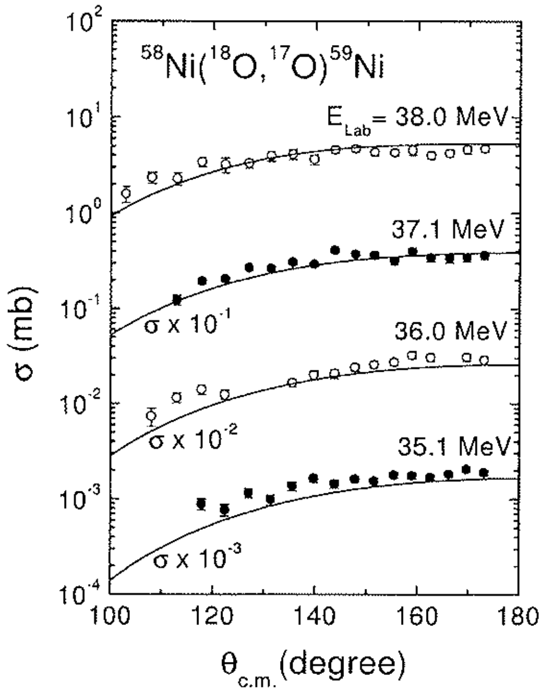

Fig. 5. One-neutron transfer cross sections for the $^{18}O + ^{58}Ni$ system at several sub-barrier energies. The data include transitions for the ground-state, the first ^{17}O excited state, and four ^{59}Ni excited states. The lines represent the results of channel-coupled calculations using an energy-independent bare potential.

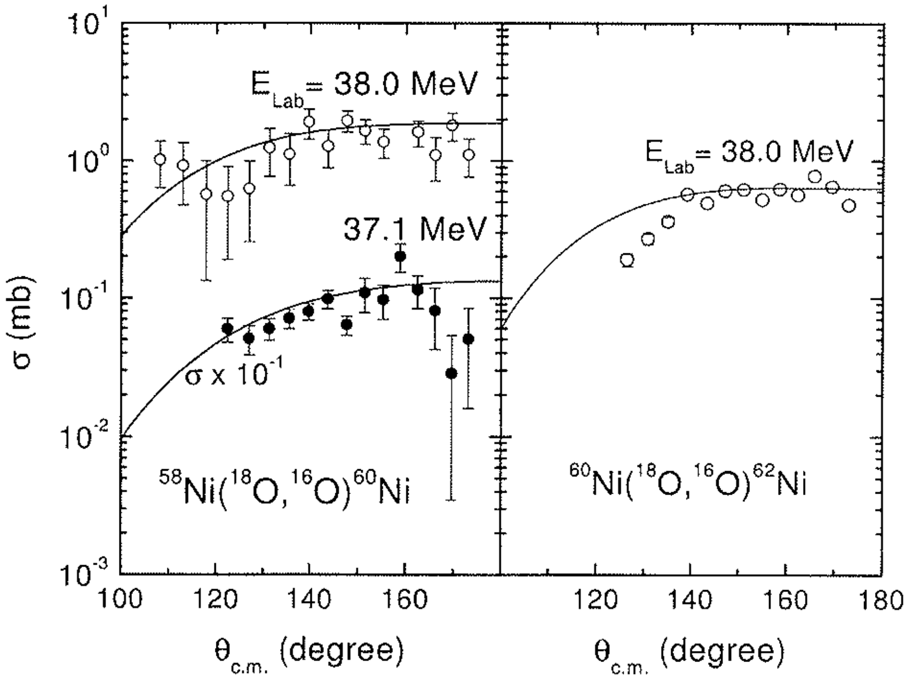

Fig. 6. Two-neutron transfer cross sections for the $^{18}O + ^{58,60}Ni$ systems at sub-barrier energies. The data include transitions to the set of states with excitation energy from 0 to 6.5 MeV (see Tables 1 and 2). The lines represent the results of channel-coupled calculations using energy-independent bare potentials.

Table 1
The inelastic, one- and two-neutron transfer channels considered in the coupled-channel calculations for the $^{18}O + ^{58}Ni$ system. The excitation energy is quoted in MeV

^{18}O	^{58}Ni	^{17}O	^{59}Ni	^{16}O	^{60}Ni
0^+ (g.s.)	0^+ (g.s.)	$\frac{5}{2}^+$ (g.s.)	$\frac{3}{2}^-$ (g.s.)	0^+ (g.s.)	0^+ (g.s.)
0^+ (g.s.)	2^+ (1.45)	$\frac{5}{2}^+$ (g.s.)	$\frac{5}{2}^-$ (0.34)	0^+ (g.s.)	2^+ (1.33)
2^+ (1.98)	0^+ (g.s.)	$\frac{5}{2}^+$ (g.s.)	$\frac{1}{2}^-$ (0.47)	0^+ (g.s.)	2^+ (2.16)
		$\frac{1}{2}^+$ (0.87)	$\frac{3}{2}^-$ (g.s.)	0^+ (g.s.)	0^+ (2.28)
		$\frac{5}{2}^+$ (g.s.)	$\frac{3}{2}^-$ (0.88)	0^+ (g.s.)	4^+ (2.51)
		$\frac{5}{2}^+$ (g.s.)	$\frac{5}{2}^-$ (1.19)	0^+ (g.s.)	4^+ (3.12)
				0^+ (g.s.)	2^+ (3.12)
				0^+ (g.s.)	2^+ (3.27)
				0^+ (g.s.)	2^+ (3.38)
				0^+ (g.s.)	0^+ (3.53)
				0^+ (g.s.)	4^+ (3.67)
				0^+ (g.s.)	2^+ (3.87)
				0^+ (g.s.)	2^+ (4.01)
				0^+ (g.s.)	2^+ (4.08)
				0^+ (g.s.)	2^+ (4.32)
				0^+ (g.s.)	2^+ (4.50)
				0^+ (g.s.)	2^+ (4.55)
				0^+ (g.s.)	4^+ (5.02)
				0^+ (g.s.)	4^+ (5.11)
				0^+ (g.s.)	4^+ (5.24)
				0^+ (g.s.)	2^+ (5.43)
				0^+ (g.s.)	0^+ (5.53)
				0^+ (g.s.)	2^+ (5.58)
				0^+ (6.05)	0^+ (g.s.)
				3^- (6.13)	0^+ (g.s.)

This procedure must be adopted in the analysis because peripheral reaction channels that were not included in the quasi-elastic data present negligible cross sections. Concerning depth variations of this absorptive potential, no sensitivity in the quasi-elastic cross section predictions has been detected. The depth and diffuseness parameters of the real part of the optical potential were searched for the best data fits. For each angular distribution, we have found a family of potentials which give equivalent fits. These potentials cross (see Fig. 7) at a particular distance R_S, hereafter referred as the sensitivity radius. Therefore, the nuclear potential is determined without ambiguity at R_S from the optical model quasi-elastic data analysis.

The sensitivity radius is energy-dependent, because at sub-barrier energies it is related to the classical turning point. We have used this fact to characterize the nuclear potential in the surface region (see Fig. 8). For such large interaction distances, the shape of the potential is nearly an exponential (solid lines in Fig. 8), with a diffuseness value about 0.77 fm, and with strength values at $R = 10.5$ fm of 1.02 and 1.17 MeV for the $^{18}O + ^{58,60}Ni$ systems, respectively. Considering energy-independent nuclear potentials (Woods–Saxon shape) with such characteristics, good predictions for the quasi-elastic cross sections are obtained (dashed lines in Fig. 3).

Table 2
The inelastic and two-neutron transfer channels considered in the coupled-channel calculations for the $^{18}O + ^{60}Ni$ system. The excitation energy is quoted in MeV

^{18}O	^{60}Ni	^{16}O	^{62}Ni
0^+(g.s.)	0^+(g.s.)	0^+(g.s.)	0^+(g.s.)
0^+(g.s.)	2^+(1.33)	0^+(g.s.)	2^+(1.17)
2^+(1.98)	0^+(g.s.)	0^+(g.s.)	0^+(2.05)
		0^+(g.s.)	2^+(2.30)
		0^+(g.s.)	4^+(2.34)
		0^+(g.s.)	0^+(2.89)
		0^+(g.s.)	2^+(3.06)
		0^+(g.s.)	2^+(3.16)
		0^+(g.s.)	4^+(3.17)
		0^+(g.s.)	2^+(3.26)
		0^+(g.s.)	2^+(3.27)
		0^+(g.s.)	4^+(3.27)
		0^+(g.s.)	2^+(3.37)
		0^+(g.s.)	2^+(3.52)
		0^+(g.s.)	2^+(3.86)
		0^+(g.s.)	2^+(3.97)
		0^+(g.s.)	4^+(3.99)
		0^+(g.s.)	4^+(4.05)
		0^+(g.s.)	2^+(4.06)
		0^+(g.s.)	0^+(4.23)
		0^+(g.s.)	2^+(4.32)
		0^+(g.s.)	2^+(4.42)
		0^+(g.s.)	2^+(5.00)
		0^+(6.05)	0^+(g.s.)
		3^-(6.13)	0^+(g.s.)

From a theoretical point of view, the nuclear potentials extracted from our optical model quasi-elastic (OMQE) data analysis would be expected to be different from the bare potentials used in a full coupled-channel (CC) calculation. However, as commented in Section 1, CC calculations for systems with ^{16}O have indicated that the real part of the polarization represents about 10% of the bare potential in the sub-barrier energy region that corresponds to our data analysis. Thus, we have investigated whether the potentials extracted from the OMQE analysis might represent a good approximation to the real CC bare potentials in the present case of the $^{18}O + ^{58,60}Ni$ systems. We remind the reader that only an inner imaginary potential ($W_0 = 50$ MeV, $r_{i0} = 1.06$ fm, $a_i = 0.2$ fm) has been used in the OMQE analysis because the peripheral reaction channels that were not included in the quasi-elastic data present negligible cross sections. The same consideration (no surface imaginary potential) must be applied to a complete CC calculation because in this case the relevant reaction channels are explicitly considered. In Tables 1 and 2 we present the channels included in the CC calculations, which have been performed using the FRESCO code [9]. In order to test our hypothesis, the diagonal potentials were assumed to have a Woods–Saxon shape, with diffuseness value 0.77 fm, radii given by $R_0 = r_0(A_1^{1/3} + A_2^{1/3})$, with $r_0 = 1.06$ fm, and depth of $V_0 = 113$ and 122 MeV for the $^{18}O + ^{58}Ni$ and $^{18}O + ^{60}Ni$

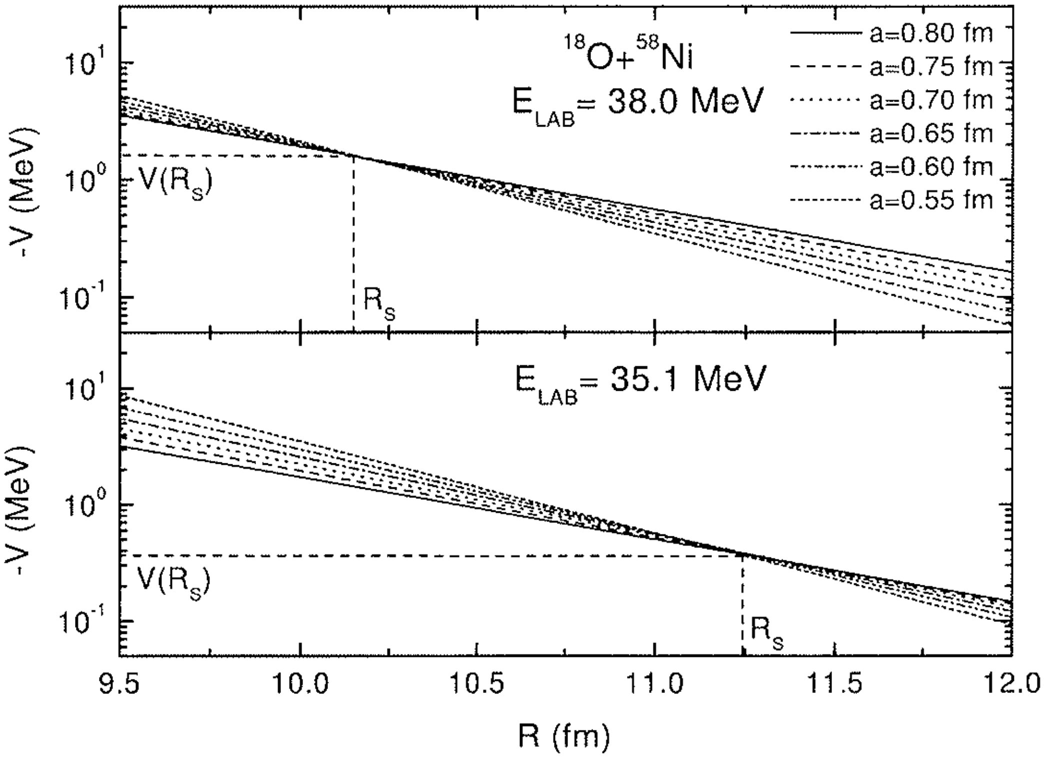

Fig. 7. The real part of the optical potential for the ^{18}O + ^{58}Ni system at two different energies, as obtained by optical-model quasi-elastic data fits for several values of the diffuseness parameter. The potentials cross at the sensitivity radius, R_S, where the corresponding potential strength is determined without ambiguity.

systems, respectively. In the entrance channel, these potentials are the same as those obtained in the OMQE analyses. For transfer processes, the small variation of R_0 for the entrance and exit channels, due to the different number of nucleons of the nuclei (A_i), provides a small variation of the corresponding diagonal potentials. The inelastic couplings were treated within the vibrational model, with deformation lengths (see Table 3) obtained in Refs. [2,10]. A one step cluster transfer of an $s = 0$ neutron pair was assumed for the two-neutron transfer process. Due to the large number of states for neutron transfer, most of them with unknown spectroscopic factors, we have assumed in the calculations an energy-independent average spectroscopic value for all the states, which has been searched in the data fits. Under such conditions, we have found reasonable values (≈ 0.87) for the spectroscopic factors for both systems. The CC calculations have provided good descriptions for the cross sections of all measured channels (see Figs. 3 to 6). We consider this result a demonstration that the potentials extracted from the OMQE analysis actually represent a good approximation to the CC bare potentials. Obviously, the quasi-elastic cross section has been obtained in the CC calculations by adding the cross sections of all channels including the elastic scattering. Note the very similar results obtained for the quasi-elastic cross section from the optical model (dashed lines in Fig. 3) and the CC calculations (solid lines in Fig. 3). This means that, at sub-barrier energies, the optical model quasi-elastic data analysis incorporates in an approximate way the main contributions of the couplings,

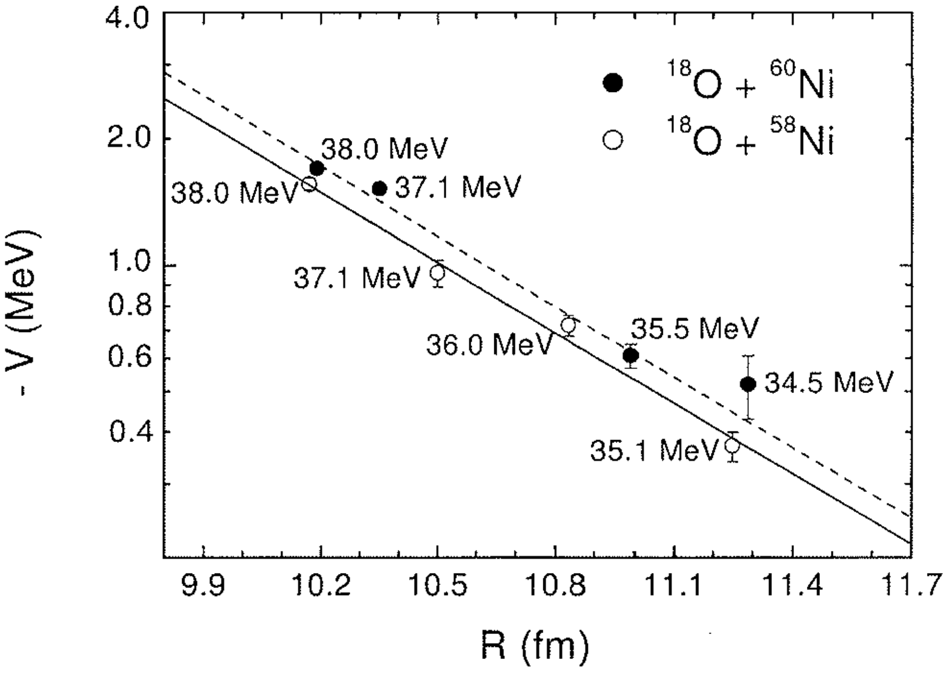

Fig. 8. The nuclear potential strength as a function of the sensitivity radius for the $^{18}O + ^{58,60}Ni$ systems. The bombarding energies of the angular distributions in which the sensitivity radii have been determined are indicated in the figure. The lines represent exponentials with diffuseness 0.77 fm.

Table 3
The Coulomb (δ_c) and nuclear (δ_n) deformation lengths, $B(E2)$ and excitation energies for inelastic excitation considered in the coupled-channel calculations

Nucleus	δ_c (fm)	δ_n (fm)	$B(E2)$ (e^2b^2)	E^* (MeV)
^{18}O	1.26	1.26	45.1	1.98
^{58}Ni	0.96	0.90	688	1.45
^{60}Ni	1.10	1.08	931	1.33

which mostly represent loss of flux from the elastic to the peripheral reaction channels, but with conservation of the quasi-elastic cross section. This should be valid if the couplings are not too strong and for energies not too close the barrier. An inspection of Fig. 3 indicates that the bombarding energy of 38 MeV seems to be the limit for which the optical model and the coupled-channel calculations give similar predictions for the quasi-elastic cross sections. This energy is about 4 MeV below the fusion barrier for both systems. The two approaches would probably result in different data-extracted potentials if the data analyses had been realized at higher energies. Very similar results have also been obtained in the case of systems with ^{16}O as the projectile [11] (see Fig. 9). Therefore, our studies have indicated that two methods can be used to determine the bare potential in this sub-barrier energy region: an optical model quasi-elastic data analysis or a full coupled-channel data analysis, the latter being more precise.

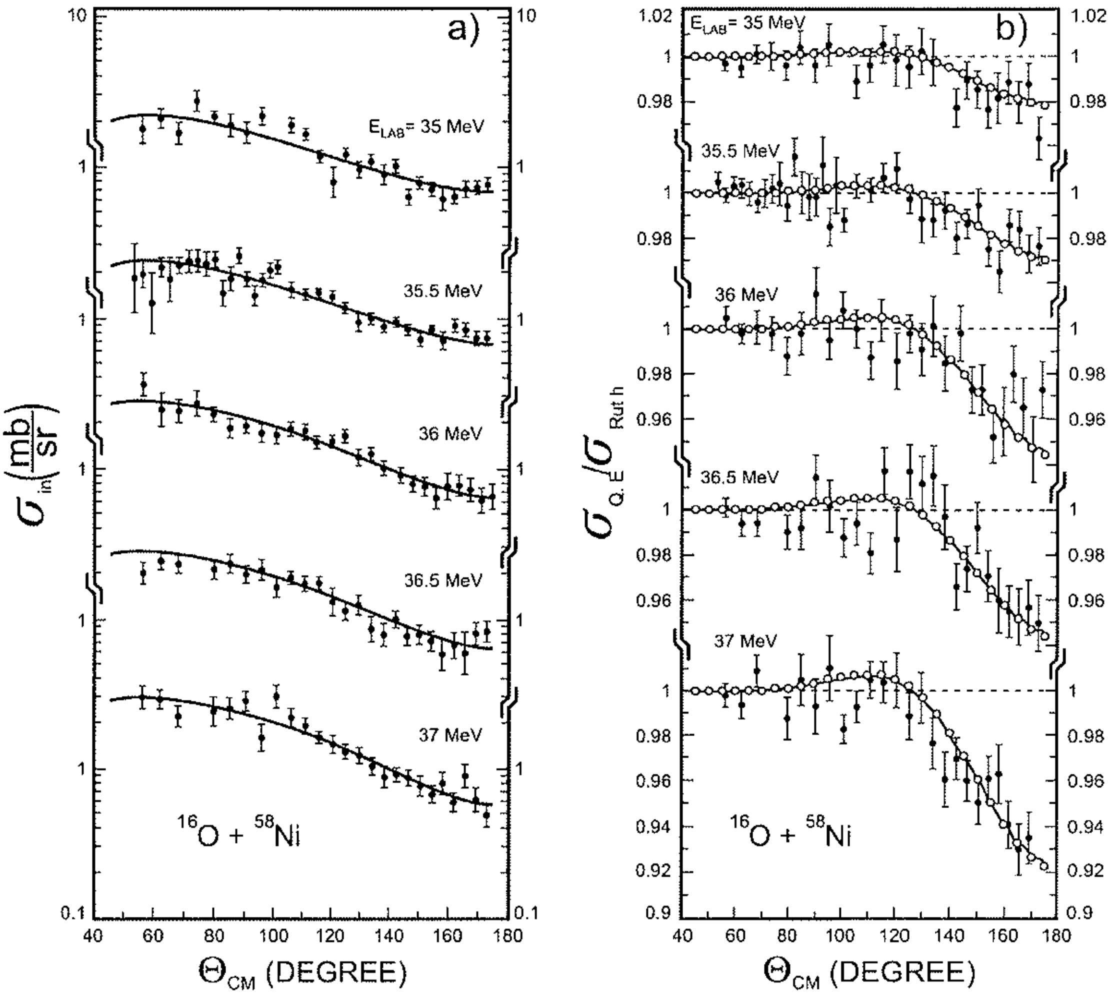

Fig. 9. (a) Inelastic (excitation of the 2_1^+Ni state) and (b) quasi-elastic (elastic + inelastic) cross sections for the $^{16}O + ^{58}Ni$ system in several sub-barrier energies. In the CC data analysis, the parameters of the bare potential have been searched for the best data fits. The solid lines in the figure represent the result of these CC calculations. The open symbols represent optical model (OM) predictions for the quasi-elastic (QE) cross sections. The OMQE calculations have been performed by assuming that the corresponding optical potential is very similar to the bare potential obtained in the CC data analysis.

4. Comparison between potentials for systems involving the ^{16}O and ^{18}O nuclei

The elastic scattering data analyses for different systems in a very large energy range have resulted in phenomenological optical potentials with significant dependence on the bombarding energy [12]. Several theoretical models have been developed to account for this energy-dependence; one of these associates the energy-dependence with nonlocal quantum effects related to the exchange of nucleons between target and projectile [5–8]. Within this model, the bare interaction V_N is connected with the folding potential V_F through

$$V_N(R, E) \approx V_F(R)e^{-4v^2/c^2}, \qquad (2)$$

where c is the speed of light and v is the local relative speed between the two nuclei,

$$v^2(R,E)=\frac{2}{\mu}\big[E-V_C(R)-V_N(R,E)\big]. \tag{3}$$

For the Coulomb interaction, V_C, we have used the expression for the double sharp cutoff potential [13].

The folding potential depends on the densities of the two partners in the collision

$$V_F(R)=\int \rho_1(r_1)\rho_2(r_2)u_0(\vec{R}-\vec{r}_1+\vec{r}_2)\,d\vec{r}_1\,d\vec{r}_2. \tag{4}$$

With the aim of providing a global description of the nuclear interaction, a systematization of nuclear densities has been proposed in Ref. [5], with basis on an extensive study involving charge distributions extracted from electron scattering experiments and theoretical densities calculated through the Dirac–Hartree–Bogoliubov model. This study has indicated that the two-parameter Fermi (2pF) distribution can be adopted to describe the nuclear densities, and a useful distinction between nucleon and matter distributions has been made. The radii of the 2pF distributions are well described by

$$R_i=1.31\,A_i^{1/3}-0.84\ \text{fm}, \tag{5}$$

where A is the number of nucleons of the nucleus. The nucleon and matter densities present average diffuseness values $a_N=0.50$ fm and $a_M=0.56$ fm, respectively. Due to effects of the structure of the nuclei, along the table of stable nuclides the R_i and a parameters vary around the corresponding average values. However, concerning the nuclear potential, the effects of the structure of the nuclei are mostly present at the surface and mainly related only to the diffuseness parameter [5].

Within this context, an extensive systematization of optical potential strengths extracted from heavy-ion elastic scattering data analyses at low and intermediate energies was performed [5]. The experimental potential strengths have been described within 25% precision, by combining Eqs. (2) and (4) through two different and equivalent methods. In the first alternative, the double-folding potential is treated in the usual interpretation: the nucleon densities and an effective nucleon–nucleon interaction for $u_0(\vec{r})$ are adopted in Eq. (4). The standard M3Y interaction "frozen" at 10 MeV/nucleon [5,7] has been assumed for the effective nucleon–nucleon interaction. In the other alternative, the matter densities are adopted in Eq. (4), with a zero-range delta function assumed for $u_0(\vec{r})$:

$$u_0(\vec{r})=V_0\delta(\vec{r}), \tag{6}$$

with $V_0=-456$ MeV fm^3. This zero-range alternative is interesting because it results in approximate analytical expressions for the folding potential [5]. For example, in the surface region

$$V_F(R\geqslant R_1+R_2)\approx V_0\rho_{01}\rho_{02}\pi a_M^2\mathcal{R}g(\tau)(1+s/a_M)e^{-s/a_M}, \tag{7}$$

with $s=R-(R_1+R_2)$, $\mathcal{R}=2R_1R_2/(R_1+R_2)$, $\tau=s/\mathcal{R}$. The ρ_{0i} are obtained from the normalization of the densities

$$4\pi\int_0^\infty \frac{\rho_{0i}}{1+e^{(r-R_i)/a_M}}r^2\,dr=A_i, \tag{8}$$

and the function g is defined by:

$$g(\tau) = \frac{1 + \tau + \tau^2\zeta/3 + a_M/\mathcal{R} + (a_M/\mathcal{R} + 1/2)e^{-s/a_M}}{1 + \zeta\tau}, \tag{9}$$

$\zeta = \mathcal{R}/(R_1 + R_2)$.

Expression (2) has accounted for the energy-dependence of experimentally extracted potential strengths for a large number of different systems in a very wide energy range [5–8]. At sub-barrier energies and for radii close to the barrier radius, Eq. (2) indicates that $V_N \approx V_F$. In order to compare potentials from different systems, we have defined a reduced quantity, V_{red}, which removes the dependence of the sub-barrier potential strengths on the radii of the nuclei,

$$V_{red} = \frac{V_N}{V_0 \rho_{01} \rho_{02} \mathcal{R} g(\tau)}. \tag{10}$$

Taking into account Eqs. (7) and (10), the reduced potential should be a universal function of s

$$V_{red}(s \geqslant 0) \approx \pi a_M^2 \left(1 + \frac{s}{a_M}\right) e^{-s/a_M}, \tag{11}$$

with the matter diffuseness close to the average value $a_M \approx 0.56$ fm [5].

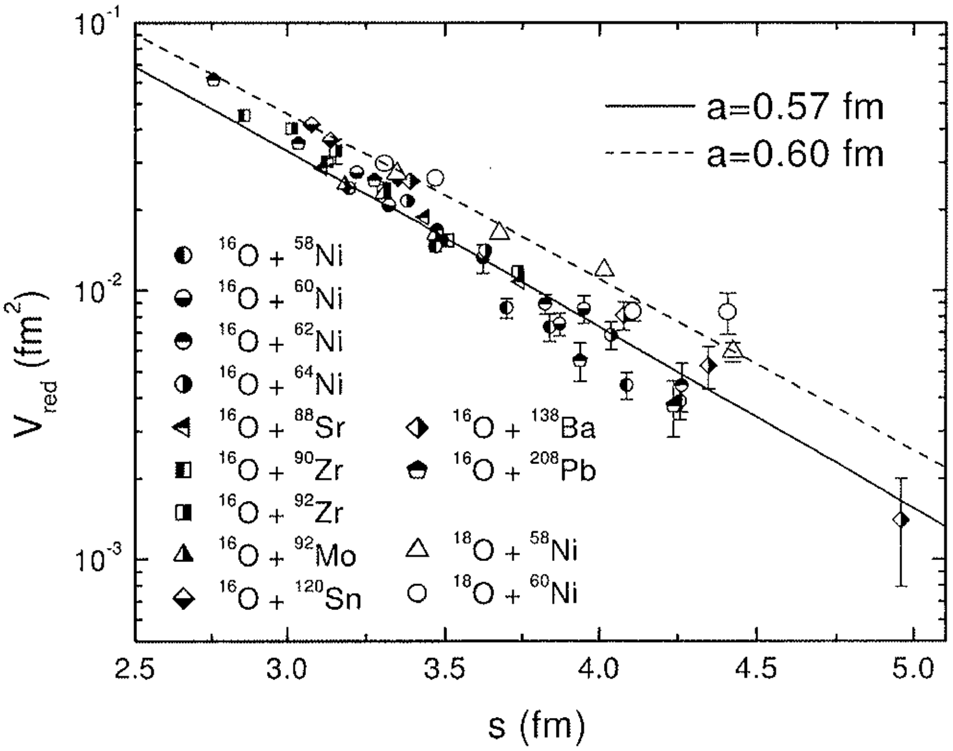

Fig. 10. The experimental reduced potential strength as a function of the reduced distance, s, for several systems involving the ^{16}O (semi-closed symbols) and ^{18}O (open symbols) nuclei as projectiles. The lines represent theoretical predictions, Eq. (11), with different diffuseness values.

In Fig. 10, the experimental reduced potential strengths (calculated from Eq. (10)) are presented for several systems involving the ^{16}O and ^{18}O nuclei, as obtained from sub-barrier data analyses. The experimental results are in agreement with the theoretical prediction, Eq. (11), but different matter diffuseness values $a_{\mathrm{M}} = 0.57$ fm and 0.60 fm are found for the ^{16}O and ^{18}O sets, respectively (see Fig. 10).

5. Determination of the nuclear density for the two valence neutrons of the ^{18}O nucleus

As we have discussed in Section 4, the experimentally extracted potential strengths for systems with ^{16,18}O as projectiles are compatible with the folding potential, using densities with the shape of Fermi distributions, radii obtained from Eq. (5), and matter diffuseness values $a_{\mathrm{M}} = 0.57$ fm and $a_{\mathrm{M}} = 0.60$ fm. In this sense, the analysis presented in Section 4 provides information about the nuclear densities of the partners in the collision. Another form of analysing the same set of cross section data, which determines the densities in a more direct procedure than that of Section 4, has been presented in Refs. [14,15]. If the nonlocal model is assumed for the heavy-ion interaction and the density of one nucleus is known, an unfolding method can be used to extract the density of the other nucleus from the data analyses. The density is obtained from a procedure similar to that used in the determination of potential strengths at the sensitivity radii. Details of the method can be found in Refs. [14,15]. Fig. 11 contains the ^{16}O and ^{18}O experimental density values at the corresponding sensitivity radii obtained from the data analyses of several angular distributions for different systems. We mention that the results presented in Fig. 11 refer to the nucleon densities instead of the matter densities. In obtaining the experimental density values for the projectile through the unfolding procedure, the choice of the density of the target nucleus is a possible source of systematical errors [14,15]. In our analysis, we have used different theoretical models to calculate the densities of the several target nuclei [14]. Taking into account this point, the good agreement among the results for the density of a same projectile obtained from data analyses for systems with different targets is indicative of the consistency of our analyses. As a further test of our method, we also have shown that the theoretical densities assumed for the targets provide good predictions for electron scattering data [14,15]. We point out that the same theoretical ^{58,60}Ni densities were used in the extraction of the densities for both projectiles ^{16,18}O. Therefore, even if systematical errors would exist they probably would partly cancel in the comparison between the results for the ^{16}O and ^{18}O nuclei. The sub-barrier data analysis gives information about the density at the surface region, while inner distances are probed through the data at intermediate energies. For example, the analysis for the ^{16}O + ^{16}O system at $E_{\mathrm{Lab}} = 1120$ MeV has provided information (see Fig. 11) about the ^{16}O density at $r \approx 2$ fm. Eq. (2) shows that at such high energy the nonlocality reduces the nuclear potential strength by about one order of magnitude in comparison with the folding potential, and this effect is very important in obtaining a reasonable experimental value for the density.

Theoretical predictions (dashed lines in Fig. 11) from the Dirac–Hartree–Bogoliubov (DHB) model [16] do not match the experimental results at the surface region. Consistent

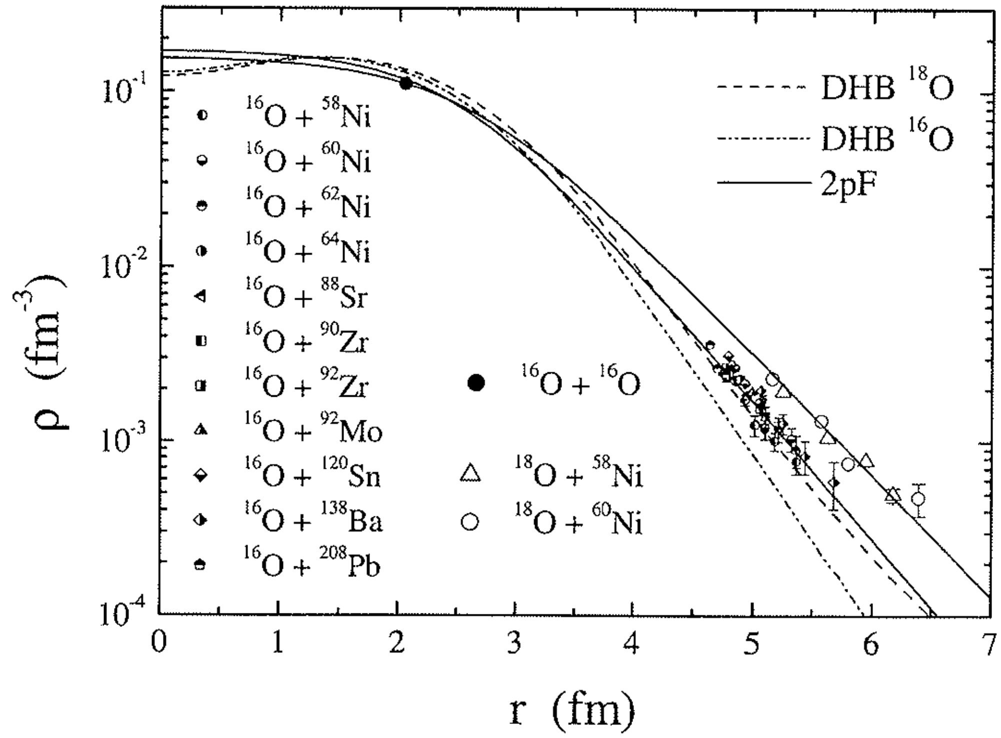

Fig. 11. Experimental nucleon density values for the ^{16}O (semi-closed symbols) and ^{18}O (open symbols) nuclei, as obtained from sub-barrier data analyses for different systems and bombarding energies. The closed symbol represents a density value for the ^{16}O nucleus from intermediate energy data analyses. The lines correspond to theoretical Dirac–Hartree–Bogoliubov (DHB) calculations and two-parameter Fermi (2pF) distributions.

with this fact, theoretical predictions for electron scattering on the ^{16}O nucleus using the DHB charge distribution also do not fit the data [14]. The solid lines in Fig. 11 represent Fermi distributions for the ^{16,18}O nuclei, with radii obtained from Eq. (5). The diffuseness found for the ^{16}O nucleus ($a_N = 0.55$ fm) is significantly smaller than that for the ^{18}O ($a_N = 0.60$ fm). The DHB theoretical calculations indicate that the difference between the ^{18}O and ^{16}O total nucleon densities is mainly due to the corresponding difference between the respective neutron distributions (see Fig. 12). Fig. 13 presents the contributions to the ^{18}O neutron density of different DHB wave-function components. The results for the ^{16}O nucleus are very similar to those for the ^{18}O, but without the d5/2$^+$ component. We have found experimental values for the d5/2$^+$ component by considering the difference between the total ^{16,18}O nucleon densities at the sensitivity radii. In such a subtraction, we have assumed that the Fermi distribution with $a_N = 0.55$ fm (see Fig. 11) is representative of the experimental ^{16}O density. The experimental results for the d5/2$^+$ component present a similar slope but larger density values in comparison with the theoretical DHB prediction (see Fig. 13). An analysis of the single-particle levels of the theoretical calculations shows, as one might expect, that the falloff of the density in the surface region is roughly determined by the least bound levels. The NL3 potential parameters [17,18] that have been used in the Dirac–Hartree–Bogoliubov calculations [16] were adjusted to reproduce binding energies and charge and neutron radii across the periodic table. It did not take into

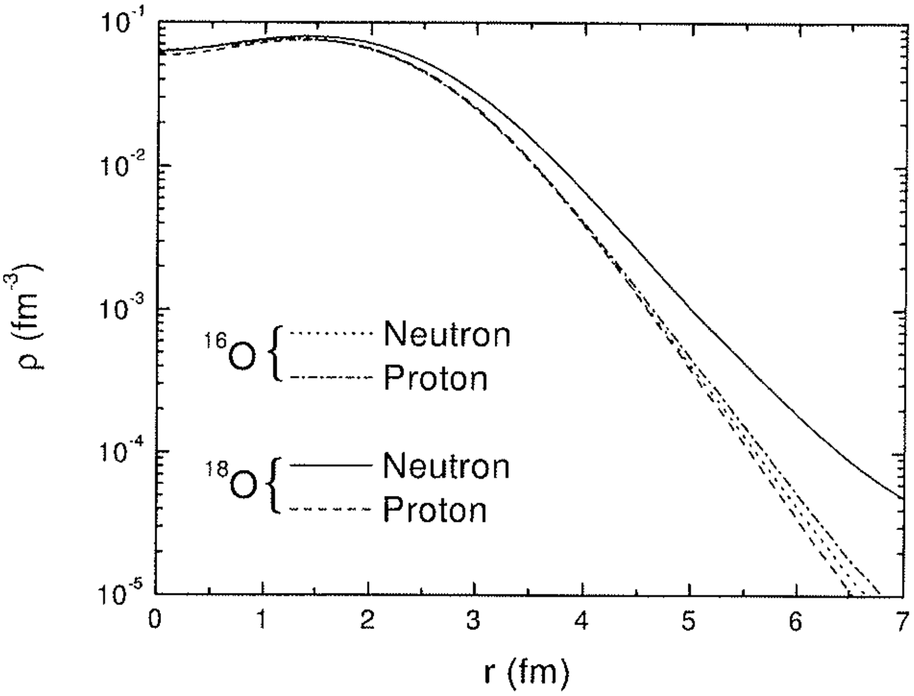

Fig. 12. Comparison among proton and neutron theoretical Dirac–Hartree–Bogoliubov densities for the ^{16,18}O nuclei.

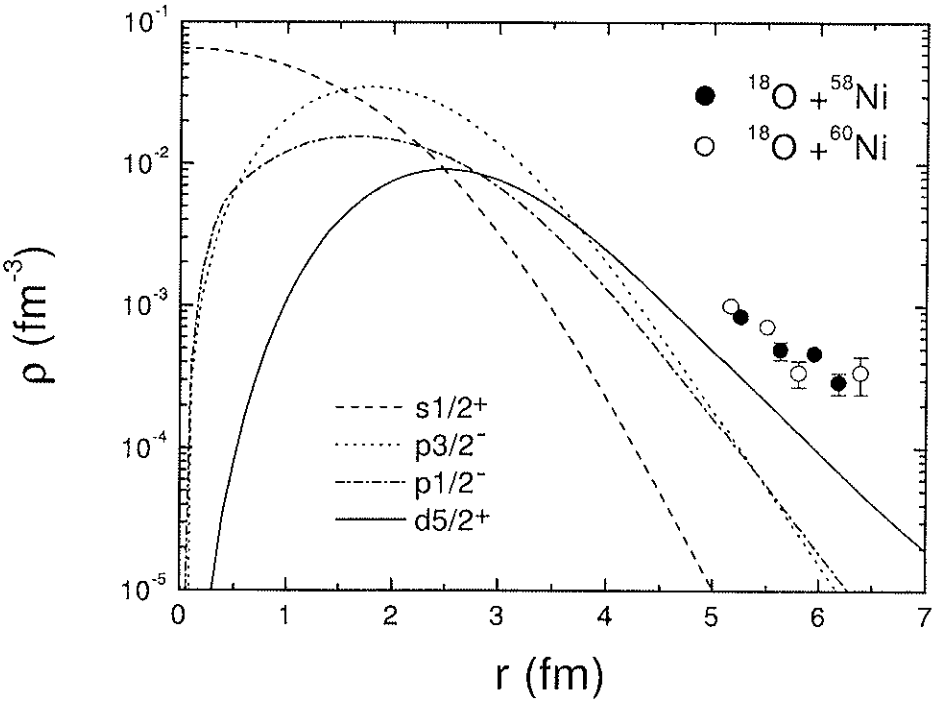

Fig. 13. Theoretical DHB predictions for the ^{18}O neutron density distributed in the main orbitals. The data (open and closed symbols) correspond to the difference between the experimental total nucleon densities for the ^{16,18}O nuclei (see text for details).

account single-particle properties, which suggest a direction for future improvements in such a parameter set.

6. Conclusion

In this work, we have presented quasi-elastic and reaction channel data at sub-barrier energies for systems involving the ^{18}O as projectile and we have extended our study to other data sets earlier obtained for systems with the ^{16}O nucleus. In our optical model quasi-elastic data analysis, the imaginary part of the potential is based only on very fundamental grounds: the lack of extra surface absorption. A nonlocal model is assumed to describe the real part of the interaction, which at sub-barrier energies can be associated directly with the folding potential. The energy-dependence of the sensitivity radius has permitted the determination of the nuclear potential over a large range of distances around the barrier radius. The experimental diffuseness value found for the potentials of systems with ^{18}O is significantly larger than that for the ^{16}O nucleus. Within this context, a significant difference between the diffuseness for the densities of the ^{16,18}O nuclei is expected.

If the target densities are known, the density of the projectile can be extracted from the data analysis in a more direct procedure. In these cases, the results for the ^{16,18}O nuclear densities are consistently independent of the target nucleus. The extracted value for the diffuseness of the ^{18}O nucleus is significantly larger than that for ^{16}O. The corresponding difference gives information about the contribution of the two ^{18}O extra neutrons, in particular that in the $d5/2^+$ level.

Acknowledgements

This work was partially supported by Financiadora de Estudos e Projetos (FINEP), Fundação de Amparo à Pesquisa do Estado de São Paulo (FAPESP), and Conselho Nacional de Desenvolvimento Científico e Tecnológico (CNPq).

References

[1] L.C. Chamon, D. Pereira, E.S. Rossi Jr., C.P. Silva, R. Lichtenthaler Filho, L.C. Gomes, Nucl. Phys. A 582 (1995) 305.
[2] L.C. Chamon, D. Pereira, E.S. Rossi Jr., C.P. Silva, H. Dias, L. Losano, C.A.P. Ceneviva, Nucl. Phys. A 597 (1996) 253.
[3] M.A.G. Alvarez, L.C. Chamon, D. Pereira, E.S. Rossi Jr., C.P. Silva, L.R. Gasques, H. Dias, M.O. Roos, Nucl. Phys. A 656 (1999) 187.
[4] C.P. Silva, M.A.G. Alvarez, L.C. Chamon, D. Pereira, M.N. Rao, E.S. Rossi Jr., L.R. Gasques, M.A.E. Santo, R.M. Anjos, J. Lubian, P.R.S. Gomes, C. Muri, B.V. Carlson, S. Kailas, A. Chatterjee, P. Singh, A. Shivastava, K. Mahata, S. Santra, Nucl. Phys. A 679 (2001) 287.
[5] L.C. Chamon, B.V. Carlson, L.R. Gasques, D. Pereira, C. De Conti, M.A.G. Alvarez, M.S. Hussein, M.A. Candido Ribeiro, E.S. Rossi Jr., C.P. Silva, Phys. Rev. C, in press.
[6] M.A.C. Ribeiro, L.C. Chamon, D. Pereira, M.S. Hussein, D. Galetti, Phys. Rev. Lett. 78 (1997) 3270.

[7] L.C. Chamon, D. Pereira, M.S. Hussein, M.A.C. Ribeiro, D. Galetti, Phys. Rev. Lett. 79 (1997) 5218.
[8] L.C. Chamon, D. Pereira, M.S. Hussein, Phys. Rev. C 58 (1998) 576.
[9] I.J. Thompson, Comput. Phys. Rep. 7 (1988) 167.
[10] S. Raman, C.H. Malarkey, W.T. Milner, C.W. Nestor Jr., P.H. Stelson, At. Data Nucl. Data Tables 36 (1987) 1.
[11] E.S. Rossi Jr., PhD Thesis, Universidade de São Paulo, Brazil, 2001.
[12] M.E. Brandan, G.R. Satchler, Phys. Rep. 285 (1992) 142, and references therein.
[13] R.M. Devries, M.R. Clover, Nucl. Phys. A 243 (1975) 528.
[14] M.A.G. Alvarez, E.S. Rossi Jr., C.P. Silva, L.R. Gasques, L.C. Chamon, D. Pereira, M.N. Rao, B.V. Carlson, C. De Conti, R.M. Anjos, P.R.S. Gomes, J. Lubian, S. Kailas, A. Chatterjee, P. Singh, Phys. Rev. C 65 (2002) 014602.
[15] L.R. Gasques, L.C. Chamon, C.P. Silva, D. Pereira, M.A.G. Alvarez, E.S. Rossi Jr., V.P. Likhachev, B.V. Carlson, C. De Conti, Phys. Rev. C 65 (2002) 044314.
[16] B.V. Carlson, D. Hirata, Phys. Rev. C 62 (2000) 054310.
[17] G.A. Lalazissis, J. Konig, P. Ring, Phys. Rev. C 55 (1997) 540.
[18] Z. Patyk, A. Baran, J.F. Berger, J. Decharge, J. Dobaczewski, P. Ring, A. Sobiczewski, Phys. Rev. C 59 (1999) 704.

PHYSICAL REVIEW C, VOLUME 65, 044314

Determination of the ^{12}C nuclear density through heavy-ion elastic scattering experiments

L. R. Gasques,[1] L. C. Chamon,[1] C. P. Silva,[1] D. Pereira,[1] M. A. G. Alvarez,[1] E. S. Rossi, Jr.,[1] V. P. Likhachev,[2] B. V. Carlson,[3] and C. De Conti[3]

[1]*Departamento de Física Nuclear, Instituto de Física da Universidade de São Paulo, Caixa Postal 66318, 05315-970 São Paulo, SP, Brazil*

[2]*Departamento de Física Experimental, Instituto de Física da Universidade de São Paulo, Caixa Postal 66318, 05315-970 São Paulo, SP, Brazil*

[3]*Departamento de Física, Instituto Tecnológico de Aeronáutica, Centro Técnico Aeroespacial, São José dos Campos, SP, Brazil*

(Received 14 December 2001; published 25 March 2002)

Precise elastic scattering differential cross sections have been measured for the ^{12}C+^{58}Ni,^{208}Pb systems at sub-barrier energies. The corresponding bare potentials have been determined at interaction distances larger than the respective barrier radii, and the results have been compared with those from an early extensive systematics for the nuclear potential. The present data have been combined with others for the ^{12}C + ^{12}C,^{208}Pb systems at intermediate energies, in order to extract the ^{12}C ground-state nuclear density through an unfolding method.

DOI: 10.1103/PhysRevC.65.044314 PACS number(s): 24.10.Ht, 21.10.Ft, 21.10.Gv

I. INTRODUCTION

In this work, we present elastic scattering differential cross sections for the ^{12}C+^{58}Ni,^{208}Pb systems at sub-barrier energies. One of the purposes of the experiments was the determination of the corresponding nuclear potentials in a surface region near the respective barrier radii. The method was earlier applied to several systems involving the ^{16}O nucleus as projectile [1–4]. As discussed in these previous works, the imaginary part of the optical potential is negligible at sub-barrier energies due to the corresponding very small reaction cross sections. Thus, provided that a realistic shape in the surface region is assumed for the potential, the elastic scattering data analysis in this sub-barrier energy region unambiguously determines the real part of the interaction. The optical potential is composed of the bare and polarization potentials, the latter containing the contribution arising from nonelastic couplings. The real part of the polarization has been estimated earlier [1–3] through extensive coupled-channel calculations for the ^{16}O sub-barrier data set, and represents about 10% in comparison with the bare interaction. A quite complete coupled-channel calculation has also been performed for the ^{12}C+^{208}Pb system [5], and a good description of elastic, inelastic, transfer, and fusion cross section data has been obtained for energies above the barrier. An extrapolation of the calculation (see Fig. 8 of Ref. [5]) to $54.5 \leqslant E_{\mathrm{lab}} \leqslant 57$ MeV, an energy region which corresponds to the data of the present work, indicates that the polarization represents about 13% of the real part of the optical potential. Therefore, it is reasonable to assume that the experimentally extracted potential strengths for the ^{12}C + ^{58}Ni,^{208}Pb systems at sub-barrier energies can be associated to the bare potential within about 10% precision.

In a recent work [6], an extensive systematics of optical potential strengths extracted from heavy-ion elastic scattering data analyses at low and intermediate energies was presented. The energy dependence of the nuclear potential has been accounted for within a model based on the nonlocal nature of the interaction [6–9]. The systematics indicates that the heavy-ion potential can be described in a global way, through a double-folding shape which basically presents a simple dependence only on the number of nucleons of the colliding nuclei. The results for the nuclear potential of the ^{12}C+^{58}Ni,^{208}Pb systems obtained in the present work are in good agreement with such systematics for the bare interaction.

If the nonlocal model is assumed for the interaction, an unfolding method can be used to extract ground-state nuclear densities from heavy-ion elastic scattering data analyses. The method has been successfully applied in the experimental determination of densities for the ^{16,18}O nuclei [10]. In the present work, we apply the same procedure in the data analyses for the ^{12}C+^{58}Ni,^{208}Pb systems at sub-barrier energies, with the aim of obtaining the ^{12}C nuclear density at the surface region. The method is extended to the ^{12}C + ^{12}C,^{208}Pb systems at intermediate energies, and in this case information about the ^{12}C density at much inner distances is obtained.

The paper is organized as follows. In Sec. II, we present the experimental results and the determination of the bare potential strengths from optical model data analyses for the ^{12}C+^{58}Ni,^{208}Pb systems. A brief summary of the nonlocal model, and a comparison between the present results and the early systematics for the nuclear potential are contained in Sec. III. The extraction of the ^{12}C density and the limitations of the method are discussed in details in Sec. IV. Section V contains the main conclusions.

II. EXPERIMENTAL RESULTS AND DATA ANALYSIS

The measurements were made at the São Paulo 8UD Pelletron Accelerator, Brazil. The detecting system has already been described in Ref. [1]. The thickness of the targets were about 60 μg/cm^2. Figure 1 exhibits the elastic scattering cross sections for the ^{12}C+^{58}Ni,^{208}Pb systems in several sub-barrier energies.

In the optical model calculations, we have adopted a procedure similar to that described in the analysis of the sub-barrier data for the ^{16}O+^{58,60,62,64}Ni, ^{88}Sr, ^{90,92}Zr, ^{92}Mo,

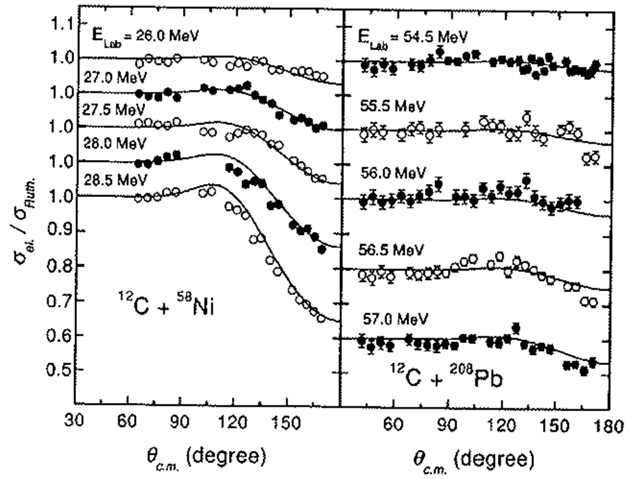

FIG. 1. Elastic scattering angular distributions for the ^{12}C $+^{58}$Ni, ^{208}Pb systems at several sub-barrier energies. The solid lines represent optical model predictions, in which the nonlocal model is assumed for the real part of the interaction. Note that the cross section is represented in a linear scale.

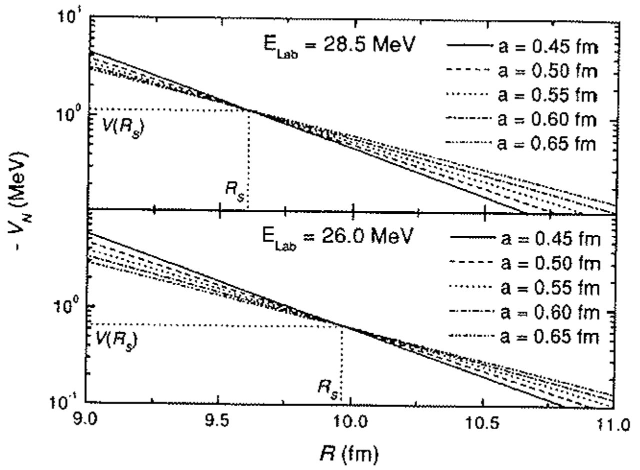

FIG. 2. The real part of the optical potential for the ^{12}C+^{58}Ni system at two different energies, as obtained by optical model data fits for several values of the diffuseness parameter. The potentials cross at the sensitivity radii R_S, where the corresponding potential strengths are determined without ambiguities.

^{120}Sn, ^{138}Ba, ^{208}Pb systems [1–4]. We have adopted a Woods-Saxon shape for the optical potential, with an inner imaginary part which takes into account the rather small internal absorption from barrier penetration. The values assumed for the parameters of the imaginary part of the potential result in very small strengths at the surface region. This procedure must be adopted in the sub-barrier data analysis due to the negligible cross sections of peripheral reaction channels. Concerning depth variations of this absorptive potential, no sensitivity in the elastic scattering cross section predictions has been detected. The radius parameters of the real part of the optical potential were fixed at $r_0(A_1^{1/3}+A_2^{1/3})$, with $r_0=1.06$ fm, and the depth and diffuseness parameters were searched for the best data fits. For each angular distribution, we have found a family of potentials which give equivalent fits. These potentials cross (see Fig. 2) at a particular distance R_S, hereafter referred to as the sensitivity radius.

The heavy-ion elastic scattering is sensitive to averages of the potential over distances comparable to the wavelength of the relative motion; therefore the determination of a sharply defined sensitivity radius presents some dependence on the shape assumed for the real part of the optical potential [11]. In most cases, including those of the present work, the scattering of heavy ions is sensitive only to the potential for a very restricted range of surface distances around the sensitivity radius. In this region, a realistic potential, such as the double folding, should present an approximately exponential shape with diffuseness values around 0.6 fm [12]. Thus, in order to avoid ambiguities in the potential determination, we have assumed a realistic shape for the potential in the surface region. Indeed, such an exponential behavior with realistic diffuseness values is presented by the Woods-Saxon potential adopted in our analyses (see Fig. 2).

The sensitivity radius is energy dependent (see Fig. 2), because at sub-barrier energies it is related to the classical turning point. We have used this fact to characterize the nuclear potential in the surface region (see Fig. 3). For such large interaction distances, the shape of the potential is nearly an exponential (solid lines in Fig. 3), with a diffuseness value about 0.64 fm. Similar behavior has been observed for systems with ^{16}O as the projectile [1–4]. The nuclear potentials equal 1 MeV at $R=9.7$ fm and $R=12.5$ fm (see Fig. 3) for the ^{12}C+^{58}Ni and ^{12}C+^{208}Pb systems, respectively. As discussed in the next section, this difference between the nuclear potentials is directly connected with the corresponding different densities of the ^{58}Ni and ^{208}Pb nuclei.

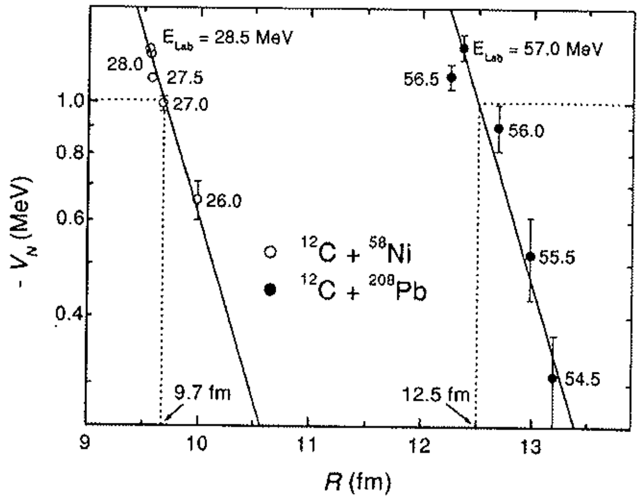

FIG. 3. The nuclear potential strength as a function of the sensitivity radius for the ^{12}C+^{58}Ni, ^{208}Pb systems. The bombarding energies of the elastic scattering angular distributions in which the sensitivity radii have been determined are indicated in the figure. The solid lines represent exponentials with diffuseness value 0.64 fm. The radii at which the potentials equal 1 MeV are indicated in the figure.

III. COMPARISON WITH THE NONLOCAL MODEL

The elastic scattering data analyses for different systems in a very large energy range have resulted in phenomenological optical potentials with significant dependence on the bombarding energies [13]. Several theoretical models have been developed to account for this energy dependence; one of them associates this dependence with nonlocal quantum effects related to the exchange of nucleons between target and projectile [6–9]. Within this model, the bare interaction V_N is connected with the folding potential V_F through

$$V_N(R,E) \approx V_F(R) e^{-4v^2/c^2}, \tag{1}$$

where c is the speed of light and v is the local relative speed between the nuclei

$$v^2(R,E) = \frac{2}{\mu}[E - V_C(R) - V_N(R,E)]. \tag{2}$$

For the Coulomb interaction V_C we have used the expression for the double sharp cutoff potential [14].

The folding potential depends on the densities of the two partners in the collision

$$V_F(R) = \int \rho_1(r_1)\rho_2(r_2) u_0(\vec{R} - \vec{r}_1 + \vec{r}_2) d\vec{r}_1 d\vec{r}_2. \tag{3}$$

With the aim of providing a global description of the nuclear interaction, in Ref. [6] a systematization of nuclear densities has been proposed, based on an extensive study involving charge distributions extracted from electron scattering experiments and theoretical densities calculated through the Dirac-Hartree-Bogoliubov model. This study has indicated that the two-parameter Fermi (2PF) distribution can be adopted to describe the nuclear densities, and an useful distinction between nucleon and matter distributions has been made. The radii of the 2PF distributions are well described by

$$R_i = 1.31 A_i^{1/3} - 0.84 \text{ fm}, \tag{4}$$

where A is the number of nucleons of the nucleus. The nucleon and matter densities present average diffuseness values $a_N = 0.50$ fm and $a_M = 0.56$ fm, respectively. Due to effects of the structure of the nuclei, along the table of stable nuclides the R_i and a parameters vary around the corresponding average values . However, concerning the nuclear potential, the effects of the structure of the nuclei are mostly present at the surface and mainly related only to the diffuseness parameter [6].

Within this context, an extensive systematization of optical potential strengths extracted from heavy-ion elastic scattering data analyses at low and intermediate energies was performed [6]. The experimental potential strengths have been described within 25% precision, by combining Eqs. (1) and (3) through two different and equivalent methods. In the first alternative, the double-folding potential is treated in the usual interpretation [12]: the nucleon densities and an effective nucleon-nucleon interaction for $u_0(\vec{r})$ are adopted in Eq. (3). The standard M3Y interaction "frozen" at 10 MeV/nucleon [6,8] has been assumed for the effective nucleon-nucleon interaction. In the other alternative, the matter densities are adopted in Eq. (3), with a zero-range delta function assumed for $u_0(\vec{r})$:

$$u_0(\vec{r}) = V_0 \delta(\vec{r}), \tag{5}$$

with $V_0 = -456$ MeV fm^3. This zero-range alternative is interesting because it results in approximate analytical expressions for the folding potential [6]. For example, in the surface region

$$V_F(R \geq R_1 + R_2) \approx V_0 \rho_{01} \rho_{02} \pi a_M^2 \mathcal{R} g(\tau)(1 + s/a_M) e^{-s/a_M}, \tag{6}$$

with $s = R - (R_1 + R_2)$, $\mathcal{R} = 2R_1R_2/(R_1 + R_2)$, $\tau = s/\mathcal{R}$. The ρ_{0i} are obtained from the normalization of the densities

$$4\pi \int_0^\infty \frac{\rho_{0i}}{1 + e^{(r - R_i)/a_M}} r^2 dr = A_i, \tag{7}$$

and the function g is defined by

$$g(\tau) = \frac{1 + \tau + \tau^2 \zeta/3 + a_M/\mathcal{R} + (a_M/\mathcal{R} + 1/2) e^{-s/a_M}}{1 + \zeta \tau}, \tag{8}$$

$\zeta = \mathcal{R}/(R_1 + R_2)$.

Expression (1) has accounted for the energy dependence of experimentally extracted potential strengths for a large number of different systems in a very wide energy range [6–9]. At sub-barrier energies and for radii close to the barrier radius, Eq. (1) indicates that $V_N \approx V_F$. In order to compare potentials from different systems, we have defined a reduced quantity V_{red}, which removes the dependence of the sub-barrier potential strengths on the radii of the nuclei:

$$V_{\text{red}} = \frac{V_N}{V_0 \rho_{01} \rho_{02} \mathcal{R} g(\tau)}. \tag{9}$$

Taking into account Eqs. (6) and (9), the reduced potential should be a universal function of s

$$V_{\text{red}}(s \geq 0) \approx \pi a_M^2 (1 + s/a_M) e^{-s/a_M}, \tag{10}$$

with the matter diffuseness approximately system independent and close to the average value $a_M \approx 0.56$ fm [6].

The experimental reduced potential strengths for the ^{12}C + ^{58}Ni,^{208}Pb systems, calculated through Eq. (9), are in good agreement (see Fig. 4) with the predictions [Eq. (10) with $a_M = 0.56$ fm] of the early systematics for the bare potential. Assuming the nonlocal model with the densities proposed in such a systematics, good predictions for the elastic scattering cross sections are obtained (see the solid lines in Fig. 1).

In order to extend the analysis to higher energies, experimental elastic scattering angular distributions (from Refs. [15–17]) at several intermediate energies for the ^{12}C + ^{12}C,^{208}Pb systems have been included in our study. In the sub-barrier case the imaginary potential used in the optical

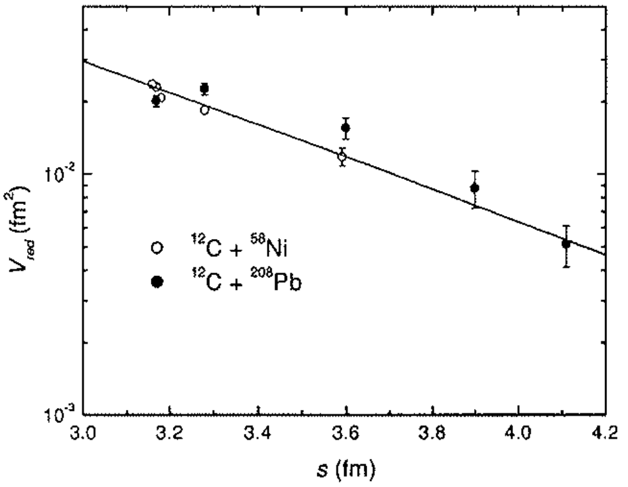

FIG. 4. The experimental reduced potential strength as a function of the reduced distance s for the ^{12}C+^{58}Ni, ^{208}Pb systems. The solid line represents the theoretical prediction, Eq. (10) with $a_M = 0.56$ fm.

model calculations is based on very fundamental ground: the lack of surface absorption. Provided this condition is assumed, the results of the analyses at sub-barrier energies are independent of the parameters adopted for the imaginary potential. With the purpose of treating the absorptive part of the potential within a fundamental context also for intermediate energies, we have assumed [Eq. (11)] the Lax-type interaction with Pauli blocking [18], which is the single-scattering term of the Glauber multiple scattering theory [19]

$$W(R,E) = -\frac{E}{k_N}\sigma_T^{NN}(E)\int \rho_1(|\vec{R}-\vec{r}|)\rho_2(r)d\vec{r}, \quad (11)$$

where $\sigma_T^{NN}(E)$ is the average nucleon-nucleon total cross section. In Fig. 5, a comparison between data and theoretical predictions (solid lines) for the angular distributions at intermediate energies is presented. Again we have assumed the nonlocal model for the real part of the interaction with the densities proposed in the systematics of Ref. [6]. Although the calculated cross section shows stronger oscillatory behavior, the magnitude, however, is in reasonable agreement with the data. Part of the theoretical oscillatory pattern could be damped in the data due to the angular aperture of the collimation system used in the experiments. We point out that no adjustable parameter has been used in either of the real and imaginary parts of the potential. It must be also remembered that only the single-scattering term of the multiple scattering series of Glauber has been included in the absorptive part of the potential, although higher order terms are quite likely to contribute significantly to the cross section. As we showed before [8], better fits can be obtained using a Woods-Saxon shape for the imaginary potential with three adjustable parameters. However, we regard the present approach as more fundamental.

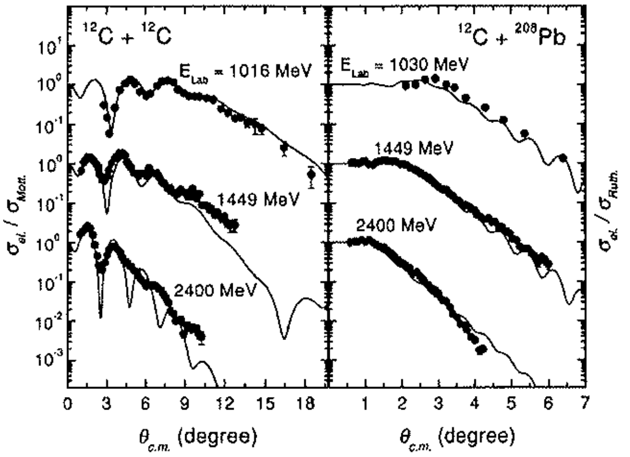

FIG. 5. Elastic scattering angular distributions for the ^{12}C + ^{12}C, ^{208}Pb systems at several intermediate energies. The solid lines represent optical model predictions, in which the free-parameter nonlocal model and the Lax-type interaction are assumed for the real and imaginary parts of the potential, respectively.

IV. DETERMINATION OF THE ^{12}C NUCLEAR DENSITY

As we have discussed in Sec. III, the experimentally extracted potential strengths for the ^{12}C+^{58}Ni,^{208}Pb systems are compatible with the systematics for the nuclear potential of Ref. [6]. That systematics is based on densities with the shape of Fermi distributions, radii obtained from Eq. (4), and average diffuseness values $a_M = 0.56$ fm and $a_N = 0.50$ fm for the matter and nucleon distributions, respectively. In this sense, the analysis presented in Sec. III provides information about the nuclear densities of the partners in the collision. In this section, we present another form of analyzing the same set of cross section data, which determines the densities in a more direct manner than that of Sec. III. If the nonlocal model is assumed for the heavy-ion interaction and the density of one nucleus is known, an unfolding method can be used to extract the density of the other nucleus from the elastic scattering data analyses. In Fig. 6, we compare the data (from Refs. [20–22]) with predictions for electron scattering cross sections on several nuclei. In the theoretical calculations, we have used charge distributions derived from the Dirac-Hartree-Bogoliubov (DHB) model [23]. The predictions are in good agreement with the data for the heavier nuclei, but discrepancies are observed for the ^{12}C and ^{16}O. This fact is an indication that the heavier the nucleus is, the more realistic is the theoretical density calculated through the DHB model. Therefore, we consider that the ^{58}Ni and ^{208}Pb densities are well described by the DHB calculations, and we have used the unfolding method to determine the ^{12}C nuclear density.

In this section, the double-folding potential is considered in the usual interpretation: the nucleon densities and the M3Y effective nucleon-nucleon interaction are adopted in Eq. (3). The ^{12}C density is extracted from data analyses within a procedure similar to that used in the determination of potential strengths at the sensitivity radii. We have assumed the Fermi distribution to describe the ^{12}C nucleon density, with diffuseness (a_N) and radius (R_i) searched for the best data fits, and with the ρ_{0i} parameter determined by

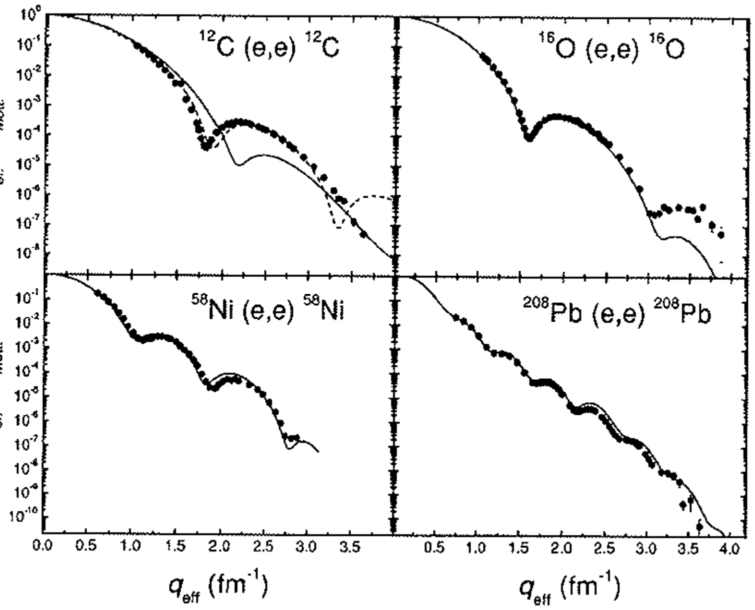

FIG. 6. Experimental electron scattering cross sections for the ^{12}C, ^{16}O, ^{58}Ni, and ^{208}Pb nuclei as a function of the effective momentum transferred. The solid lines represent theoretical predictions using charge distributions derived from Dirac-Hartree-Bogoliubov calculations. The dashed line in the ^{12}C case represents calculations based on a 2PF distribution (see text for details).

the normalization condition [Eq. (7)]. The real part of the optical potential is obtained from Eqs. (1) and (3), and has no adjustable parameters except those (a_N and R_i) connected only with the quantity to be determined: the ^{12}C nucleon density. For each angular distribution, we have found a family of densities which give equivalent data fits. These densities cross at two particular radii (see Fig. 7, top), and we associate only one of these radii to the sensitivity radius (r_S) for the density. To choose r_S, we have used the notch test (Fig. 7, bottom), in which a spline with a Gaussian shape is included in the ^{12}C density, and the variation of the chi-square is studied as a function of the position of this perturbation. The crossing chosen as the sensitivity radius is that closest to the center of the region which affects significantly the elastic scattering data fit.

The determination of the error bar for the density at the sensitivity radius is illustrated in Fig. 8 for a particular elastic scattering angular distribution. At r_S the data extracted density value does not depend on the diffuseness assumed for the distribution. Thus, the dependence of the total chi-square on R_i is studied for a fixed a_N value, and the parameters that correspond to the minimum value $\chi^2_{\min}$ and to $\chi^2_{\min}+\chi^2_{\min}/n$ are found [see the determination of $R_{0\min}$, R_{0-}, and R_{0+} in Fig. 8(a)]; n is the number of experimental data points of the angular distribution. Figure 8(b) presents the Fermi distributions for the $R_{0\min}$, R_{0-}, and R_{0+} values, and the respective determination of the error bar for the density at r_S.

Similar to the case of the potential determination, the sensitivity radius for the density is energy dependent and this fact allows the characterization of the density over a large range of distances. Figure 9(a) contains the ^{12}C experimental nucleon density values at the corresponding sensitivity radii obtained from data analyses of several angular distributions. The sub-barrier elastic scattering data gives information about the density at the surface region, while inner distances are probed through the data at intermediate energies. We point out that data analyses for different systems provide consistent similar results for the ^{12}C density. The theoretical prediction from the DHB model (see Fig. 9) does not match the experimental results at the surface region. Taking into account the discussion about the nuclear potential of Sec. III,

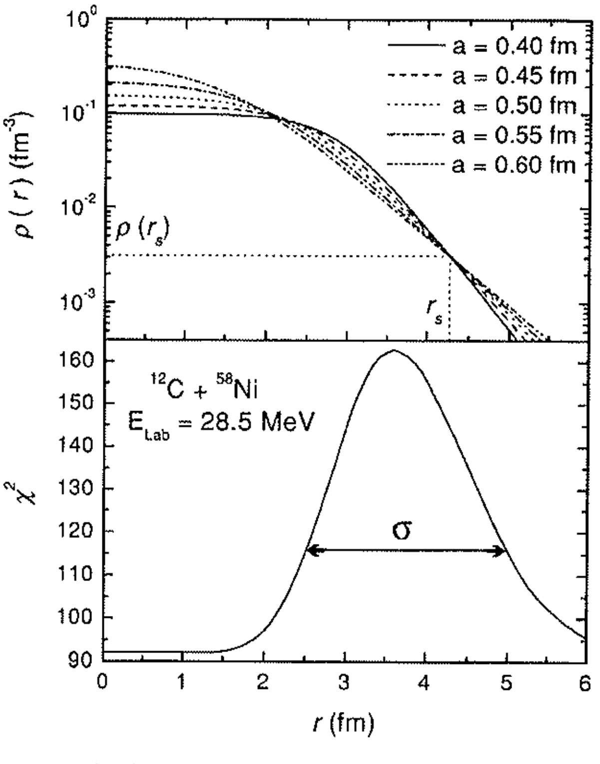

FIG. 7. (Top) Example of the determination of the sensitivity radius r_S and the corresponding experimental value for the ^{12}C nucleon density, using two-parameter Fermi distributions which give equivalent data fits for the angular distribution of the ^{12}C + ^{58}Ni system at $E_{\mathrm{lab}}=28.5$ MeV. (Bottom) The sensitivity region for the ^{12}C nucleon density characterized by the notch test.

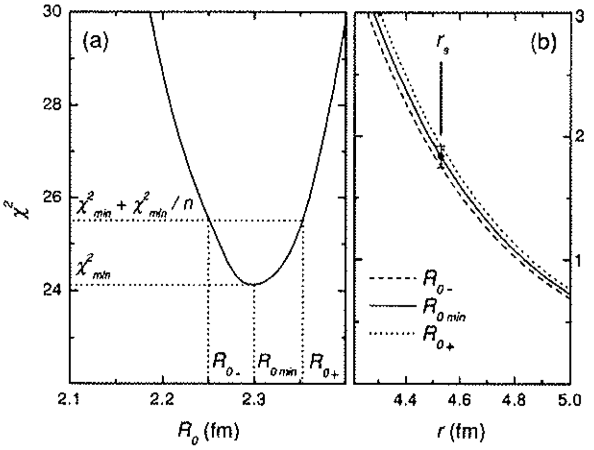

FIG. 8. The figure presents an example of the determination of the error bar for the ^{12}C density at r_S for the angular distribution of the ^{12}C+^{58}Ni system at $E_{\rm lab}$=27 MeV. (a) The total chi-square as a function of the radius of the Fermi distribution for the fixed diffuseness parameter $a=0.5$ fm, and the determination of the $R_{0\rm min}$, R_{0-}, and R_{0+} values. (b) The Fermi distributions which correspond to the $R_{0\rm min}$, R_{0-}, and R_{0+} values, and the determination of the error bar for ρ at r_S.

another consistent result of our analysis is the agreement (see Fig. 9) between the Fermi distribution that has been assumed in the potential systematics of Ref. [6] and the experimental density values from sub-barrier data analyses. We mention that other experimental data for the ^{12}C density in the region $2\leq r\leq 4$ fm could be found through the analyses of other angular distributions in an energy region in between the sub-barrier and intermediate energies analyzed in the present work, but in this case the imaginary potential would have adjustable parameters and the reliability of the results for the density should be studied much more carefully.

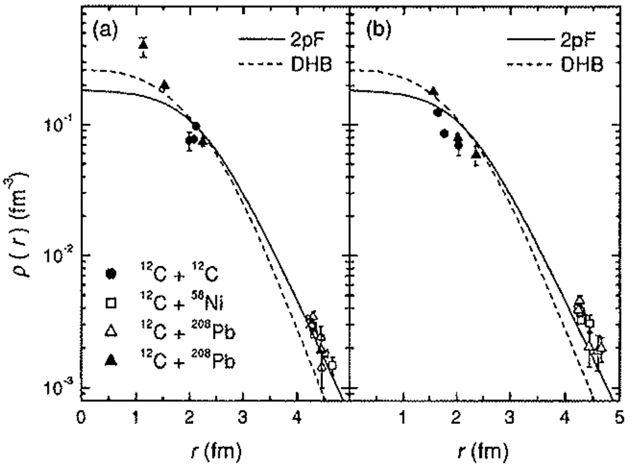

FIG. 9. Experimental nucleon density values for the ^{12}C nucleus, as obtained from elastic scattering data analyses for different heavy-ion systems at sub-barrier (open symbols) and intermediate (closed symbols) energies. Parts (a) and (b) of the figure concern the results of analyses considering the Fermi or harmonic oscillator shapes for the ^{12}C density, respectively. The lines correspond to theoretical Dirac-Hartree-Bogoliubov (DHB) calculations, and to the Fermi distribution (2PF) proposed in Ref. [6].

Now we evaluate the effects of two possible sources of systematical errors in the density determination: the polarization potential and the shape of the density distribution. As discussed in Sec. I, coupled-channel calculations have indicated that the polarization represents about 10% of the real part of the optical potential at sub-barrier energies. In the data analysis, we have neglected the polarization and associated the real part of the optical potential only with the bare interaction, which is directly proportional to the nuclear densities. Thus, a systematical error of about 10% is expected in our results for the density in the surface region, due to the procedure of neglecting the polarization potential for sub-barrier energies. The threshold anomaly [24] indicates that the contribution of the polarization to the real part of the optical potential should be more significant in the region of the Coulomb barrier, so we estimate this contribution at intermediate energies (inner density distances) to be even less than 10%. Another source of systematical errors is the shape assumed for the density distribution. Similar to the case of the potential determination, the notch test indicates that the data fit is sensitive to a density region of width (σ =2.5 fm, see Fig. 7) comparable to the wavelength of the relative motion. However, in contrast with the potential case, in such a region ($2.5\leq r\leq 5.0$ fm) a realistic shape for the density may present a significant deviation from a pure exponential form (see Fig. 7). Therefore, one could expect some dependence of the results for the sensitivity radius on the shape adopted for the density distribution, particularly for intermediate energies in which inner distances are probed. Thus, in order to investigate the dependence of the method on the shape assumed for the ^{12}C distribution, we have also performed data analyses using the harmonic oscillator (HO) shape [Eq. (12)], with two adjustable parameters (w and α):

$$\rho(r)=\rho_0\left(1+\alpha\frac{r^2}{w^2}\right)e^{-r^2/w^2}. \tag{12}$$

The corresponding results for the densities at the sensitivity radii are presented in Fig. 9(b). At the surface region an average difference of 22% between the HO and 2PF results has been found. Therefore, within this precision, our studies indicate that the results for the ^{12}C density at the surface region are rather independent of the model assumed for the shape of the distribution. The results from intermediate energies are more sensitive to the shape, but even in this case the different models (HO and 2PF) provide similar overall trends for the density.

As a further test of the consistency of our results for the ^{12}C density, in Fig. 6 we compare the data with predictions for electron scattering cross sections. In the theoretical calculations, we have obtained the ^{12}C charge distribution by folding the proton density of the nucleus (ρ_p) with the intrinsic charge distribution of the proton in free space (ρ_{chp})

$$\rho_{ch}(r)=\int \rho_p(\vec{r}\,')\rho_{chp}(\vec{r}-\vec{r}\,')d\vec{r}\,', \tag{13}$$

where ρ_{chp} is an exponential with diffuseness $a_{chp} = 0.235$ fm. We have estimated the ^{12}C proton distribution as one half of the total (proton + neutron) nucleon distribution. The dashed line in Fig. 6 represents the results for the cross sections obtained by considering the 2PF distribution of Ref. [6] for the total ^{12}C density (solid lines in Fig. 9). Such results are much closer to the data than the DHB predictions.

V. CONCLUSION

In this work, we have presented elastic scattering data at sub-barrier energies for systems involving ^{12}C as projectile, and we have extended our studies to other data sets earlier obtained at intermediate energies. In our optical model data analysis, the imaginary part of the potential is based only on very fundamental grounds and has no adjustable parameters. The nonlocal model is assumed to describe the energy dependence of the real part of the interaction, which is connected to the folding potential through the very simple Eq. (1). Within this context and assuming the systematics of Ref. [6] for the nuclear densities, a reasonable prediction of the elastic scattering cross sections is obtained for the whole data set without the use of any adjustable parameter.

If the target densities are known, we have shown that the density of the projectile can be extracted from the data analysis in a direct procedure. The sub-barrier elastic scattering data gives information about the density at the surface region, while inner distances are probed through the data at intermediate energies. The results for the ^{12}C nuclear density are consistently independent of the target nucleus, and in reasonable agreement with the Fermi distribution resulting from the systematics of Ref. [6]. We estimate in 20 to 30 % the overall systematical error in the density results, from two main sources: the polarization potential and the shape assumed for the density of the projectile. The method should be a powerful tool to determine densities of exotic nuclei, particularly at the surface region where the difference between the densities of exotic and neighboring stable nuclei is emphasized.

ACKNOWLEDGMENTS

This work was partially supported by Financiadora de Estudos e Projetos (FINEP), Fundação de Amparo à Pesquisa do Estado de São Paulo (FAPESP), and Conselho Nacional de Desenvolvimento Científico e Tecnológico (CNPq).

---

[1] L. C. Chamon, D. Pereira, E. S. Rossi, Jr., C. P. Silva, R. Lichtenthaler Filho, and L. C. Gomes, Nucl. Phys. **A582**, 305 (1995).

[2] L. C. Chamon, D. Pereira, E. S. Rossi, Jr., C. P. Silva, H. Dias, L. Losano, and C. A. P. Ceneviva, Nucl. Phys. **A597**, 253 (1996).

[3] M. A. G. Alvarez, L. C. Chamon, D. Pereira, E. S. Rossi, Jr., C. P. Silva, L. R. Gasques, H. Dias, and M. O. Roos, Nucl. Phys. **A656**, 187 (1999).

[4] C. P. Silva, M. A. G. Alvarez, L. C. Chamon, D. Pereira, M. N. Rao, E. S. Rossi, Jr., L. R. Gasques, M. A. E. Santo, R. M. Anjos, J. Lubian, P. R. S. Gomes, C. Muri, B. V. Carlson, S. Kailas, A. Chatterjee, P. Singh, A. Shivastava, K. Mahata, and S. Santra, Nucl. Phys. **A679**, 287 (2001).

[5] S. Santra, P. Singh, S. Kailas, A. Chatterjee, A. Shrivastava, and K. Mahata, Phys. Rev. C **64**, 024602 (2001).

[6] L. C. Chamon, B. V. Carlson, L. R. Gasques, D. Pereira, C. De Conti, M. A. G. Alvarez, M. S. Hussein, M. A. Candido Ribeiro, E. S. Rossi, Jr., and C. P. Silva, Phys. Rev. C (to be published).

[7] M. A. C. Ribeiro, L. C. Chamon, D. Pereira, M. S. Hussein, and D. Galetti, Phys. Rev. Lett. **78**, 3270 (1997).

[8] L. C. Chamon, D. Pereira, M. S. Hussein, M. A. C. Ribeiro, and D. Galetti, Phys. Rev. Lett. **79**, 5218 (1997).

[9] L. C. Chamon, D. Pereira, and M. S. Hussein, Phys. Rev. C **58**, 576 (1998).

[10] M. A. G. Alvarez, E. S. Rossi, Jr., C. P. Silva, L. R. Gasques, L. C. Chamon, D. Pereira, M. N. Rao, B. V. Carlson, C. De Conti, R. M. Anjos, P. R. S. Gomes, J. Lubian, S. Kailas, A. Chatterjee, and P. Singh, Phys. Rev. C **65**, 014602 (2002).

[11] M. H. Macfarlane and S. C. Pieper, Phys. Lett. **103B**, 169 (1981).

[12] G. R. Satchler and W. G. Love, Phys. Rep. **55**, 183 (1979).

[13] M. E. Brandan and G. R. Satchler, Phys. Rep. **285**, 142 (1992), and references therein.

[14] R. M. Devries and M. R. Clover, Nucl. Phys. **A243**, 528 (1975).

[15] J. Y. Hostachy, M. Buenerd, J. Chauvin, D. Lebrun, Ph. Martin, J. C. Lugol, L. Papineau, P. Roussel, N. Alamanos, J. Arviex, and C. Cerruti, Nucl. Phys. **A490**, 441 (1988).

[16] M. Buenerd, A. Lounis, J. Chauvin, D. Lebrun, P. Martin, G. Duhamel, J. C. Gondrand, and P. de Saintignon, Nucl. Phys. **A424**, 313 (1984).

[17] M. Buenerd, J. Pinston, J. Cole, C. Guet, D. Lebrun, J. M. Loiseaux, P. Martin, E. Monnand, J. Mougey, H. Nifenecker, R. Ost, P. Perrin, Ch. Ristori, P. de Saintgnon, F. Schussler, L. Carlen, H. A. Gustafsson, B. Jakobsson, T. Johansson, G. Jonsson, J. Krumlinde, I. Otterlund, H. Ryde, B. Schroder, G. Tibell, J. B. Bondorf, and O. B. Nielsen, Phys. Lett. **102B**, 242 (1981).

[18] See, e.g., M. S. Hussein, R. A. Rego, and C. A. Bertulani, Phys. Rep. **201**, 279 (1991).

[19] R. J. Glauber, *Lectures in Theoretical Physics* (Interscience, New York, 1959), Vol. 1, p. 315; *High-Energy Physics and Nuclear Structure* (Plenum, New York, 1970), p. 207.

[20] J. R. Ficenec, W. P. Trower, J. Heisenberg, and I. Sick, Phys. Lett. **32B**, 460 (1970).

[21] I. Sick and J. S. MacCarthy, Nucl. Phys. **A150**, 631 (1970).

[22] B. Frois, J. B. Bellicard, J. M. Cavedon, M. Huet, P. Leconte, P. Ludeau, A. Nakada, and Phan Zuan Hô, Phys. Rev. Lett. **38**, 152 (1977).

[23] B. V. Carlson and D. Hirata, Phys. Rev. C **62**, 054310 (2000).

[24] G. R. Satchler, Phys. Rep. **199**, 147 (1991).

A parameter-free optical potential for the heavy-ion elastic scattering process

M. A. G. Alvarez, L. C. Chamon, M. S. Hussein, D. Pereira, L. R. Gasques, E. S. Rossi Jr., C. P. Silva.
Departamento de Física Nuclear, Instituto de Física da Universidade de São Paulo,
Caixa Postal 66318, 05315-970, São Paulo, SP, Brazil.

Thirty elastic scattering angular distributions for seven heavy-ion systems, in wide energy ranges, have been studied with the aim of systematizing the optical potential, real and imaginary parts, in a global way. The framework is: i) an extensive systematization of nuclear densities, ii) the energy dependence of the bare potential accounted by a model based on the nonlocal nature of the interaction, and iii) the real and imaginary parts of the optical potential assumed to have the same radial shape.

PACS: 24.10.Ht, 25.70.-z, 25.70.Bc
Keywords: Heavy-ion optical potential. Heavy-ion elastic scattering.

Elastic scattering is the simplest and most direct process involved in a nuclear reaction, and it can be used as the starting point to understand more complicated reaction channels. Over the last decades, different models were used for the real and imaginary parts of the optical potential to reproduce a large number of elastic scattering data involving heavy-ion systems. The optical model analysis using the conventional Woods-Saxon (WS) shape for the real and imaginary parts of the potential, although far from being fundamental, has presented the best means for the reproduction of the elastic scattering angular distributions, with six free parameters used in the data fits. However, there are problems in terms of obtaining a simple model for systematizing the WS optical potential parameters, in order to take into account the energy dependence, refractive effects in light heavy-ion systems, exotic nuclei systems etc. Particularly, for some systems the variation with the bombarding energy requires arbitrarily different sets of parameters, with different shapes and strengths for the potential. This arbitrariness calls for a more realistic model for the optical potential, which has been accomplished to a large extent by our work [1–5] on the nonlocal model for the real part of the nucleus-nucleus interaction. The central idea of the present work is to perform a further test of consistency of this model for the real part of the interaction, by using a very simple form to describe the imaginary part of the optical potential, and avoiding as much as possible the use of free parameters in accounting to the data.

A previous investigation [6–8] to identify similarities between the real and imaginary parts of the potential has been performed by considering the realistic Lax-type interaction, which has provided satisfactory fits of elastic scattering data at intermediate energies [6,7]. The Lax interaction [9] (Eq. 1) is the optical limit of the Glauber high-energy-approximation [10,11], and it is essentially the zero-range double-folding potential used for both the real and imaginary parts:

$$U(R) = -\frac{1}{2}\hbar v \int (\alpha + i)\, \sigma_T^{NN}\, \rho_T(\vec{r'})\, \rho_P(\vec{R} - \vec{r'})\, d\vec{r'} \tag{1}$$

where v is the relative velocity between the nuclei, σ_T^{NN} is a spin-isospin-averaged total nucleon-nucleon cross section, ρ_P and ρ_T are the projectile and target nuclear densities, and α is a known energy-dependent quantity that determines the real part of the nucleon-nucleon forward elastic amplitude $f_{NN}(E,0)$. Eq. (1) is obtained from the optical theorem applied to $f_{NN}(E,0)$. The Lax-type interaction is not valid for low energies where collective reaction processes are important. Thus, the parameter-free description of low energy data is an open question in the determination of a fundamental potential. However, the procedure of using the same radial shape for the real and the imaginary parts of the potential has successfully been used in the present work.

In [1–5], we have developed another realistic model for the heavy-ion bare interaction, which takes into account the Pauli nonlocality involving the exchange of nucleons between the target and projectile. This model has presented the same validity at low and high energies, and has already been tested for a large number of systems [1–3,5,12–15]. Within the nonlocal model, the bare interaction V_N is connected with the folding potential V_F through [5]

$$V_N(R,E) \approx V_F(R)\, e^{-4v^2/c^2} \tag{2}$$

where c is the speed of light and v is the local relative velocity between the two nuclei,

$$v^2(R,E) = \frac{2}{\mu}[E - V_C(R) - V_N(R;E)] \tag{3}$$

The folding potential (Eq. 4) can be obtained in two different ways [5]: i) using the nucleon distributions of the nuclei and an appropriate form for the nucleon-nucleon interaction, and ii) using the matter distributions of the nuclei with a zero-range approach for $v(\vec{r})$. By matter distribution we mean taking into account the finite size of the nucleon. Both alternatives are equivalent in describing the heavy-ion nuclear potential [5], and in the present work we have adopted the zero-range approach.

$$V_F(R) = \int \rho_1(r_1)\, \rho_2(r_2)\, v(\vec{R} - \vec{r_1} + \vec{r_2})\, d\vec{r_1}\, d\vec{r_2} \tag{4}$$

For the Coulomb interaction, V_C, we have used the expression for the double-sharp cutoff Coulomb potential [16]. This procedure is important in calculating cross sections at intermediate energies, where the internal region of the interaction is probed.

With the aim of providing a global description of the nuclear interaction, a systematization of nuclear densities has been proposed in Ref. [5], based on an extensive study involving charge distributions extracted from electron scattering experiments and theoretical densities calculated through the Dirac-Hartree-Bogoliubov model. In that study, we have adopted the two-parameter Fermi (2pF) distribution to describe the nuclear densities. The radii of the 2pF distributions are well described by

$$R_0 = 1.31 A^{1/3} - 0.84\, fm, \tag{5}$$

where A is the number of nucleons of the nucleus. The matter densities present an average diffuseness value $a = 0.56\ fm$. Owing to specific nuclear structure effects (single particle and/or collective), the parameters R_0 and a show small variations around the corresponding average values throughout the periodic table. However, as far as the nuclear potential is concerned, the effects of the structure of the nuclei are mostly present at the surface and mainly related only to the diffuseness parameter [5]. This systematization of the nuclear distributions is essential to obtain a parameter-free interaction, since the folding potential depends on the densities of the partners in the collision. Within this context, an extensive systematization of optical potential strengths extracted from heavy-ion elastic scattering data analyses at low and intermediate energies was performed [5], and the experimental potential strengths have been described within 25% precision.

As mentioned above, an important point that stands out in obtaining a description of the optical potential in a global way is the difficulty encountered in describing the imaginary part of the interaction within a simple model. A fully microscopic description based on the Feshbach theory is very difficult, and basically out of reach at low energies where collective as well as single particle excitations are involved in the scattering process. In previous works involving elastic scattering data fits [2,3,12–15], we have already used the nonlocal model for the real part of the interaction, and adopted a more modest procedure for the imaginary part by assuming two different models: WS with three free parameters, which has presented an excellent description of the data; and the parameter-free Lax-type approximation, which is based on a more fundamental theory but has not been used to describe low energy data. Motivated by the concept from the Lax approximation of using similar shapes for the real and imaginary parts of the potential, in this work we have extended Eq. (2), developed for the real part of the interaction, to the imaginary part of the potential, by simply multiplying it by N_i, where N_i is a number to be fixed by adjusting the data.

$$W(R,E) = N_i\, V_N(R,E) \tag{6}$$

We have chosen the ^{12}C + ^{12}C, ^{16}O, ^{40}Ca, ^{90}Zr, ^{208}Pb; ^{16}O + ^{208}Pb and ^{40}Ar + ^{208}Pb systems as test cases due to the extensive experimental data available [17–26] over wide energy ranges, and principally because the special refractive characteristics involving some of these systems which makes them more sensitive to the real part of the interaction. In Figures (1) to (7) the solid lines correspond to the best data fits obtained by searching the N_i parameter. We have opted for keeping the average density diffuseness value $a = 0.56\, fm$ in the calculations, even though we could improve the quality of the data fits by allowing the diffuseness to be a free parameter. As one can observe (see Fig. 8), the N_i parameter is approximately system-independent, with an average value $N_i = 0.78$. Good elastic scattering cross section predictions are obtained using this average value for the whole data set (see the dotted lines in Figs. 1 to 7).

In summary, using the procedure described above we have obtained a good description of the whole data set, which has further validated our assumption for the real part of the interaction: the nonlocal model. We have also assumed a very simple model for the imaginary part of the potential, with only one, system- and energy-independent, free parameter: the average value for $N_i \approx 0.8$. In fact, the details of the imaginary part of the interaction seems not to be of much importance to the data fit. For example, in Fig. 7 (bottom) quite different values for N_i ($N_i = 0.44$ and $N_i = 0.78$) provide very similar predictions for the elastic scattering cross sections. The same behavior can be observed for the other systems (see Figs. 1 to 7). At a first glance this result seems to be surprising, but upon second thought one does expect that the data are more sensitive to the real part of the potential, which determin the quantal transmission through the ℓ-dependent barriers. In order to confirm this point, we have compared (se table 1) the reaction cross sections resulting from our optical model (OM) calculations (using the average value fo N_i) with those from the geometrical limit of the barrier penetration model (Eq. 7)

$$\sigma_{BP} = \pi R_B^2 \left(1 - V_B/E\right) \quad (7$$

In most cases both forms of calculating the reaction cross section agree within about 20% precision. However, th values obtained from the OM calculations are more realistic. Indeed the reaction cross section values obtained wit our OM calculations are very similar (see table 1) to those obtained through different methods in earlier work [6,17,18,22–24,27–32]. Our results suggest using the present parameter-free model to get reliable estimates for heavy ion elastic scattering and reaction cross sections. Extension of our findings to halo-nuclei is being pursued and wi be presented elsewhere.

This work was partially supported by Financiadora de Estudos e Projetos (FINEP), Conselho Nacional de Desenvolvimento Científico e Tecnológico (CNPq) and Fundação de Amparo à Pesquisa do Estado de São Paulo (FAPESP) under contract number 1998/11401-4.

---

[1] M. A. Candido Ribeiro, L. C. Chamon, D. Pereira, M. S. Hussein and D. Galetti, Phys. Rev. Lett. **78**, 3270 (1997).

[2] L. C. Chamon, D. Pereira, M. S. Hussein, M. A. Candido Ribeiro and D. Galetti, Phys. Rev. Lett. **79**, 5218 (1997).

[3] L. C. Chamon, D. Pereira, and M. S. Hussein, Phys. Rev. **C58**, 576 (1998).

[4] D. Galetti, S. S. Mizrahi, L. C. Chamon, D. Pereira, M. S. Hussein and M. A. Candido Ribeiro, Phys. Rev. **58**, 162 (1998).

[5] L. C. Chamon, B. V. Carlson, L. R. Gasques, D. Pereira, C. De Conti, M. A. G. Alvarez, M. S. Hussein, M. A. Candid Ribeiro, E. S. Rossi Jr. and C. P. Silva, Phys. Rev. **C66**, (2002) 014610.

[6] M. E. Brandan, H. Chehime and K. W. McVoy, Phys. Rev. **C55**, 1353 (1997).

[7] S. K. Charagi and S. K. Gupta, Phys. Rev **C56**, 1171 (1997).

[8] M. E. Brandan, K. W. Mc Voy, Phys. Rev. **C55**, 1362 (1997).

[9] see, e.g., M. S. Hussein, R. A. Rego and C. A. Bertulani, Phys. Rep. **201**, 279 (1991).

[10] R. J. Glauber, in Lectures in Theoretical Physics, edited by W. E. Brittin and L. G. Dunham (Wiley-Interscience, Nev York, 1959), **Vol. 1**, p. 315; in High Energy Physics and Nuclear Structure, edited by G. Alexander (Wiley, New York 1967), p 311; in High Energy Physics and Nuclear Structure (Plenum, New York, 1970), p. 207.

[11] W. Czyz and L. C. Maximon, Ann. Phys. (N. Y.) **52**, 59 (1969).

[12] M. A. G. Alvarez, L. C. Chamon, D. Pereira, E. S. Rossi Jr., C. P. Silva, L. R. Gasques, H. Dias and M. O. Roos, Nucl. Phys. **A656**, 187 (1999).

[13] M. A. G. Alvarez, E. S. Rossi Jr., C. P. Silva, L. R. Gasques, L. C. Chamon, D. Pereira, M. N. Rao, B. V. Carlson, C. De Conti, R. M. Anjos, P. R. S. Gomes, J. Lubian, S. Kailas, A. Chatterjee and P. Singh, Phys. Rev. **C65**, 014602 (2002).

[14] L. R. Gasques, L. C. Chamon, C. P. Silva, D. Pereira, M. A. G. Alvarez, E. S. Rossi Jr., V. P. Likhachev, B. V. Carlson and C. De Conti. Phys. Rev. **C65**, (2002) 044314.

[15] E. S. Rossi Jr., D. Pereira, L. C. Chamon, C. P. Silva, M. A. G. Alvarez, L. R. Gasques, J. Lubian, B. V. Carlson and C. De Conti, Nuc. Phys. **A707**, 325 (2002).

[16] R. M. Devries and M. R. Clover, Nucl. Phys., **A243**, 528 (1975).

[17] D. T. Khoa, W. von Oertzen and H. G. Bohlen, Phys. Rev. **C49**, 1652 (1994).

[18] A. A. Ogloblin, Y. A. Glukhov, V. Trzaska, A. S. Demyanova, S. A. Goncharov, R. Julin, S. V. Klebnikov, M. Mutterer, M. V. Rozhkov, V. P. Rudakov, G. P. Tiorin, D. T. Khoa and G. R. Satchler. Phys. Rev. **C62**, 44601 (2000).

[19] V. Chiste, R. Lichtenthaler, A. C. C. Villari and L. C. Gomes, Phys. Rev. **C54**, 784 (1996).

[20] J. B. Ball, C. B. Fulner, E. E. Gross, M. L. Halbert, D. C. Hensley, C. A. Ludemann, M. J. Saltmarsh and G. R. Satchler. Nucl. Phys. **A252**, 208 (1975).

[21] Y. T. Oganessian and Y. E. Penionzhkevich, V. I. Man'Ko and V. N. Polyansky, Nucl. Phys. **A303**, 259 (1978).

[22] C. C. Sahm, T. Murakami, J. G. Cramer, A. J. Lazzarini, D. D.Leach, D. R. Tieger, R. A. Loveman, W. G. Lynch, M. B. Tsang and J. Van der Plicht. Phys. Rev. **C34**, 2165 (1986).

[23] P. Roussel-Chomaz, N. Alamanos, F. Auger, J. Barrette, B. Berthier, B. Fernandez and L. Papineau, Nucl. Phys. **A477**, (1988) 345.

[24] J. Y. Hostachy, M. Buenerd, J. Chauvin, D. Lebrun, Ph. Martin, J. C. Lugol, L. Papineau, P. Roussel, N. Alamanos, J. Arviex, and C. Cerruti, Nucl. Phys. **A490**, 441 (1998).

[25] M. Buenerd, J. Pinston, J. Cole, C. Guet, D. Lebrun, J. M. Loiseaux, P. Martin, E. Monnand, J. Mougey, H. Nifenecker, R. Ost, P. Perrin, Ch. Ristori, P. de Saintgnon, F. Schussler, L. Carlen, H. A. Gustafsson, B. Jakobsson, T. Johansson, G. Jonsson, J. Krumlinde, I. Otterlund, H. Ryde, B. Schroder, G. Tibell, J. B. Bondorf, and O. B. Nielsen, Phys. Lett. **102B**, 242 (1981).

[26] M. Buenerd, A. Lounis, J. Chauvin, D. Lebrun, P. Martin, G. Duhamel, J. C. Gondrand, and P. de Saintgnon, Nucl. Phys. **A424**, 313 (1984)

[27] N. Ohtsuka, R. Linden and Amand Faesler, Phys. Lett. **199B**, 330 (1987).

[28] S. K. Charagi, Phys. Rev. **C51**, 3521 (1995).

[29] C. Olmer, M. Mermaz, M. Buerned, C. K. Gelbke, D. L. Hendrie, J. Mahoney, D. K. Scott, M. H. Macfarlane and S. C. Pieper, Phys. Rev. **C18**, 205 (1978).

[30] W. Treu, H. Frohlich, W. Galster, P. Duck and H. Voit, Phys. Rev. **C22**, 2462 (1980).

[31] H. G. Bohlen, M. R. Clover, G. Ingold, H. Lettan and W. von Oertzen, Z. Phys. **A308**, 121 (1982).

[32] S. Kox, A. Gamp, C. Perrin, J. Arvieux, R. Bertholet, J. F. Bruandet, M. Buenerd, R. Cherkaoui, A. J. Cole, Y. El-Masri, N. Longequeue, J. Menet, F. Merchez and J. B. Viano, Phys. Rev. **C35**, 1678 (1987).

Table 1: The optical model (σ_{OM}) and geometrical (σ_{BP}) reaction cross sections obtained in this work for severa systems and bombarding energies. The table also presents the values (and corresponding references) for the reactio cross sections (σ_R) obtained through different methods in earlier works.

System	E_{Lab} (MeV)	σ_{OM} (mb)	σ_{BP} (mb)	σ_R (mb)	Ref.
^{12}C + ^{12}C	16	542	508	600	30
	112	1477	1759	1444	32
	300	1374	1834	1296	31
	1016	1055	1680	1000	24
	1449	910	1560	907	24
^{16}O + ^{12}C	21	209	167	-	-
	260	1560	1877	1481	18
	608	1420	1881	1374	18
	1503	1143	1716	1136	23
^{12}C + ^{40}Ca	180	2022	2083	2165	22
	300	2015	2168	2030	22
	420	1969	2180	2000	22
^{12}C + ^{90}Zr	120	2310	2113	2219	22
	180	2540	2406	2297	22
	300	2652	2610	2415	22
	420	2650	2670	2840	22
^{12}C + ^{208}Pb	96	1854	1498	1791	28
	116	2323	1944	2235	28
	300	3205	3013	3300	22
	420	3611	3393	3561	22
	480	3634	3441	-	-
	1030	3560	3501	-	-
	1449	3344	3331	3136	6
	2400	2905	2882	2960	27
^{16}O + ^{208}Pb	129.5	1993	1553	2023	28
	192	2878	2408	2847	28
	312.6	3504	3067	3432	29
	1500	3708	3530	3485	23
^{40}Ar + ^{208}Pb	302	2476	1740	-	-
	1760	4783	4059	-	-

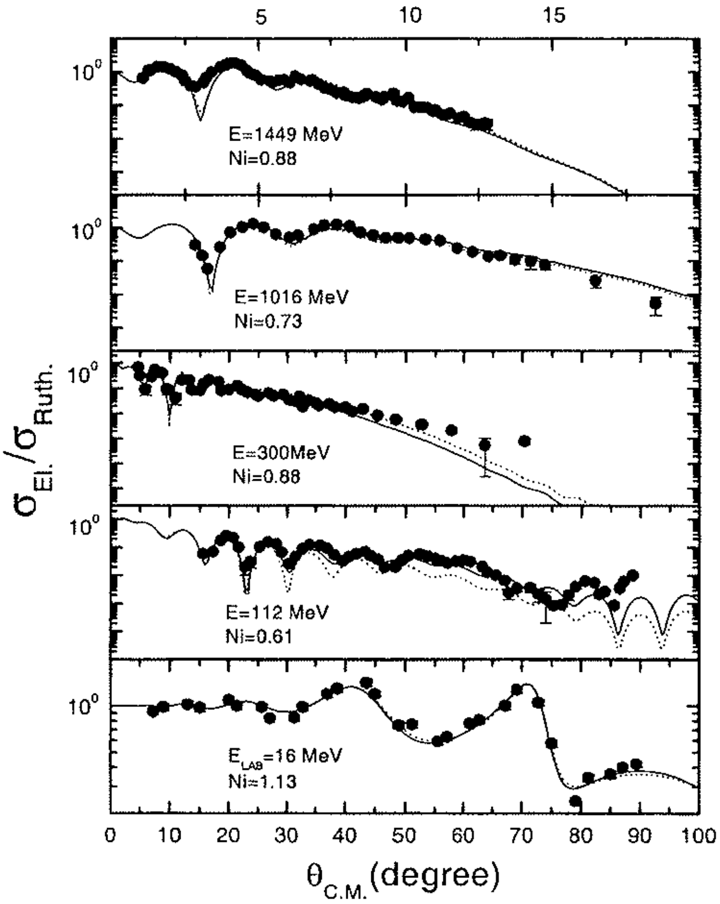

FIG. 1. Elastic scattering angular distributions for the $^{12}C + ^{12}C$ system in several bombarding energies. The solid lines correspond to the best fit using the same radial shape for both the real and imaginary parts of the optical potential, with the N_i parameter searched for the best data fits. The dotted lines correspond to the predictions obtained with the average value $N_i = 0.78$ (see text for details).

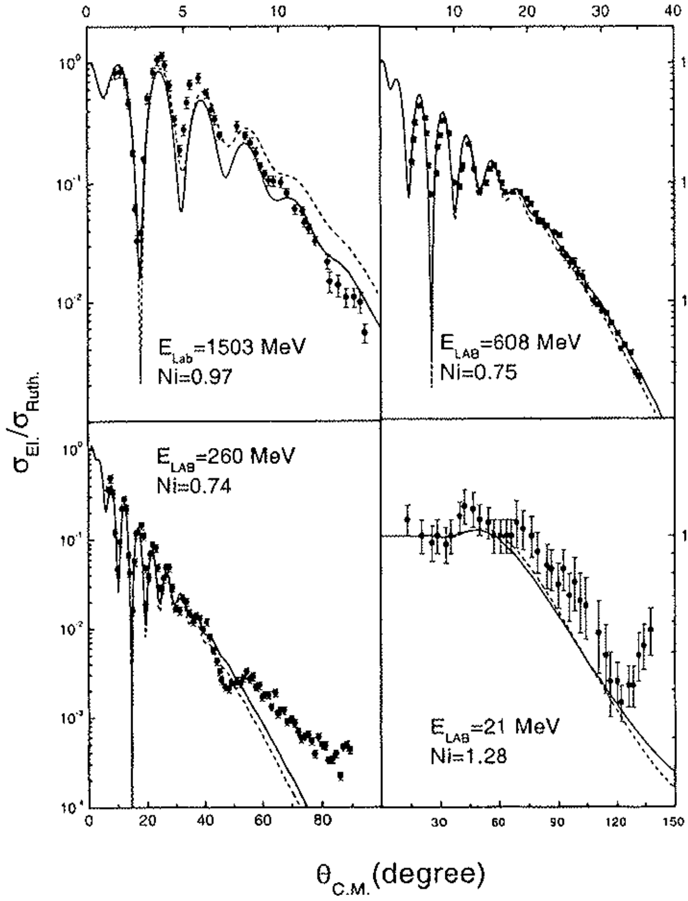

FIG. 2. The same of Fig. 1 for the ^{16}O + ^{12}C system.

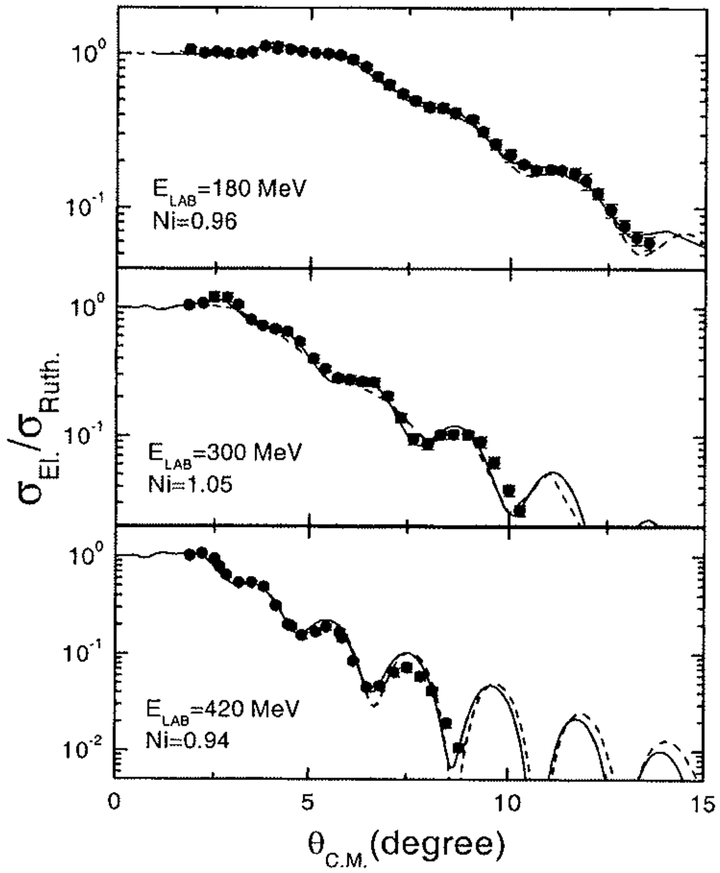

FIG. 3. The same of Fig. 1 for the $^{12}C+^{40}Ca$ system.

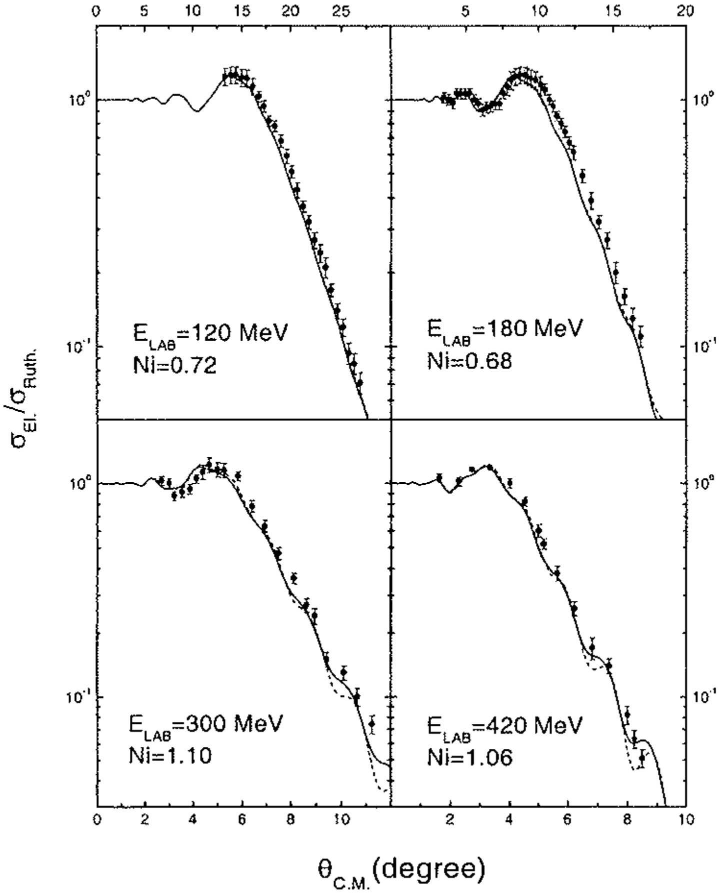

FIG. 4. The same of Fig. 1 for the $^{12}C+^{90}Zr$ system.

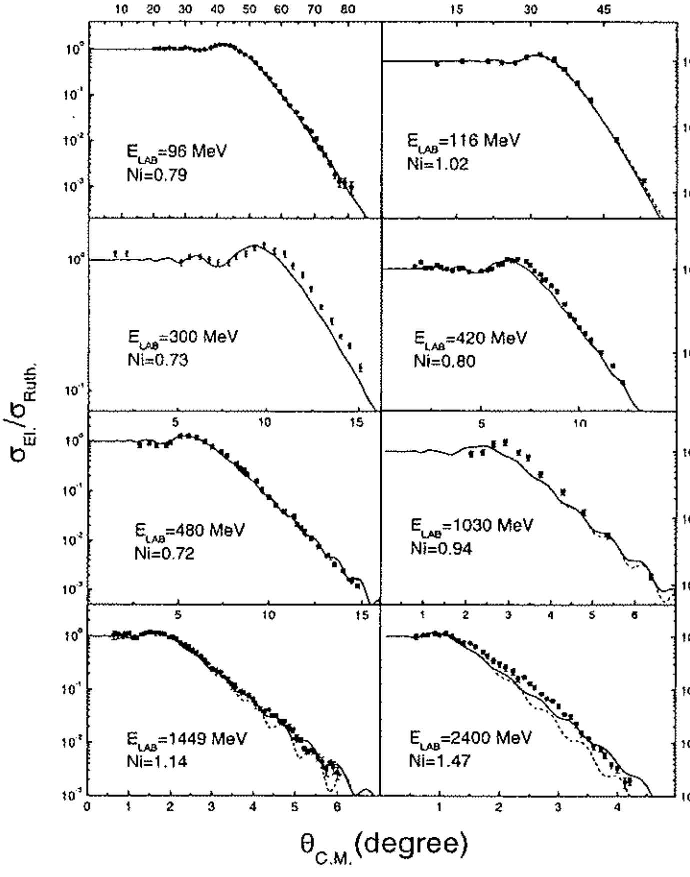

FIG. 5. The same of Fig. 1 for the ^{12}C+^{208}Pb system.

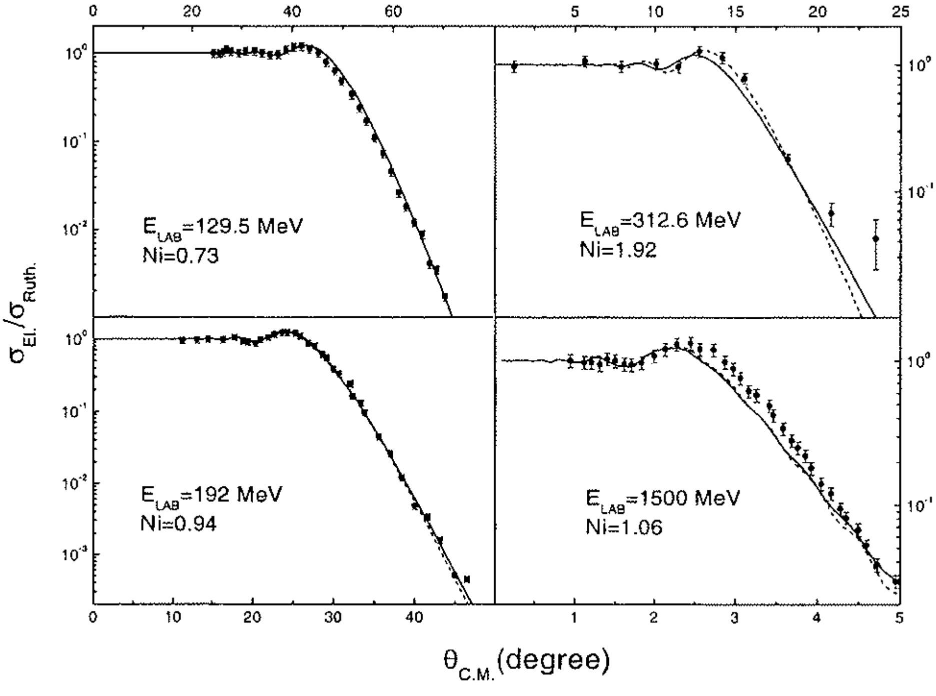

FIG. 6. The same of Fig. 1 for the ^{16}O+^{208}Pb system.

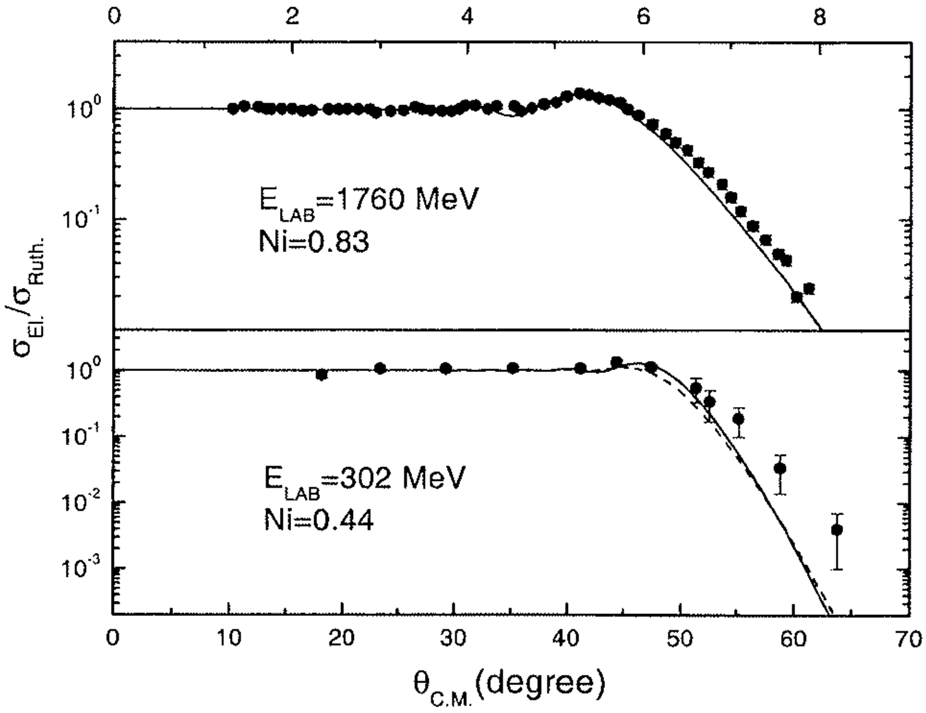

FIG. 7. The same of Fig. 1 for the ^{40}Ar+^{208}Pb system.

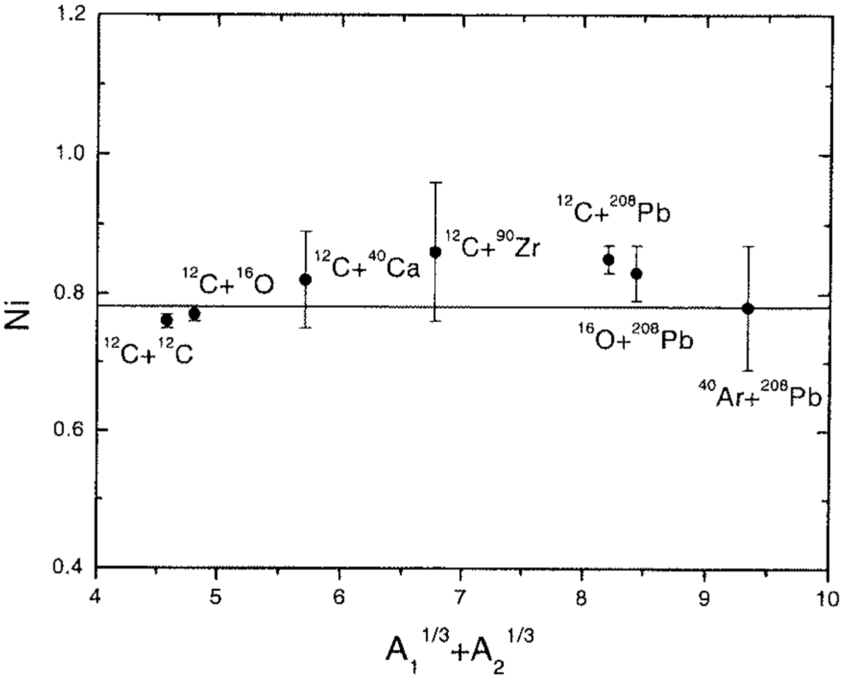

FIG. 8. The N_i values for different systems obtained by adjusting the corresponding elastic scattering angular distributions. The solid line represents the average value $N_i = 0.78$.

Experimental determination of the surface density for the ^{6}He exotic nucleus.

L. R. Gasques[1], L. C. Chamon[1], D. Pereira[1], V. Guimarães[1], A. Lépine-Szily[1], M. A. G. Alvarez[1], E. S. Rossi Jr.[1], C. P. Silva[1], B. V. Carlson[2], J. J. Kolata[3], L. Lamm[3], D. Peterson[3], P. Santi[3], S. Vincent[3], P. A. De Young[4], G. Peasley[4]

1. Laboratório Pelletron, Instituto de Física da Universidade de São Paulo, 05315-970, São Paulo, SP, Brazil.
2. Depto. de Física, Instituto Tecnológico de Aeronáutica, Centro Técnico Aeroespacial, São José dos Campos, SP, Brazil.
3. Physics Department, University of Notre Dame, Notre Dame, Indiana 46556, USA .
4. Physics Department, Hope College, Holland, Michigan 49422, USA.

Angular distributions for the elastic scattering of ^{4,6}He on ^{58}Ni have been measured at near-barrier energies. The present data, combined with others for the ^{4}He + ^{58}Ni system at intermediate energies, allowed the determination of the ^{4,6}He ground-state nuclear densities through an unfolding method. The experimentally extracted nuclear densities are compared with the results of theoretical calculations.

PACS Numbers: 21.10.Gv; 25.70.Bc; 24.10.Ht.

One of the most exciting recent events in nuclear physics has been the discovery of extended neutron distributions in exotic neutron-rich nuclei, as e.g. ^{11}Li, ^{11}Be and ^{6,8}He. The advent of facilities that produce radioactive ion beams made possible the search for experimental evidence of thick neutron skins and haloes for nuclei near the drip line. This phenomenon was first observed by obtaining the interaction radii from reaction cross section measurements for systems involving exotic nuclei [1], followed by the experimental determination of transverse momentum distributions from the breakup products [2]. Several recent works with radioactive beams use the elastic scattering process at intermediate energies to demonstrate the existence of such extended neutron distributions. However, from a theoretical point of view, the near-barrier energy region should be more appropriate for studying the densities in the surface region, where the difference between exotic and neighbouring stable nuclei is much more emphasized. In fact, for distances close to the barrier radius, the nuclear potential is mostly determined by the folding of the nucleon-nucleon interaction with the surface region of the densities. This idea has already been successfully applied to determine densities of stable nuclei [3-5]. Taking this point of view, we present elastic scattering differential cross sections for the ^{4,6}He + ^{58}Ni systems at near-barrier energies, with the aim of obtaining the ^{4,6}He densities in the surface region. The analysis is extended to the ^{4}He + ^{58}Ni system at intermediate energies, and in this case information about the ^{4}He density at much smaller distances is obtained.

The experiment was carried out at the Nuclear Structure Laboratory of the University of Notre Dame. The ^{6}He secondary beam with $E_{Lab} = 9.0$ MeV was produced using the *TwinSol* radioactive ion beam facility [6]. In this system, two superconducting solenoids act as thick lenses to collect and focus the secondary beam onto the target. The ^{6}He beam was produced using the proton transfer process of the ^{7}Li primary beam at an energy of 19.95 MeV incident on a 12.7 μm thick ^{9}Be production target ^{9}Be(^{7}Li,^{6}He). Ions with the same magnetic rigidity of the ^{6}He were present in the secondary beam. The detection system was composed of four telescopes consisting of thin Si detectors (energy loss), backed by thicker Si detectors (remaining energy), making it possible to identify particles with different charges and masses. A typical ΔE *vs* E spectrum for the ^{6}He + ^{58}Ni system is shown in Fig. 1a. The elastic ^{6}He group is clearly visible and scattered ^{4}He ions can also be easily identified. In recent works [7,8], a strong ^{4}He group resulting from transfer and/or breakup modes has been observed in the scattering of ^{6}He on ^{209}Bi in energies below the nominal Coulomb barrier. With the purpose of investigating the importance of such channels for the ^{6}He + ^{58}Ni system, we have also performed measurements for the ^{6}He + ^{197}Au system (see Fig. 1b), with the same secondary beam conditions as those for the ^{6}He + ^{58}Ni. For the ^{6}He + ^{197}Au system, the contributions arising from other reaction channels, besides the elastic scattering, are expected to be negligible, since the 9 MeV bombarding energy corresponds to about 10 MeV below the Coulomb barrier. Indeed, the elastic scattering cross section for this system is in agreement with the corresponding Rutherford cross section. The energy projection spectra corresponding only to ^{4}He ions are also shown in figure 1(c,d). The very similar background for both targets (^{197}Au and ^{58}Ni) indicates that no significant transfer and/or breakup contributions were present in our experiment. We estimate the contribution of these processes for the ^{6}He + ^{58}Ni system as less than 2% of the elastic scattering cross section, by comparing the ^{4}He background for both targets. Due to the energy resolution of our experiment, any contribution of inelastic scattering to low-lying states is included in our "elastic scattering" data. The secondary beam of ^{4}He was produced in a similar way, but using the elastic scattering process of the ^{4}He primary beam. In this case, the secondary beam is much more intense than that for ^{6}He, since the cross section for elastic scattering is much greater than that for the transfer process. Fig. 2 exhibits the elastic scattering cross section for the ^{4,6}He + ^{58}Ni systems at several near-barrier energies. Contributions to the count rate in the region of the elastic scattering process can also arise from the compound-elastic (CE) decay. Since this process is mixed (experimentally) with the elastic channel, in our analyses the Hauser-Feshbach theory has been used to estimate the CE cross section. We checked that the contribution of the CE cross section for the ^{4}He + ^{58}Ni system at intermediate energies and for the ^{6}He + ^{58}Ni system at the near-barrier region is negligible. Fig. 3 exhibits the elastic scattering data (from Refs. [9–12]) for the ^{4}He + ^{58}Ni system at intermediate energies.

The extraction of information on nuclear densities from elastic scattering is a question of using the folding model for the interaction, including all the important effects from first principles and avoiding the use of adjustable parameters as much as possible. In this work, we use a model for the real part of the potential that is based on nonlocal quantum effects related to the exchange of nucleons between the target and the projectile [13–16]. The nonlocal model has provided a good description of the elastic scattering for several systems in a very wide energy range [4,5,14–17]. It also has been successful checked for inelastic scattering and transfer processes at sub-barrier and intermediate energies [5,15–17]. We also point out that the nonlocal model has provided good predictions for a very extensive systematic of potential strengths extracted from heavy-ion elastic scattering data analyses at low and intermediate energies [13]. Within this model, the bare interaction is connected with the folding potential V_F through

$$V_N(R,E) \approx V_F(R)\, e^{-4v^2/c^2} , \qquad (1)$$

where c is the speed of light and v is the local relative speed between the two nuclei,

$$v^2(R,E) = \frac{2}{\mu}\left[E - V_C(R) - V_N(R,E)\right] . \qquad (2)$$

For the Coulomb interaction, V_C, we have used the expression for the double sharp cutoff potential [18]. This procedure is important in calculating cross sections at intermediate energies, in which the internal region of the potential is probed. The folding potential depends on the densities of the two partners in the collision

$$V_F(R) = \int \rho_1(r_1)\, \rho_2(r_2)\, u_0(\vec{R} - \vec{r_1} + \vec{r_2})\, d\vec{r_1}\, d\vec{r_2} \qquad (3)$$

where $u_0(\vec{R} - \vec{r_1} + \vec{r_2})$ is the "frozen" M3Y effective nucleon-nucleon interaction [13,15].

The imaginary part of the interaction used in our calculations has also been based on general assumptions. For the angular distributions at intermediate energies, we have used the imaginary part of the parameter-free Lax-type interaction, which is known to be quite appropriate in this energy region [19,20]. At near-barrier energies we have used a Woods-Saxon (WS) shape for the imaginary potential, with parameters that result in complete internal absorption from barrier penetration, but with small strengths in the surface region. Within these conditions, the results obtained for the experimental density values from data analysis are quite insensitive to variations of the WS potential parameters. This result should be contrasted with the strong dependence on the imaginary part of the potential in the data analysis for the ^{6}He + ^{209}Bi system [7,8]. In that case, very large cross sections for transfer and/or breakup processes have been detected at sub-barrier energies, and an imaginary potential that results in strong surface absorption was used in the elastic scattering data analysis. However, no significant transfer and/or breakup contributions were detected for the ^{6}He + ^{58}Ni system here, and possible inelastic contributions are already included in the "quasi"- elastic data. Thus, there are no extra significant peripheral reaction processes to be accounted for in the present case, and the use of optical potentials with strong surface absorption clearly would be a mistake in the present data analysis.

If the nonlocal model is assumed for the interaction, and the density of one nucleus is known, an unfolding method can be used to extract the ground-state nuclear density of the other nucleus from the elastic scattering data analyses. The method has already been successfully applied in the experimental determination of densities for the ^{12}C and ^{16,18}O nuclei [3–5]. In the present paper we describe the method in a quite concise form, and we invite the reader to obtain further details of the method in a complete discussion presented in the references above. In the data analyses, we have used a theoretical Dirac-Hartree-Bogoliubov density for the ^{58}Ni nucleus [21], since the corresponding predictions for electron scattering cross sections are in very good agreement with the data [3,4]. This theoretical density was also assumed in the previous works for stable nucleus systems and the corresponding results obtained for the densities were quite satisfactory. For obtaining the ^{4,6}He densities, we have assumed the two parameter Fermi (2pF) distribution to describe the ^{4,6}He densities. The diffuseness (a) and radius (R_0) were searched for the best data fits, with the ρ_0 parameter determined by the normalization condition. For each angular distribution, we have found a family of densities which give equivalent data fits. These densities cross at the sensitivity radius, where the value of the density is determined without ambiguity. To ensure that the sensitivity radius is in a region that is important to the data fits, we have used the notch test, in which a spline with a gaussian shape is included in the ^{4,6}He densities, and the variation of the chi-square is studied as a function of the position of this perturbation.

The sensitivity radius is energy-dependent and therefore the density can be obtained over a large range of radial distances. Fig. 4 contains the experimental nucleon density values for the ^{4,6}He at the corresponding sensitivity radii obtained from data analyses of several angular distributions. Information about the density at the surface region is obtained through the near-barrier elastic scattering data analyses, while the data at intermediate energies probes the density in the inner region. The statistical error bars for the density values have been determined using the procedure described in [4]. In earlier works [3,4], we have demonstrated for stable nuclei that the results obtained for the density values at the sensitivity radii are rather independent of the shape assumed for the density distribution. However, as ^{6}He is expected to be an exotic nucleus with an extended neutron tail, in the present work we have also used another shape to describe the ^{6}He density, the harmonic oscillator (HO) shape, with the aim of further checking the validity of our results. Fig. 4 shows that the two models for the distribution result in sensitivity radii only slightly different (about 0.3 fm), with corresponding experimental density values compatible with the expected behaviour (slope) of the ^{6}He density in the surface region. Actually, the dependence of the experimental results on the model assumed for the distribution is expected to be weak, since the near-barrier data analysis is mostly sensitive to the surface region of the density, where any realistic model provides a shape close to an exponential (see the theoretical calculations for the ^{6}He density in Fig. 4). For intermediate energy data analyses, besides the Lax interaction we have also used a Woods-Saxon shape imaginary potential with three free parameters, in order to evaluate any possible change in the sensitivity radius. The different models for the imaginary potential provide very similar results for the ^{4}He density.

The solid and dotted lines in Fig. 2 represent optical model predictions for the elastic scattering cross section, with (solid) or without (dotted) the CE contribution. For the ^{4}He + ^{58}Ni system, these theoretical predictions were obtained by using the best fit 2pF distribution with $R_0 = 1.64\ fm$ and $a = 0.28\ fm$ (see Fig. 4). Fig. 3 shows that the elastic scattering data fits using a Woods-Saxon shape for the imaginary potential are better than those obtained using the Lax-type interaction. Despite the differences in the elastic scattering data fits, we stress that both models for the imaginary part of the interaction provide very similar values for the density.

In this paper, we have studied the ^{4}He nucleus with the purpose of comparing the results for the ^{4}He and ^{6}He densities, and also with the aim of checking the validity of the method in this light mass region. Thus, in Fig. 4 we have compared our ^{4}He experimental density values with the total (proton + neutron) alpha density derived from the charge distribution obtained in ^{4}He electron scattering experiments. We have estimated the total distribution as twice the proton distribution. We have obtained the ^{4}He proton distribution (ρ_p) by unfolding the charge density of the nucleus (ρ_{ch}) with the intrinsic charge distribution of the proton in free space (ρ_{chp})

$$\rho_{ch}(r) = \int \rho_p(\vec{r'})\ \rho_{chp}(\vec{r} - \vec{r'})\ d\vec{r'}\ , \qquad (4)$$

where ρ_{chp} is an exponential with diffuseness a_{chp} = 0.235 fm. In Fig. 4 we also present the results of theoretical calculations [22] for the ^{4}He nuclear density, which have been performed in the context of the generator coordinate method, with the Skyrme SIII nucleon-nucleon effective interaction and elimination of center of mass effects. We estimate the overall systematical error of ou ^{4}He surface density values to be about 20%, by comparing our experimental results at the surface region wit those from electron scattering and with the theoretica prediction. A similar estimate for systematical errors wa already obtained in the previous works using the sam method for the ^{12}C, ^{16,18}O stable nuclei [3,4].

We have obtained the ^{6}He experimental density (se Fig. 4) from the data analyses of the angular distribution for the ^{6}He + ^{58}Ni system at $E_{Lab} = 9.0$ MeV. I Ref. [23], the ^{4,6}He nuclear densities were obtained fro elastic scattering data analyses for the ^{4,6}He + p systems at 700 MeV/nucleon, using the Glauber multipl scattering theory for the interaction. In that work, different parametrizations for the ^{6}He density have been tested: symmetrized Fermi (SF) distribution; Gaussian with halo (GH); a gaussian for the core and two different models for the valence nucleons, Gaussian (GG) and 1p-shell harmonic oscillator-type density (GO). All these distributions provided very similar density values (from data analyses) for the ^{6}He density in the radial distance region $0 \leq r \leq 5\ fm$. For the purpose of comparison, the corresponding SF distributions for the ^{4,6}He nuclei are included in Fig. 4 (solid lines). The experimentally extracted densities of that work are in good agreement with our density values at the sensitivity radii, in spite of the very different energies, systems, and assumptions of the two works.

In Fig. 4, we also show two theoretical calculations (from [24,25]), using Faddeev wave function models, for the ^{6}He density. These models incorporate different n-n and n-p potentials with variation of the two-neutron binding energy. The different shapes (2pF or HO) assumed for the distribution in the present work provide results for the ^{6}He density that approach both theoretical calculations at different sensitivity radii (see Fig. 4). Thus, the statistical and systematical errors of our method do not allow one to distinguish which theoretical calculation for the ^{6}He is better. However, the good agreement between experimental and theoretical results is evident, corroborating that the effect of the two extra neutrons of the ^{6}He greatly increases the density at the surface region in comparison with that of the ^{4}He nucleus.

In Ref. [13], with the aim of systematizing the heavy-ion nuclear densities for stable nuclei, we have calculated theoretical distributions for a large number of nuclei using the Dirac-Hartree-Bogoliubov model. We have determined that the average value for the density diffuseness is 0.50 fm and the dispersion associated with this value, due to effects of the structure of the nuclei, is about 0.025 fm. The value for the diffuseness of the exotic ^{6}He, obtained from the theoretical calculations [24,25] (see Fig.4), is about 0.65 fm, very far from the average value for stable nuclei. Within this context, we could also say that the ^{4}He is an eccentric nucleus, since the corresponding 2pF and SF distributions (see Fig. 4) provide $a \approx 0.3\ fm$.

In summary, in this work we have obtained experimental density values in the surface region for the ^{4,6}He nuclei from low energy data analyses. The assumptions of the method have been fully discussed and several checks of the results have been provided. The parameter-free real part of the interaction used in this work contains as basic inputs just the well known M3Y effective nucleon-nucleon interaction and our model for the Pauli nonlocality, which has been extensively tested. Also the imaginary part of the interaction has been based on very general assumptions: the lack of surface absorption at low energies and the parameter-free Lax type interaction, which is known to be quite appropriate for intermediate energies. We have also determined statistical and systematical errors for the experimental density values. The systematical errors arise from several possible sources: the dependence of the position of the sensitivity radius on the shape assumed for the projectile distribution; the theoretical density assumed for the target; the contribution of the real part of the polarization potential, that arises from nonelastic couplings, which has not been included in our analysis; etc. The value of about 20% obtained for the systematical error in the ^{4}He case is very similar to those found for other nuclei in previous works. Thus, we consider that the systematical error for the ^{6}He should also be about 20%, or even somewhat greater because in this case the effect of the reaction channels on the real part of the polarization might be more significant. Therefore, efforts to decrease cross section data uncertainties would not be very useful in the present case. Even so, for purpose of comparison between the ^{6}He and ^{4}He densities, this systematical error ($\approx 20\%$) is actually not very significant, because at the surface region the ^{6}He density is about two orders of magnitude greater than that for ^{4}He. Finally, within the precision of the method, our experimentally extracted result for the ^{6}He density in the surface region is in very good agreement with theoretical predictions, and it is also compatible with other experimental results obtained under quite different conditions in a previous work.

This work was partially supported by Financiadora de Estudos e Projetos (FINEP), Fundação de Amparo à Pesquisa do Estado de São Paulo (FAPESP), and Conselho Nacional de Desenvolvimento Científico e Tecnológico (CNPq).

---

[1] I. Tanihata *et al*, Phys. Lett. **B160**, 380 (1985).

[2] T. Kobayashi *et al*, Phys. Rev. Lett. **60**, 2599 (1988).

[3] M. A. G. Alvarez, E. S. Rossi Jr., C. P. Silva, L. R. Gasques, L. C. Chamon, D. Pereira, M. N. Rao, B. V. Carlson, C. De Conti, R. M. Anjos, P. R. S. Gomes, J. Lubian, S. Kailas, A. Chatterjee and P. Singh, Phys. Rev. **C65** 014602 (2002).

[4] L. R. Gasques, L. C. Chamon, C. P. Silva, D. Pereira, M. A. G. Alvarez, E. S. Rossi Jr, V. P. Likhachev, B. V. Carlson and C. De Conti, Phys. Rev. **C65** 044314 (2002).

[5] E. S. Rossi Jr., D. Pereira, L. C. Chamon, C. P. Silva, M. A. G. Alvarez, L. R. Gasques, J. Lubian, B. V. Carlson and C. De Conti, Nuc. Phys. **A707** 325 (2002).

[6] M. Y. Lee, F. D. Becchetti, T. W. O'Donnell, D. A. Roberts, J. A. Zimmerman, V. Guimarães, J. J. Kolata, D. Peterson, P. Santi, P. A. De Young, G. F. Peaslee and J. D. Hinnefeld, Nucl. Instr. and Meth in Phys. Res. **A422** 536 (1999).

[7] E. F. Aguilera, J. J. Kolata, F. M. Nunes, F. D. Becchetti, P. A. De Young, M. Goupell, V. Guimarães, B. Hughey, M. Y. Lee, D. Lizcano, E. Martinez-Quiroz, A. Nowlin, T. W. O'Donnell, G. F. Peaslee, D. Peterson, P. Santi and R. White-Stevens, Phys. Rev. Lett. **84** 5058 (2000).

[8] E. F. Aguilera, J. J. Kolata, F. D. Becchetti, P. A. De Young, J. D. Hinnefeld, Á. Horváth, L. O. Lamm, Hye-Young Lee, D. Lizcano, E. Martinez-Quiroz, P. Mohr, T. W. O'Donnell, D. A. Roberts and G. Rogachev, Phys. Rev. **C63** 061603 (2001).

[9] H. H. Chang, B. W. Bridley, T. M. Braid, T. W. Colon, E. F. Gibson and N. S. P. King, Nucl. Phys. **A270**, 413 (1976).

[10] D. A. Goldberg, S. M. Smith, H. G. Pugh, P. G. Roos and N. S. Wall, Phys. Rev. **C7** 1938 (1973).

[11] J. Albinski, A. Budzanowski, H. Dabrowski, Z. Rogalska, S. Wiktor, H. Rebel, D. K. Srivastava, C. Alderlieste, J. Bojowald, W. Oelert, C. Mayer-Böricke and P. Turek, Nucl. Phys. **A445** 477 (1985).

[12] B. Bonin, N. Alamanos, B. Berthier, G. Bruge, H. Faraggi, J. C. Lugol, W. Mittig, L. Papineau, A. I. Yavin, J. Arvieux, L. Farvacque, M. Buenerd and W. Bauhoff, Nucl. Phys. **A445** 381 (1985).

[13] L. C. Chamon, B. V. Carlson, L. R. Gasques, D. Pereira, C. De Conti, M. A. G. Alvarez, M. S. Hussein, M. A. Candido Ribeiro, E. S. Rossi Jr. and C. P. Silva, Phys. Rev. **C66** 014610 (2002).

[14] M. A. Cândido Ribeiro, L. C. Chamon, D. Pereira, M. S. Hussein and D. Galetti, Phys. Rev. Lett. **78** 3270 (1997).

[15] L. C. Chamon, D. Pereira, M. S. Hussein, M. A. Cândido Ribeiro and D. Galetti, Phys. Rev. Lett. **79** 5218 (1997).

[16] L. C. Chamon, D. Pereira and M. S. Hussein, Phys. Rev. **C58** 576 (1998).

[17] M. A. G. Alvarez, L. C. Chamon, D. Pereira, E. S. Rossi Jr., C. P. Silva, L. R. Gasques, H. Dias and M. O. Roos, Nucl. Phys. **A656** 187 (1999).

[18] R. M. Devries and M. R. Clover, Nucl. Phys. **A243** 528 (1975).

[19] M. S. Hussein, R. A. Rego and C. A. Bertulani, Phys. Rep. **201** 279 (1991).

[20] R. J. Glauber, Lectures in theoretical physics, (Interscience, New York, 1959) vol 1, p. 315; High-energy physics and nuclear structure, (Plenum, New York, 1970), p. 207.

[21] B. V. Carlson and D. Hirata, Phys. Rev. **C62** 054310 (2000).

[22] D. Galetti, M. A. Talarico and A. F. R. de Toledo Piza, to be submitted.

[23] G. D. Alkhazov et al., Phys. Rev. Lett. **78** 2313 (1997).

[24] J. S. Al-Khalili, J. A. Tostevin and I. J. Thompson, Phys. Rev. **C54** 1843 (1996).

[25] M.V. Zhukov, D.V. Fedorov, B.V. Danilin, J.S. Vaagen, J.M. Bang and I.J. Thompson, Nucl. Phys. **A552** 353 (1993).

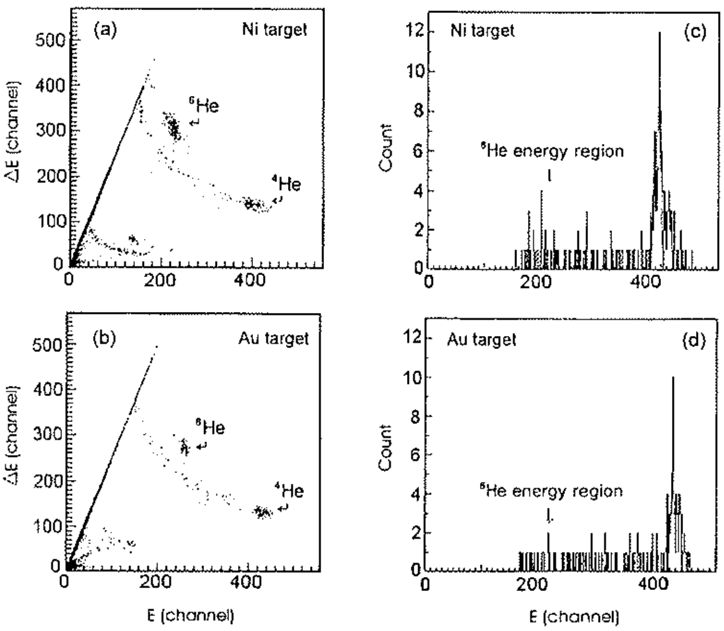

FIG. 1. Typical ΔE *vs* E spectra obtained using (a) ^{58}Ni and (b) ^{197}Au targets. The corresponding energy projections for the ^{4}He ions are shown in (c) and (d), respectively. The arrows in (c) and (d) indicate the energy region that corresponds to the elastic scattering of the ^{6}He.

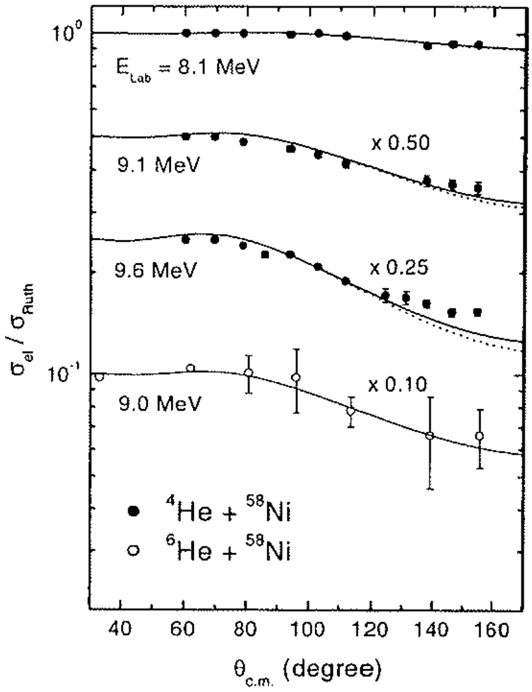

FIG. 2. Elastic scattering angular distributions for the ^{4,6}He + ^{58}Ni systems at several near-barrier energies. The lines represent optical model predictions with (solid lines) or without (dotted lines) considering the compound-elastic contribution.

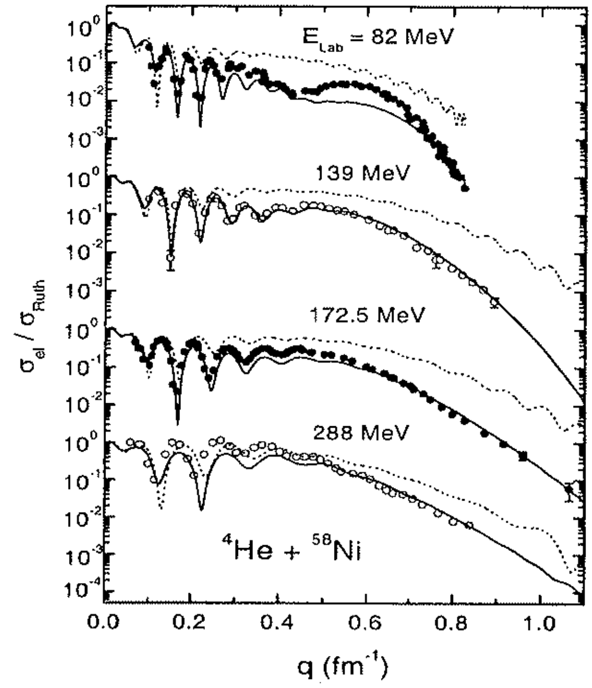

FIG. 3. Elastic scattering angular distributions as a function of the momentum transferred for the ^{4}He + ^{58}Ni system at several intermediate energies. The lines represent optical model predictions, in which the nonlocal model has been assumed for the real part of the interaction, with a Lax-type (dashed lines) or a Woods-Saxon shape (solid lines) for the imaginary part of the potential.

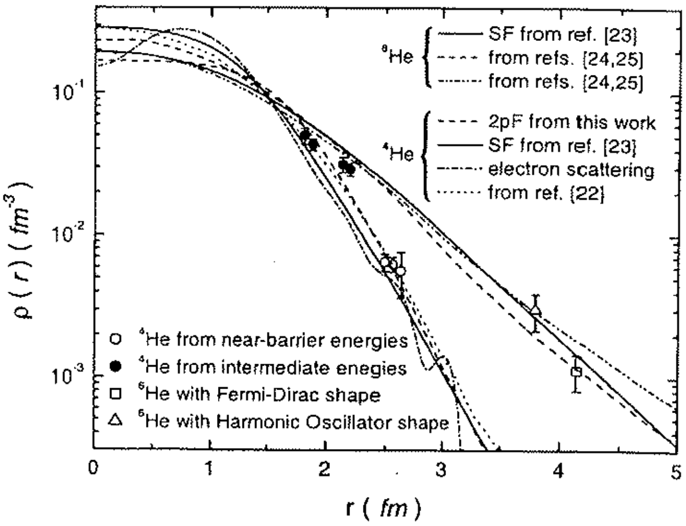

FIG. 4. Experimental nuclear density values at the sensitivity radii for the ^{4,6}He nuclei (open symbols), as obtained from near-barrier elastic scattering data analyses for the ^{4,6}He + ^{58}Ni systems. The closed symbols represent density values (^{4}He) from intermediate energy data analyses, using the nonlocal model and the Lax-type interaction for the real and imaginary parts of the potential. Also presented in the figure are our best fit two-parameter Fermi (2pF) distribution for the ^{4}He, the experimentally extracted symmetrized Fermi (SF) distributions from Ref. [23], theoretical densities for the ^{4}He (Ref. [22]) and ^{6}He (Refs. [24,25]), and a total nucleon density for ^{4}He obtained from electron scattering experiments.